University of Wollongong

Research Online

University of Wollongong Thesis Collection 2017+

University of Wollongong Thesis Collections

2019

Silicon microdosimetry in hadron therapy using Geant4

David Bolst
University of Wollongong

Follow this and additional works at: https://ro.uow.edu.au/theses1

University of Wollongong

Copyright Warning

You may print or download ONE copy of this document for the purpose of your own research or study. The University does not authorise you to copy, communicate or otherwise make available electronically to any other person any copyright material contained on this site.

You are reminded of the following: This work is copyright. Apart from any use permitted under the Copyright Act 1968, no part of this work may be reproduced by any process, nor may any other exclusive right be exercised, without the permission of the author. Copyright owners are entitled to take legal action against persons who infringe their copyright. A reproduction of material that is protected by copyright may be a copyright infringement. A court may impose penalties and award damages in relation to offences and infringements relating to copyright material. Higher penalties may apply, and higher damages may be awarded, for offences and infringements involving the conversion of material into digital or electronic form.

Unless otherwise indicated, the views expressed in this thesis are those of the author and do not necessarily represent the views of the University of Wollongong.

Recommended Citation

Bolst, David, Silicon microdosimetry in hadron therapy using Geant4, Doctor of Philosophy thesis, School of Physics, University of Wollongong, 2019. https://ro.uow.edu.au/theses1/619

Research Online is the open access institutional repository for the University of Wollongong. For further information contact the UOW Library: research-pubs@uow.edu.au

UNIVERSITY
OF WOLLONGONG
AUSTRALIA

Silicon microdosimetry in hadron therapy using Geant4

David Bolst

This thesis is presented as part of the requirements for the conferral of the degree:

Doctor of Philosophy

Supervisor:
Associate Professor S. Guatelli

Co-supervisors:
Professor A. B. Rosenfeld & Dr. L. T. Tran

The University of Wollongong
School of Physics, Centre for Medical Radiation Physics

2019

This research has been conducted with the support of an Australian Government Research Training Program Scholarship.

Declaration

I, *David Bolst*, declare that this thesis is submitted in partial fulfilment of the requirements for the conferral of the degree *Doctor of Philosophy*, from the University of Wollongong, is wholly my own work unless otherwise referenced or acknowledged. This document has not been submitted for qualifications at any other academic institution.

David Bolst

July 26, 2019

Abstract

Hadron therapy, referring to treating cancer with protons and heavier ions, provides many advantages over conventional X-ray radiotherapy, including better dose conformity and dose sparing to healthy tissue. One open problem associated with hadron therapy is that the radiobiological effectiveness (RBE), which is an important input parameter in the clinical treatment planning, changes significantly along the Bragg peak/spread out Bragg peak. It is paramount to be able to estimate the RBE to improve the treatment in terms of clinical outcome. The solution proposed by the Centre For Medical Radiation Physics (CMRP), University of Wollongong, is given by silicon-based microdosimetry technology, which offers a powerful solution to estimate the RBE with sub-mm spatial resolution. Such high spatial resolution is particularly important at the distal edge of the Bragg peak/spread out Bragg peak where organs at risk may be positioned.

Microdosimetry is conventionally performed using tissue equivalent proportional counters which feature complex and bulky operation and do not achieve a sub-mm spatial resolution. Silicon microdosimetry offers a more simple compact design, which is more well suited to the sharp dose gradients of hadron therapy beams and for routine quality assurance measurements. However, silicon microdosimetry is not without its difficulties, namely the measurement is not tissue equivalent and the design is not angularly independent.

This thesis describes the in-silico characterisation and design optimisation of novel silicon microdosimeters developed at the CMRP. The study has been performed by means of the Geant4 Monte Carlo Toolkit, which has been validated against experimental measurements in this project to quantify its accuracy for hadron therapy and for microdosimetric studies.

The tissue equivalence and angular dependence have been investigated. A method to convert the response of the detector from silicon to tissue was developed, which is now routinely used at the CMRP to convert experimental microdosimetric measurements to tissue, in proton and carbon ion therapy.

Due to the strong directionality of hadron therapy beams and the angular dependence of the silicon microdosimeter designs, it was found that the traditional method of converting the energy deposition to lineal energy using the mean chord length of the silicon sensitive volumes (SVs) of the device was inappropriate. Instead, the mean path length was found to be more appropriate to generate the lineal energy deposition. Based on the results of this project, the SV design was optimised to reduce the variance of the path length to reduce the angular dependence.

Acknowledgments

I would like to thank everyone who has contributed to making this thesis, but if forced to point some fingers I must give particular thanks to the following people.

Firstly I would like to thank A/Prof. Susanna Guatelli for all her help and guidance over the years of being my supervisor and the opportunities she has provided me with in this project.

Prof. Anatoly Rosenfeld for all his invaluable knowledge and input over the years to help shape this work.

Thanks to Dr. Linh Tran and Lachlan Chartier for their chats about microdosimetry and commiseration over hot food.

Finally I would like to thank my partner Vanja for all her support over the years during this thesis.

Publications

List of first author peer-reviewed publications:

- **D. Bolst**, S. Guatelli, L. Tran, L. Chartier, M. Lerch, N. Matsufuji and A. Rosenfeld, “Correction factors to convert microdosimetry measurements in silicon to tissue in 12C ion therapy”, *Physics in Medicine Biology*, (62), 2017
- **D. Bolst**, G.A.P. Cirrone, G. Cuttone, G. Folger, S. Incerti, V. Ivanchenko, T. Koi, D. Mancusi, L. Pandola, F. Romano, A. Rosenfeld and S. Guatell, “Validation of Geant4 fragmentation for Heavy Ion Therapy”, *Nuclear Inst. and Methods in Physics Research, A*, (869), 2017
- **D. Bolst**, L. Tran, L. Chartier, D. Prokopovich, A. Pogossov, S. Guatelli, M. Reinhard, M. Petasecca, M. Lerch, N. Matsufuji, V. Perevertaylo, C. Fleta, G. Pellegrini, M. Jackson and A. Rosenfeld, “RBE study using solid state microdosimetry in heavy ion therapy”, *Radiation Measurements*, (106), 2017
- **D. Bolst**, S. Guatelli, L. Tran, and A. Rosenfeld, “Optimisation of the design of SOI microdosimeters for hadron therapy quality assurance”, *Physics in Medicine Biology*, (63), 2018

List of first author peer-reviewed publications currently under review:

- **D. Bolst**, S. Guatelli, L. Tran, and A. Rosenfeld, “The impact of sensitive volume thickness for silicon on insulator microdosimeters in hadron therapy”
- **D. Bolst**, S. Guatelli, L. T. Tran, L. Chartier, J. Davis, D. A. Prokopovich, A. Pogossov1, M. I. Reinhard M. Petasecca, M. L. F. Lerch, N. Matsufuji , M. Povoli, A. Summanwar, A. Kok, M. Jackson and A. B. Rosenfeld, “Validation of the Geant4 simulation for silicon microdosimetry in heavy ion therapy”

List of book chapters:

- S Guatelli, **D Bolst**, Z Francis, S Incerti, V Ivanchenko and A Rosenfeld, “Physics Models for Monte Carlo Simulations in Carbon Ion Therapy”, (Accepted)

List of co-author peer-reviewed publications:

- L Tran, L Chartier, **D Bolst**, D Prokopovich, M Reinhard, M Petasecca, M Lerch, A Kok, N Matsufuji, M Nancarrow, and A Rosenfeld, "3D Silicon Microdosimetry and RBE Study Using^{12}CIon of Different Energies", *IEEE Transactions on Nuclear Science*, (62), 2015
- L Chartier, L Tran, **D Bolst**, D Prokopovich, S Guatelli, M Nancarrow, M Reinhard, M Petasecca, M Lerch, V Pereverlaylo, N Matsufuji, D Hinde, M Dasgupta, A Stuchbery, M Jackson, and A Rosenfeld, "3D Silicon Microdosimetry and RBE Study Using^{12}CIon of Different Energies", *IEEE Transactions on Nuclear Science*, (62), 2015
- F Cadini, **D Bolst**, S Guatelli, C Beltran, M Jackson, A. Rosenfeld, "Neutron shielding for a new projected proton therapy facility: A Geant4 simulation study", *Physica Medica*, (32), 2016
- M Zarifi, S Guatelli, **D Bolst**, B Hutton, A Rosenfeld, Y Qi, "Characterisation of prompt gamma-ray emission with respect to the Bragg peak for proton beam range verification: A Monte Carlo study", *Physica Medica*, (33), 2017
- V Gracanin, S Guatelli, D Cutajar, I Cornelius, L. Tran, **D Bolst**, R Preston, R Gupta, J Yuen, M Petasecca, M Lerch, V Prevertaylo, A Rosenfeld, "A convenient verification method of the entrance pho-neutron dose for an 18MV medical linac using silicon p-i-n diodes", *Radiation Measurements*, (106), 2017
- L Tran, L Chartier, **D Bolst**, A Pogossov, S Guatelli, M Petasecca, M Lerch, D Prokopovich, M Reinhard, B Clasie, N Depauw, H Kooy, J Flanz, A McNamara, H Paganetti, C Beltran, K Furutani, V Perevertaylo, M Jackson, A Rosenfeld, "Characterisation of proton pencil beam scanning and passive beam using a high spatial resolution solid state microdosimeter", *Medical Physics*, (44), 2017
- L Chartier, L Tran, **D Bolst**, S Guatelli, A Pogossov, D Prokopovich, M Reinhard, V Perevertaylo, S Anderson, C Beltran, N Matsufuji, M Jackson, A Rosenfeld, "Microdosimetric Applications in Proton and Heavy Ion Therapy using Silicon Microdosimeters", *Radiation Protection Dosimetry*, (180), 2018
- L Tran, **D Bolst**, S Guatelli, G Biasi, A Fazzi, E Sagia, D Prokopovich, M Reinhard, Y Keat, M Petasecca, M Lerch, A Pola, S Agosteo, N Matsufuji, M Jackson, A Rosenfeld, "High spatial resolution microdosimetry with monolithic ΔE-E detector on ^{12}C beam: Monte Carlo simulations and experiment", *Nuclear Inst. and Methods in Physics Research, A*, (887), 2018

- L Tran, **D Bolst**, S Guatelli, M Petasecca, M Lerch, L Chartier, D Prokopovich, M Reinhard, M Povoli, A Kok, V Perevertaylo, N Matsufuji, T Kanai, M Jackson, A Rosenfeld, “The relative biological effectiveness for carbon, nitrogen and oxygen ion beams using passive and scanning techniques evaluated with fully 3D silicon microdosimeters”, *Medical Physics*, (45), 2018
- L Tran, L Chartier, **D Bolst**, J. Davis, D Prokopovich, A. Pogossov, S Guatelli, M Reinhard, M Petasecca, M Lerch, M Povoli, A Kok, V Perevertaylo, N Matsufuji, M Jackson, A Rosenfeld, “In-field and out-of-file application in 12C ion therapy using fully 3D silicon microdosimeters”, *Radiation Measurements*, (115), 2018
- E Debrot, **D Bolst**, B James, L Tran, S Guatelli, M Petasecca, D Prokopovich, M Reinhard, N Matsufuji, M Lerch, A Rosenfeld, “Investigating variable RBE in a ^{12}C minibeam field with microdosimetry and Geant4”, *Radiation Measurements*, (Accepted)
- E Debrot, L Tran, L Chartier, **D Bolst**, S Guatelli, C Vandevoorde, E de Kock, P Beukes, J Symons, J Nieto-Camero, D A Prokopovich, S Chiriotti, A Parisi, M De Saint-Hubert, F Vanhavere, J Slabbert, A B Rosenfeld, “SOI microdosimetry and modified MKM for evaluation of relative biological effectiveness for a passive proton therapy radiation field”, *Physics in Medicine Biology*, (63), 2018
- B. James, L. T. Tran, J. Vohradsky, **D. Bolst**, V. Pan, M. Carr, S. Guatelli, A. Pogossov, M. Petasecca, M. Lerch, D. A. Prokopovich, M. I. Reinhard, M. Povoli, A. Kok, D. Hinde, M. Dasgupta, A. Stuchbery, V. Perevertaylo, A. B. Rosenfeld, “SOI Thin Microdosimeter Detectors for Low Energy Ions and Radiation Damage Studies”, *IEEE Transactions on Nuclear Science*, (Accepted)
- A Parisi, S Chiriotti, M De Saint-Hubert, O Van Hoey, C Vandevoorde, P Beukes, E de Kock, J Symons, J Nieto-Camero, J Slabbert, P Megret, E Debrot, **D Bolst**, A Rozenfeld, F Vanhavere, ”A novel methodology to assess linear energy transfer and relative biological effectiveness in proton therapy using pairs of differently doped thermoluminescent detectors”, *Physics in Medicine Biology*, (Accepted)

List of conference proceedings:

- **D Bolst**, L Tran, S Guatelli, N Matsufuji, A Rosenfeld, “Modelling the Biological Beamline at HIMAC using Geant4”, *Journal of Physics Conference Series*, 2019

Thesis Outline

This thesis investigates the use of novel silicon microdosimeters developed by the Centre For Medical Radiation Physics, University of Wollongong, in hadron therapy by means of the Monte Carlo toolkit Geant4.

Chapter 1 provides a literature review of the main physical interactions in hadron therapy and the concepts of microdosimetry.

Chapter 2 shows the benchmarking study of Geant4 against experimental measurements for carbon ion therapy, necessary to quantify the accuracy of the Monte Carlo code in the context of this project.

Chapter 3 reports the investigation of methods to convert silicon energy deposition measurements to tissue equivalent lineal energy, in hadron therapy.

Chapter 4 describes the optimisation of silicon sensitive volume's design for silicon microdosimetric devices, when used in hadron therapy, based on the methods found in chapter 3.

Chapter 5 investigates the impact which different sized sensitive volumes has on the microdosimetric spectra and quantities.

Chapter 6 describes the validation of Geant4 for silicon microdosimetry by comparing Geant4 against experimental measurements for ^{12}C , ^{14}N and ^{16}O beams, adopting the methods found in chapter 3.

Chapter 7 - illustrates the characterisation of the response of the “Bridge” microdosimeter in proton therapy.

Chapter 8 presents the conclusions and recommendations deriving from the results of this project.

Contents

Chapter 1

Literature Review

This chapter provides a brief overview of the main concepts investigated in this thesis, namely, the physical interactions involved in hadron therapy and the concepts of microdosimetry/silicon microdosimetry important for hadron therapy quality assurance. Finally, a brief introduction to the Geant4 Monte Carlo toolkit is provided.

1.1 Introduction

Radiotherapy was first used two months after the discovery of x-rays in 1895 by Röntgen [1]. Radiotherapy is the treatment of cancer by delivering radiation to cancer cells to kill them, whilst at the same time trying to minimise the radiation delivered to healthy tissues. Since the start of radiotherapy the most common radiation used remains to be photons, generated using medical linear accelerators (LINACs). The idea to harness heavy charged particles was first proposed by Robert R. Wilson in 1946 [2]. The first patient was treated with proton therapy in 1954 at the Lawrence Berkeley Laboratory (LBL) led by Cornelius Tobias who later investigated the use of alpha particles and other heavier ions. Using ions larger than protons to treat patients in clinical trials was first carried out with ^{4}He beams at the Bevalac facility at the LBL beginning in 1975 [3] and shortly after in 1977 ^{20}Ne ions, as well as other ions, began being trialled. Up until the closure of Bevalac in 1992 there had been 2054 patients treated using ^{4}He and a further 433 patients treated using other ions (predominately ^{20}Ne ions) [4] [5]. Following the closure of Bevalac, treatment using ions has been dominated by ^{12}C , with 21,580 patients worldwide having been treated with ^{12}C ion radiotherapy by 2016 [4]. First clinical trials using ^{12}C ions were performed in Japan starting in 1994 by the National Institute of Radiological Sciences (NIRS) at the Heavy Ion Medical Accelerator in Chiba (HIMAC).

In Australia, one in two men and one in three women are diagnosed with cancer by the age of 85, with approximately half of cancer treatments using radiotherapy [6]. Radiotherapy treatments in Australia are currently performed using only photon sources, with some electron treatments used occasionally; these treatments are predominantly delivered using a medical LINAC. The way which photons from a LINAC deposit energy in a patient is characterised by a large amount of energy at the surface (a few millimetres under the skin, after the build-up) and a tailing dose. Hadron therapy is a type of radiotherapy which uses hadrons, including protons (proton therapy) and other larger ions such as carbon nuclei (carbon ion therapy). Protons and heavier ions are charged particles which lose energy continuously via electromagnetic interactions and have nuclear interactions with the target, producing nuclear recoils and fragments. They deposit the maximum of energy at the end of their well-defined range, called the Bragg Peak (BP). Figure 1.1 shows how different beams deposit energy in a water box representing a patient (call a phantom). It can be seen that the charged particles deposit energy in a much more localised region, which is advantageous for sparing dose to healthy tissue outside the tumour.

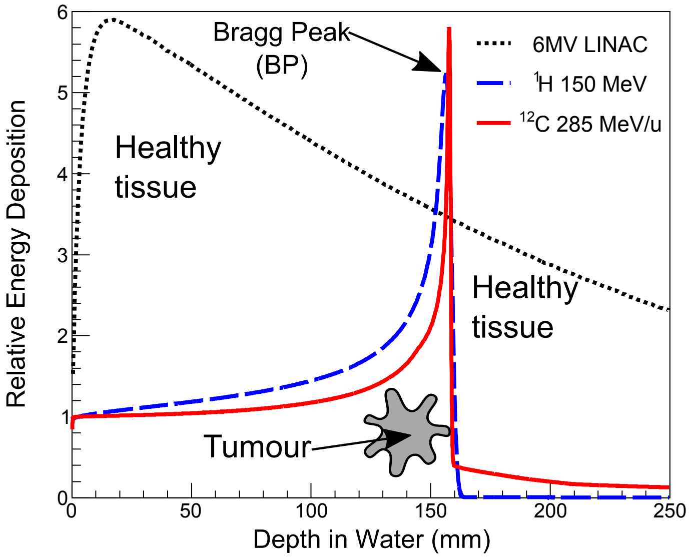

Figure 1.1: Comparison of how different radiotherapy beams deposit energy in a water phantom. The 6MV LINAC curve is a photon beam and is representative of the most common radiotherapy beam currently used in Australia, ^{1}H and ^{12}C are proton and carbon 12 nuclei beams, respectively.

Despite the reduction of radiation to healthy tissue, hadron therapy poses some added challenges compared to conventional photon radiotherapy which include:

- a sharp energy deposition gradient at the BP, meaning measurement equipment require high spatial resolution, less than a millimetre for accurate measurements,
- a more complex radiation field due to nuclear interactions,
- a changing biological effectiveness along the Bragg curve, meaning less radiation dose is required to achieve the same biological endpoint.

It is important to ensure that the radiation treatment delivered to a patient matches with the planned treatment.

Microdosimetry is the approach developed by Rossi and Zaider [7] to study the effect of radiation at the cellular level, starting from the energy deposition distribution in micron sized volumes representing biological cells. Microdosimetry is particularly suitable for hadron therapy because it can be applied to mixed radiation fields.

Microdosimetry measurements are traditionally performed using tissue equivalent proportional counters (TEPCs), which are detectors with measuring volumes of the order of 10 mm in diameter, filled with a low pressure gas which mimics the same energy losses which would occur in a cell. TEPC's large size mean that they are not well suited to the sharp dose gradients at the end of the BP and their large size and operation can make them difficult and time consuming to make measurements.

Silicon microdosimeters offer many advantages over TEPCs including true micron sizes for the detector volumes, making detailed measurements of the end beam's path possible. Silicon designs also permit compact and simple operation, this makes it ideal for quality assurance since measurements can be performed quickly and the biological effect of the beam can be estimated and compared to the planned treatment. Silicon microdosimeters have the potential to improve the quality assurance of hadron therapy treatments, improving the effectiveness of the treatments delivered to patients [8] [9] [10]. The need for such devices is becoming more important as the number of hadron therapy facilities around the world continues to increase.

Despite the potential advantages of silicon microdosimetry, such technology has some complications compared to TEPCs, including the lack of tissue equivalence and not being able to manufacture spherical sensitive volumes.

This thesis investigates the use of silicon microdosimetry for quality assurance in hadron therapy by means of Monte Carlo simulations. It provides a methodology to convert experimental measurements from silicon to tissue and to reduce the angular dependence of the device. The results are then used to improve the design of the device. Monte Carlo simulations were used because, once their accuracy is established, they allow to the effects of the complex mixed radiation field of hadron therapy to be studied and in the case of the microdosimetric response, allowing a better understanding of experiments.

1.2 Monte Carlo in radiotherapy

Monte Carlo simulations are extensively used in radiotherapy and are considered the gold standard when calculating the radiation dose from a source [11]. Some example applications which Monte Carlo is used for include: secondary radiation dose to a patient [12], patient motion [13], shielding of facilities [14] and the optimisation of designs such as beam shaping equipment [15] and detectors [16]. The work presented throughout this thesis uses the Geant4 toolkit to perform Monte Carlo simulations.

Geant4 (**GE**ometry **AN**d **T**racking) [17] [18] [19] is a widely used Monte Carlo toolkit which emerged from a research project based at CERN in 1994 to replace the existing Monte Carlo code, Geant3, which had been released in 1974 [20]. The first public release of Geant4 was in 1998 and was written in the C++ language to take advantage of object-orientated functionality, Geant4 differs from many other commonly used general purpose Monte Carlo codes such FLUKA [21], MCNP [22] and PHITS [23] which are FORTRAN based codes. The development of Geant4 is currently carried out by over a 100 scientists from various institutes around the world.

Being a toolkit a user cannot simply "run" Geant4 "out of the box" but must write an application built upon the Geant4 kernel. A user application requires a minimum of a description of the experimental set-up where primary particles are generated and tracked while interacting with the target. Secondary particles, emerging from the interactions in the experimental set-up, are tracked as well. The minimum requirements for a Geant4 application is the inclusion of three classes which are called the *DetectorConstruction*, *PrimaryGeneratorAction* and the *PhysicsList* classes.

Geant4 is used in a wide range of applications, with available physics ranging from energies as low as eV and up to TeV. Both electromagnetic and hadronic physics interactions are modelled. Specific models exist to describe the interactions of optical photons and low energy particles down to few eV.

When using Monte Carlo codes, it is important to quantify the accuracy of the models being used compared to experimental measurements, particularly when used for studies relevant to human safety. There have been many studies applicable to medical physics performed using Geant4, which have compared experimental measurements against simulation results for a range of different applications. Some of these tests include: X-ray imaging [24], range of beams in materials [25] [26] and fragmentation of ion beams [27] [28]. Performing routine testing of Monte Carlo releases is important to monitor any changes to the results. In Geant4 there exists many tests which are performed for each release with many being able to be viewed online at `https://geant-val.cern.ch/`.

1.3 Electromagnetic interactions in hadron therapy

This section summarises the main physical concepts concerning the electromagnetic (EM) interactions of particles in matter, relevant for hadron therapy. Physics models used in Geant4 to describe such interactions are included as well.

1.3.1 Stopping Power

The main appeal of hadron therapy, using protons or heavier ions, is its ability to spare dose to healthy tissue compared to conventional photon radiotherapy. As shown earlier in figure 1.1, photon beams have a tailing dose profile. Charged beams instead have a well-defined finite range and a maximum dose deposited at the end of its range, the Bragg Peak (BP). The shape of the BP is mainly[a] due to electromagnetic (EM) interactions which occur more or less continuously as a charged particle traverses a medium. The average amount of energy, dE, an ion loses to a medium per unit of path dx is termed the *stopping power*, S or dE/dx, shown in equation 1.1.

$$-\frac{dE}{dx} = S_e + S_n + S_r \tag{1.1}$$

The three terms are the electronic or collision stopping power (S_e), the nuclear stopping power (S_n) and the radiative stopping power (S_r) [29]. Nuclear stopping power describes the elastic energy loss between the projectile and target nuclei while the radiative stopping power describes the emission of bremsstrahlung radiation.

At therapeutic energies the energy lost by ions to a medium is dominated by in-elastic Coulomb interactions with atomic electrons, which are either excited or ionised [30]. This phenomenon is described by the electronic stopping power term.

Nuclear stopping power only becomes significant below 10^{-1} MeV/u and becomes the dominant term at $\sim 10^{-3}$ MeV/u for a ^{12}C ions, while radiative stopping power can be neglected entirely.

There have been many formulations to quantify the electronic stopping power, starting from 1905 by Bragg and Kleeman [31] and by Bohr in 1915 [32] to Bethe in 1930 [33], which had quantum effects added soon after by Bloch in 1933 [34]. The description of stopping power formulated by Bloch, usually referred to as the Bethe-Bloch formula, is widely used to calculate the stopping power of ions and is shown in equation 1.2. This can then be used to calculate the range of ions in a medium.

$$S_e = \frac{dE_e}{dx} = \frac{4\pi e^4 k_e^2 N Z_p^2}{m_0 c^2 \beta^2}\left[\ln\left(\frac{2m_0 c^2 \beta^2}{I(1-\beta^2)}\right) - \beta^2\right] \tag{1.2}$$

- e^- magnitude of an electron's charge equal to 1.602×10^{-19}C
- m_0 rest mass of an electron equal to 511 keV/c^2
- k_e is Coulomb's constant equal to 8.99×10^9Nm^{2}C^{-2}
- N is the electron density of the target material

---

[a] As shown later, hadronic interactions at the energies of interest for hadron therapy influence the shape of the BP and are responsible for the dose tail behind the distal edge.

- Z_p is the projectile charge
- c is the speed of light in a vacuum equal to 3×10^8 m/s
- β is the ratio of the projectile's velocity to c
- I is the mean excitation energy of the medium, which for water is ∼75-78 eV

In Geant4, electronic stopping power is calculated using the Bethe-Bloch formula for energies above 2 MeV/u. For energies below 2 MeV/u the ICRU parameterised values are used. For proton and α particles ICRU49 [35] values, for larger ions, if the target/projectile target exists in the ICRU73 tables [36] they are used, otherwise the ICRU49 values are scaled based on the mass and charge of the ion [26].

1.3.2 Linear energy transfer

A similar term which is sometimes used interchangeably with stopping power is the *linear energy transfer*, LET or L, and is shown in equation 1.3. Equation 1.3 is what is referred to as the "restricted" LET or restricted linear electronic stopping power form of LET [29]. The quotient dE/dx is the mean energy lost to a medium by a charged particle via electronic interactions in a unit path length, dx, excluding any electrons created with an energy above Δ. For example $\mathrm{LET}_{100\mathrm{eV}}$ would be the energy a charged particle loses to a medium excluding any electrons it generates with an energy of or above 100 eV. The distinction between stopping power and the restricted LET (LET_Δ) is that LET_Δ is more representative of the energy imparted to a certain local region defined by the value of Δ while the stopping power represents the total energy a charged particle loses when traversing a medium. When no subscript is written LET should be assumed to be the *unrestricted* LET or LET_∞ or L_∞, the unrestricted LET is identical to the stopping power.

$$\mathrm{LET}_\Delta = \left(\frac{dE}{dx}\right)_\Delta \tag{1.3}$$

1.3.3 Straggling

Due to the stochastic nature of energy loss at microscopic scales, there are fluctuations in the amount of energy lost to a medium which causes variations in the range of ions. This straggling of the range becomes more prominent for higher energy beams where the range increases in the target medium.

The fluctuations of energy lost in a medium by a charged particle are dependent on the number of ionisations and excitations which occur and how much energy is transferred in each of these collisions.

The number of ionisations/excitations follow a Poisson distribution while the energy transferred in these events depend on single collision spectra for the projectile and medium

[7]. Single collision spectra for thick targets follow a Gaussian distribution, while for thin targets follow more complex asymmetrical distributions. Many theoretical descriptions have been formulated to describe experimental collision spectra such as Vavilov [37].

The number of ionisations and excitations in a medium are proportional to Z^2/v^2, where Z is the charge of the projectile and v is its velocity. This increased ionisation for higher atomic ions reduces the overall variation of energy lost per length and is reflected in figure 1.2. Figure 1.2 shows the Bragg curves of different ion beams with the same range in water, it can be seen that the lighter ions have an increased broadening at the BP.

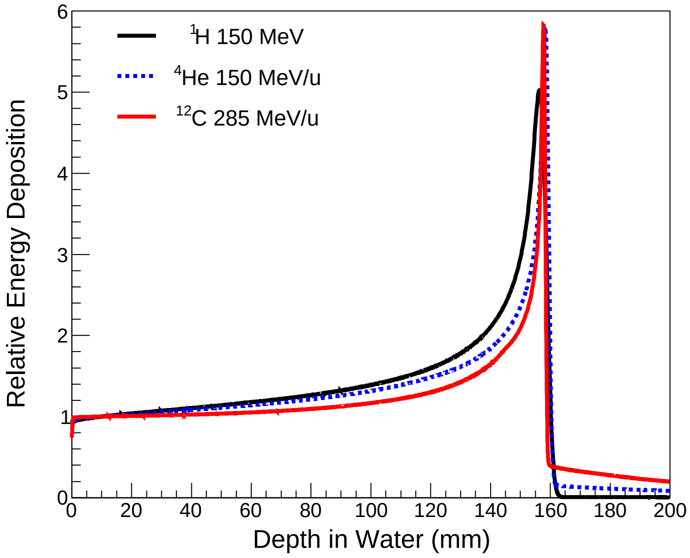

Figure 1.2: Comparison of the depth dose profile for different ions in water, illustrating the effect of range straggling.

1.3.4 Coulomb scattering

As a projectile traverses a medium, its path can be deflected when interacting with target nuclei via Coulomb interactions. Single deflections, called single Coulomb scattering, generally will not cause a large deflection of the particle's trajectory but after multiple scatters with target nuclei the change in the trajectory can become noticeable, this effect is referred to as multiple Coulomb scattering (MCS) [38]. The amount of scattering that a projectile will undergo within a medium was analytically described by Moliére [39] and was found to agree well with experimental scatter results. For small angles, which are representative of protons and heavier ions, the angle, θ, which a projectile has scattered at some depth, d, in a target can be approximated by equation 1.4 [40].

$$\sigma_\theta = \frac{14.1MeV}{\beta pc} Z_p \sqrt{\frac{d}{L_{rad}}} \left[1 + \frac{1}{9}\log_{10}\left(\frac{d}{L_{rad}}\right)\right] \tag{1.4}$$

Here Z_p and p is the charge and momentum of the projectile particle, respectively. The radiation length, L_{rad}, describes how charged particles and photons interact with matter based upon the target's density and charge [41]. The values of L_{rad} for water and air are similar to one another with values of 36.08 and 36.66 g/cm^2 with larger element targets having lower values of L_{rad}, lead having a value of 6.37 g/cm^2 [42]. The p term in the denominator means that for larger projectiles such as ^{12}C ions with a mass 12 times larger than protons results in ^{12}C and other larger ions having much less lateral beam spread, allowing for a potentially more conformal treatment plan. Comparing a 150 MeV proton to a 285 MeV/u ^{12}C ion beam the lateral beam spread is approximately three times higher with the proton beam than the ^{12}C beam [43]. A comparison of the effect of multiple Coulomb scattering can be seen in figure 1.3 which shows the lateral dose profile of a spot beam of a proton, ^{4}He and ^{12}C ion beam 10 mm before the BP.

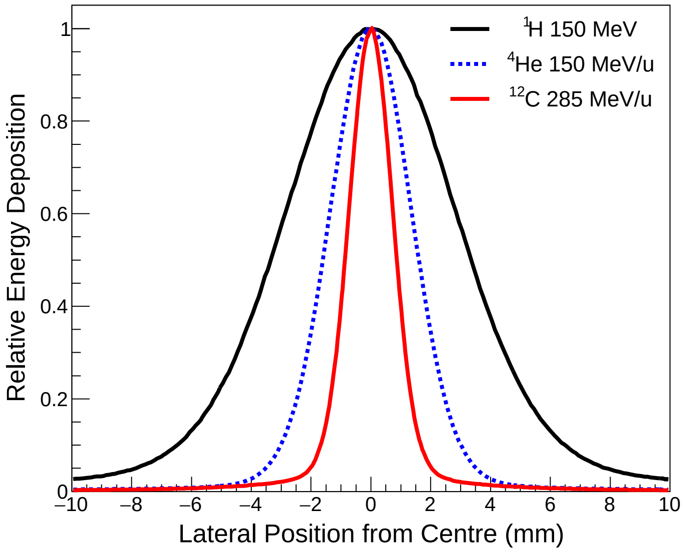

Figure 1.3: Comparison of the lateral energy deposition 10 mm before the BP for different ions in water and illustrating the effect of the projectile ion scattering off target nuclei.

1.4 Nuclear interactions in hadron therapy

As a hadron beam traverses a medium its fluence will reduce due to inelastic nuclear interactions with target nuclei, examples of different beams being attenuated are shown in 1.4. The amount which a beam is attenuated represents its total reaction cross section, σ_R, also called the absorption cross section.

In order for an inelastic nuclear reaction to occur the energy of the incident projectile must surpass the Coulomb barrier, B, to overcome the Coulomb repulsion. The value of B can be calculated by $B = Zze^2/R$ where Z and z are the atomic numbers of the target and

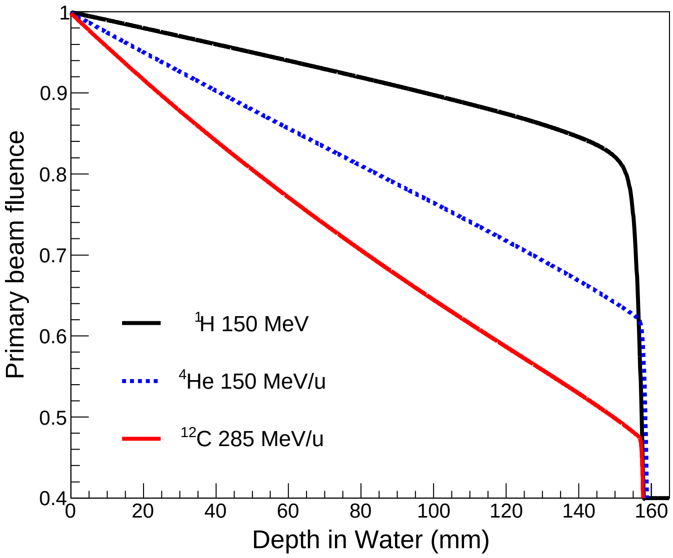

Figure 1.4: Comparison of the attenuation of different ion beams in water.

projectile, e is the electric charge and R is the distance at which the nuclear strong force can overcome the Coulomb repulsion [44]. Due to quantum tunnelling there exists a small probability of inelastic nuclear reactions when the energy is smaller than B, which can be seen in figure 1.5. Figure 1.5 shows the total inelastic cross section of protons incident upon carbon and oxygen targets, both these reactions are particularly relevant for hadron therapy. The Coulomb barrier for these reactions involving protons is $\sim$8 MeV [45] and it can be seen how reactions still occur slightly below B.

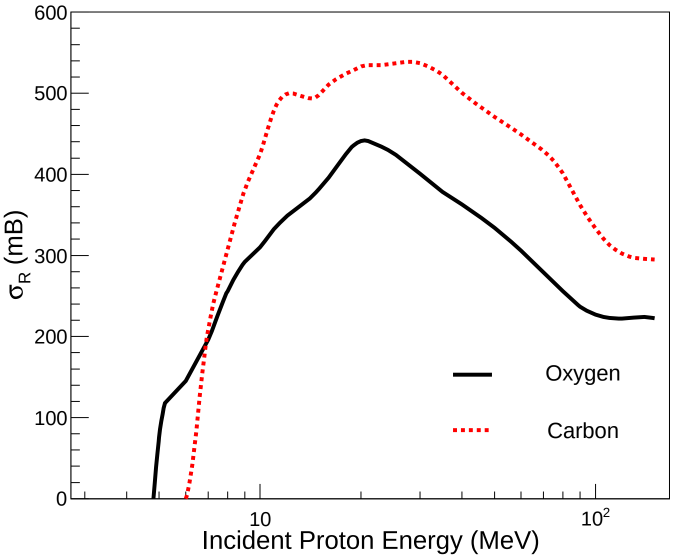

Figure 1.5: Example total reaction cross section of a proton incident upon carbon and oxygen targets. Data come from [46] and [47] for the carbon and oxygen, respectively.

σ_R values more specific to ^{12}C ion therapy are shown in table 1.1 for ^{12}C beams incident upon thin ^{12}C targets which have been measured by Kox et al. [48]. The results show that the production of fragments does not vary largely for therapeutic energies above ∼100 MeV/u for ^{12}C beams. A similar study was also performed by Menet et al. [49] using proton beams incident upon ^{12}C targets also and are shown in table 1.2. It can be seen that the chance of a ^{12}C beam interacting in-elastically with the medium is ∼2-3 times larger than with protons. Due to the much higher cross section in carbon beams, and other similar heavier ions, compared to proton beams the nuclear reactions are much more prominent and important to consider, such as fragmentation processes.

Energy (MeV/u)	σ_R (mb)
9.33	1444±50
83	965±30
200	864±45
250	873±60
300	858±60

Table 1.1: The total reaction cross section, σ_R, for ^{12}C ions of various energies incident upon a thin ^{12}C target. Values come from [48].

Energy (MeV)	σ_R (mb)
30	447±20
40	371±11
60.8	310±13

Table 1.2: The total reaction cross section, σ_R, for proton beams of various energies incident upon a thin ^{12}C target. Values come from [49].

1.4.1 Fragmentation

With all external beam radiation treatment modalities, irradiation to healthy tissue cannot be avoided, with higher doses increasing the chance of inducing secondary cancer as a result from the treatment [50]. At therapeutic energies (up to 400 MeV/u), the ^{12}C ion beam generates a complex radiation field, with ∼70% of the primary ions undergoing fragmentation before the BP [51].

A representation of the nuclear fragmentation process is depicted in figure 1.6 using the abrasion-ablation model [52]. The process involves the overlap of nucleons from the projectile nucleus with nucleons of the target nucleus. Such overlapping nucleons produce an excited pre-fragment product. The excited product de-excites into smaller nuclei, the projectile fragment continues to travel on a path close to the original trajectory with a similar velocity, while the target fragment remains almost stationary, receiving only a small amount of kinetic energy. Both the projectile and target fragments may also de-excite.

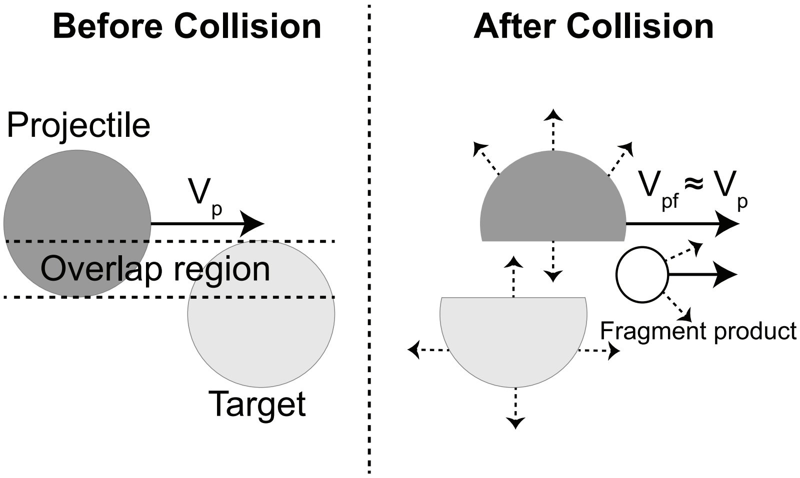

Figure 1.6: Representation of the fragmentation process of the projectile and target nucleus having an overlap region which results in the creation of an excited product which will de-excite by emitting nucleons and smaller fragments (depicted by the dashed arrows).

Nuclear fragmentation is an important process to be considered in ^{12}C therapy since it transports dose from the treatment target and deposits it beyond the BP and laterally, delivering dose to healthy tissue as well as altering the relative biological effectiveness (discussed below). The effect of fragmentation can be seen in figure 1.7, which shows the the relative dose deposited in a $30 \times 30 \times 30$ cm^3 water phantom from a $10{\times}10$ cm^2 290 MeV/u incident ^{12}C beam. The top left plot shows the 1D depth dose distribution, showing the contribution of the primary ^{12}C beam as well as secondary fragments. It can be seen that the contribution from the primary ^{12}C beam slightly decreases with depth due to it continuously undergoing fragmentation up until the start of the BP. The secondary fragments extend quite far beyond the range of the primary ^{12}C . The bottom left plot of figure 1.7 shows a 2D dose distribution from the primary ^{12}C beam while the top right shows the total dose being distributed within the phantom while the bottom right shows the dose due to helium fragments, one of the fragments with the highest yields in ^{12}C therapy.

The modelling of a nuclear interaction between a projectile and a target is treated by Geant4 in three stages at relevant energies for hadron therapy [53], [54]:

1. A cascade model is used to sample interactions between the projectile and target nuclei and generates high energy secondary particles, leaving the target nucleus excited.
2. A pre-compound model is then used to describe the nucleus from the excited state to the nuclear equilibrium. Equilibrium is reached when the number of all transitions are equally probable.
3. A de-excitation model is then used to de-excite the nucleus

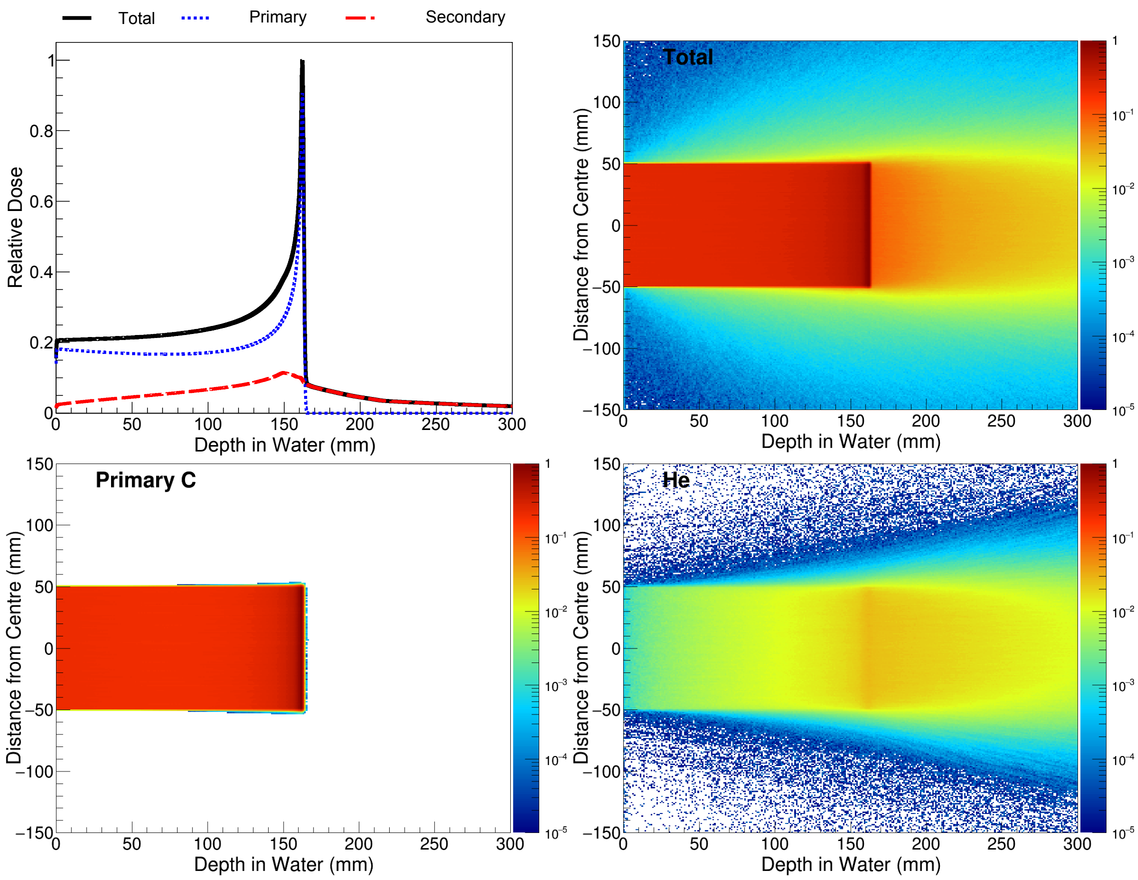

Figure 1.7: The radiation field produced by a mono-energetic 290 MeV/u ^{12}C beam incident upon a water phantom. Top left shows the 1D depth dose distribution of the beam including the primary and secondary components of the radiation field. Bottom left shows a 2D distribution of the primary ^{12}C beam in the water phantom. Top right shows the distribution of the total dose in the phantom including from the primary beam and the secondary particles it generates. Bottom right shows the dose which Helium fragments deposit in the phantom which extends beyond the BP and laterally from the primary beam.

Due to the complexity of hadronic interactions there does not exist a single model which describes all possible processes for the entire energy range (0-100 TeV in Geant4), instead multiple models are used to describe processes over a certain energy range and for different particles.

Figure 1.8 shows the relevant hadronic processes for projectile energies up to 100 TeV. Each process must have cross sections assigned, the probability of a process occurring (cross section) is independent of the model used, with the model deciding the final state of the projectile and target system. Multiple models may be used to describe a single process with default energy ranges for the model being able to be changed by the user. Processes require that there are no energy ranges which have no model available and that models do not cover the same energy range (for example two models cannot both start and end from energies x-y). When multiple models overlap in a certain energy range the model is chosen randomly via uniform linear sampling.

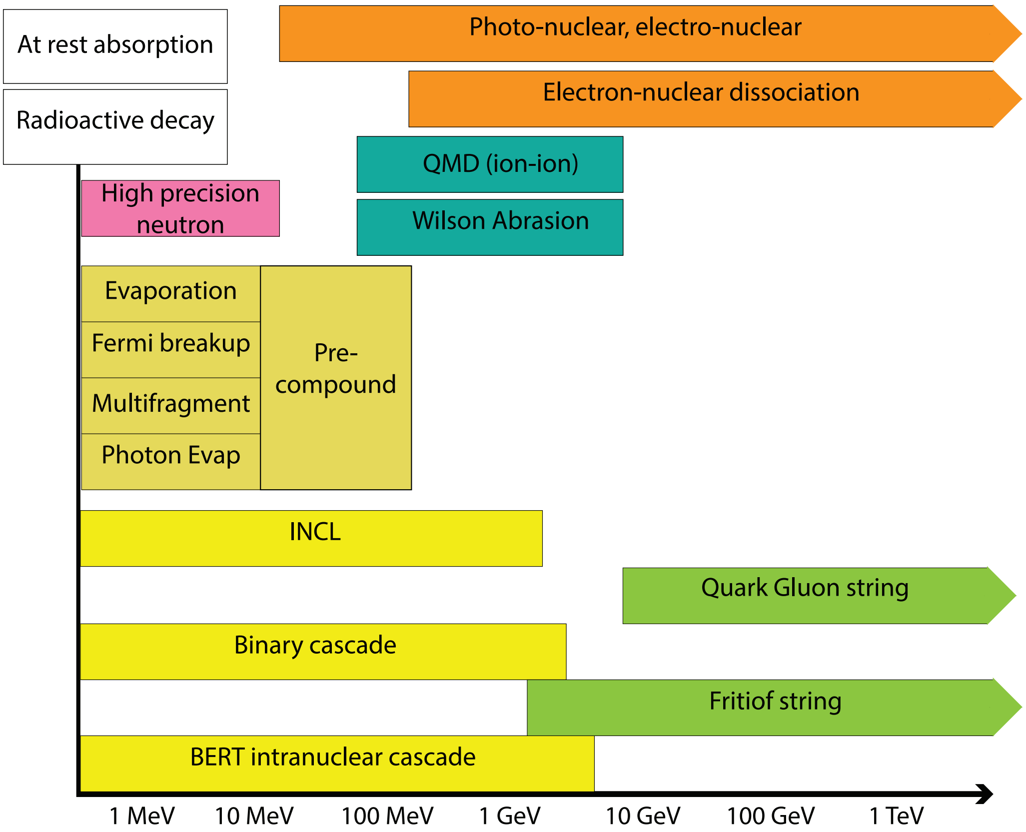

Figure 1.8: A sample of the hadronic physics models available in Geant4.

For fragmentation at therapeutic energies and targets there exists three main applicable models in Geant4, the Binary Intranuclear Cascade (BIC), the Quantum Molecular Dynamics (QMD) and the Liege Intranuclear Cascade (INCL++). The BIC model describes the interaction between a projectile and a single nucleon of the target nucleus interacting in the overlap region as Gaussian wave functions. The QMD model instead considers all nucleons of the target and projectile, each with their own wave function; this inherently causes QMD to have greater computation times than BIC. Unlike the other two models, INCL++ models the nucleons as a free Fermi gas in a static potential well. The targets and projectiles which can be modelled by the INCL++ model are limited to a mass number of $A = 18$. For higher A values of both the projectile and target the fragmentation is modelled using BIC. More details on the BIC, QMD and INCL++ physics models can be found in the Geant4 Physics Reference Manual [55].

Due to the impact on the radiation field, it is important to accurately model the fragmentation to predict and minimise the dose to healthy tissue delivered by the treatment plan. Thus it is important to benchmark and to validate the models used to study the radiation field against experimental measurements, which is performed in a chapter of this thesis.

1.5 Microdosimetry

Microdosimetry is the method of measuring the energy deposition from radiation in volumes of the order of microns, representing the dimensions of biological cells/nuclei [7], [56]. At these scales the stochastic nature of energy loss due to the fluctuations in the number of ionisations/excitations in the medium and the amount of energy transferred in each of these events becomes significant [57], [58]. Microdosimetry is a particularly convenient method for estimating the biological effect of a radiation field, regardless if it is a single particle source or a complicated mixed radiation field. The radiation field produced in hadron therapy is particularly complex due to the various inelastic hadronic interactions [30], making microdosimetry particularly well suited for characterising the radiation field for both in-field [10] and out-of-field [59].

1.5.1 Microdosimetric Quantities

The fundamental quantity in microdosimetry is the mean lineal energy, y, which is defined in equation 1.5, where ε is the energy deposited in the sensitive volume (SV) with micrometer sizes and $\langle l \rangle$ is the mean chord length.

$$y = \frac{\varepsilon}{\langle l \rangle}, \tag{1.5}$$

A similar quantity is the specific energy, z, which is defined in equation 1.6, where m is the mass of the sensitive volume. The mean specific energy, $\langle z \rangle$ is equivalent to the non-stochastic quantity of dose.

$$z = \frac{\varepsilon}{m} \tag{1.6}$$

Returning to lineal energy, the value of $\langle l \rangle$ for a convex solid with a volume of V and surface area S can be calculated by Cauchy's formula as shown in equation 1.7. Equation 1.7 is applicable when the distribution of random chords in the volume follow a μ-randomness [60], or isotropic, distribution.

$$\langle l_{Cauchy} \rangle = \frac{4V}{S} \tag{1.7}$$

There have been many equations formulated to describe the distribution of chords in different shaped volumes under a μ-randomness distribution [61], [62]. Example chord distributions of a sphere and a cube are shown in figure 1.9 with the equations of these distributions shown below.

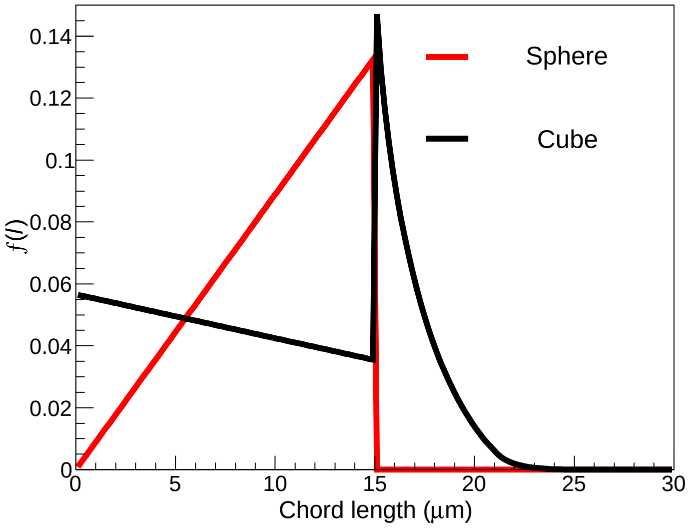

Figure 1.9: Example chord distributions for a sphere with a diameter of 15 μm and a cube with edges of 15 μm, these distributions have a mean chord length of 10 μm.

$$f(l) = \begin{cases} l, & l \le d \\ 0, & l > d \end{cases}$$

$$\text{where } d = \text{diameter of sphere}$$

$$f(l) = \begin{cases} \frac{8}{3s\pi}, & l = 0 \\ k(8x^3 - 3x^4), & 0 < l \le 1 \\ k(6\pi + 6x^4 - 1 - 8(2x^2+1)\sqrt{x^2-1}), & 1 < l \le \sqrt{2} \\ k(6\pi - 3x^4 - 5 + 8(x^2+1)\sqrt{x^2-2} - 24\tan^{-1}(\sqrt{x^2-2})), & \sqrt{2} < l \le \sqrt{3} \end{cases}$$

$$\text{where } x = l/s, s = \text{cube's side length }, k = \frac{1}{3s\pi x^3}$$

The lineal energy is usually measured experimentally by using a multi-channel analyser (MCA) which enables the amount of energy deposited in a certain timing window to be recorded. An example MCA, or energy deposition spectrum, at the BP of a mono-energetic 290 MeV/u ^{12}C ion beam is shown in figure 1.10 (top plot). Using the energy deposition spectrum the lineal energy frequency distribution, $f(y)$, can then be obtained by dividing the energy deposition (x-axis) by $\langle l \rangle$ and normalising the distribution to 1. From $f(y)$, a number of useful quantities can be calculated, these include the frequency mean lineal energy y_F and the dose mean lineal energy y_D. y_F is the first moment of $f(y)$ and y_D is the ratio of the second and first moment of $f(y)$ which is shown in equations 1.8

and 1.9, respectively.

$$y_F = \int y f(y) dy \tag{1.8}$$

$$y_D = \frac{\int y^2 f(y) dy}{\int y f(y) dy} = \frac{\int y^2 f(y) dy}{y_F} \tag{1.9}$$

An alternative to $f(y)$ is the dose distribution, $d(y)$, this is shown in equation 1.10. Unlike $f(y)$, which represents the proportion of events with a certain lineal energy, $d(y)$ represents the proportion of the dose in the SV due to a particular lineal energy.

$$d(y) = \frac{y f(y)}{y_F} \tag{1.10}$$

Example $f(y)$ and $d(y)$ distributions generated from the energy deposition spectrum in figure 1.10 (top) are shown in figure 1.10 (middle plots). Due to the stochastic nature of the energy distribution, as well as the complicated mix of different particles making up a radiation field, the range of lineal energies which are deposited in a SV can extend over many orders of magnitude. Because of the large range in the energy deposition, microdosimetric measurements are commonly displayed on a semi-log plot with the x-axis being log and bin sizes being logarithmically spaced. The example spectra shown in figure 1.10 (top and middle plots) were plotted on a logarithmic x-axis but used linearly spaced bins, using logarithmic spaced bins greatly reduce the visual effects of noise. Example logarithmically binned data is shown in figure 1.10 (bottom) using the same data from the middle plots, it should be noted that the y-axis is now $yf(y)$ and $yd(y)$ for the $f(y)$ and $d(y)$ distributions, respectively. The reason for the change in the y-axis comes from re-binning the linear spaced y bins to log spaced bins, with the relation shown in equation 1.11. More details on the method of re-binning linear bins to log can be found in Appendix B of the ICRU 36 report [57], just note that equation B.9 contains a typographical error and should be $\int d(y)dy = 1$ instead of $\int yd(y)dy = 1$.

$$\begin{aligned} \int d(y) dy &= \int y d(y) d(\ln y) \\ &= \ln(10) \int y d(y) d(\log y) \end{aligned} \tag{1.11}$$

1.5.2 Different particle types

As shown above, the calculation of the lineal energy assumes a constant value for the $\langle l \rangle$. This assumption is valid provided that the particles depositing energy in the SV originate outside of the SV and exit the SV before stopping. Such an event where the particle originates outside the SV and exits the SV is what is referred to as a *crosser*. When performing microdosimetric measurements it is usually important that the majority of

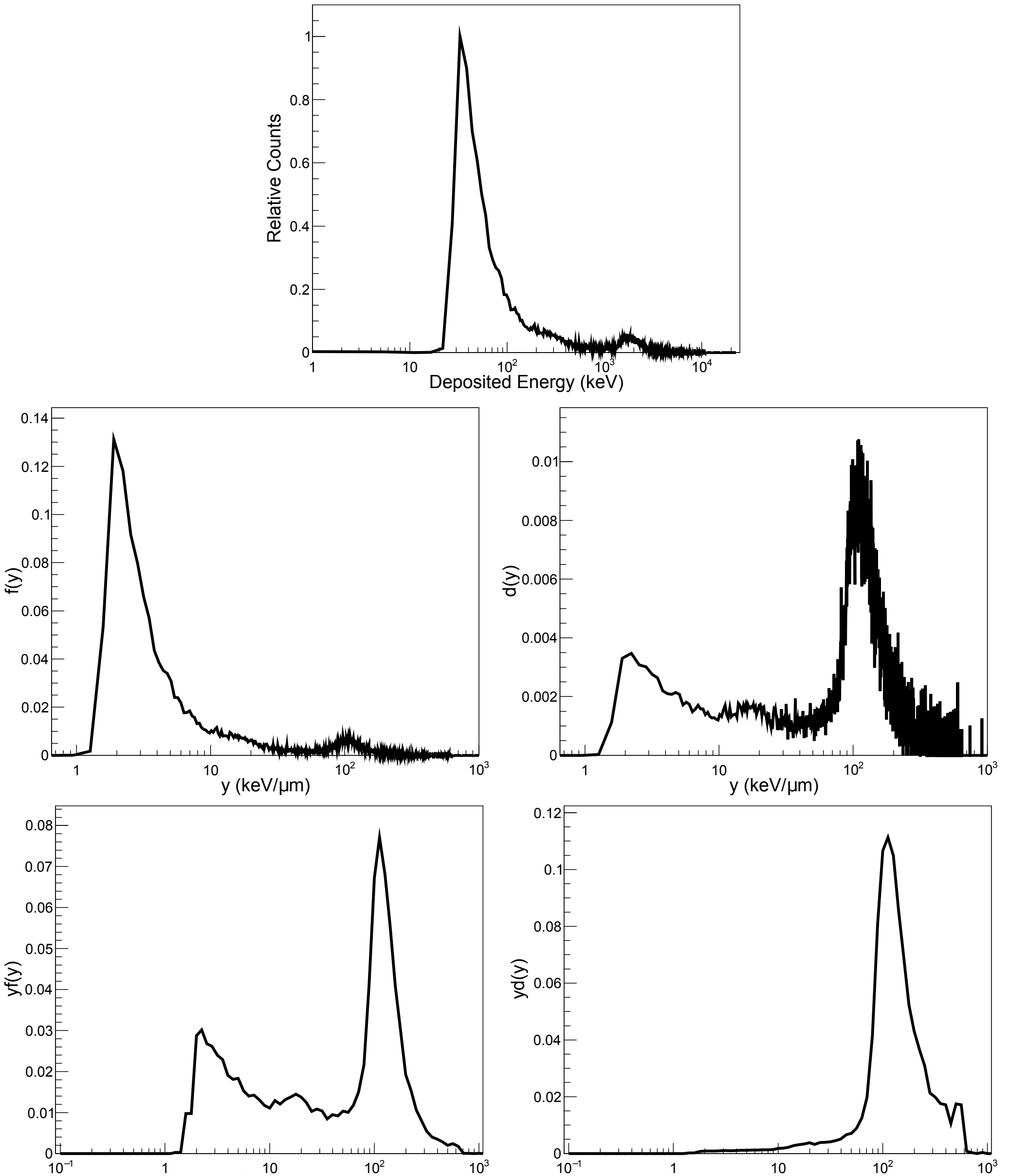

Figure 1.10: The top plot shows an example energy deposition spectrum (MCA) obtained from irradiating a 10 μm thick SV silicon microdosimeter at the BP of a 290 MeV/u ^{12}C ion in water, this data is in linear bins but plotted on a logarithmic x-axis. The middle images show the $f(y)$ and $d(y)$ distributions generated from the top energy deposition spectrum, left and right respectively, this data is in linear bins but plotted on a logarithmic x-axis. The bottom plots shows the same data as the middle plots except that the data has been re-binned into logarithmic spaced bins, due to this rebinning the quantities change from $f(y)$ and $d(y)$ to $yf(y)$ and $yd(y)$, respectively.

events recorded in a SV are due to crossers so that equation 1.7 is valid, however, it is not possible to guarantee that all events are crossers, particularly when measuring at the distal edge of a BP. To describe the different types of radiation fields which a microdosimeter is placed in, there are a number of different types of particle events which are summarised below [63].

- Crosser - the particle enters and exits the SV
- Stopper - the particle enters but stops in the SV
- Starter - the particle is generated within the SV and exits
- Insider - the particle is generated and stops in the SV

Of the different event types the stopper is usually the most observable type, forming a *stopper peak*. A stopper peak occurs at the very right of a microdosimetric spectrum and represents the maximum energy a type of particle can deposit in the material.

1.6 Biological response from radiation

When targeting a tumour for treatment, the aim is to destroy the cancer cells, however, because it is not possible to kill all cells, without significantly endangering healthy cells, a proportion of cells is chosen to be considered sufficient to prevent continued growth [64].

It is crucial to understand how a cell type will respond to radiation in order to know how much dose needs to be administered to kill the target cancer cells. Determining the response of a certain cell type to radiation is characterised by a cell survival curve. Cell survival curves involve irradiating cells *in vitro* and tracking the number of surviving cell colonies against the dose. An example of a cell survival curve is shown in figure 1.11. In particular, it illustrates the survival of cells after being irradiated alternatively with a photon and an ion beam. It can be seen in figure 1.11 that the cells die with noticeably less dose with the ion beam than the photon beam. This increased killing efficiency is described by the *relative biological effectiveness* (RBE).

The RBE quantifies how efficient a radiation source is to cause a biological effect. One common biological endpoint to compare radiation sources with is the dose required to have only 10% of irradiated cells survive in a population of cells. The RBE is defined as the ratio of dose from a radiation source, D_{Test}, required to give the same biological effect as a reference radiation source when dose D_{Ref} is delivered, shown in equation 1.12. The reference radiation source is commonly photons from cobalt 60.

$$\text{RBE} = \frac{D_{Test}}{D_{Ref}} \tag{1.12}$$

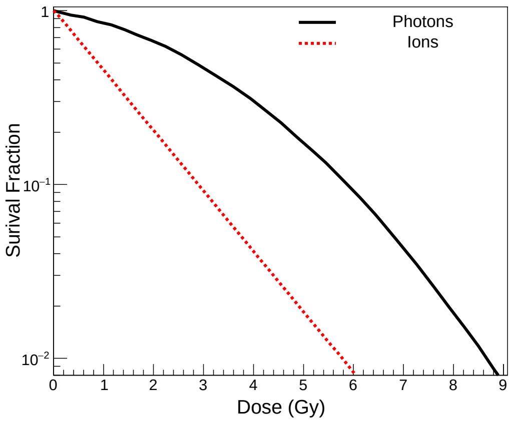

Figure 1.11: Example of cell survival data for cells irradiated in vitro by photons and heavy ions. Plot adapted from [43].

Due to less dose needed to achieve the same biological endpoint, when delivering a plan in heavy ion therapy, instead of using the standard quantity of physical dose ,D, (energy deposited per unit mass) the biological dose, defined as $D\times$RBE, is instead used to prescribe a treatment. It should be emphasied that heavy ion therapy, referring to ions larger than protons, and not hadron therapy (including protons) uses a variable RBE since proton therapy currently uses a constant value of 1.1 for RBE in clinical treatments [65]. The use of a fixed RBE in proton therapy will be discussed further in a later chapter.

The RBE and response of the cells is influenced by many factors including:

- Radiation type
- Cell type
- Dose rate
- Treatment type (Fractionation)
- Oxygen concentration

Overkilling refers to when the DNA has already been killed and further radiation is delivered, since extra dose is being added but no change to the biological effect occurs (the DNA is already dead) means that the RBE decreases, the value of LET where overkilling begins usually starts from ~100-150 keV/μm [66] [67].

The influence of radiation type to cell damage is largely due to different particles producing different track structures with different ionisation densities. Figure 1.12 shows different beams traversing in water with a range of ~30 μm, this figure was generated in Geant4 using the Livermore low energy model with the production threshold set to 10 eV. The figure has been obtained with a Geant4 simulation. Blue and red represent the tracks of positively charged particles and electrons, respectively. Each yellow dot represents an interaction such as an ionisation. Figure 1.12 shows how drastically the density of the different beams varies and this density corresponds to how likely a double strand break (at the basis of the cellular damage) is likely to occur. If the track density increases to a certain amount then overkilling will begin to occur.

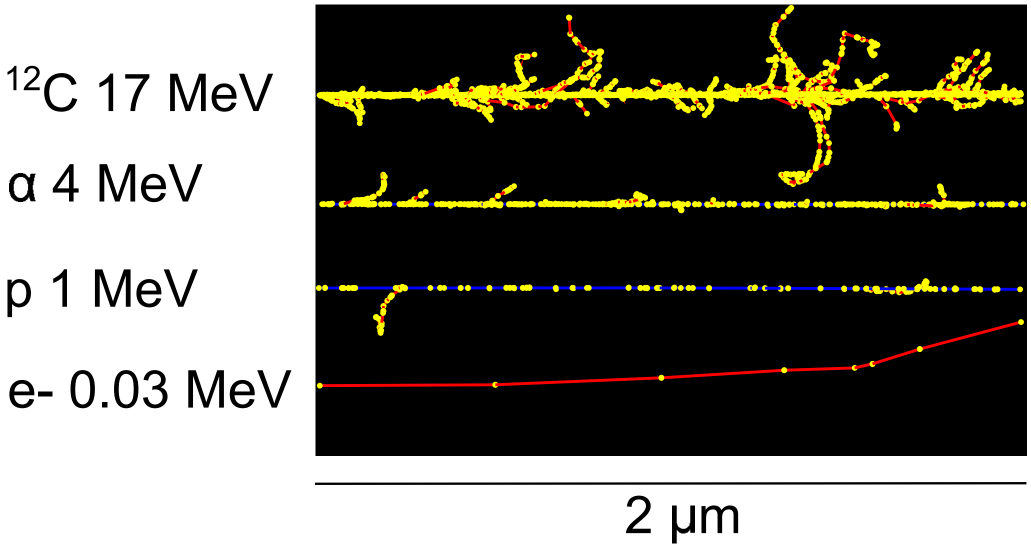

Figure 1.12: Comparison of different ionisation densities of particles in water. The path of electrons and positively charged particles are red and blue, respectively. Each yellow dot representing an interaction, the range of all the particles is $\sim$30 μm in water.

In order to create an effective treatment plan it is paramount that enough dose is delivered to the target volume so that a suitable amount of cells are killed. At the same time it is important that excessive dose is not delivered, to reduce the chance of inducing secondary cancer in healthy tissue. Many different models exist which aim to describe the response of cells to radiation, with hadron therapy, particularly heavy ion therapy, requiring more complex models due to the RBE changing with depth. There have been a number of models developed over the years to describe the response of cells to radiation exposure, some of these models include:

- Linear Quadratic Model (LQM)
- Local Effect Model (LEM)
- Microdosimetric Kinetic Model (MKM)

1.6.1 Linear quadratic model

The linear quadratic model (LQM) is the most common model for describing the cell survival probability and is stated in equation 1.13.

$$S = \exp\left(-\left(\alpha D + \beta D^2\right)\right) \tag{1.13}$$

The survival, S, represents the proportion of surviving cells after some irradiation of dose D, with an S of 1 meaning that all cells survived after being irradiated with dose D. The α and β terms are constants dependent on the cell type, the α term describes the first part of the survival curve, lower LET radiation is characterised with a shoulder at the start of the curve. The β term instead describes the second part of the curve, governed by damage from double hits. The values of the α and β terms are obtained from cell survival experiments [68].

1.6.2 Linear effect model

The local effect model, LEM, was formulated at GSI by Scholz and Kraft [69] for treatment planning of ^{12}C ion beams to estimate their RBE. The basis for the LEM is that the biological response of cells from radiation is due to the track structure of the radiation. The LEM begins with the assumption that after the irradiation of a group of cells with a dose D, that there will be on average N lethal events which cause cell's death. By assuming a Poisson distribution in the number of lethal events, the fraction of cells surviving after being irradiated with a dose D, $S(D)$, can be expressed by equation 1.14.

$$S(D) = \exp(-N(D))N(D) = -\ln S(D) \tag{1.14}$$

Using the LQM (equation 1.13) for the surviving fraction of cells, equation 1.14 can be re-written as:

$$N(D) = \alpha D + \beta D^2 \tag{1.15}$$

If now the nucleus of a cell with volume, V, is assumed to be made up of sensitive sub-nuclear sites then the density of lethal events in the nucleus, $l(D)$, can be expressed as:

$$l(D) = \frac{N(D)}{V} = \frac{-\ln(S(D))}{V} \tag{1.16}$$

It is assumed that one lethal event in a sub-nuclear volume will cause the cell to die. If a cell is irradiated with X-rays the density of lethal events ($l(D)$) will follow a homogenous distribution. If however, the cell volume is only partially irradiated with a volume of ΔV, with a some varying dose distribution of $D(x,y,z)$ to calculate the number of sub-nucleus volumes which receive a lethal dose N_{lethal} the dose distribution must be integrated over the entire volume as shown in equation 1.17.

$$N_{lethal} = \int_x \int_y \int_z \frac{\alpha D(x,y,z) + \beta D(x,y,z)^2}{V} dxdydz \tag{1.17}$$

The proportion of cells which survive will be those which have no lethal events occur and can be written as:

$$S = \exp(-N) \tag{1.18}$$

The LEM calculates the RBE by using α and β values of cells derived X-ray from experiments.

1.6.3 Microdosimetric kinetic model

The microdosimetric kinetic model (MKM) was first formulated by Hawkins in 1994 [70] and was an extension of the theory of dual radiation action (TDRA), which was formulated in the 1970's by Rossi and Kellerer in order to explain the observation that the RBE of neutrons between 100 keV and a few MeV was dependent upon the absorbed dose [71]. The MKM was extended by Kase et al [67] for the model to be used in high LET radiation by accounting for *overkilling*, this form of the MKM is referred to as the modified MKM.

The MKM considers that cell nuclei are made up of sub-nuclear spherical volumes called "domains", the "size" of these domains are cell specific. If a particle track traverses a cell, due to the stochastic nature of energy deposition, there will be a distribution in the amount of energy deposited in the domain volumes. It is then assumed that the probability that a domain survives, S, after some dose, G_d, follows the same form as for low-LET radiation (LQM).

$$S = \exp\left(-AG_d - BG_d^2\right) \tag{1.19}$$

Where A and B are cell specific like α and β in equation 1.13 for LQM. The number of hits occurring in each domain is assumed to follow a Poisson distribution.

The average number of lethal hits, H, for each domain after receiving a specific energy, z, is:

$$H = Az + Bz^2 \tag{1.20}$$

The average number of lethal hits in a nucleus, H_n, with N domains is:

$$\begin{aligned} H_n &= N\langle H\rangle \\ &= N\left(A\langle z\rangle + B\langle z\rangle^2\right) \\ &= (\alpha_0 + \beta z_{1D})D + \beta D^2 \\ &= -\ln S \end{aligned} \tag{1.21}$$

Where D is the dose, z_{1D} is the specific energy in a single event in a domain. The size of a domain can be calculated by:

$$\begin{aligned} z_{1D} &= \frac{\langle l\rangle}{m} y_D \\ &= \frac{y_D}{\rho\pi r_d^2} \end{aligned} \tag{1.22}$$

Where ρ, r_d and $\langle l\rangle$ is the density, radius and mean chord length of the domain, respectively.

To take into account overkilling effects, also called saturation effects, the saturation parameter, y_0, is introduced and can be shown to be equal to:

$$y_0 = \frac{\rho \pi r_d R_n^2}{\sqrt{\beta \left(r_d^2 + R_n^2\right)}} \tag{1.23}$$

Where R_n is the radius of the nucleus instead of the domain (r_d).

The saturation-corrected dose mean lineal energy, $y*$, is defined in equation 1.24. $y*$ is similar to y_D but incorporates over-killing effects at high lineal energies.

$$y^* = y_0^2 \frac{\int (1 - \exp(-y^2/y_0^2)) f(y) dy}{\int y f(y) dy} \tag{1.24}$$

$$\alpha = \alpha_0 + y^* \frac{\beta}{\rho \pi r_d^2} \tag{1.25}$$

$$RBE_{10} = \frac{2\beta D_{10,x-ray}}{\sqrt{\alpha^2 - 4\beta \ln(0.1)} - \alpha} \tag{1.26}$$

By fitting cell survival data for human salivary glands (HSG), exposed to several ions with varying LET, Kase [67] found values for y_0 equal to 150 keV/μm fitted survival data the best. Additionally, the cell specific parameters for HSGs were found to have values of: $r_d = 0.42\mu$m (the radius of the domain), $\rho = 1$g/cm^3 (density of cell's domain), $\alpha_0 = 0.13$Gy^{-1} and $\beta = 0.05$Gy^{-2}. Then the RBE for 10% cell survival, RBE$_{10}$, can be calculated using equation (1.26), where $D_{10,x-ray}$ is the dose required for 10% survival for 200keV x-rays and has a value of 5Gy.

Compared to heavy ion therapy, which does not have a significant dose dependence on RBE, proton beams have been shown to have a dependency with dose which is observed for fractions less than ~4 Gy [72], with RBE increasing with smaller dose fractions. This dose dependency is relevant since proton plans generally deliver single fractions using the Atomic Energy Agency standard of 2 Gy [73]. Due to this dose dependency of RBE in proton beams, the MKM needs to use a slightly altered version to take into account the dose variability [74]. So instead of the RBE taking the form shown in equation 1.26 for ions heavier than protons, the RBE takes the form as shown in equation 1.27.

$$RBE_D = \frac{2\beta D_p}{\sqrt{\alpha_X^2 + 4\beta \left(\alpha D_p + \beta D_p^2\right)} - \alpha_X} \tag{1.27}$$

Here α_X is cell specific and has a value of 0.164 Gy^{-1} and D_p is the physical dose delivered to the cell from the proton beam, RBE is labeled as RBE_D for the dose dependency.

1.7 Experimental microdosimetry

1.7.1 Tissue equivalent proportional counters

Microdosimetry measurements have traditionally been performed using tissue equivalent proportional counters (TEPCs), also called Rossi chambers, the physical sensitive volumes of commercial TEPCs are commonly of the order of 10 mm in diameter and are filled with a tissue equivalent gas which is often methane or propane based [75]. A diagram of a TEPC is shown in figure 1.13. The relatively large volume of the TEPC performs energy deposition measurements, E_g, which represent the energy deposited in micron sized tissue volumes, E_t. The TEPC is capable of making these micron equivalent measurements by using a low pressure gas (approximately a hundredth of atmospheric pressure usually) with a mass stopping power $(S/\rho)_g$ which when scaled by the density and diameter of the SV is equivalent to the product for a micron sized tissue volume, this relationship is summarised in equation 1.28 and is represented in figure 1.14 (where the mass stopping power is the same for both volumes).

$$\begin{gathered}\Delta E_g = \Delta E_t \\ \left(\frac{S}{\rho}\right)_g \rho_g d_g = \left(\frac{S}{\rho}\right)_t \rho_t d_t\end{gathered} \tag{1.28}$$

Traditional commercial TEPCs have a number of limitations, one is its large size, which makes measurements of the BP at the end of an ion's track, which have sharp dose gradients, to have averaging effects. Furthermore, the operation of the TEPC requires a high voltage supply, of the order of several hundred volts and a complex gas supply, meaning portability and setup can be challenging. Furthermore, the design and size of a TEPC with the large SV gas enclosed introduces a number of *wall effects*. These wall effects effect the energy deposition which differs from what would occur for an actual micron sized volume [63].

1.7.2 Silicon Microdosimetry

As an alternative solution, the Centre for Medical Radiation Physics (CMRP), University of Wollongong, has adopted a solid state approach which addresses the limitations of the TEPC and allows a compact portable design with much simpler operation and is free of wall effects. The use of silicon for microdosimetry dates back to 1980 when Dicello et al. performed microdosimetric measurements with a silicon diode [76]. From the late 1990's the CMRP has been extensively involved in the development and use of silicon microdosimeters.

An important challenge in silicon microdosimetry is creating a SV which has a well

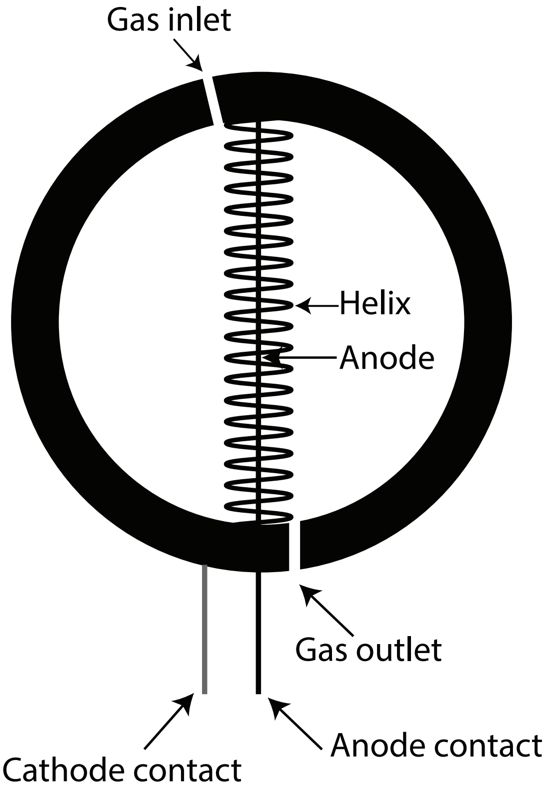

Figure 1.13: A simple diagram showing the main components of a tissue proportional counter (TEPC).

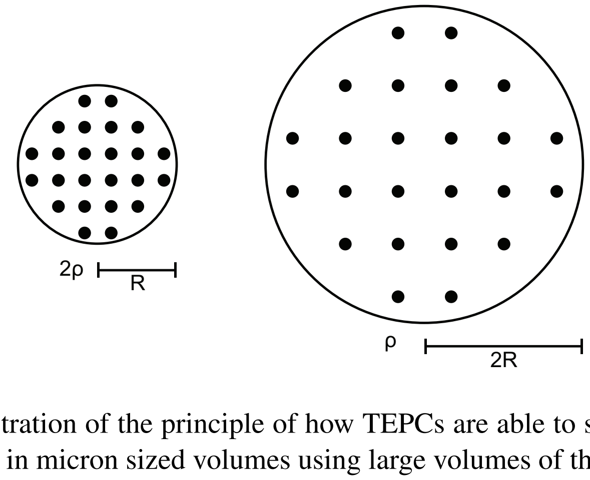

Figure 1.14: Illustration of the principle of how TEPCs are able to simulate the energy deposition spectra in micron sized volumes using large volumes of the order of millimeters by using a very low gas pressure.

defined shape, this is achieved by having a uniform charge collection. The importance of achieving a uniform charge collection and well defined SV is due to the lineal energy being reliant upon the mean chord length of the solid. To determine the charge collection of a device, CMRP uses the ion beam induced charge collection (IBICC) technique. For IBICC studies CMRP uses the ANSTO Heavy Ion Microprobe [77] which raster scans an ion beam which is commonly a 5.5 MeV α beam with a diameter of $\sim$1 μm. By using an analogue to digital converter, the charge collected can be read out into an x-y map, an example of an IBICC image is shown in figure 1.15 (left). Figure 1.15 is from the readout of a plannar device with an 18 μm diameter SV and the right plot shows the energy deposition spectrum of the device when irradiated with a 5.5 MeV α beam. Ideally, the charge collection of the device would be uniform for the SV and not have any charge outside of the intended SV, corresponding to an energy deposition with only a single Gaussian peak. However, due to the complex fabrication techniques at micron sizes means that fabricating a well defined volume proves challenging [78]. Another difficulty with fabrication of micron devices is the yield of SVs which are active on a device. Over the decades, each CMRP designed silicon microdosimeter which has been fabricated has been tested and through testing the devices it has allowed the above properties of charge/SV uniformity and SV yield to be incrementally improved over the years.

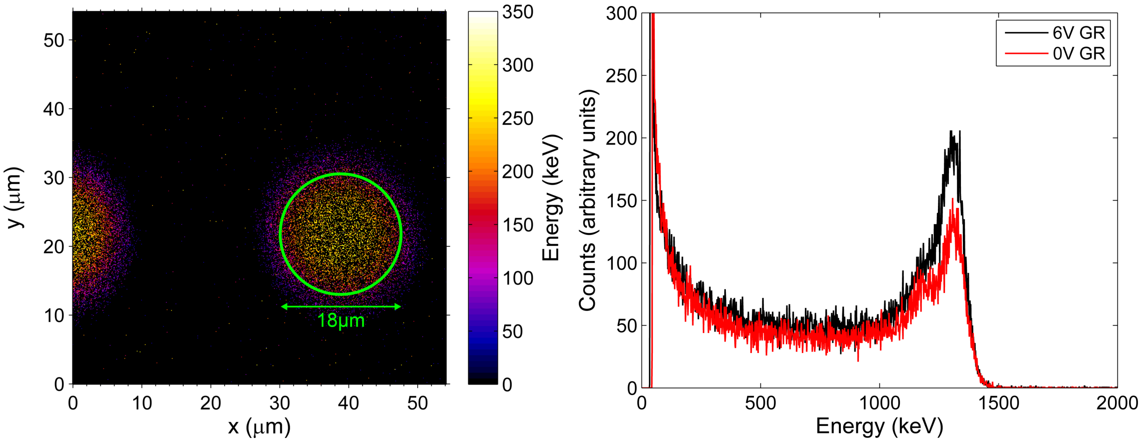

Figure 1.15: Left: Example charge collection of a planar silicon device obtained by scanning a 5.5 MeV α particle, the drawn circle represents the intended "size" of the SV. Right: Shows the corresponding energy deposition spectrum from the device when biased at 0 V (red curve) and 6 V (black curve), the left IBICC image was performed at 6 V. Images reproduced from the honour's thesis of Lachlan Chartier [79], a publication on the device can be found in [80].

1.7.3 CMRP Silicon Microdosimeter Designs

First generation CMRP silicon microdosimeters used a silicon on insulator (SOI) design which was a diode array manufactured by Fujitsu Research Laboratories and was extensively investigated in the thesis of Peter Bradley [63]. In total there were 4800 diodes connected together in parallel with a single signal readout, the area of each diode was 10×10 μm^2 with three different designs with thicknesses of 2, 5 and 10 μm. Charge collection measurements on the designs showed lateral diffusion and the electric field being distorted dependent upon the LET of particles, resulting in a poor definition of the sensitive volume shape.

Second generation devices attempted to improve the charge uniformity to better define the SV with two different second generation designs fabricated, both using planar processing techniques. The first version aimed to remove lateral diffusion from the SV by creating a raised mesa SV structure by etching. However, charge collection studies on the device revealed that lateral diffusion still occurred and had low SV yields due to the complicated aluminium evaporation required to produce the raised mesa structures [81]. A revised design removed the raised mesa design and incorporated p+ guard rings to isolate charge collection to the SV. The change to the more conventional guard-ring design from the more complicated evaporation technology greatly improved the yield of functioning SVs to almost 100%. Despite the improvement to the SV yield, the charge collection still featured noticeable lateral diffusion [82].

Third generation devices were similar to the revised second generation devices, using a planar design with guard rings. Changes to the previous design included an increased diameter of the SV to 6-10 μm and increasing the active area $\sim$16 times compared to the previous area of 1 mm^2. Besides the changes to the number and size of SVs the third generation devices used a high-resistivity n-type silicon (3 kΩcm) substrate with a thickness of 10 μm and featured p+ electrode cores. The incorporation of a p+ electrode gave the possibility to discard laterally diffused events by having coincidence of the core and p+ guard ring. This generation design had 100% yield of SVs and had improved charge collection properties due to the ability to have co-incidence filtering using the p+ core [83].

The current fourth generation designs, which are the main focus of this thesis, are fully etched design which come in two varieties, a “Bridge” and a “Mushroom” design. These have the advantages of much improved charge collection uniformity and SV definition compared to planar detectors as well as being more radiation hard and having better timing properties [84]. Greater details of these devices will be described in detail in future chapters.

1.7.4 Considerations for silicon microdosimetry

Despite the advantages of silicon microdosimeters over traditional TEPC designs they still have some complications which need to be addressed. The most obvious of these complications is that the signal measured in silicon does not represent a biological equivalent response. There have been various studies which have investigated the conversion of the silicon response to a tissue equivalent response. Many of these studies have used a method of finding the equivalent sized tissue volume which the silicon represents. Once the equivalent sized tissue volume of the silicon SV is found the lineal energy is calculated by using the mean chord length of the tissue instead, as shown in equation 1.29. Or more generally the chord length of the silicon is scaled by some factor κ, however this factor is usually stated in equations to be a scaling factor of the energy deposition, ε, instead of increasing the $\langle l \rangle$ as shown in equation 1.30.

$$y = \frac{\varepsilon}{\langle l_{Tissue} \rangle} \tag{1.29}$$

$$y = \frac{\kappa\varepsilon}{\langle l_{Silicon} \rangle} \tag{1.30}$$

Bradley and Rosenfeld [85] investigated the tissue equivalence (using ICRU muscle as the reference material) of a silicon microdosimeter for a boron neutron capture therapy field and found the scaling value of κ to be 0.63. Guatelli et al. [86] investigated the tissue equivalence of silicon, using water as the reference tissue material, for therapeutic proton energies and found a scale factor of 0.56. Tran [87] investigated the tissue equivalence of silicon design in aviation radiation fields, characterised by fast neutrons, by comparing the energy deposition in a cubic silicon design to a spherical tissue design a scaling factor of 0.58 was found appropriate.

A less investigated complication with silicon devices, which is particularly important in hadron therapy fields, is the use of the mean chord length determined by Cauchy's equation for calculating the lineal energy. This complication arises due to silicon SVs not being able to be fabricated into spherical shapes and the radiation fields associated with hadron therapy fields being very conformal. Due to these two factors the accuracy and appropriateness of using the mean chord length which is relevant for isotropic radiation fields should be considered when using silicon microdosimeters in hadron fields.

Chapter 2

Validation of hadronic physics models in Geant4

Due to the complexity and importance of fragmentation in heavy ion therapy, Monte Carlo codes are extensively used for studying the secondary radiation fields in heavy ion therapy [88] and to study associated dosimetry and quality assurance technology [89]. This chapter presents benchmarking and validation of alternative fragmentation models available in Geant4. The models were benchmarked against experimental measurements of a mono-energetic 400 MeV/u ^{12}C beam incident upon a water target. This work has subsequently been integrated into the system testing of Geant4, which monitors for changes to results in new releases of Geant4. The results and use of this test can be found online at `https://geant-val.cern.ch/stat` under the test name of *FragTest*. Part of this chapter has been published in:

- "Validation of Geant4 fragmentation for Heavy Ion Therapy", *Nuclear Inst. and Methods in Physics Research, A*, (869), 2017
- "Physics Models for Monte Carlo Simulations in Carbon Ion Therapy", 2019

2.1 Introduction

As figure 1.7 of section 1.4.1 showed, the effect of fragmentation is important to be considered in heavy ion therapy when planning the treatment of a patient. The importance of fragmentation is due to the attenuation of the original beam and creating lighter particles which deposit dose away from the target volume to healthy tissue, beyond the end of the Bragg peak and laterally from the primary beam. This work investigates the accuracy of three different nuclear fragmentation models available in the Monte Carlo Toolkit Geant4 [17] [18] [19], the Binary Intranuclear Cascade (BIC), the Quantum Molecular Dynamics (QMD) and the Liege Intranuclear Cascade (INCL++).

The BIC model describes the interaction between a projectile and a single nucleon of the target nucleus interacting in the overlap region as Gaussian wave functions. The QMD model instead considers all nucleons of the target and projectile, each with their own wave function; this inherently causes QMD to have greater computation times than BIC. Unlike the other two models, INCL++ models the nucleons as a free Fermi gas in a static potential well. The targets and projectiles which can be modelled by the INCL++ model are limited to a mass number of $A = 18$. For higher A values of both the projectile and target the fragmentation is modelled using BIC. More details on the BIC, QMD and INCL++ physics models can be found in the Geant4 Physics Reference Manual [55].

The models were benchmarked against experimental data for a pristine 400 MeV/u ^{12}C beam incident upon a water phantom performed at GSI in Germany by Haettner *et al.* [51]. The experimental data are available as an EXFOR file [90], which provides data for fragment yields per water thickness, fragment angular and kinetic energy distributions.

The experiment was conducted using a variable thickness water phantom, time of flight measurements for fragments were carried out using a start detector before the phantom and a second detector placed on a linear drive after the phantom.

Previous benchmarking studies have been performed by Böhlen *et al.* [27] who performed similar experimental comparison to [51] using the BIC and QMD models in Geant4 version 9.3. Napoli *et al.* [28] compared BIC and QMD to thin carbon target data for a 62 MeV/u ^{12}C beam using version 9.4 of Geant4. More recently Dudouet *et al.* [91] has compared cross-sections for 95 MeV/u ^{12}C incident upon PMMA using both: BIC, QMD and INCL++ using version 9.6 of Geant4.

This work was motivated by the observation that the Geant4 Toolkit evolves in time and therefore it is necessary to develop a testing suite for carbon ion fragmentation, which plays a crucial role in heavy ion therapy (HIT). Results presented here are obtained with Geant4, version 10.2p2, which was the most recent version of Geant4 when developing the project (June 2016). This work includes regression testing of the alternative fragmentation models with the Geant4 versions: 9.6p4 (December 2015), 10.0 (December 2013), 10.1 (December 2014), 10.2p1 (February 2016), 10.3 (December 2016) and 10.4Beta (June 2017). Note that the date in the parenthesis are the date the version was released.

2.2 Materials and Methods

2.2.1 Simulation Setup

The simulation setup was defined based on the experimental setup adopted in Haettner *et al.* [51]. A mono-energetic 400 MeV/u ^{12}C pencil beam is incident on a water phantom with an area of $50\times$ cm^2. In the experiment the thickness of water was varied with a piston setup while in the simulation the water is simulated as a standalone water box with different thicknesses depending on the measurement being simulated. In the simulation the water phantom is positioned in a vacuum. The pencil beam has a FWHM of 5 mm and energy sigma of 0.15% representing a FWHM of $\sim$1.4 MeV/u.

The electromagnetic interactions were modeled using the *G4 Standard EM option 3* Physics List. G4HadronElasticPhysicsHP was used to describe the elastic scattering of hadrons which uses the Wentzel model [92]. The neutron High Precision (HP) model was adopted to describe neutron interactions up to 20 MeV. All three fragmentation models are implemented using their default options. In addition to using their default options the QMD and INCL++ models are also compared using alternative configurations denoted as QMD-F and INCL-A respectively. The QMD-F uses the “USE-Frag” option which alters the interaction criterion, while INCL-A uses the ablation model for de-excitation of nuclei. The QMD-F option was observed not to significantly alter the angular or energy distribution of fragments compared to the default QMD model for these energies of ^{12}C ions and so only fragment yield results are shown for the QMD-F option.

The beam fragmentation comparisons were made with water slabs of varied thickness while for Bragg curve comparisons the water phantom was fixed to 60 cm thick, with the energy deposition for every depth along the phantom retrieved simultaneously. A step limit of 0.1 mm was applied within the phantom as well as a production cut size of 0.1 mm. The energy deposited was scored within a 20×20 cm^2 area at the centre of the beam with a voxel thickness of 0.1 mm along the direction of incidence of the beam. The lateral area corresponds to the physical dimensions of the ionisation chamber (IC) used in the experiment. The thickness of the IC used in the experiments was 3.7 cm [93]. The uncertainty of 1 mm quoted in the experiment refers to the uncertainty in the water equivalent thickness (WET) of materials positioned in front of the IC used. The uncertainty of the BP position quoted in the simulation of 0.1 mm is due to the thickness of the voxels used; because of the relatively large thickness of the experimental IC, this may cause a smearing of the shape of the BP.

The BP position corresponds to a depth in water of 275 mm. The thickness of the water slab, L, varied with values: 59, 159, 258, 279, 288, 312 and 347 mm, 10^7 primary ^{12}C ions were generated for each water slab thickness. The fragments emerging from the phantom were tallied when traversing a hemisphere with a radius of 2.94 m, placed after the water phantom, as shown in figure 2.1. The radius R of 2.94 m corresponds the distance from the mid target to the detector used in the experiment.

The species, energy, time and position of the fragments when reaching the hemisphere were scored. For comparing the total fragment yields to the reference experimental data, the number of fragments within a 10 degree cone given by equation 2.1 were recorded, the 10 degree cone matches the angular range integrated in the experiment. Equation 2.1 corresponds to figure 2.1 with angle θ_C being 10 degrees. The yields are normalised to

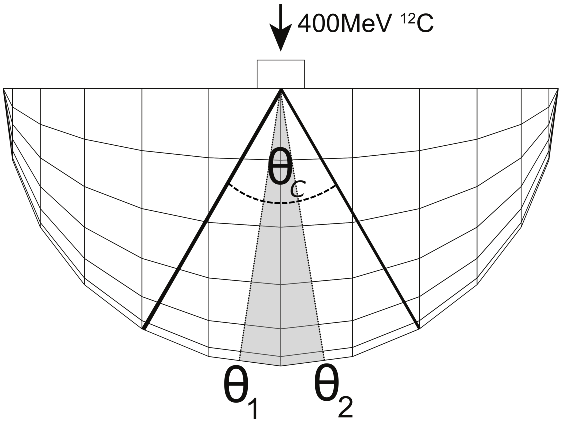

Figure 2.1: Sketch of the simulation set-up, showing the incident mono-energetic 400 MeV/u ^{12}C beam incident onto the water slab with variable thickness. The fragments, emerging from the phantom, are scored when reaching the hemisphere depicted in the figure.

the number of ^{12}C ions incident upon the water slab.

$$\theta_C = \sin^{-1}\left(\frac{\sqrt{x^2+z^2}}{R}\right) \tag{2.1}$$

θ_1 and θ_2 in figure 2.1 represent the angles made with the left and right edge of the detector. For the angular distribution, fragments were recorded within a 40 mm spherical wedge between angles θ_1 and θ_2, as shown in figure 2.1, corresponding to the width of the detector used in the experiment. Figure 2.1 shows the collection of fragments for an angle of 0° corresponding to θ_1= -θ_2. Fragments recorded in the wedge were normalised to the solid angle Ω formed by the wedge, given by equation 2.2, as well as being normalised to the number of incident ^{12}C ions.

$$\Omega = 2\pi\left(\cos\theta_1 - \cos\theta_2\right) \tag{2.2}$$

For kinetic energy distributions, fragments were recorded in the same solid angle used for the angular distribution. The kinetic energy of the fragment, KE_F, as it reached the hemisphere was calculated using the same method as adopted in [51]. This method assumes that all fragments were produced in the middle of the water phantom and by determining how long it would theoretically take for the primary ^{12}C ion with energy of 400 MeV/u to reach the middle of water phantom (depicted in 2.2), this time being t_P. The time for the fragment to reach the detector, t_F, is determined by subtracting t_P from the total time it takes for the primary particle to be fired and for the fragment to be recorded at the hemisphere. With t_F being known KE_F can be calculated by means of equation 2.3, where c is the speed of light and m_0 the rest mass of the fragment.

$$KE_F = \left(\frac{1}{\sqrt{1-\beta^2}} - 1 \right) m_0 c^2 \tag{2.3}$$

The underlying assumption when using the rest mass is that the fragments recorded are only due to the most abundant isotope ie ^{1}H, ^{4}He, ^{7}Li, ^{9}Be and ^{11}B. The value of β is calculated using equation 2.4, where R is the radius of the hemisphere (2.94 m). The timing error associated with the experimental setup of 0.53 ns (FWHM) was incorporated to the simulation's time of flight.

$$\beta = \frac{R}{ct_F} \tag{2.4}$$

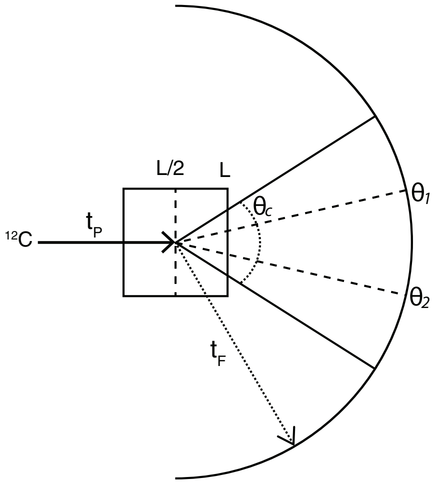

Figure 2.2: Diagram depicting the method to calculate the kinetic energy of the fragments recorded in the collection hemisphere based on the time it takes for the fragment to reach the hemisphere (not to scale).

For both the angular and kinetic energy distributions they were normalised to obtain the same area under the curve of the corresponding experimental measurements.

Quantitative comparisons of each Geant4 fragmentation model to experimental results for each physical distribution under study were done by adopting the quantity X^2, shown in equation (2.5), where n is the number of bins in the distribution being compared. The quantity X^2 is the same as χ^2 in Pearson's χ^2 test except no p-value calculations were performed with the distributions due to the test being over-conservative for the large population sizes being investigated and because the main interest was to rank the performance of each model against one another with lower values of X^2 representing better agreement with experiment.

$$X^2 = \sum_{i=1}^{n} \frac{(\mathrm{Sim}_i - \mathrm{Exp}_i)^2}{\mathrm{Exp}_i} \tag{2.5}$$

To provide a simple indication of how closely each Geant4 fragmentation model agrees with the experiment the percentage errors (PEs) are also presented. The PEs are derived from taking the mean PE of all points in the distribution being compared, as shown in equation (2.6). *n* represents the size of the distribution being compared.

$$\langle PE \rangle = \frac{100}{n}\left(\sum_{i=1}^{n}\left|\frac{\mathrm{Sim}_i - \mathrm{Exp}_i}{\mathrm{Exp}_i}\right|\right) \tag{2.6}$$

2.3 Results and Discussion

2.3.1 Bragg Curve

The comparison between the Bragg curves obtained from the experiment and Geant4 is shown figure 2.3. The experiment and simulation curves were normalised based on the average value of dose between 100 and 150 mm in the phantom. There is no significant difference in the calculation of the position of the BP between the three models, this is to be expected since the position of the BP is mainly dictated by the primary ^{12}C through its continuous energy losses, governed by the electromagnetic physics. One notable difference between the response of the different models is that QMD-F has a significant higher relative energy deposition at the BP region (right plot of figure 2.3). The response of QMD-F is probably due to its implementation changing the total nuclear cross-section, while all other models use the same total cross sections. The lower total cross-section for QMD-F results in a higher proportion of primary ^{12}C ions reaching the BP, thus depositing greater energy in this region.

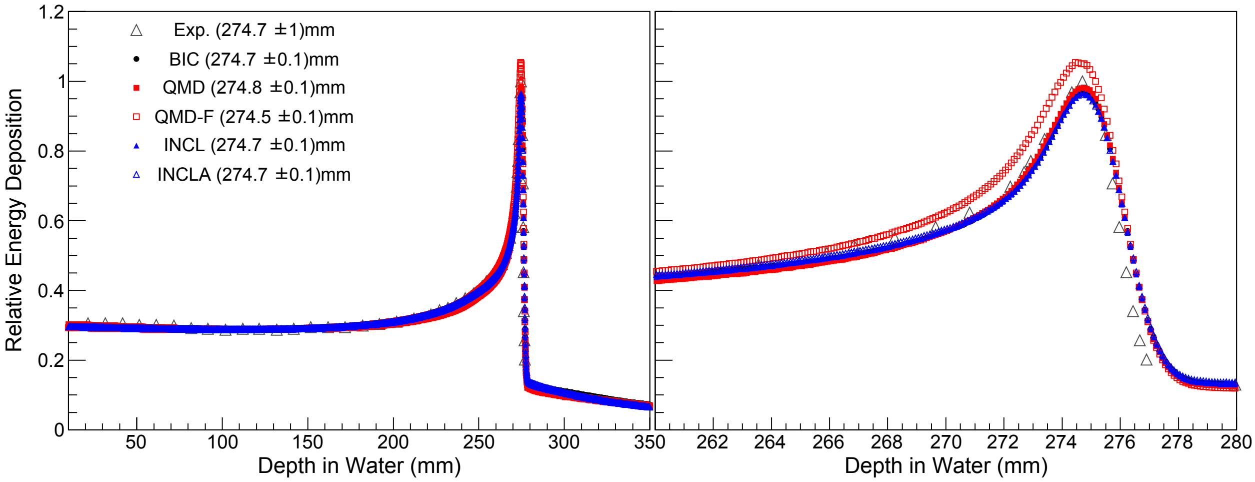

Figure 2.3: Comparison of the Bragg curve of the experiment (large open black triangle marker) compared to the different models used in Geant4, with the right side showing a zoomed view of the Bragg peak. The statistical error of the simulation is less than 0.2%. The QMD-F entry of the legend refers to QMD with the *Frag* option activated.

We observe a good agreement between the experiment and simulation, the X^2 values calculated using equation (2.5) to quantify the agreement between the Geant4 simulation and the experiment are shown in table 2.1. It can be observed that all the default fragmentation models provide similar agreement with the reference data when calculating the Bragg curve. However, QMD with the *Frag* option (QMD-F) provides the best agreement with the experiment, in terms of the X^2 value. In addition to the X^2 values the mean PE values of the different models are presented in table 2.2. The “Total” region used all 51 experimental data points to compare to while “Upstream” calculates the mean PE using all points before 264 mm and “Downstream” uses points after this position. Comparing the mean PE presents a much different result than the X^2 values with QMD-F resulting in highest difference between experiment overall. Instead the base QMD model gives the lowest different overall with experiment and also the lowest difference for downstream positions. The difference between the two comparison methods is likely due to X^2 normalising the entire distribution to the same area while the mean PE compares the absolute difference when the curves are normalised at the entrance of the BP.

	BIC	**QMD**	**QMD-F**	**INCL**	**INCL-A**
X^2	53.098	54.335	46.720	52.021	53.845

Table 2.1: X^2 values resulting from the comparison of the Bragg Curve calculated with Geant4 and from reference experimental data, lower values represent better agreement. These calculated values were obtained by comparing 51 data points of the experiment to the simulation.

Model	**BIC**	**QMD**	**QMD-F**	**INCL**	**INCL-A**
Total Mean PE	2.90	1.96	4.88	2.67	3.25
Upstream Mean PE	1.44	2.73	1.49	1.50	1.35
Downstream Mean PE	6.95	0.46	5.85	1.63	2.09

Table 2.2: Mean PE values resulting from the comparison of the Bragg Curve calculated with Geant4 and from reference experimental data. The “Total” region used all 51 experimental data points to compare to while “Upstream” calculates the mean PE using all points before 264 mm and “Downstream” uses points after this position.

2.3.2 Fragment Yields

Figure 2.4 shows the fragment yields Y scored at the hemisphere, within the cone with $\theta_1 = 10$ degrees, with respect to the water thickness. Y is calculated as the number of the scored fragments N divided by the number N_0 of incident ^{12}C ions.

Table 2.3 reports the mean PE averaged over all the water thicknesses under study using equation 2.6. It can be observed that overall BIC, INCL++ and the QMD models provide Y values which agree between 5% and 35%, depending on the type of fragment.

Table 2.4 reports the X^2 values calculated by comparing the fragment yields calculated by means of the Geant4 simulation with the reference data.

Z	BIC	QMD	QMD-F	INCL	INCL-A
1	19 ± 2	14 ± 2	5 ± 2	8 ± 2	13 ± 2
2	6 ± 1	17 ± 1	5 ± 1	10 ± 1	18 ± 1
3	4 ± 7	25 ± 7	31 ± 7	21 ± 7	8 ± 7
4	33 ± 10	14 ± 10	22 ± 10	15 ± 10	25 ± 10
5	19 ± 8	20 ± 8	26 ± 8	33 ± 8	15 ± 8

Table 2.3: Mean percentage error PE of the Geant4 ion fragmentation models compared to experiment, when calculating the fragment yields for each element reported on the column in the left.

When comparing the QMD model with *Frag* (labelled as QMD-F) against the default QMD, it can be seen that the QMD-F shows better agreement for H and He yields. For the remaining fragment species, QMD-F produces lower Y values which reduce the agreement with the experimental measurements. It can be noted that the error bars affecting experimental measurements of H and He fragments is $\sim$5%, while for heavier fragments they increase to $\sim$20%, with errors being larger for positions before the BP. Given such larger error bars, it is difficult to provide a conclusive comment on the accuracy of the Geant4 fragmentation models for heavier fragments before and at the Bragg Peak. However, the impact of fragments is most important beyond the BP, where the experimental errors are smaller due to the primary ^{12}C beam not masking fragment events. In this region, the experimental error bars decrease by $\sim$10%. After the distal edge the Geant4 fragmentation models have a reasonable agreement with the experimental measurements for Be and B ions. In the case of the Li fragment yield, the BIC model performs better than the other Geant4 fragmentation models.

Z	BIC	QMD	QMD-F	INCL	INCL-A
1	1.25×10^{6}	7.97×10^{5}	$\mathbf{9.16}\times10^{4}$	3.09×10^{5}	8.51×10^{5}
2	2.00×10^{5}	1.02×10^{6}	$\mathbf{9.35}\times10^{4}$	5.17×10^{5}	1.17×10^{6}
3	$\mathbf{1.01}\times10^{4}$	1.90×10^{5}	3.04×10^{5}	1.34×10^{5}	2.52×10^{4}
4	1.62×10^{5}	$\mathbf{2.77}\times10^{4}$	6.62×10^{4}	3.31×10^{4}	8.53×10^{4}
5	$\mathbf{6.12}\times10^{4}$	1.45×10^{5}	2.44×10^{5}	2.41×10^{5}	$\mathbf{3.69}\times10^{4}$

Table 2.4: X^2 values of the three fragmentation models compared to experiment in the case of fragment yields calculation, for each element reported in the left column. The best agreement is indicated by a lower X^2 value and it is shown in bold characters. The number of data points used correspond to those shown in figure 2.4, which is six for H and seven for all other elements.

H represents the majority of produced fragments, with He being the second most dominant, each having $\sim$10 times higher production than the remaining fragments. They also leave the treatment region the most due to their larger range and increased scatter compared to other heavier fragments. Based on this observation, the QMD with *Frag* may be indicated as the best fragmentation model of Geant4 to estimate more correctly the fragmentation yields of lighter, more abundant isotopes.

2.3.3 Angular Distribution

Figure 2.5 shows the angular distribution for a selection of fragments and water phantom thicknesses which there are 35 distributions in total. Table 2.5 presents the PE for the fragmentation models under study. Here, for the case of calculating the mean PE for each fragment element the mean PE is averaged over the total number of distributions for each element, m, as shown in equation 2.7, where n_j is the number of points for the j^{th} distribution of m.

$$\langle PE \rangle = \frac{1}{m}\sum_{j=1}^{m}\left(\frac{100}{n_j}\left(\sum_{i=1}^{n_j}\left|\frac{\mathrm{Sim}_{i,} - \mathrm{Exp}_i}{\mathrm{Exp}_i}\right|\right)\right) \tag{2.7}$$

Z	BIC	QMD	INCL	INCL-A
1	14 ± 4	7 ± 4	15 ± 4	31 ± 4
2	24 ± 2	16 ± 2	7 ± 2	10 ± 2
3	29 ± 8	26 ± 8	16 ± 8	25 ± 8
4	47 ± 14	43 ± 14	18 ± 14	12 ± 14
5	131 ± 12	135 ± 12	27 ± 13	22 ± 12

Table 2.5: PE calculated for four Geant4 fragmentation configurations compared to experimental values, in the case of the angular distribution, for each type of fragment under study. The PE is averaged over all water phantom thicknesses considered.

Figure 2.6 shows the X^2 values for each thickness of water for each element. The QMD model and BIC to a lesser extent commonly produce noticeably broader angular distributions than INCL++ which agrees with the experimental measurements the most. We observe that the INCL++ model with the exception of H performs the best quite significantly over the other models, particularly for heavier fragments. BIC and QMD both reproduce the angular distributions of the larger elements very poorly, particularly Boron. However Be and B suffer from much higher experimental error than the lighter fragments in general, with Be and B having many angles with an error of more than 40%. Figure 2.6 again shows the better performance of the INCL++ model compared to the other models except for H where the INCL++ performs similar to BIC for each distribution.

2.3.4 Fragment kinetic energy distribution

Figure 2.7 shows example energy distributions from the total 151 distributions for different combinations of: thickness, fragment element and angle. It can be observed that in general the models perform reasonably well at reproducing the general experimental energy distributions. The energy distributions predicted by the INCL++ model are systematically shifted to lower energies compared to the other models. Table 2.6 summarises the mean PE for each element. Figure 2.8 shows the distribution of X^2 values for all 151 kinetic energy distributions divided up for each different fragment species, the dashed lines separate the X^2 values for each water thickness. For each water thickness, the points represent smaller angles on the left, with a minimum of 0°; points further to the right represent larger angles with a maximum of 8°.

Z	BIC	QMD	INCL	INCL-A
1	26 ± 6	21 ± 6	45 ± 6	71 ± 6
2	30 ± 7	33 ± 7	72 ± 7	69 ± 7
3	41 ± 8	43 ± 8	95 ± 8	116 ± 8
4	60 ± 9	55 ± 9	113 ± 9	102 ± 9
5	220 ± 11	196 ± 10	404 ± 10	435 ± 10

Table 2.6: PE of four fragmentation configurations compared to the experiment for energy distributions for each type of fragment, calculated over all water phantom thicknesses.

Apart from the large errors in the experimental distributions, with many having values greater than 20%, another factor for the discrepancy between the experimental and simulation results may be partially attributed to the shift of the energy spectrum of the primary ^{12}C beam. The experiment was performed over two separate occasions with the calculated kinetic energy of the incident carbon ion beam shifting from 358 ± 23 MeV/u to 402 ± 26 MeV/u, from 256 ± 13 MeV/u to 261 ± 13 MeV/u and from 85 ± 3 MeV/u to 92 ± 3 MeV/u, for 59 mm, 159 mm and 258 mm water thickness, respectively [93]. The expected energies for these thicknesses of water are 350 MeV/u, 250 MeV/u and 80 MeV/u, respectively, as calculated by the ATIMA code [94]. Based on this, Table 2.7 shows the mean PEs for the separate sets of experimental measurements. The results show a minor improvement for the INCL++ model when considering only results obtained with the expected incident energy of the carbon ion beam (59 and 288 mm), with results being $\sim$10% closer to BIC and QMD. This happens because INCL++ produces consistently lower peak energies, so the disagreement becomes amplified when comparing to the experimental results obtained with slightly higher incident beam energy.

The kinetic energy distribution peak position was retrieved from the experimental and simulated distributions, the mean PE was calculated using equation 2.7 $(n_j = 1)$, figure 2.9 shows the results. It can be observed that overall QMD is the best fragmentation model reproducing the kinetic energy distribution and its associated peak and INCL++ produces consistently lower kinetic energy distributions.

2.3.5 Computation Times

Table 2.8 shows a summary of the relative computational intensity for each model using different water thicknesses. The first column reports the average computation time of ten

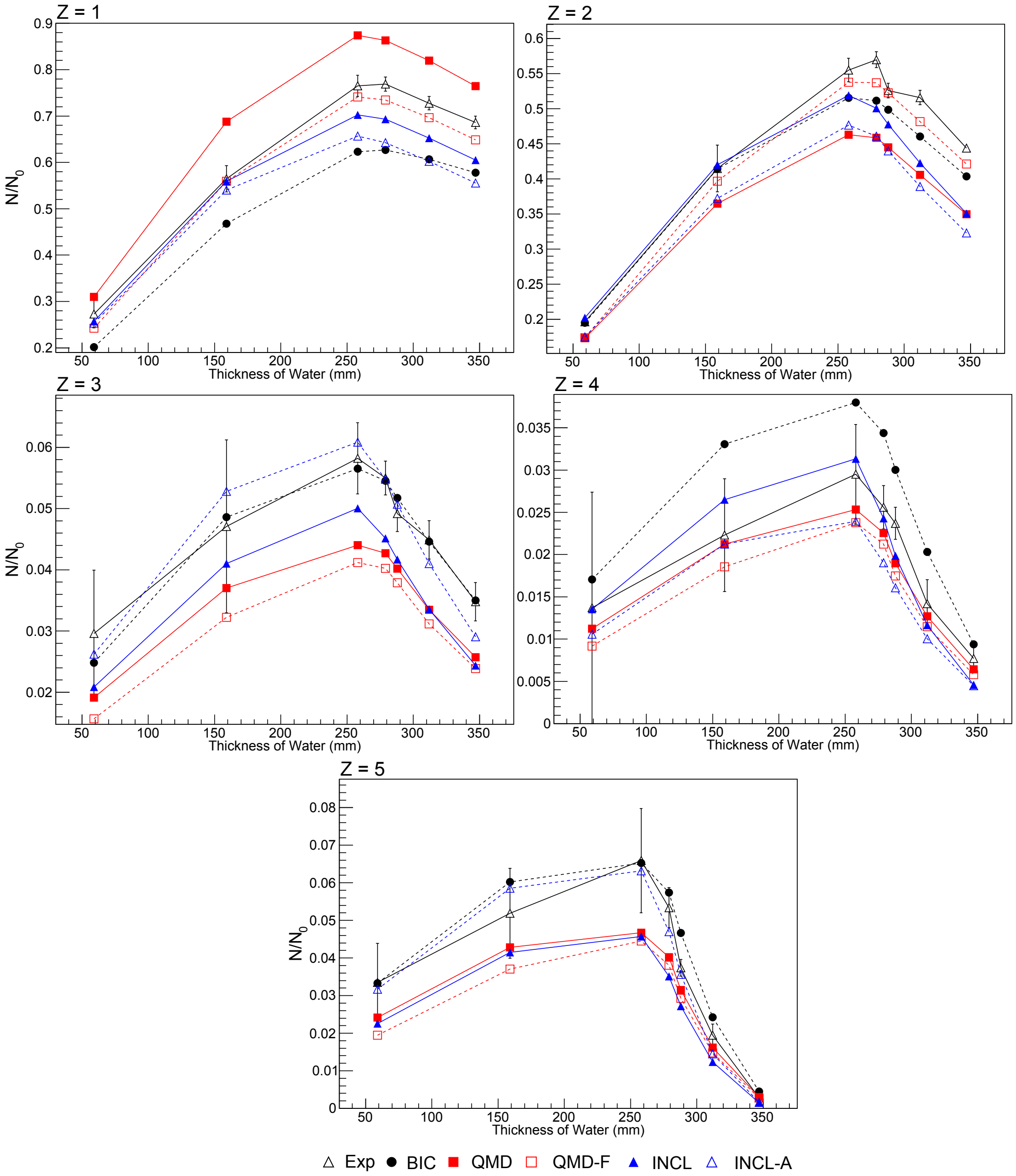

Figure 2.4: Fragment yields for elements: H, He, Li, Be and B for different thicknesses of water.

	59 and 288 mm				279, 312 and 347 mm			
Z	BIC	QMD	INCL	INCL-A	BIC	QMD	INCL	INCL-A
1	40 ± 6	31 ± 6	55 ± 6	81 ± 3	15 ± 5	14 ± 5	33 ± 5	50 ± 1
2	47 ± 7	53 ± 9	88 ± 8	81 ± 5	16 ± 6	17 ± 5	39 ± 6	38 ± 2
3	35 ± 10	35 ± 9	47 ± 10	62 ± 6	47 ± 6	50 ± 6	89 ± 6	97 ± 3
4	49 ± 10	45 ± 10	78 ± 11	71 ± 7	76 ± 7	61 ± 7	120 ± 8	100 ± 3
5	129 ± 14	116 ± 12	204 ± 12	246 ± 8	387 ± 8	333 ± 7	635 ± 8	679 ± 4

Table 2.7: Comparison of the mean PE of the energy distributions for each fragment species. 59 and 288 mm are the depths under investigation in the experimental data set with the expected incident carbon ion energy. 279, 312 and 347 mm are the depths of the experiments with higher than expected carbon ion energy.

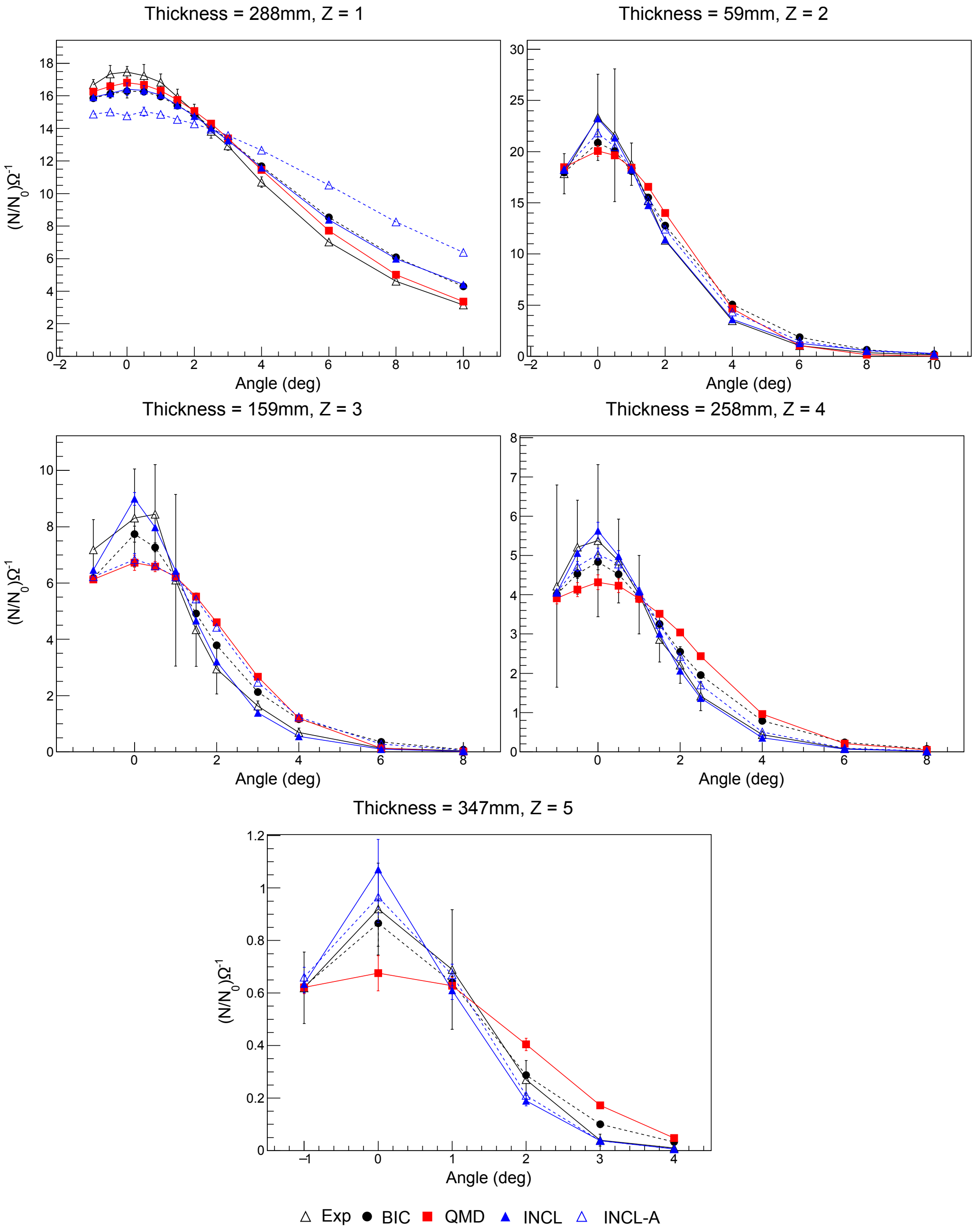

Figure 2.5: Angular distributions of a selection of fragments types and thicknesses of water.

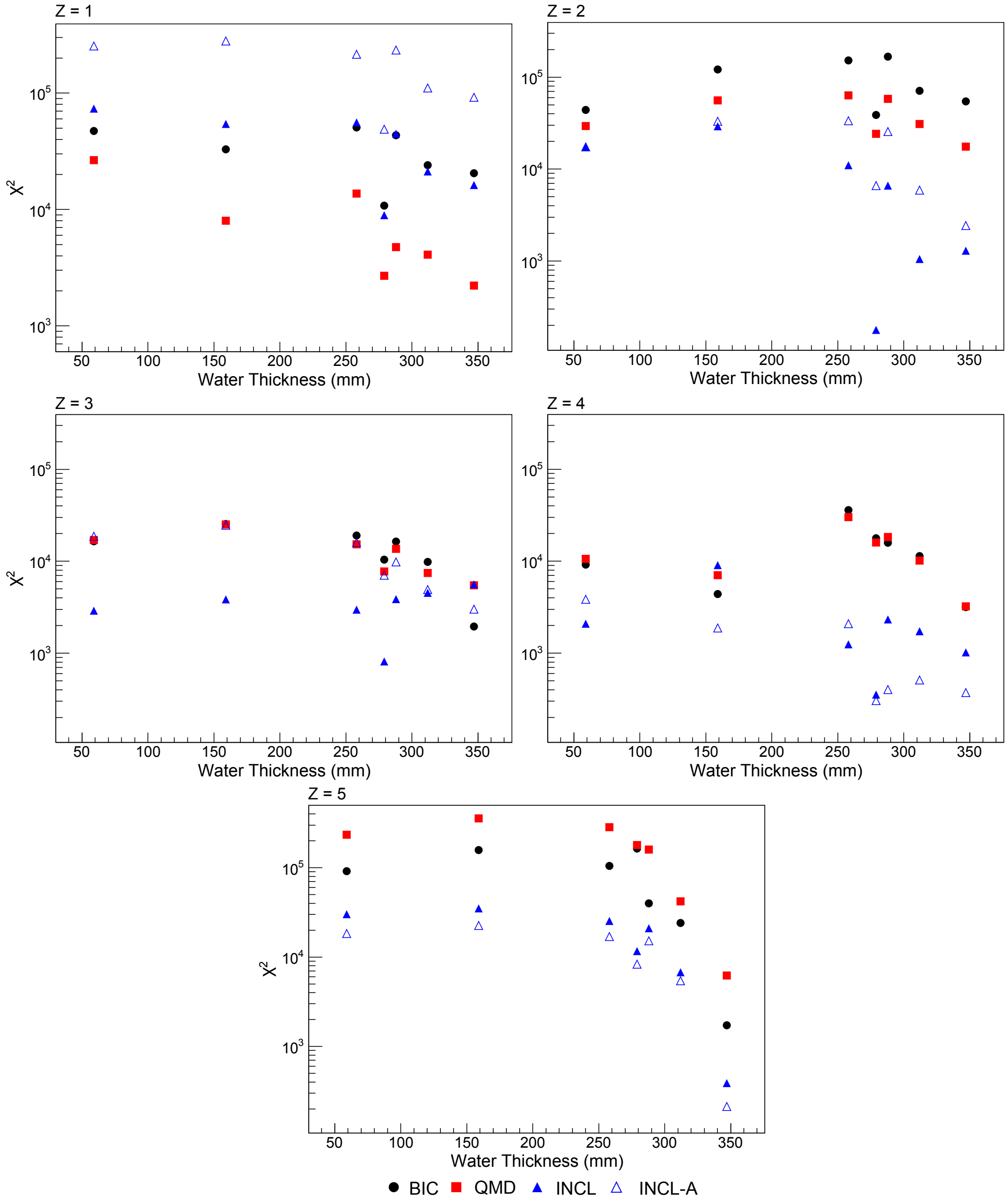

Figure 2.6: X^2 values of the different angular distributions compared for each model at different thicknesses of water for each element, lower values represent better agreement.

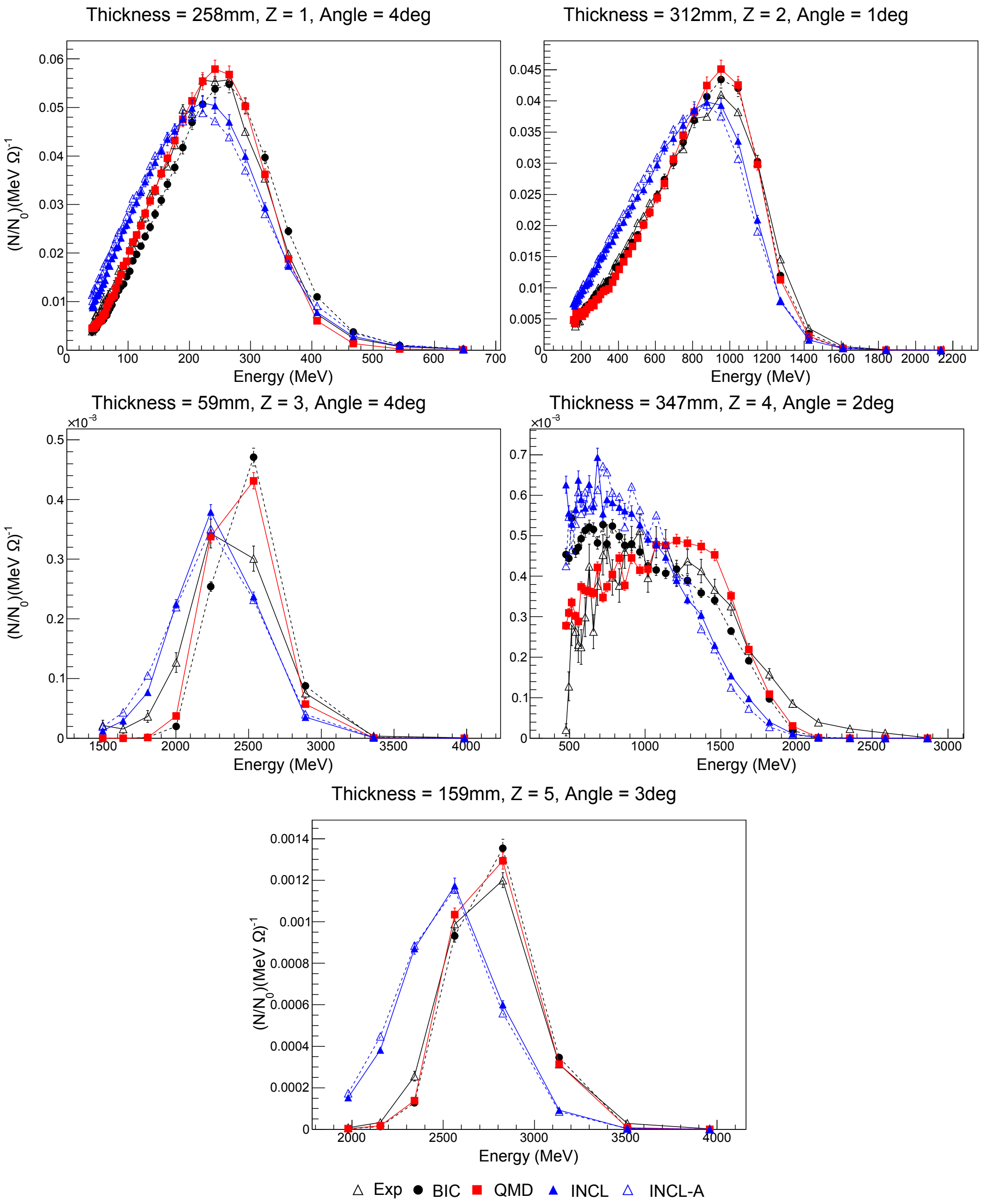

Figure 2.7: Kinetic energy distributions of a selection of fragments types and thicknesses of the water phantom.

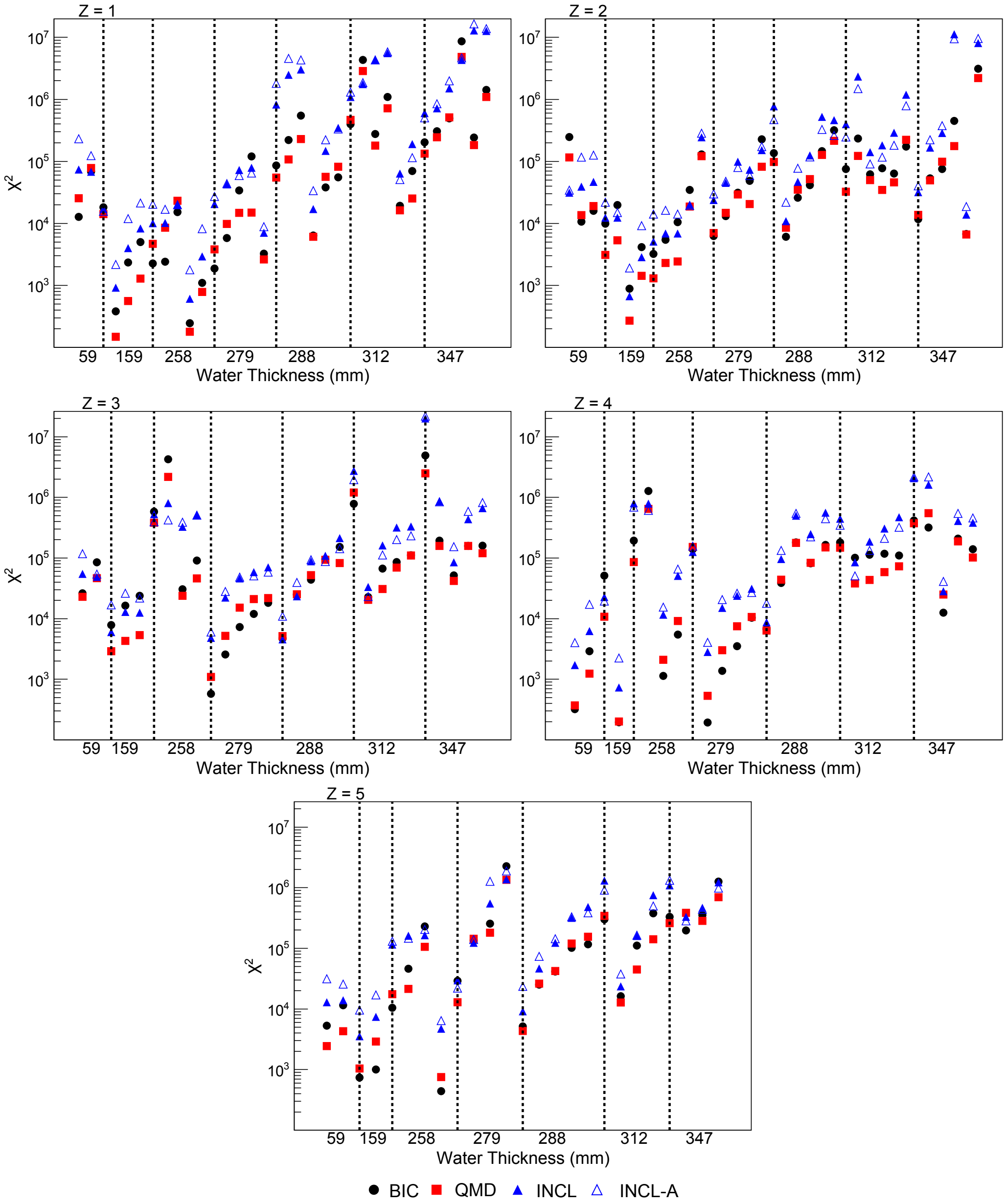

Figure 2.8: X^2 values of the different kinetic energy distributions compared for each atomic element. The dashed lines separate the X^2 for each water thickness. For each water thickness the left most points represent the smallest angle and the right most being the largest angle for the particular element and water thickness.

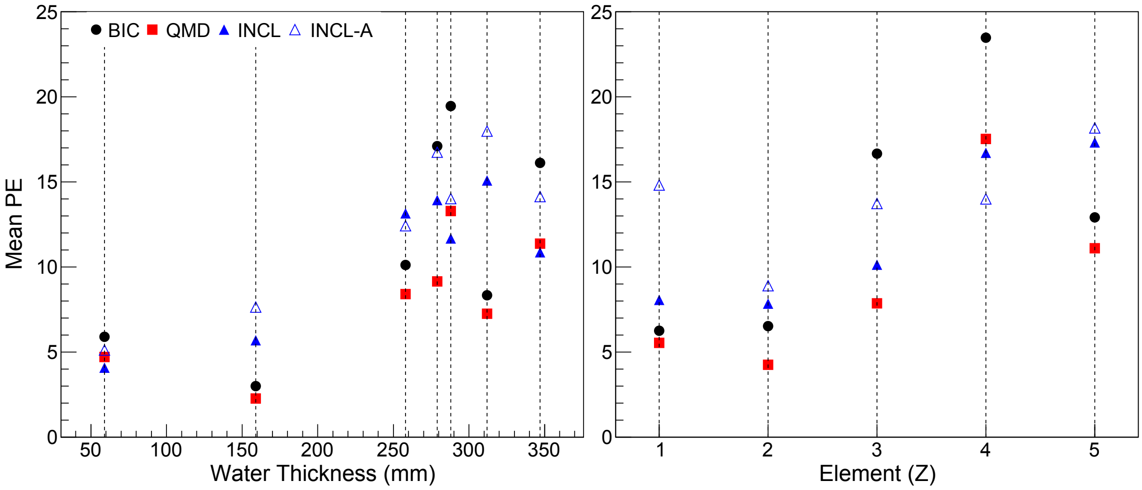

Figure 2.9: Mean PE calculated from the simulation and experiment maximum energy. Left shows the mean calculated for each depth and Right shows the mean PE calculated for each element.

simulation runs firing 10^5 primary ^{12}C ions for different water thicknesses using the BIC model, the reported error is the standard deviation. The remaining columns to the right give the ratio of each model with respect to the BIC model. The simulations were run using Intel® Xeon® E5-2650v3 processors clocked at 2.30 GHz.

Thickness	BIC (seconds)	QMD/BIC	QMD-F/BIC	INCL/BIC	INCL-A/BIC
59	97.5 ± 3.3	10.83 ± 0.45	7.73 ± 0.29	0.79 ± 0.05	1.01 ± 0.07
159	569 ± 18.2	5.40 ± 0.18	3.94 ± 0.14	0.97 ± 0.03	1.28 ± 0.06
258	1382.9 ± 90.7	3.67 ± 0.25	2.85 ± 0.24	1.04 ± 0.06	1.37 ± 0.11
279	1643.4 ± 57.9	3.41 ± 0.15	2.46 ± 0.31	1.03 ± 0.12	1.38 ± 0.09
288	1765 ± 63.6	3.29 ± 0.13	2.11 ± 0.22	1.01 ± 0.10	1.42 ± 0.11
312	1979.1 ± 73.9	3.16 ± 0.13	2.26 ± 0.13	1.03 ± 0.05	1.39 ± 0.06
347	2380.3 ± 47.6	2.86 ± 0.06	2.17 ± 0.08	1.00 ± 0.04	1.34 ± 0.05

Table 2.8: Comparison of the computation times for the different models investigated. The BIC column gives the average computation time of ten simulations each generating 10^5 primary ^{12}C ions for different water thicknesses using the BIC model. The reported error is the standard deviation. The remaining columns to the right give the ratio of each model with respect to the BIC model.

As expected the QMD model was much more computationally intensive than BIC since QMD considers wave functions for all nucleons of the target and projectile, as mentioned in section 2.1. QMD using the *Frag* option resulted in execution times which were approximately a third faster than the default QMD. This is convenient since QMD-F gave better agreement than the default for smaller fragment's yields as shown in section 2.3.2 but not differing for the angular and energy distributions.

Thinner thicknesses of water showed the greatest separation of the models with QMD having more than 10 times the computation time than BIC and INCL++ being 20% faster than BIC. For thicknesses greater than 59 mm BIC and INCL++ showed no significant differences.

2.3.6 Regression Testing

The fragment yields for each version of Geant4 from version 9.6p4 to 10.4B using the BIC model can be seen in figure 2.10. It can be seen that between different versions of Geant4 that the yield can have a large change. The mean percentage difference for each fragment element and fragmentation model in each version of Geant4 can be seen in figure 2.11. It can be seen that every model experiences a similar fluctuation as seen with BIC in figure 2.10. A notable observation is that the QMD-F model which gave the best agreement for H and He in versions 10.1 to 10.2 however in version 10.3 QMD becomes the second worst for H and the worst for He. This shows the importance of performing regression testing for each release of Geant4 and that for any study of clinical ^{12}C energies where fragments are of particular interest that the version and model used in Geant4 should be considered.

A further observation is that from version 10.3 all models gave much poorer agreement for Li, with the yield being reduced. One change which occurred in version 10.3 of Geant4 was that with the exception of the QMD/QMD-F model the default number of decay channels available for de-excitation was changed from 68 to 8. A comparison between fragment yields are shown in figure 2.12 for 10.4Beta when using the new default of 8 decay channels and 68 decay channels. It can be seen that there is no observable difference between the the 8 and 68 decay channels so conveniently this additional option does not need to be worried about in applications compiled in version 10.3 and higher for ^{12}C therapy applications.

INCL++ with the ablation model for de-excitation has not been included due to it being in *alpha* development [55] and is not recommended for use particularly before version 10.1 which had a bug in its implementation.

In contrast to the fragment yields the angular and energy distributions were not seen to vary from version to version with the exception of the INCL++ model between versions 9.6p4 and 10.0, where INCL++ gave much better agreement in the angular distributions. The changes of the INCL++ between versions 9.6p4 and 10.0 for angular and energy yields are summarised in table 2.9.

Z	**9.6p4**	**10.0**	**9.6p4**	**10.0**
	Angular Distribution		Energy Distribution	
1	5 ± 4	14 ± 4	16 ± 5	29 ± 5
2	16 ± 2	5 ± 2	39 ± 6	44 ± 6
3	29 ± 8	14 ± 8	101 ± 6	92 ± 6
4	53 ± 15	17 ± 14	93 ± 7	117 ± 7
5	51 ± 13	27 ± 12	576 ± 9	648 ± 8

Table 2.9: The mean PE of the INCL++ model between version

It was observed that between each version of Geant4 that when comparing the fragment, angular and energy distributions that the angular and energy distributions remained unchanged while the fragment yields were seen to vary from version to version. As of writing the hadronic models in Geant4 are tuned based high energy thin target data, unfortunately this differs from the requirements for therapeutic ^{12}C energies so for future development it would be advantageous if an option for the hadronic models was implemented which used values in the models which were optimised for therapy applications.

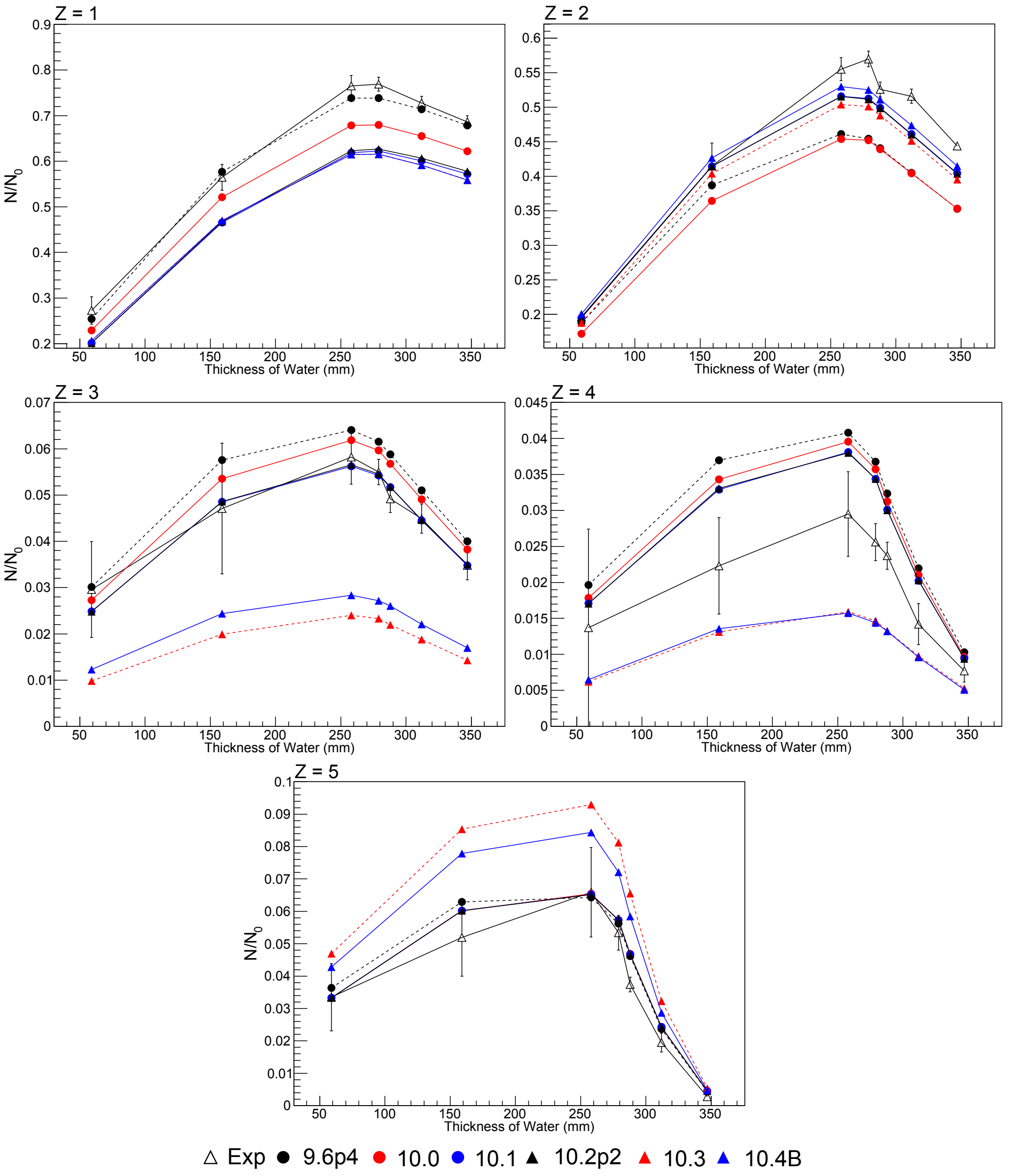

Figure 2.10: Fragment yields for BIC using every different version of Geant4.

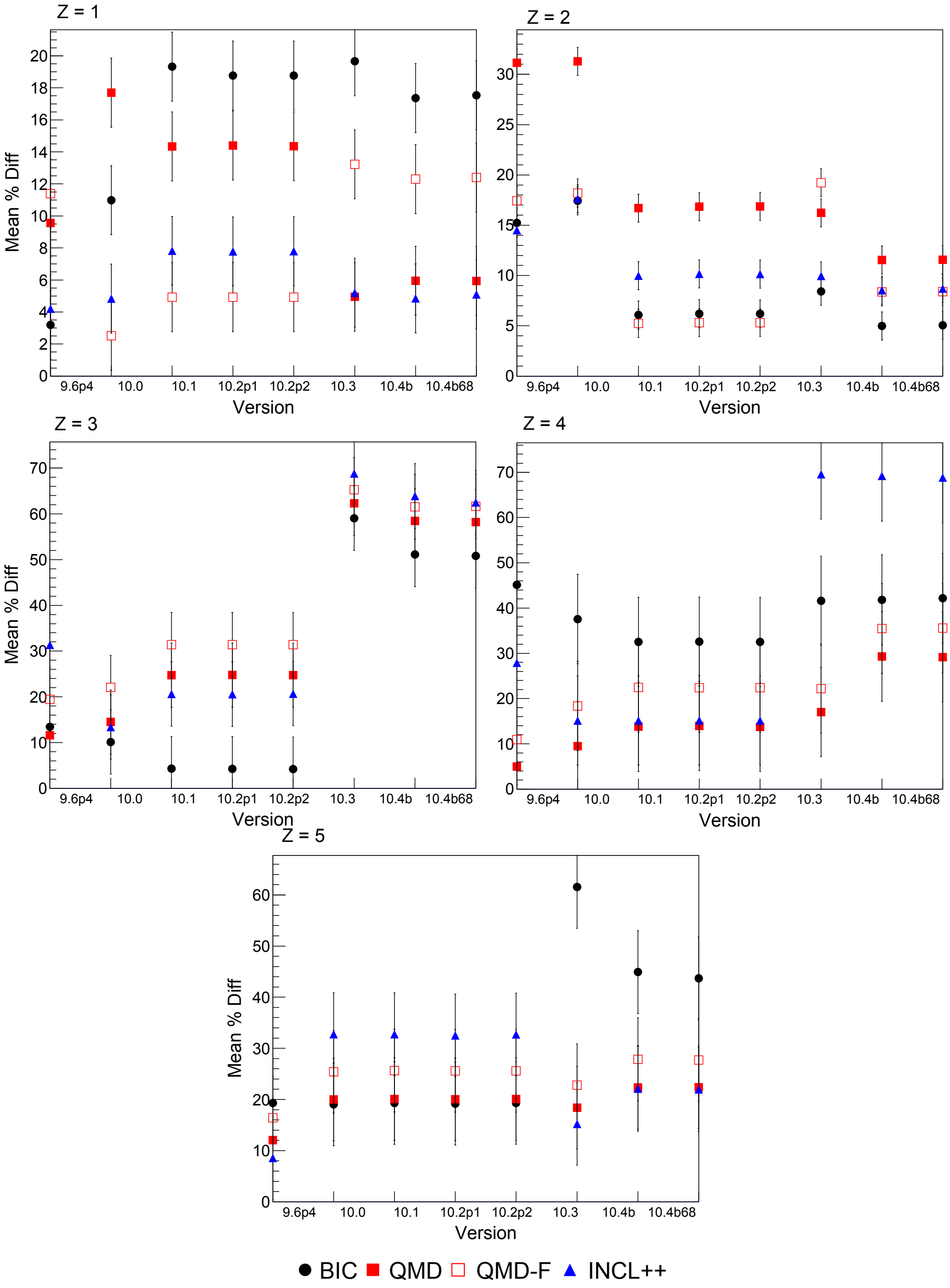

Figure 2.11: Summary of how the fragment yield of different models varied between different releases of Geant4, showing the percentage difference between the model and experimental measurements.

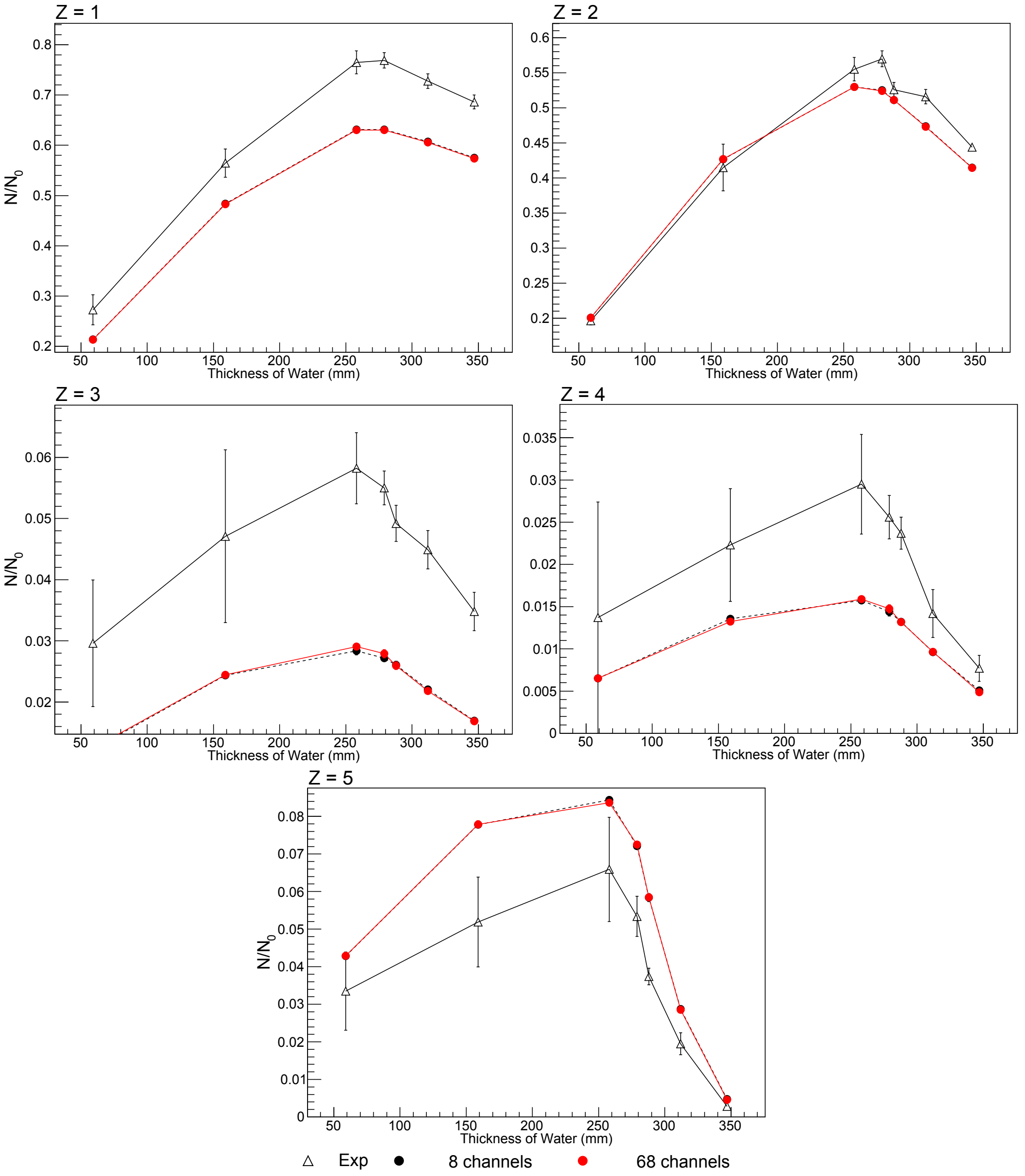

Figure 2.12: Comparison of the fragment yields between using the default option of 8 decay channels (in version 10.3 and higher) and using the previous default number of decay channels of 68. Results are shown for version 10.4B using the BIC model.

2.4 Conclusions

Nuclear fragmentation is a vital factor to be considered in hadrontherapy. The BIC, QMD and INCL++ models were benchmarked in Geant4 against experimental data for a pristine 400 MeV/u ^{12}C ion beam using version 10.2p2. It was found that for fragment yields the models agreed within $\sim$5%-35% compared to experimental values, with the QMD model using the Frag option giving the best overall agreement.

For angular distributions of fragments the INCL++ model was shown to reproduce experimental measurements significantly better than the other two models. For kinetic energy distributions the QMD model was seen to produce the best agreement, however the energy distribution results show noticeably less agreement, which can in part, be attributed to systematic errors in the experiment.

In general, when considering the angular and energy distributions BIC and QMD are seen to perform much similar to one another compared to INCL++. This is not surprising considering that both BIC and QMD models the fragmentation process as Gaussian wave functions while INCL treats the process as a free Fermi gas. Unfortunately, there is no clear superior model overall, with INCL++ performing much better in reproducing angular distributions but noticeably more worse for energy distributions with lower shifted energies. Additionally, all the tested fragmentation models showed that the agreement between simulation and experimental measurements deteriorated with larger fragments. Larger fragments have a larger RBE and can contribute significantly to the distal edge beyond the Bragg Peak, where organs at risk may be located. Therefore further developments in fragmentation modelling are recommended at clinical energies (up to 400 MeV/u), to obtain a better description of the mixed radiation field and of the RBE associated with HIT.

One key point that emerged from this study is that a detailed knowledge of the experimental measurements is crucial to perform an accurate validation study of Monte Carlo codes for Heavy Ion Therapy. There is also the need to have more detailed experimental measurements available, made by independent sources, which can be used as reference to comprehensively benchmark Monte Carlo codes, limiting the effect of possible systematics affecting the experimental data.

The simulation application developed in this work will be used for the regression testing of public releases of Geant4 to benchmark the effect of the evolution of the Toolkit on important physical quantities, such as the yield, angular and kinetic energy distributions of fragments, typical of the radiation field of Heavy Ion Therapy. Monitoring the behavior of Geant4 and its available models is very important to track any potential bugs which have been introduced; if performing studies relating to patient dose being aware of any changes/bugs is vital to consider. This also particularly helpful when performing studies with a certain version of Geant4 and comparing them to results from another version of

Geant4, with differences potentially being more easily understood.

Chapter 3

Correction factors for silicon microdosimetry in heavy ion therapy

This chapter investigates the use of silicon microdosimeters in ^{12}C ion therapy, in particular, converting the energy deposition spectrum obtained from the silicon microdosimeter to a tissue equivalent lineal energy spectrum. Due to the strong directionality of the radiation field, associated with heavy ion therapy, the concept of the mean path length is investigated as an alternative to the conventional use of the mean chord length.

Part of the work in this chapter has been published in “Correction factors to convert microdosimetry measurements in silicon to tissue in ^{12}C ion therapy”, *Physics in Medicine Biology*, (62), 2017. Certain figures in this chapter have been reproduced from the publication.

3.1 Introduction

As mentioned previously in section 1.7.4, SOI microdosimeters have many attributes which make them attractive for routine quality assurance in hadron therapy, including high spatial resolution, portability and the ability to estimate the biological response through the concepts of microdosimetry. However, there are several complications, including the recorded energy deposition not being tissue equivalent and the design not being able to be fabricated as a spherical sensitive volume (SV), which are instead limited to cubic and cylindrical designs.

A previous simulation study by Guatelli et al. [86], developed a method to convert microdosimetric spectra from silicon to tissue in a radiation field typical of therapeutic proton beams. However, a method to convert the energy deposition spectrum in silicon when irradiated by a therapeutic ^{12}C ion beam has yet to be performed and is studied in this chapter. Compared to the conversion method found in [86] for proton therapy of a fixed 0.56, ^{12}C may present a more complex conversion method due to the complicated mixed radiation field.

The radiation field of ^{12}C ion therapy is very directional, particularly for the primary ^{12}C ion, Cauchy's formula however only applies to isotropic distributions. Due to the directionality of the field, together with silicon SVs not being able to be fabricated as spheres, the distribution of charged particles in the sensitive volume of the microdosimeter is examined. The study of charged particles in the SV is performed to determine how appropriate the use of the mean chord length, calculated by Cauchy's formula (equation 1.7) of $\langle l \rangle = 4V/S$, for the conversion from energy deposition to lineal energy.

This work studies this concept of converting the energy deposition in silicon into tissue equivalent lineal energy by using a fourth generation CMRP silicon microdosimeter. This detector adopts a "Mushroom" design which refers to a SOI microdosimeter which has etched SVs in a cylindrical shape.

3.2 Method

For this study of tissue equivalence and chord length distribution of the Mushroom microdosimeter design, version 10.0 of Geant4 was adopted.

3.2.1 The Geant4 simulation application

The geometry of the simulation consists of a simple geomtry which is shown in figure 3.1 (a). A mono-energetic 290 MeV/u ^{12}C ion beam, 5×5 mm^2 in size, is normally incident upon a $30 \times 30 \times 30$ cm^3 water phantom with an air gap of 4 cm between the primary beam position and the face of the phantom.

The size of the beam was chosen because it is similar to the pencil scanning beam voxel dimension adopted in treatment planning systems [30]. The microdosimeter is placed in the centre of the beam, for the silicon to tissue conversion study the depths are 50 mm, 130 mm and 160 mm in the water phantom, corresponding to upstream, midstream and the Bragg peak along the Bragg curve. These positions correspond to average kinetic energies of approximately: 232 MeV/u, 111 MeV/u and 9 MeV/u, respectively, for the primary ^{12}C ion beam when it reaches the Mushroom detector.

The Mushroom design modelled features a fully 3D design with cylindrical silicon SVs with a height and diameter of 10 μm and a pitch of 40 μm between the centre of electrodes and embedded in PMMA as shown in figure 3.1 (b). The Mushroom is orientated such that the beam is perpendicular to the face of the cylinder, as indicated in figure 3.1 (b). The reason for the cylinder dimensions being chosen as 10 μm in height and diameter is because this corresponds to a cylinder where the elongation (ratio of height to diameter) is one, which for traditional microdosimetry measurements corresponds to chord length distribution which will have the least variance [7]. Additionally, the thickness of 10 μm

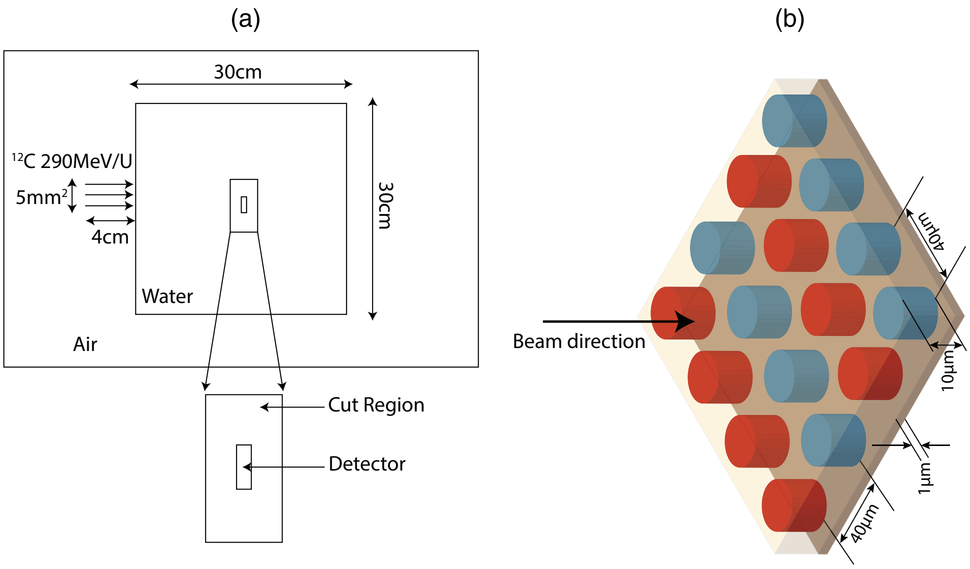

Figure 3.1: (a) Setup of the Geant4 simulation used for this study. (b) Diagram of a region of the Mushroom microdosimeter showing 16 of the 2500 SVs. The blue and the red SVs represent the two different channels, over which the signal is integrated. The Mushroom is orientated such that the beam is incident perpendicular with the face of the cylinder as indicated in the figure.

was chosen as this corresponds closely to the most common thickness which SOI microdosimeters are currently fabricated. In total there are 2500 sensitive volumes which cover an area of 2×2 mm^2, these SVs are divided into even and odd channels (shown as red and blue in the diagram) to reduce the capacitance (for real devices) and co-incident events with each channel being summed into an individual preamplifier.

One event in the simulation includes the tracking of one primary carbon ion and its associated secondary particles. The readout of the detector was done by scoring the energy deposited in each channel over one event. The energy deposited per event is then integrated over the even and odd channels, separately, to mimic the readout of a real microdosimeter device.

To describe electromagnetic interactions the *G4 Standard EM option 3* physics list was adopted. For elastic and inelastic hadron interactions the *G4HadronElasticPhysicsHP* and *G4HadronPhysicsQGSP_BIC_HP* models were used, respectively. The *G4IonBinaryCascadePhysics* was used to describe hadronic interactions of ions. For neutron interactions up to 20 MeV the neutron High Precision (HP) model was used.

In order to improve the speed of the simulation, the microdosimeter was placed in a water region located in the water phantom. Using this region the *G4Region* and *G4ProductionCuts* classes allows different thresholds of production for secondary particles in different volumes. By choosing a suitable threshold means that electrons are only generated close to the microdosimeter, in the water region the microdosimeter is placed in, as shown in figure 3.1 (a). The region has a thickness twice the maximum range of electrons generated by the incident beams plus the thickness of the detector itself. The cut is fixed to 2.8 mm outside of the cut region for the incident ^{12}C beam, while inside the water region the cut size required for secondary particles to be produced was 1 μm.

3.2.2 Determination of Tissue Equivalence for Heavy Ion Therapy

To convert the silicon energy deposition to a tissue equivalent spectrum, when irradiated with a ^{12}C ion beam, the same method adopted by Guatelli *et al.* [86] was used to find a conversion factor κ. The first stage involves irradiating the actual silicon microdosimeter at different depths in the water phantom with the ^{12}C ion beam. Once the energy deposition in the silicon SVs is calculated, SV_{Si}, the silicon detector is then replaced with an array of cylindrical SVs made of ICRU striated muscle and irradiated by the ^{12}C ion beam at the same depths as the silicon microdosimeter. In addition to striated muscle an array of water volumes is also irradiated due to it commonly used to represent tissue. The dimensions of the muscle and water cylinders have the same elongation as the silicon SV.

To determine which sized muscle/water cylinder gives the most similar energy deposition ($\mathrm{SV}_{water/muscle}$) as the true silicon SV (SV_{Si}) the energy spectra were compared by using the χ^2 test. A p-value larger than the significance level α (0.05) means that the two distributions do not vary significantly. The tissue equivalence correction factor, κ, was then defined as the ratio of l_{Si} to $l_{water/muscle}$ for which the best equivalent response to silicon was obtained.

Once the equivalent sized tissue volume of the silicon SV is found, the lineal energy is calculated by using the mean chord length of the tissue instead, as shown in equation 3.1. Or more generally the chord length of the silicon is divided by κ, as shown in equation 3.2.

$$y = \frac{\varepsilon}{\langle l_{Tissue} \rangle} \tag{3.1}$$

$$y = \frac{\kappa\varepsilon}{\langle l_{Silicon} \rangle} \tag{3.2}$$

3.2.3 Path Length Distributions

To investigate the appropriateness of the mean chord length provided by the Cauchy formula, $\left\langle l_{Cauchy} \right\rangle$, the mean path length, $\langle l_{Path} \rangle$, was introduced. Instead of being the mean of randomly distributed chords within the SV the $\langle l_{Path} \rangle$ is the mean of the path lengths of charged particles which traverse the SV in the radiation field of interest. This allows for the directionality of the radiation field to be considered, which is not taken into account by Cauchy's formula.

The path length for an incident ^{12}C ion beam was calculated by replacing the SVs silicon material of the Mushroom detector with vacuum to remove any physical interactions as particles traversed the SV, whilst maintaining the angular dependency of the radiation field incident on the microdosimetric device. The length of the track within the SV was recorded and the mean path length $\langle l_{Path} \rangle$ was then calculated and compared to the mean chord length ($\langle l_{Cauchy} \rangle$) given by Cauchy's formula which is 6.7 μm for each SV of the modelled Mushroom microdosimeter.

The kinetic energy of electrons entering the SVs was recorded and their CSDA range was determined in silicon using the NIST *ESTAR* database [95]. If the distance the electron travelled inside the detector was greater than the CSDA range then this event was classified as a stopper and not included in the determination of the chord length distribution and the final value of the mean path length of the simulation, $\langle l_{\text{sim}} \rangle$. The same method was used for ions however ions where found to have less impact on the mean path length than electrons in terms of being stoppers.

To compare the effect of using the mean path length and the mean chord length for the silicon microdosimeter in a ^{12}C ion beam the quantity of RBE$_{10}$, as estimated by the MKM (equation 1.26), was compared. The RBE$_{10}$ values for the silicon microdosimeter were calculated using the $\langle l_{Cauchy} \rangle$ and the $\langle l_{Path} \rangle$, calculated in the simulation. In addition, the thickness of the SV (10 μm) in the direction of the primary beam was also used to calculate the RBE$_{10}$ as an approximation to the $\langle l_{Path} \rangle$. The RBE$_{10}$ values calculated using the silicon microdosimeter were then compared to the RBE$_{10}$ values calculated using an array of 10 μm diameter spheres made of striated muscle.

All vertical error bars shown in this work represent one standard deviation which come from the statistical fluctuation of ten different runs of the simulation. Horizontal error bars represent the bin width of the binned data.

3.3 Results and Discussion

3.3.1 Tissue Equivalence

Figure 3.2 shows the energy deposition spectra for silicon and muscle, at depths of 50, 130 and 160 mm. Table 3.1 summarises the p-values, resulting from the comparison of the energy deposition spectra calculated in the SV$_{Si}$ (l_{Si}=10 μm) and SV$_{water/muscle}$ with varying sizes of l.

As can be seen in Table 3.1, at 50 and 130 mm depth in the phantom the best agreement is obtained with l_{muscle} equal to 17.5μm, with 17.25 μm also not differing statistically significantly ($\alpha > 0.05$) but having a value lower than the 17.25 μm muscle. At a depth of 160 mm l_{muscle} sizes of 17.25 and 17.5 μm do not differ significantly from the response in the silicon SV but the 17.25 μm volume has a slightly higher α value. For this reason a scaling factor κ for muscle was chosen based on the SV l_{muscle} equal to 17.5 μm, corresponding to a κ of 0.57. For water the best agreement for energy deposition spectra for silicon was found to be for 18.5 μm corresponding to a κ of 0.54.

To perform validation of the implemented method, the simulation was also performed with a proton beam with a primary energy of 160 MeV (using a maximum electron range of 1 mm for the cut region). The *p*-values, comparing the energy deposition of the silicon and muscle/water volumes when irradiated by a proton beam are summarised in table 3.2. The conversion value for the water volume (18 μm) corresponds to a value of 0.56, which is the same value found in the work of Guatelli et al. for proton beams in water. Additionally, the 17.25 μm diameter muscle cylinder was found to best agree with the 10 μm thick silicon SV, which corresponds to a value of 0.58.

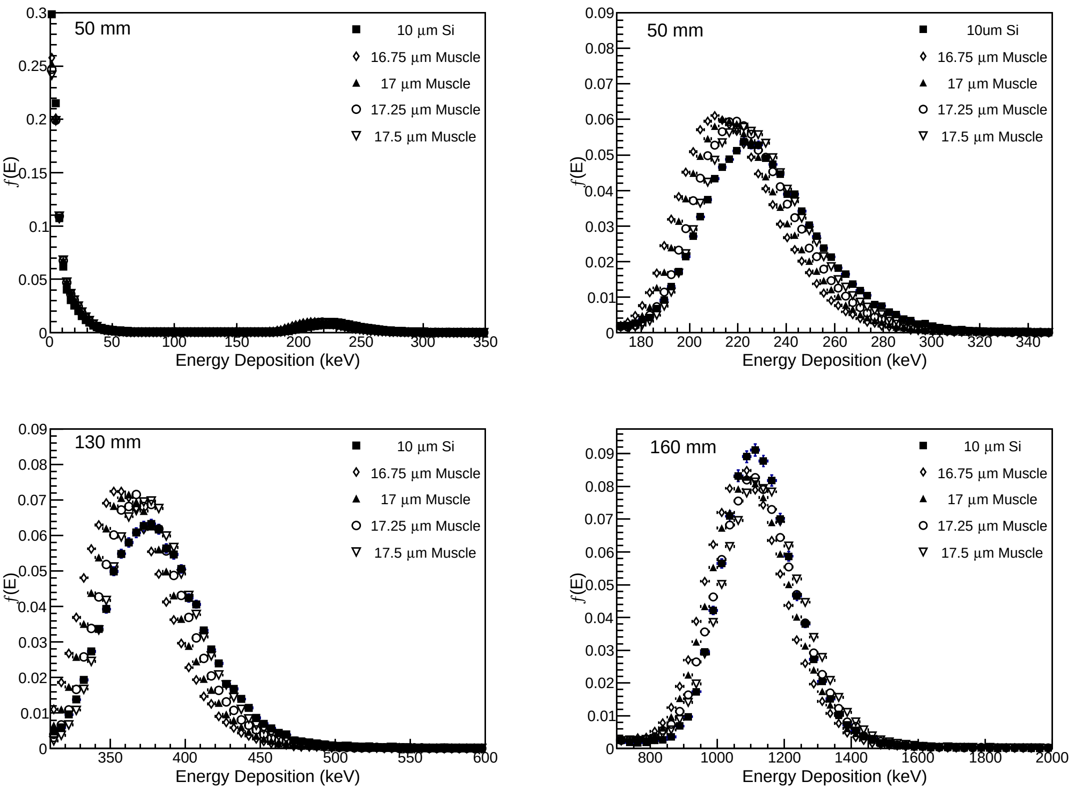

Figure 3.2: Energy deposition spectra obtained in SV$_{Si}$ and in SV$_{muscle}$ with varying size *l* (indicated in the legend), at depths of 50, 130 and 160 mm. The top left shows the entire energy deposition distribution at 50 mm depth, including the primary ^{12}C beam (right peak), electrons (far left tail) as well as fragments and other secondaries. The top right plot shows a zoomed in view of only the primary ^{12}C energy deposition peak at 50 mm, with the bottom two plots also only showing a zoomed in view of the ^{12}C ion peak for 130 and 160 mm depths.

For comparison against the ratio of silicon to muscle/water to give the same energy deposition, as found by Monte Carlo, the ratio of LET (MeV/cm) values of muscle/water to silicon are also shown in tables 3.3 and 3.3 for ^{12}C ions and protons of various energies, respectively. The ratios of LET tend to be slightly lower than the values found from comparing the energy deposition, except at lower energies, where the range of delta electrons produced are shorter and the difference between the energy deposited and energy lost by the ion/proton in a microscopic volume becomes insignificant. The difference between

Depth (mm)	Muscle SV l (μm)	p-value	Water SV l (μm)	p-value
50 232 MeV/u	17	1.98E-08	18	0.0405789
	17.25	0.775748	18.5	1
	17.5	1	19	0.239555
130 111 MeV/u	17	1.85E-07	18	0.156499
	17.25	0.990125	18.5	1
	17.5	1	19	2.46E-06
160 9 MeV/u	17	3.28E-03	18	0.0774045
	17.25	0.995066	18.5	0.85756
	17.5	0.986345	19	1.66E-18

Table 3.1: p-values calculated using Pearson's χ^2 test comparing the energy deposition distribution of SV_{Si} to $SV_{muscle/water}$ with different sizes l for a 290MeV/u ^{12}C beam.

Depth (mm)	Muscle SV l (μm)	p-value	Water SV l (μm)	p-value
50 132 MeV	17	0.849886	18	0.982892
	17.25	0.957487	18.5	0.0119538
	17.5	0.80295	19	7.91E-15
130 75 MeV	17	0.519712	18	0.730089
	17.25	0.829528	18.5	0.000659336
	17.5	0.297784	19	1.83E-17
160 41 MeV	17	0.473233	18	0.81992
	17.25	0.668219	18.5	0.000157537
	17.5	0.337589	19	1.00E-19

Table 3.2: p-values calculated using Pearson's χ^2 test comparing the energy deposition distribution of SV_{Si} to $SV_{muscle/water}$ with different sizes l for 160 MeV proton beam.

the ratio of LETs and energy deposition is quite small, with a maximum difference of ~4%. Due to the small difference in the methods, using the ratio of LET can provide a fairly accurate method to convert the energy deposition from one material to another.

Energy (MeV/u)	$(\text{Muscle/Si})_{\text{LET}}$	$(\text{Water/Si})_{\text{LET}}$
10	0.59	0.55
50	0.56	0.54
100	0.56	0.53
150	0.56	0.53
200	0.55	0.53
250	0.55	0.53
300	0.55	0.52
400	0.55	0.52
500	0.55	0.52

Table 3.3: Ratio of the LET values of ^{12}C ions of various energies for muscle and water to silicon LET values come from the ICRU 73 report on stopping power of ions larger than Helium [36].

Energy (MeV)	$(\text{Muscle/Si})_{\text{LET}}$	$(\text{Water/Si})_{\text{LET}}$
10	0.58	0.57
25	0.57	0.55
50	0.56	0.54
100	0.55	0.54
150	0.55	0.53
200	0.55	0.53
250	0.55	0.53
300	0.55	0.53

Table 3.4: Ratio of the LET values of protons of various energies for muscle and water to silicon LET values come from the NIST P-Star database [96].

Figure 3.3 shows a zoomed energy deposition spectra up to 50 keV in muscle and silicon SVs at 130 mm depth in the phantom. This peak comes from electrons which originate from outside of the SV, reaching the SV and depositing energy, as well as electrons being generated by photons inside the detector. It can be observed that silicon shows a higher contribution of low energy deposition events (up to a few keV) with respect to muscle (which is also the case for water), which means that a higher number of electrons deposit energy in the SV_{Si}. The extra electrons in the SV derived from photon interactions estimated from the attenuation coefficient in silicon is about 10 times higher than in water/muscle for energies >1 MeV, as shown in Figure 3.3.

To take into account the higher response of the silicon at lower energies, a *low energy correction*, *LEC*, factor was introduced to make the SV_{Si} response more similar to water/muscle. The energy deposition spectrum in the SV_{Si} between zero and an energy threshold, E_t, is scaled by the *LEC* factor as shown in Equation 3.3. Equation 3.3 shows the number of counts of a corrected silicon spectrum for all energies $(N(E_{SiCorr}))$ being the addition of the counts (N_1) in the energy range of 0 to the threshold energy $(N_1(E_{Si}))$, scaled by the *LEC* factor, plus the counts (N_2) above the threshold energy to the maximum

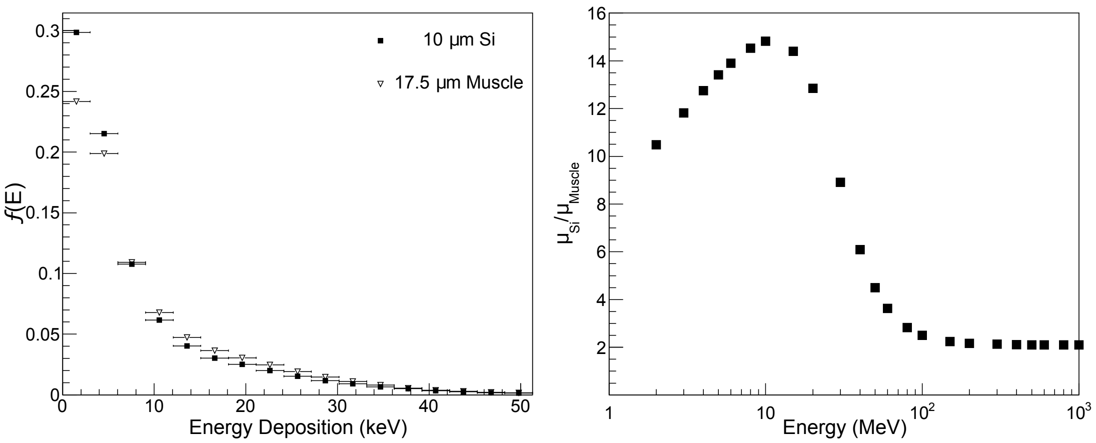

Figure 3.3: Left: A zoomed view of the energy deposition at 130 mm depth in water showing the over response of silicon at low energy depositions due to different stopping powers of electrons, the legend indicates the size and material of the SV. Right: plot of the ratio of the linear attenuation coefficients in silicon and muscle [97].

energy of the spectrum (E$_{max}$).

$$N\left(E_{\text{Si}Corr}\right) = (LEC)\left(N_1\left(E_{\text{Si}}|_0^{E_t}\right)\right) + N_2|_{E_t}^{E_{max}} \tag{3.3}$$

The *LEC* and E$_t$ were determined ad hoc to provide best agreement between the y_F, calculated in muscle and silicon SVs. Table 3.5 shows the *LEC* factor and the E$_t$ with respect to the depth in the phantom and the corresponding mean kinetic energy of the ^{12}C incident beam at the specific depth. The *LEC* factors were found to be the same for muscle and water SVs since the ratio of attenuation coefficients of water and muscle is $\sim$1.

In order to apply these corrections for other setups they may be applied based upon the mean energy of the carbon peak of the deposited energy spectrum (MCA) as shown in table 3.5.

Depth in Phantom (mm)	Mean ^{12}C ion peak (keV)	E_t (keV)	LEC
<50	<237	15	0.8
50-140	≥237	20	0.73
>140	>481	30	0.73
>160	*n/a*	15	0.8

Table 3.5: *LEC* factors to be applied up to the energy threshold E_t, based on the depth in the phantom, corresponding to the mean energy deposition peak, produced by the ^{12}C ion beam. Note the *n/a* corresponds to downstream of the BP.

Figure 3.4 summarises the effect of the *LEC* on the microdosimetric quantity y_F, which is seen to improve $\sim$10% by reducing the contribution of low energy deposition events in the SV$_{Si}$. The value y_D was seen to improve only minutely due to it being weighted for higher energy events, since y_D is more representative of the biological effect of radiation than y_F, this means that the use of a *LEC* factor can, for biological purposes, be ignored.

Figure 3.5 shows the dose weighted distributions, corrected by κ and LEC for muscle. It can be observed that there is an excellent alignment of peaks of the spectra, even after all the incident ^{12}C ions have stopped and only secondary fragments remain (corresponding to a depth of 165 mm). The agreement of the spectrum downstream of the BP is expected. Comparing the values of tables 3.1 and 3.2 for ^{12}C and protons, respectively, the conversion value between protons and ^{12}C only vary by ~0.02 for both materials.

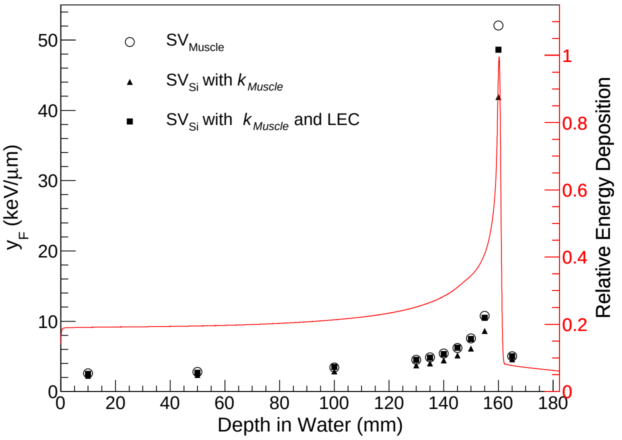

Figure 3.4: Plot showing y_F, calculated with a muscle SV (open circles), a silicon SV with κ_{muscle} correction only (triangle), and with both κ_{muscle} and LEC corrections(square).

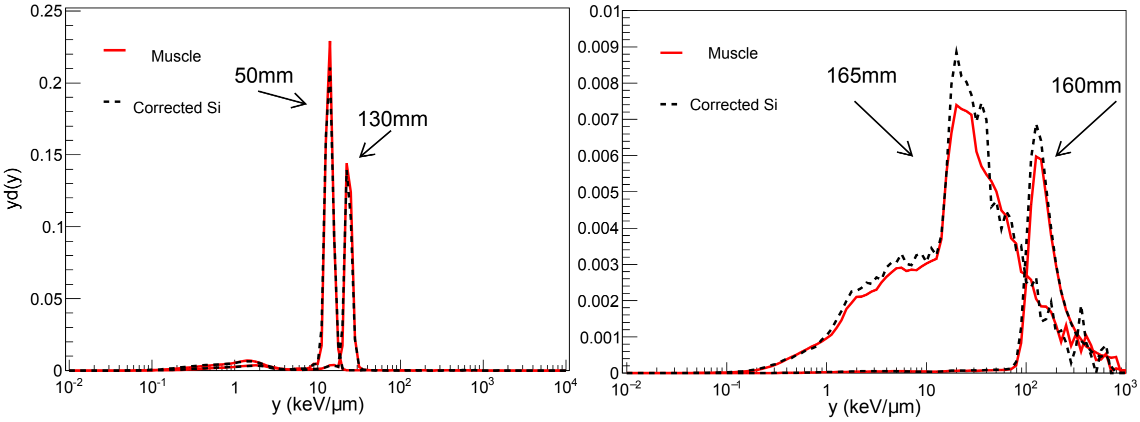

Figure 3.5: Comparison of the microdosimetric spectra calculated in muscle SVs and the corrected spectra in the silicon SVs, at depths in phantom equal to: 50, 130, 160 and 165 mm.

3.3.2 Study on the path length distribution and mean path length

The top left plot of figure 3.6 shows how the path length distributions (PLD) for all charged particles traversing the SV vary at particular depths including: near the phantom entrance (10 mm), at the BP (160 mm) and distally from the BP (165 mm). The top right plot of figure 3.6 shows the PLDs of different particle types including the primary ^{12}C ions as well as secondary ions and electrons which originate outside of the SV and traverse the detector. It can be seen that the primary and secondary ions both have peaks at 10 μm corresponding to particles entering perpendicular with the face of the SV, while electrons do not have this peak as they have a PLD more representative of an isotropic distribution. The bottom plot of figure 3.6 compares the path length distribution of the radiation field at 10 mm depth in the phantom to that of an incident isotropic ^{12}C ion radiation field, where the use of Cauchy's equation 1.7 is applicable. The path length distributions of the parallel and isotropic ^{12}C ion field differ drastically, particularly the primary ^{12}C beam component, suggesting that the use of the mean chord length is inappropriate.

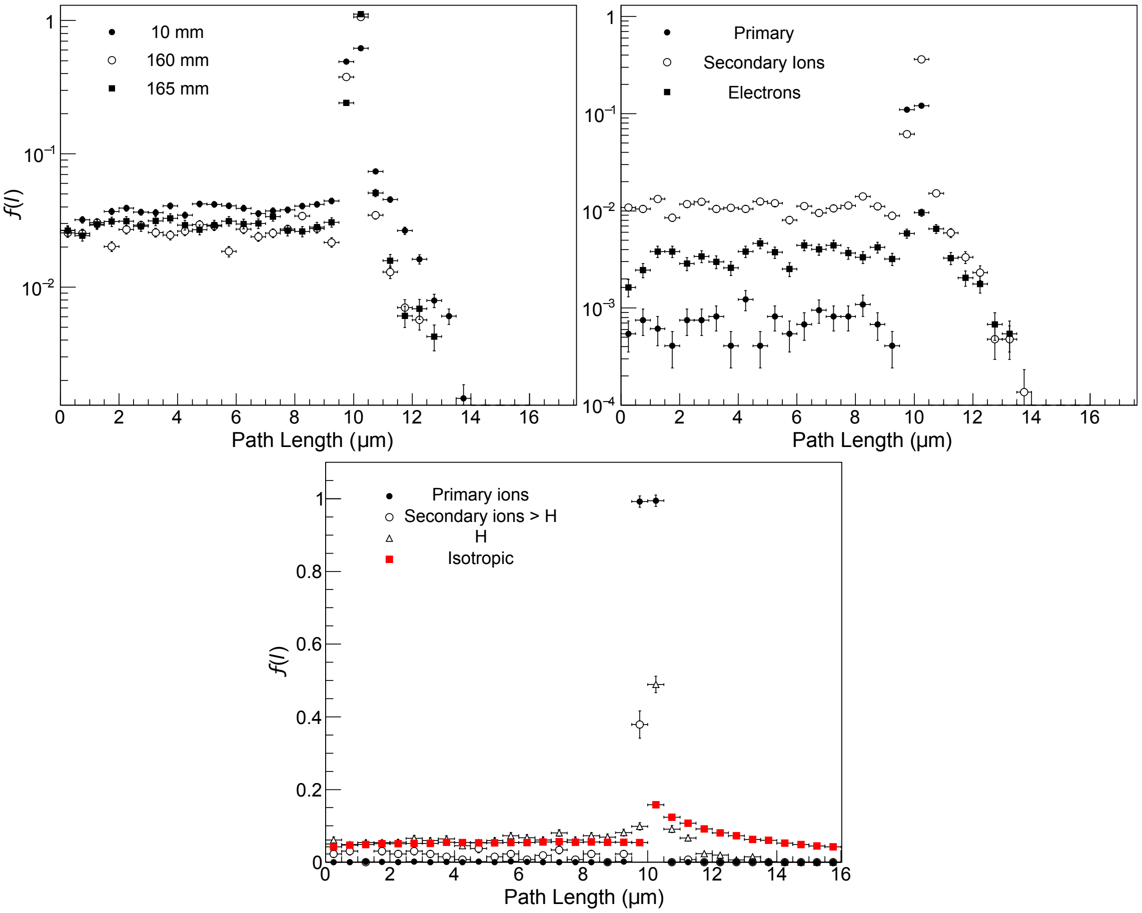

Figure 3.6: Top left: PLDs for all particles at the entrance of the phantom (10 mm) at the BP (160 mm) and distal to the BP (165 mm). Top Right: The path length distributions for different particles at the BP. Bottom: Comparison of the PLD at 10 mm of different particles compared to an isotropic ^{12}C ion source.

Figure 3.7 shows the $\langle l_{Path} \rangle$ along the depth in the phantom from taking the mean of the PLDs. The mean path lengths are then shown for secondary ions and electrons, separately. The incident carbon ions have a strong directionality, therefore their $\langle l_{Path} \rangle$ does not vary much and is approximately the same as the thickness of the SV (10 μm) in the direction of the incident ^{12}C beam. The $\langle l_{Path} \rangle$ of electrons is approximately 6.7 μm for all depths in the phantom and agrees well with $\langle l_{Cauchy} \rangle$, which is characteristic for an isotropic field. The $\langle l_{Path} \rangle$ of secondary ions varies largely in comparison to other types of particles such as the incident carbon ions and secondary electrons. At shallow depths in the phantom, $\langle l_{Path} \rangle$ is approximately 8.5 μm and then increases continuously up to the BP. This happens because of neutrons, which scatter significantly in water and are produced greatest at the surface of the phantom. Neutrons scatter target nuclei of the medium, which are mostly H for water, these nuclei have a comparatively large angular distribution, thus producing a $\langle l_{Path} \rangle$ closer to the one produced by an isotropic field. On the other hand, fragments produced from the interaction of the primary ^{12}C with target nuclei have a tendency to be more forwarded directed. This means that at increasing depths in the phantom where the neutron production decreases and the fragment production stays more consistent which causes the $\langle l_{Path} \rangle$ to steadily increase with depth in the phantom.

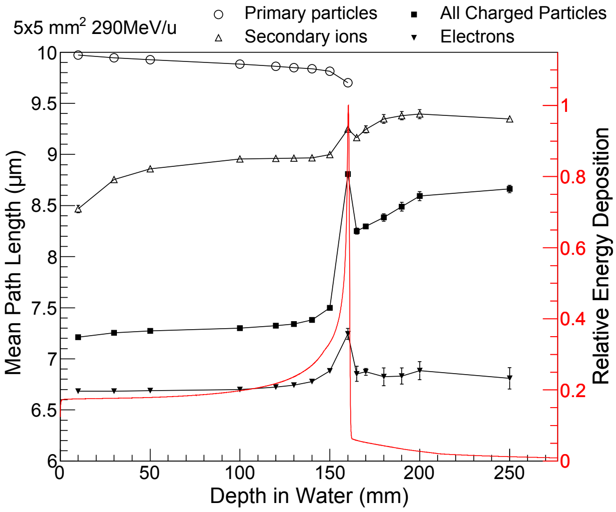

Figure 3.7: $\langle l_{Path} \rangle$ of different particles traversing the 10μm cylinder volume array at various depths in phantom. The SV is filled as a vacuum. The Bragg Curve is shown as well for reference.

Beyond the BP there is a small decrease in $\langle l_{Path} \rangle$ for secondary ions, which is due to a sharp decrease in fragmentation production due to the incident carbon ion beam having been stopped, increasing the neutron contribution. Further downstream of the BP $\langle l_{Path} \rangle$ can be seen to increase, this is due to more laterally directed particles leaving the centre of the beam, at greater depths. This causes the more forward directed particles to be more dominant.

The $\langle l_{Path} \rangle$ for secondary ions was studied with respect to the ^{12}C ion beam sizes of 5×5mm^2 and 50×50mm^2, the results are shown in figure 3.8. It can be observed that the $\langle l_{Path} \rangle$ of lighter secondary nuclear fragments decreases with larger field sizes. This happens because in larger beam sizes lighter fragments such as H have a higher probability to be scattered into the centre of the beam where the detector is positioned, contributing to a more isotropic field. Thus the mean path length value becomes closer to $\langle l_{Cauchy} \rangle$.

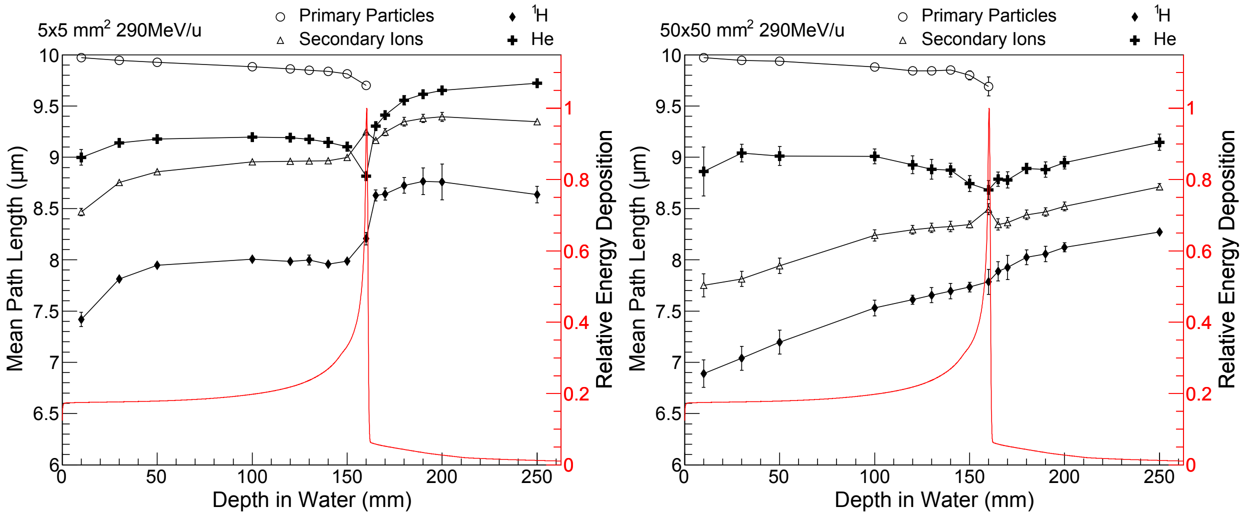

Figure 3.8: Comparison of mean path lengths for different particles for 5×5 mm^2 and 50×50 mm^2 fields sizes. The incident ^{12}C energy was 290MeV/u.

Summarising, the results of this research show that the mean path length varies quite noticeably for different components of the HIT radiation field, most pronounced between the primary carbon beam and electrons by ~30% for different depths in the phantom. Recoiled protons have a wider angular spread, while incident carbon ions and fragmented ions go largely straight through the detector.

From these results, to obtain a more constant mean path length for components of the radiation field, the SV should have dimensions with the thickness of the SV along the beam direction equal to $\langle l_{Cauchy} \rangle$. So in the case of a cylindrical SV like the Mushroom the height should be half the diameter of the SV. The resulting $\langle l_{Path} \rangle$ are shown in figure 3.9 for a 20×20 mm^2 field which is between the two extreme cases of 5×5 mm^2 and 50×50 mm^2. It can be seen that the mean path length values are between 9 μm and 10 μm for all components of the radiation field. Optimisation of the SV's design will be explored in detail in the following chapter

3.3.3 Impact of path/chord length for RBE$_{10}$ estimations

To determine the importance of the $\langle l \rangle$ on calculated RBE$_{10}$ values, using the MKM (section 1.6.3), three different RBE$_{10}$ calculations were performed, with the results shown in figure 3.10. The different methods included applying the isotropic value of 6.7 μm provided by Cauchy's formula as well as using the thickness of the SV, 10 μm. The remaining method was to use the values of $\langle l_{Path} \rangle$ calculated above in section 3.3.2, considering the specific path length for each component of the radiation field (incident carbon ions, secondary ions and electrons). These different methods were compared to the simulated RBE$_{10}$ of a simulated muscle sphere with a diameter of 10 μm and $\langle l_{Cauchy} \rangle$ of 6.7

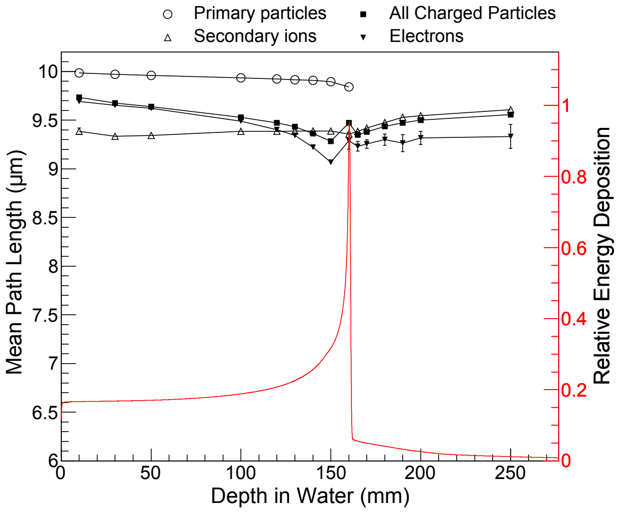

Figure 3.9: Calculated mean path length of particles traversing the cylinder of height 10μm and diameter 20μm, using a 20×20 mm^2 primary beam with energy of 290MeV/u.

μm.

It can be seen in figure 3.10 that using the $\langle l_{Cauchy} \rangle$ of 6.7 μm gives significantly different results compared to the other methods and notably differs from the spherical volume values and should not be used. The remaining two methods result in very similar RBE$_{10}$ values. Such agreement is due to the fact that the primary ^{12}C dominates the radiation field with its high LET while the secondary particles contribute less significantly to the RBE$_{10}$. The RBE$_{10}$ determined with the Si SV is similar to the one calculated with the muscle sphere of 10 μm diameter, with a difference of $\sim$2% which should be due to the different shape of the Si SV and muscle sphere. Larger differences are observed at the BP due to the sensitivity of y$*$. Beyond the BP the greatest difference is found due to the the primary carbon beam being stopped. Because the ^{12}C $\langle l_{Path} \rangle$ is very close to 10 μm for all depths, very little difference is seen between using the calculated $\langle l_{Path} \rangle$ values and the thickness of the SV. Beyond the BP, the secondary ion's $\langle l_{Path} \rangle$ approaches 9.4 μm (section 3.3.2) which is close to the thickness of the SV along the direction of the beam. This means that a constant 10 μm $\langle l_{Path} \rangle$ can be adopted instead of $\langle l_{Path} \rangle$ with no significant differences in calculated RBE$_{10}$.

Because of the dominance of the primary ^{12}C and that the secondary ions have a $\langle l_{Path} \rangle$ value very close to the thickness of the SV beyond the BP makes it conveniently accurate to use the thickness of the SV as the $\langle l_{Path} \rangle$ value. However this applies to this setup of detector and beam using ^{12}C and may not be so accurate in proton therapy where protons can scatter more frequently, contributing to a more isotropic field and more importantly has much fewer fragments produced, causing downstream of the BP to be dominated by nuclei scattered by neutrons which should produce values close to $\langle l_{Cauchy} \rangle$.

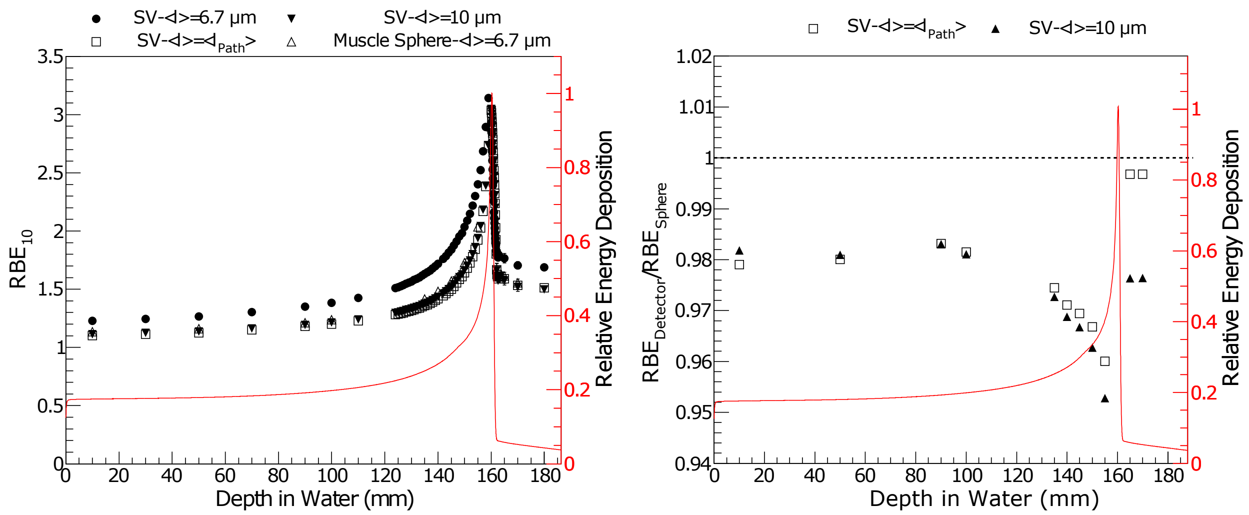

Figure 3.10: Left: RBE$_{10}$ derived from the Si microdosimeter calculated using different $\langle l \rangle$: the isotropic chord length of 6.7 μm, a constant $\langle l \rangle$ of 10 μm representing the thickness of the SV and using the $\langle l_{Path} \rangle$ values found in section 3.3.2 for each particle type. These are compared against the RBE$_{10}$ of a 10 μm muscle sphere with a $\langle l \rangle$ of 6.7 μm. Right: The ratio of the RBE$_{10}$ values of the microdosimeter using the $\langle l \rangle$ of 10 μm and $\langle l_{Path} \rangle$ with the values of the muscle sphere.

Figure 3.11 shows the RBE$_{10}$ values, estimated using the MKM, calculated from the Geant4 simulations of the Mushroom device with silicon SVs. The correction factors κ and *LEC* have been adopted to convert the microdosimetric spectra in silicon to muscle. The RBE$_{10}$ calculated in the Mushroom with SVs made of muscle are also shown in figure 3.11, together with the RBE$_{10}$. For comparison experimental measurements performed at HIMAC by Kase et al. [67], with a 12.5 mm diameter TEPC are also shown.

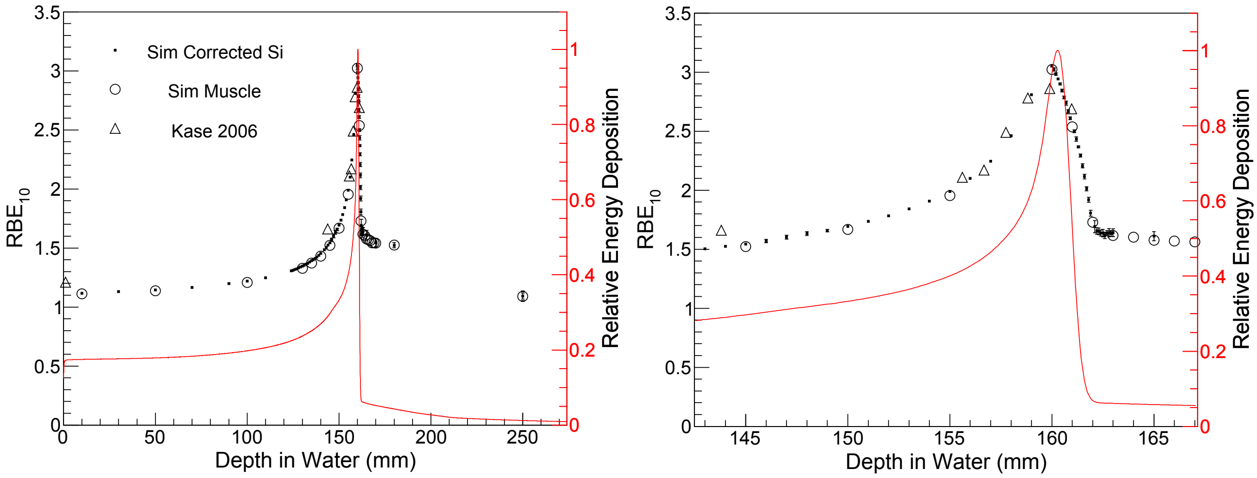

Figure 3.11: Left: Calculated RBE$_{10}$ along the depth in water, using the Mushroom detector. The RBE$_{10}$ resulting from the simulation study is compared to experimental measurements performed with the TEPC documented in Kase et al. [67]. Right: zoomed view of the results at the BP position.

It can be observed that the RBE$_{10}$ calculated in silicon and muscle SVs agree thanks to the adopted corrections. A good agreement is also observed with the experimental RBE_{10} determined with a TEPC, slight discrepancies can be attributed in part due to the differences of the beam lines. This means that in principle the Mushroom detector can be adopted to determine the RBE_{10}, but with an additional high spatial resolution, which cannot be achieved with the TEPC.

3.4 Conclusions

Being able to estimate the biological dose which is delivered to a patient is vital in HIT. It is important to be able verify that the planned biological dose of a treatment closely matches the actual treatment delivered. SOI microdosimetry provides a convenient solution to estimate the biological response of a treatment, however, because the measurement is in silicon the response must be converted to be biologically relevant. In addition, because the SVs of silicon microdosimeters are generally made in a cubic or cylindrical shape, when they are placed in a highly directional beam, generating the microdosimetric spectrum by assuming an isotropic field is not appropriate. This chapter investigated these two caveats of silicon microdosimetry and devised a method to convert the silicon energy deposition into a tissue equivalent microdosimetric spectrum.

A proposed, fully 3D CMRP silicon microdosimeter, was studied using Geant4 in a pristine 290 MeV/u ^{12}C ion beam. A conversion factor of 0.57 was calculated to convert the response in silicon to that of muscle and similarly a value of 0.54 for water. Conversion values were also calculated for a proton beam with an initial energy of 160 MeV and was found to have a value of 0.58 for striated muscle and 0.56 for water, with the later agreeing with a previous study in the literature. An additional low energy correction factor to address the over-response of silicon at low energies, which varied based on the incident beam energy, was investigated. This low energy correction factor was found to improve agreement between silicon and muscle/water by $\sim$10% for y_F but did not significantly effect y_D due to the prevalence of electrons impacting y_F significantly. However, when estimating the biological response of a radiation field y_D is more significant, meaning that the low energy correction factor does not need to be implemented for these applications.

One important consideration to make when converting silicon lineal energy spectrum to a TE material spectrum is when the microdosimetric spectrum is used as an input to a model, including the MKM (see section 1.6.3). For HSG cells the density is 1.0 g/cm^3 which is the same density of water and slightly less than the striated muscle used in this study of 1.04 g/cm^3. If a striated muscle spectrum is used as input to the MKM the resulting values may be differ slightly. However, this is the density for just a single type of cell, performing calculations with the RBE for different cells may also have a slightly different density also. However, as this chapter showed the conversion of silicon to a TE material is quite simple and stable for a range of energy ranges allowing for spectra to be easily changed to different cell types based on density/material.

An alternative method to the mean chord length was used in the form of the mean path length. The adoption of $\left\langle l_{Cauchy} \right\rangle$ was demonstrated to be less accurate than the adoption of $\langle l_{Path} \rangle$ equal to the thickness of the SV, when determining the RBE_{10}. This is due to the high directionality of the radiation field produced by the carbon ions.

It was demonstrated that the calculated correction factors allow to determine the RBE_{10} with good agreement with respect to the corresponding determined based on TEPC measurements. The maximum difference between experimental and simulation values was $\sim$8% at the very surface of the phantom. However, as discussed above, the configurations were significantly different, with experiment using a 100 mm diameter passive beam with $\sim$10 m between the nozzle and the phantom while the simulation featured a 5 mm pencil beam and 4 cm of air before the phantom. When comparing the simulated silicon cylinder SVs' response to the simulated muscle sphere SVs' response the maximum difference was $\sim$5%.

Chapter 4

Optimisation of SOI microdosimeter designs for hadron therapy

In the previous chapter, it was found that the mean chord length was not appropriate for silicon microdosimeters to convert the energy deposition to lineal energy, when used in heavy ion therapy beams. The unsuitability was due to the strong directionality of the radiation field. By comparing the RBE_{10}, as calculated by the MKM, of muscle spheres to silicon cylinders it was determined that the mean path length was more appropriate to convert the energy deposition spectrum into lineal energy. This chapter studies the optimisation of the sensitive volume design in proton and ^{12}C ion fields by reducing the variance of the mean path length.

Results of this chapter have been published in "Optimisation of the design of SOI microdosimeters for hadron therapy quality assurance", *Physics in Medicine Biology*, (63), 2018. Certain figures in this chapter have been reproduced from the publication.

4.1 Introduction

In the last chapter the conversion of the energy deposition in silicon to tissue equivalent lineal energy was studied using a "Mushroom" microdosimeter design. This Mushroom had cylindrical SVs which had the diameter equal to the height (10 μm), as mentioned previously, this was done since an elongation of one corresponds to a minimum variation of the chord length distribution for an isotropic distribution of chords in the SV [7]. For example, if you consider two cylinders, one with an elongation of 1 having a height and diameter of 10 μm and another cylinder with a diameter of 20 μm and height of 5 μm resulting in elongation of 4. Both of these cylinders have a mean chord length of 6.67 μm (calculated using Cauchy's equation), however, the chord length distribution (see section 1.5.1) of the cylinder with an elongation of 4 will correspond to a more broader distribution.

The path length is more appropriate for the highly directional HIT radiation field when the SVs are non-spherical. Admittedly, the path length is less convenient than the chord length due to it changing depending on the radiation field and its position. Ideally, especially in an experiment where the radiation field may not be well known, you would like to be able to use a single value to calculate the lineal energy. In the last chapter it was shown that using the thickness was a fairly good approximation for the mean path length. Optimisation of the SV's design to reduce the change in the mean path length should improve the approximation of the thickness used as the mean path length.

This study extends the previous work which was limited to investigating the $\langle l_{Path} \rangle$ for mono-energetic ^{12}C ion beams. Here the $\langle l_{Path} \rangle$ is examined for the case of a mono-energetic proton beam and spread out Bragg peaks (SOBP) for both incident protons and ^{12}C ions.

This work continues to further investigate the silicon-based experimental microdosimetric approach, in order to determine more accurately important quantities for treatment planning such as the dose equivalent and the RBE. It also supports the further optimisation of the SV's design, particularly in terms of its dimensions, for the application of SOI microdosimeters in hadron therapy quality assurance (QA).

When irradiated in hadron therapy beams, the SOI microdosimeters are usually set face on to the incident beam. Nevertheless, misalignments of few degrees may happen. Thus, the angular dependence of the $\langle l_{Path} \rangle$ is investigated to quantify the effect of such possible experimental misalignment on the $\langle l_{Path} \rangle$ and to see the general effect of different detector alignments with the beam.

4.2 Materials and Methods

For this study a different version of Geant4 was used than the last chapter, with version 10.2p1 being adopted to investigate the $\langle l_{Path} \rangle$ in proton and ^{12}C ion therapies.

The optimisation of the SV design was performed in two different ways. First the mean geometrical path length in the SV, $\langle l_{Geo} \rangle$, was calculated. This approach allowed the investigation of the effect on the $\langle l_{Path} \rangle$ produced by different alignments of the detector with the incident beam direction and by the angular spread or divergence of the particles incident on the SV, based on geometrical considerations only (neglecting the effect of the physical interactions). The difference between the $\langle l_{Geo} \rangle$ and the $\langle l_{Path} \rangle$ is that the $\langle l_{Path} \rangle$ considers all physical processes and particles created while $\langle l_{Geo} \rangle$ only considers different defined distributions of geometrical tracks traversing the SV. The advantage of studying the $\langle l_{Geo} \rangle$ is that it allows for the trend of the $\langle l_{Path} \rangle$ to be studied for general cases of alignment and divergence of the beam passing the SV while the $\langle l_{Path} \rangle$ represents a complicated mix of particles which have angular distributions that often vary with position in the phantom because of their physical interactions.

Secondly, the $\langle l_{Path} \rangle$ was studied in the same way as the previous chapter by placing the microdosimeter in the true radiation field and replacing the SV material with vacuum and recording the tracks of charged particles which traversed the SV.

4.2.1 Calculation of the mean geometrical path length

For calculations of the $\langle l_{Geo} \rangle$ a *geantino* beam was simulated. In Geant4 geantinos are particles which do not have any physical interactions. Such particles are well suited for geometrical studies. For both configuration studies, a 1 mm diameter beam was generated 0.01 μm from the top of the SV, independently from the SV's alignment angle (shown in figure 4.1 (a) and (b)).

For the case representing the angular alignment of the detector with the beam, a parallel beam was simulated incident upon a single SV placed at angles varying between 0° and 90° with respect to the beam as shown in figure 4.1 (a). 0° and 90° correspond to face on (with the SV perfectly aligned with the beam) and edge on configurations, respectively. For context, the accuracy of the positioning of the CMRP detector and phantom system with the beam is within 1° but larger angles are investigated for the interest of less precise setups and for general considerations. The simulated parallel beam differs slightly from real world therapeutic beams which have divergence, often a few milliradians at iso-centre, due to the shaping of the beam.

The second configuration, shown in figure 4.1 (b), investigates the effect of the angular distribution or divergence of the incident beam. In this case the $\langle l_{Geo} \rangle$ was calculated for different SV diameters when irradiated by a cone beam, varying the aperture angle θ as shown in figure 4.1 (b). The particles are generated with a random direction within the cone. In this case the incident beam originates from the same 1 mm diameter used in the alignment configuration to ensure the entire area of the SV is equally irradiated.

For both configurations the thickness of the SV is fixed to 10 μm and the geometrical path length is studied by varying the diameter of the SV. The path length in the SV was calculated as the distance between the point of entrance and exit of the geantino in the SV. The $\langle l_{Geo} \rangle$ was calculated as the average value of the geometrical path length distribution.

4.2.2 Calculation of $\langle l_{Path} \rangle$ in radiation fields of interest for hadron therapy

For optimising the $\langle l_{Path} \rangle$ a similar simulation as the previous chapter was used with a few modifications. Figure 4.1 (c) shows the simulation set-up for calculating the $\langle l_{Path} \rangle$ in different beams, both mono-energetic and SOBP beams were simulated for proton and ^{12}C ion beams. Differences between the previous chapter include the air gap between the beam generation and the phantom was increased to 40 cm and the beam's profile was

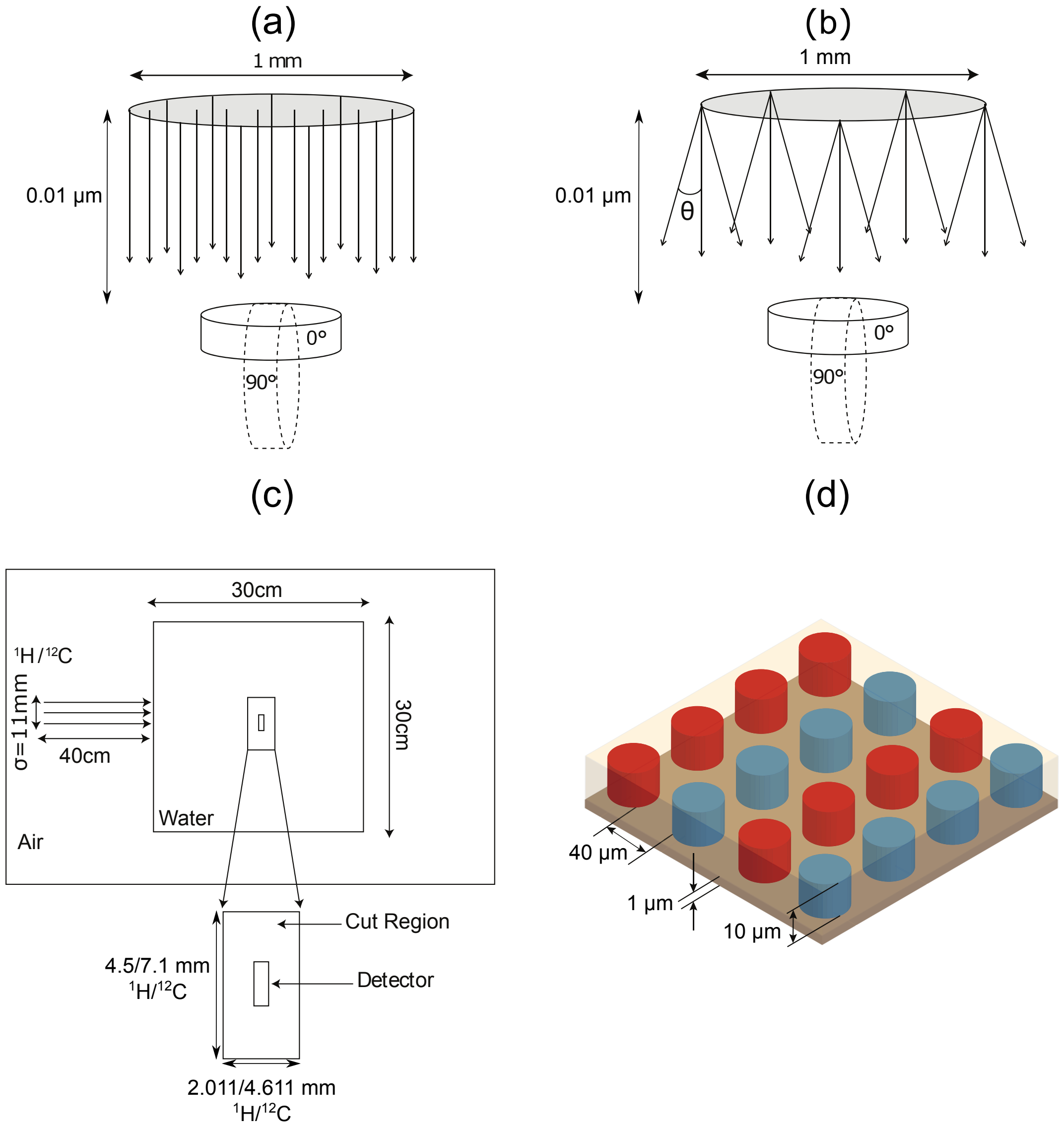

Figure 4.1: Simulation setups used in this study. (a) and (b) show the simulation setup adopted to study the effect on the $\langle l_{Geo} \rangle$. (a) studies the effect of the alignment of the SV with the beam direction, the SV is irradiated with a parallel geantino beam. (b) is the setup used to study the effect of the angular spread of the incident geantino beam. (c) depicts the simulation setup used to calculate the $\langle l_{Path} \rangle$ in the radiation fields of interest and (d) shows a region of the SOI microdosimeter modelled in the Geant4 simulation to calculate the $\langle l_{Path} \rangle$. All the investigated designs for the $\langle l_{Path} \rangle$ had the same thickness of 10 μm in the direction of the incident beam and the same distance between the outside of the SVs of 40 μm. Microdosimeter designs with larger diameter SVs have less SVs in total. The blue and red SVs represent SVs connected together on different channels.

modelled as a Gaussian with a σ of 11 mm. The mono-energetic beams were 150 MeV and 290 MeV/u for proton and ^{12}C ions, respectively, which correspond to a range of $\sim$160 mm in water. For the simulated proton beams an energy sigma of 1% was applied while for the ^{12}C ion beams a 0.2% sigma was used. The SOBPs were produced using multiple energy weights. The proton SOBP was weighted to deliver a uniform physical dose 50 mm in width while the ^{12}C ion SOBP was weighted to give a uniform biological dose 60 mm in width.

The Mushroom microdosimeter was positioned at various depths along the Bragg curve/spread out Bragg peak in water. There is one slight difference with the model of the Mushroom used in this chapter compared to the previous one, the distance between the outside edges of the SVs, is 40 μm instead of the pitch. This change from the pitch to distance from the outside edge of the SV was done to accommodate the large diameter SVs. A zoomed in region of the detector with 10 μm diameter SVs is shown in figure 4.1 (d). The thickness of the SVs along the beam direction was fixed to 10 μm. The different detector designs investigated included diameters of 10, 20, 30, 40 and 50 μm, alternatively. For larger diameter designs the distance between the SV edges and area that the SVs occupied was kept the same as the 10 μm design except that fewer total SVs were placed, with the active area populated with SVs being 2.5×2.5 mm^2.

The physics used in the previous chapter were adopted here as well. The Mushroom was again placed in a secondary cuts region. The thickness of the region was twice the maximum range of electrons plus the total thickness of the detector (10 μm SV thickness and 1 μm substrate), the width of the cut region is the active area of the detector (2.5 mm) plus twice the maximum electron range. With maximum electron ranges of 1 and 2.3 mm being used for the proton and ^{12}C ion beams, respectively.

4.2.3 Estimating the $\langle l_{Path} \rangle$ using the energy deposition spectra

The final part of this chapter examines whether the path length can be estimated based upon the energy deposition in the detector itself. The same simulation set-up depicted in figure 4.1 (c) is used but replaces the vacuum SV with silicon to calculate the energy deposition. Monte Carlo simulations are a valid tool to determine the $\langle l_{Path} \rangle$ when the beam line is well known and accurately described in the simulation. However, in experimental studies the incident radiation field on the microdosimeter by a beam line may not be well known, producing possible inaccuracies between the true and the Monte Carlo-based calculation of the $\langle l_{Path} \rangle$. The effect of the discrepancy between the actual and calculated $\langle l_{Path} \rangle$ values may be further amplified if the design of the SV causes a large variation of the $\langle l_{Path} \rangle$ along the Bragg curve leading to the SV thickness being inappropriate as an approximation to the $\langle l_{Path} \rangle$.

In order to limit possible inaccuracies in the value of the $\langle l_{Path} \rangle$, deriving from situations as the ones mentioned above, it is convenient to be able to estimate the $\langle l_{Path} \rangle$ directly from the response of the detector. Here we investigate the applicability of the same method to mono-energetic proton and ^{12}C ion beams with energy of 150 MeV and 290 MeV/u, respectively, and clinical proton and ^{12}C ion SOBP beams. Here a 10 μm diameter SV was adopted as this design was found to correspond to the worst case of variation of the $\langle l_{Path} \rangle$. The method investigated as a way to estimate the $\langle l_{Path} \rangle$ involved using the energy deposited in the SV by the incident beam. The mean energy deposited in the peak, on the right of the energy deposition spectrum, was recorded with the value of the $\langle l_{Path} \rangle$ at that position. Instead of plotting the $\langle l_{Path} \rangle$ against the depth in water it was plotted against the mean energy deposited in the peak by the primary beam. This concept is illustrated in figure 4.2 which shows two different incident energy beams with the detector placed at different depths in water so that the mean kinetic energy of the beam is the same. To have values be biologically relevant the energy deposition in the silicon SVs were converted to striated muscle using the conversion values of 0.58 and 0.57 for proton and ^{12}C , respectively, which were determined in the previous chapter.

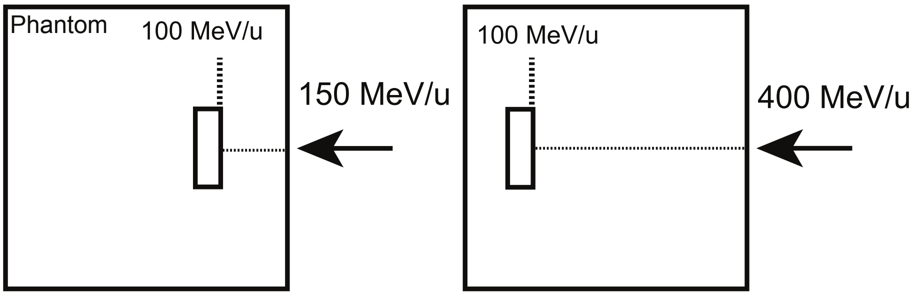

Figure 4.2: Diagram which illustrates the concept of using the energy deposited by the incident beam relating it to the mean path length instead of the depth in water. Two different incident beams have different initial energies but the detectors are placed at different depths so that each beam has the same average energy when it hits the detector.

4.3 Results

4.3.1 Study of the mean geometrical path length.

Figure 4.3 shows the calculated $\langle l_{Geo} \rangle$ when considering different tilt angles and diameters of SVs. The geantinos are incident normally to the SV when aligned at 0°. In general it can be observed that the $\langle l_{Geo} \rangle$ decreases to a minimum, whose value depends on the specific SV diameter, and then it increases with the tilt angle. The $\langle l_{Geo} \rangle$ can differ significantly from the $\left\langle l_{Cauchy} \right\rangle$, reported in table 4.1 for all the SV diameters considered. When the SV is aligned at smaller tilt angles (less than ∼30°), it can be observed that the $\langle l_{Geo} \rangle$ varies much less from its initial value at 0° for larger diameters. Compared to the $\langle l_{Geo} \rangle$ at 0°, the value at 15° for the 10 μm diameter SV has a reduction of approximately

~20%, while for the 20 μm diameter SV the reduction is ~10%. However, at larger tilt angles the larger the diameter of the SV the more rapidly their value differs from the 0° value.

Diameter (μm)	$\langle l_{Cauchy} \rangle$ (μm)
10	6.67
20	10
30	12
50	14.29
100	16.67

Table 4.1: $\langle l_{Cauchy} \rangle$ calculated for 10 μm thick SVs, with varying diameter.

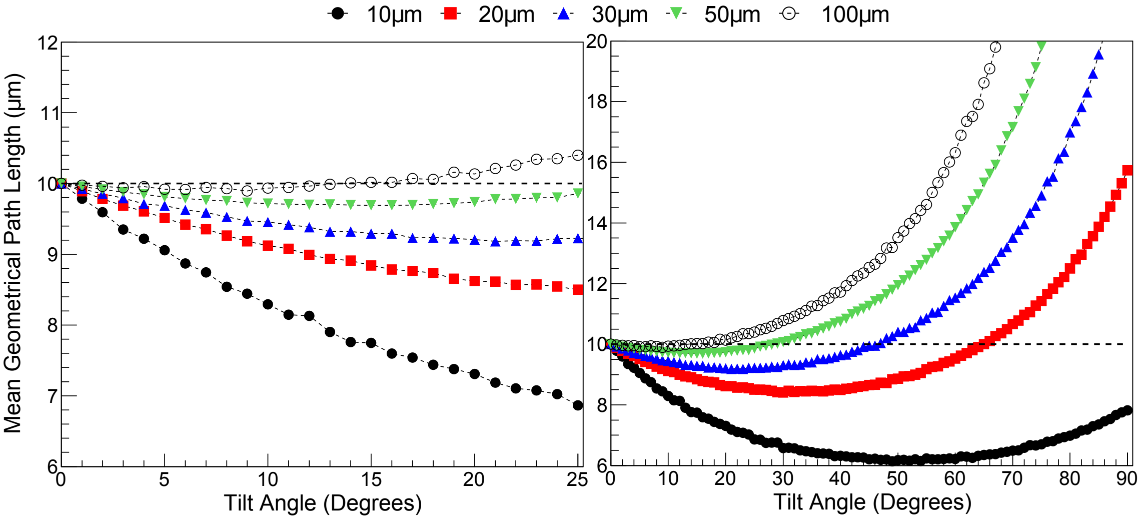

Figure 4.3: The $\langle l_{Geo} \rangle$ is plotted against the tilt angle, when varying the SV diameter (reported in the legend). The left plot shows a zoomed in range of the right plot.

Figure 4.4 shows the effect of the angular spread or divergence of the incident beam, represented in terms of θ (see figure 4.1, (b)), when varying the diameter of the SV. The $\langle l_{Geo} \rangle$ is calculated for a number of different tilt angles between 0° and 25°. For smaller θ (up to ~40°), the $\langle l_{Geo} \rangle$ varies the most for smaller diameter SVs, with the 10 μm diameter SV varying between ~7 and 10 μm. In contrast, for large θ the larger diameter SVs have values of $\langle l_{Geo} \rangle$ which extend a greater range of values compared to smaller SVs. Similar to the misalignment case, each SV is seen to reach a minimum $\langle l_{Geo} \rangle$ value depending on the specific diameter of the SV and then it increases again.

When changing the alignment of the detector by altering the tilt angle the variation of the $\langle l_{Geo} \rangle$ can be seen to reduce, with the reduction being the greatest for the smaller diameters. At a tilt angle of 25° the 10 μm diameter can be seen to provide an almost flat response of the $\langle l_{Geo} \rangle$ between beam divergences of 0° and 90°. For the 20 μm diameter SV the tilt angle to obtain a flat response is reduced to ~15°, however, the range of the flat response is reduced to a maximum of ~50°. The larger diameter SVs do not experience a strong flat response when adjusting the tilt angle, with the $\langle l_{Geo} \rangle$ generally increasing with larger beam divergence.

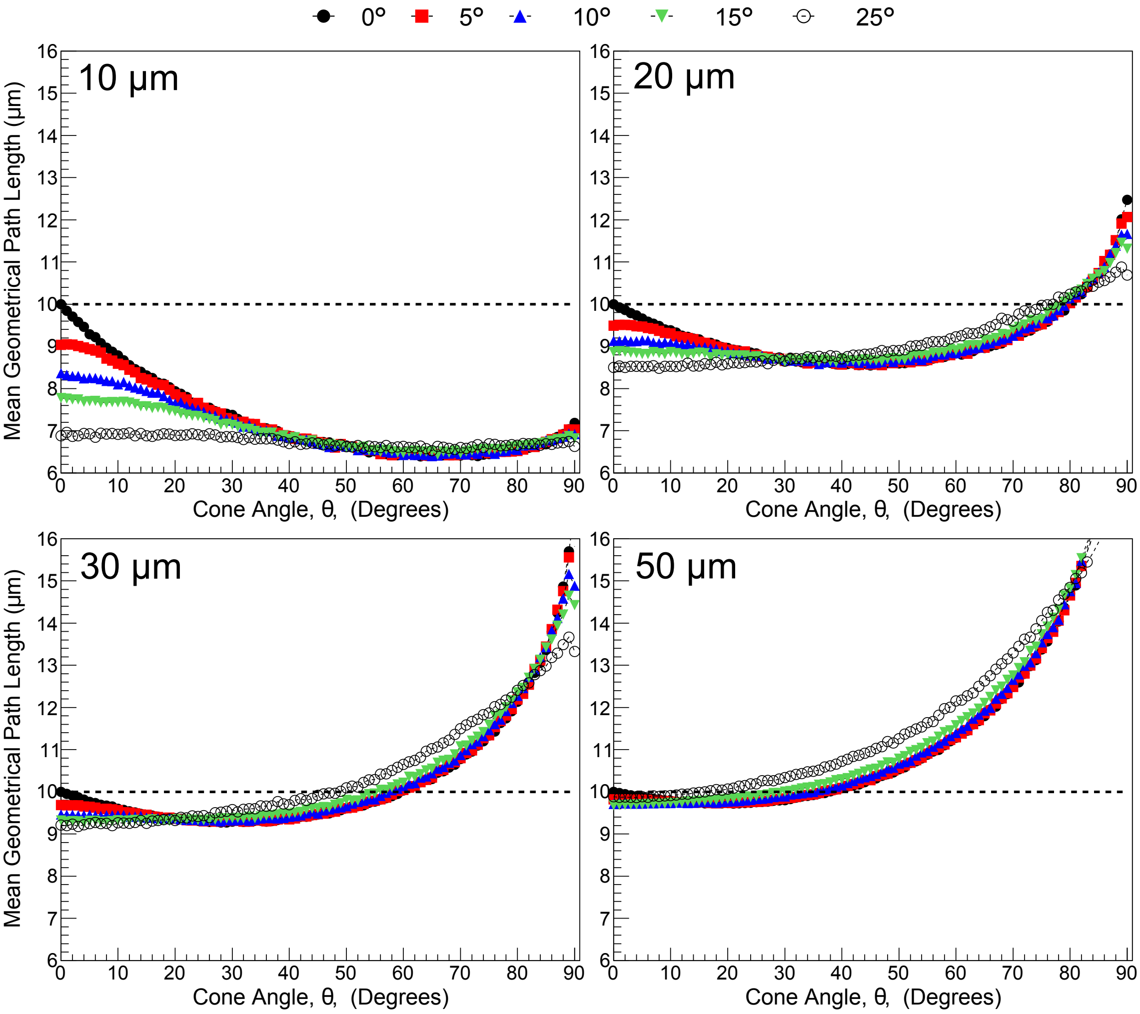

Figure 4.4: $\langle l_{Geo} \rangle$ of SVs with a diameter of: 10 μm (top left), 20 μm (top right), 30 μm (bottom left) and 50 μm (bottom right). $\langle l_{Geo} \rangle$ is calculated against the angle θ (see figure 4.1 (b)). The tilt angle of detector alignment is shown in the top legend.

4.3.2 Characterisation of the Proton and ^{12}C ion Radiation Fields

The fluence of the incident and secondary particles along the depth of the water phantom in the mono-energetic proton and ^{12}C ion radiation fields under investigation are shown in figure 4.5 (a) and (b). It can be seen that for the proton beam the fluence of neutrons and protons is fairly constant before the Bragg peak, after which the fluence of secondary protons decreases rapidly while the neutrons are attenuated more slowly. Comparing the fluence of the primary proton and ^{12}C ion beams it can be seen that the ^{12}C ion beam undergoes a much higher amount of attenuation (~50%) compared to the proton beam (~20%) when reaching the Brag Peak (BP). This is due to the significantly higher nuclear cross-sections of ^{12}C compared to proton beams, which translates to ~4 orders of magnitude higher fluence of fragments in the ^{12}C ion beam case. Due to the different dominant processes in the two fields the proton beam is dominated by neutrons with a large angular distribution while the ^{12}C ion radiation field is more dominated by more forward directed fragments.

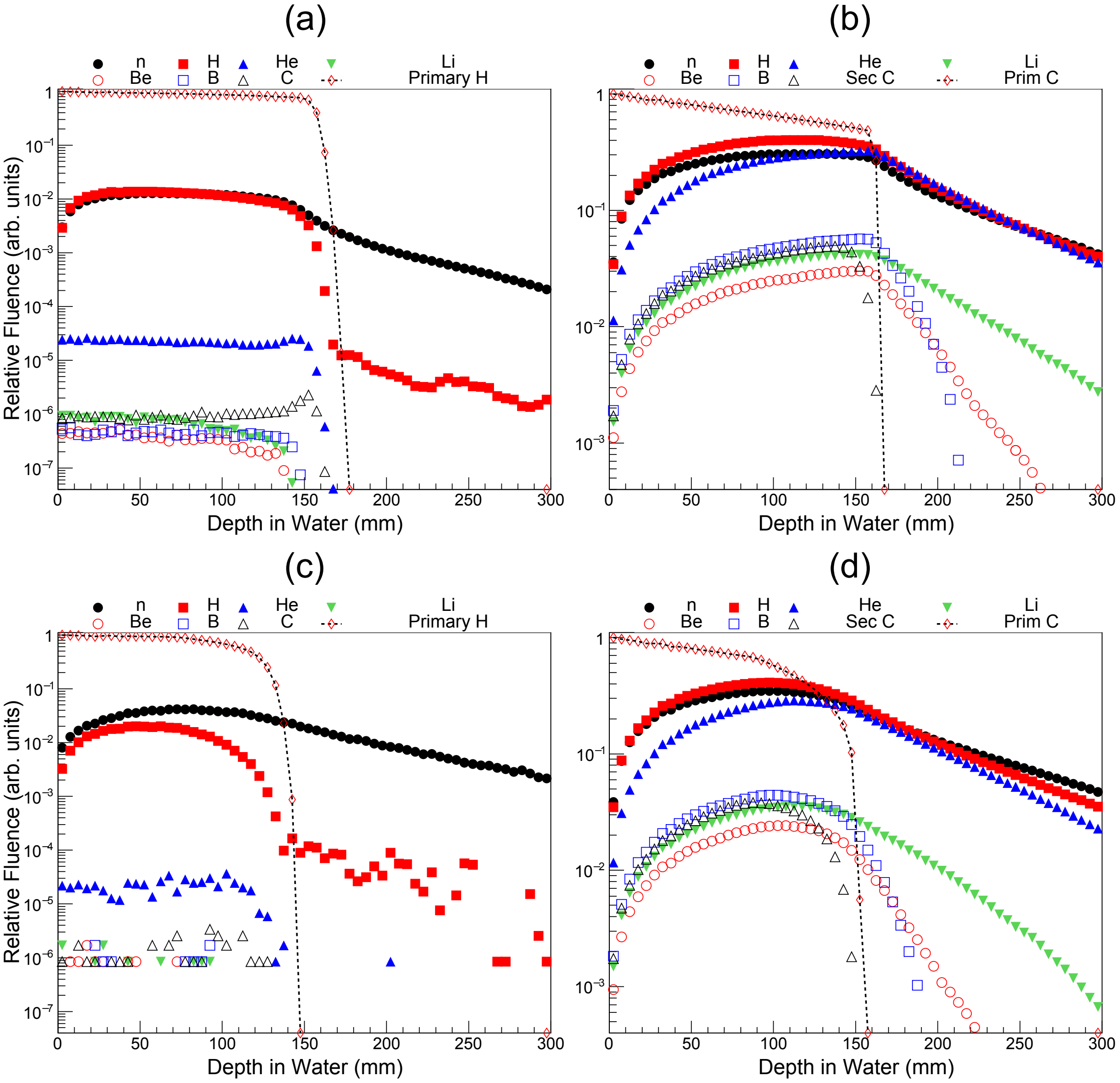

Figure 4.5: The relative fluence of different nuclear species along the depth of the water phantom for an incident: 150 MeV proton beam (a), a 290 MeV/u ^{12}C ion beam (b), a proton SOBP (c) and a ^{12}C ion SOBP (d). Note that the minimum of the proton y-axis is three orders of magnitude lower than the ^{12}C axis.

Figure 4.5 (c) and (d) shows the fluence of secondary particles along the depth in the phantom in the proton and ^{12}C ion SOBP fields. The fluences are higher than in the case of the corresponding mono-energetic beams due to the distal radiation fields from different beam energies accumulating as they stop in the phantom.

Typical proton and ^{12}C ion microdosimetric $yd(y)$ spectra are shown in figure 4.6 for a 150 MeV proton and 290 MeV/u ^{12}C ion beam both placed at a depth of 150 mm (with an angle of 0° with the beam, corresponding to the face on configuration). This depth corresponds to the BP for the proton beam and just before the BP for the ^{12}C ion beam. The spectra have been converted from silicon (using the 20 μm diameter Mushroom SV design) to striated muscle using the conversion factor of 0.58 and 0.57 found in the previous). Each plot shows the contribution that different particle types make to the total dose deposited in the detector. It can be seen that in the case of the proton beam different particle types have a similar lineal energy while the microdosimetric spectra of the ^{12}C ion beam have a well defined peak due to the primary ^{12}C ions and a lower lineal energy peak due to secondary fragments and electrons. In particular, in the case of proton therapy the lineal energy spectra of the primary and secondary protons overlap along the Bragg curve, because of this it is important to have similar $\langle l_{Path} \rangle$ for both the primary beam and secondary ions.

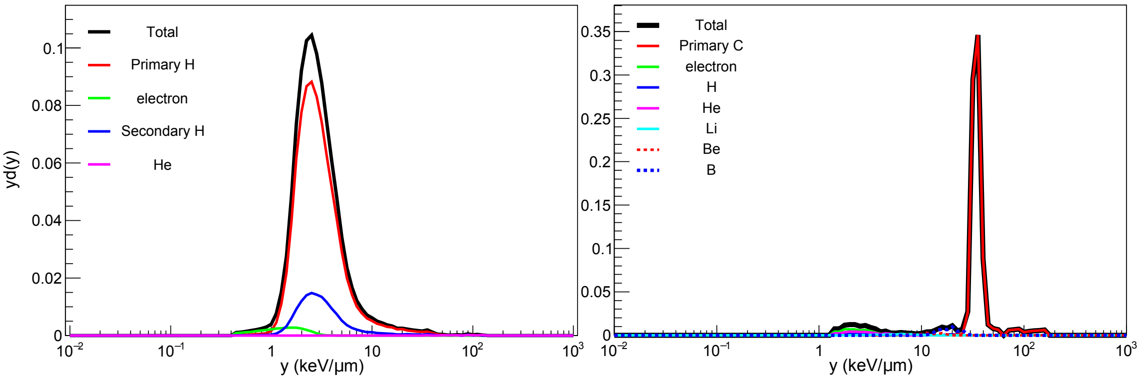

Figure 4.6: $yd(y)$ spectra of the detector for a 150 MeV proton beam (left) and a 290 MeV/u ^{12}C ion beam (right), both at 150 mm in water.

4.3.3 $\langle l_{Path} \rangle$ in mono-energetic beam

The mean path length, $\langle l_{Path} \rangle$, was calculated for SVs with various diameters, when irradiated by a 150 MeV and 290 MeV/u pristine proton and ^{12}C ion beam, respectively. The $\langle l_{Path} \rangle$ is presented for various depths in the radiation fields as well as tilt angles between the microdosimeter and the incident beam for diameter sizes of 10 and 20 μm and are summarised along with 30, 40 and 50 μm diameters at the end of this section in tables. The results are presented separately for the incident beam and the secondary ions, as these two components can have significantly different angular distributions.

Figure 4.7 (a) and (b) show the $\langle l_{Path} \rangle$ calculated separately for the primary and secondary ions, respectively, using the 10 μm diameter design when irradiated with a 150 MeV pristine proton beam. Similarly, 4.7 (c) and (d) show the calculated $\langle l_{Path} \rangle$ values for a 20 μm diameter SV. The SVs are set at different positions along the Bragg curve in the water phantom, for reference the energy deposition in the water is plotted in red on the path length plots. The error bars plotted on figure 4.7 as well as all following figures represents one standard deviation calculated over ten sets of simulation data.

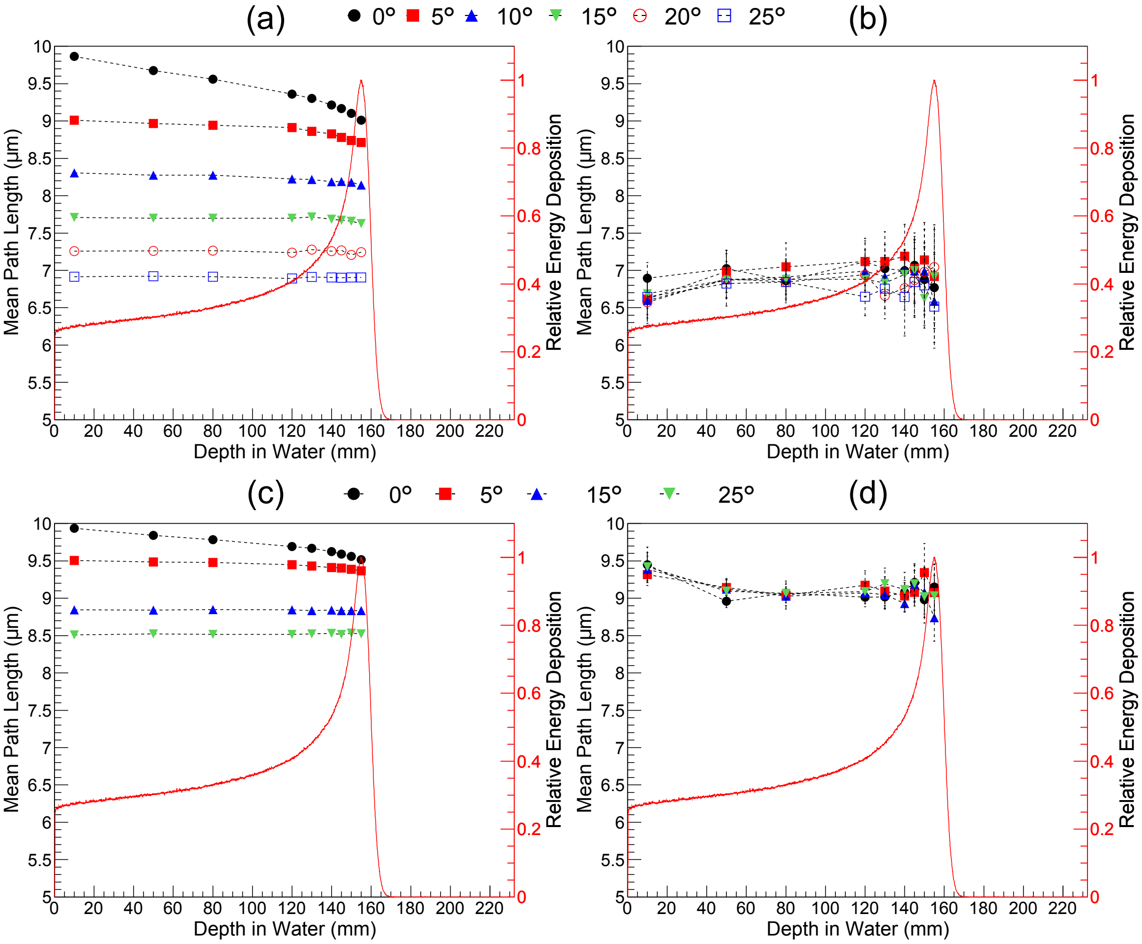

Figure 4.7: The $\langle l_{Path} \rangle$ calculated in a mono-energetic 150 MeV proton beam. (a) and (b) are calculated using the 10 μm diameter SV design for primary (a) and secondary ions (b), respectively. (c) and (d) also show the $\langle l_{Path} \rangle$ for primary and secondary ions, respectively, using a 20 μm diameter SV instead. The microdosimeter is placed at various tilt angles with respect to the direction of the beam (reported in the legends).

When considering the $\langle l_{Path} \rangle$ of incident primary protons with the detector being perfectly aligned in the phantom (0° tilt angle), the $\langle l_{Path} \rangle$ slightly decreases with increased depth in the phantom. This is due to the scattering of the beam causing an increased angle of incidence on the SV at deeper positions. At the Bragg peak the 10 μm diameter SV has a value of ∼9 μm while the 20 μm diameter is ∼9.5μm.

The results show that the value of $\langle l_{Path} \rangle$ has a strong dependence with respect to the tilt angle, with the larger diameter SV being affected less. For larger tilt angles, the $\langle l_{Path} \rangle$ of the incident beam undergoes less variation in its value. Furthermore, the secondary ion's $\langle l_{Path} \rangle$ are not seen to vary significantly for both the 10 μm or 20 μm designs. This effect agrees with what was predicted in figure 4.4 which showed that the $\langle l_{Geo} \rangle$ values converge for different tilt angles for both the designs at a cone angle (θ) of ∼60°. In particular the $\langle l_{Path} \rangle$ ranges between ∼6.5 and 7 μm and ∼9 and 9.5 μm, for the 10 μm and 20 μm diameter microdosimeter designs, respectively.

The $\langle l_{Path} \rangle$ of secondary ions for the 10 μm design is close to the isotropic value of 6.7 μm, while for the 20 μm design the $\langle l_{Path} \rangle$ is slightly lower than the isotropic value of 10 μm, with a value of 9 μm, which is expected for a large angular distribution based on figure 4.4 corresponding to a cone angle of ∼60°. At the entrance of the phantom the $\langle l_{Path} \rangle$ of the 10 μm design increases slightly while the 20 μm decreases from ∼9.4 μm, from figure 4.4 this indicates the angular distribution reaching the detector is larger at the surface of the phantom and decreases as more forwarded directed particles stay within the beam.

The $\langle l_{Path} \rangle$ calculated for 10 and 20 μm diameter SV designs in a mono-energetic 290 MeV/u ^{12}C ion beam is shown in figure 4.8 (a-b) and (c-d), respectively. It can be seen that the primary ^{12}C ion beam has a noticeably larger $\langle l_{Path} \rangle$ than for the proton beam due to it having less scattering along its trajectory.

As figure 4.5 shows, the fluence of secondary ions in the ^{12}C ion beam is orders of magnitude higher than for the proton beam. As observed in section 4.3.2, this higher fluence of fragments leads to noticeable differences between the secondary ion's $\langle l_{Path} \rangle$ of proton and ^{12}C ion beams. Since the secondary particles created via fragmentation in the ^{12}C ion beam tend to be more forwarded directed, they have a path length in the SV closer to the thickness of the SV, at any position along the Bragg curve. In the case of the proton beam, instead the secondary ions have a larger angular spread when reaching the SV, especially at the Bragg peak, producing a more constant $\langle l_{Path} \rangle$. This explains why the effect of the tilt angle is more pronounced in the ^{12}C ion beam case.

Tables 4.2 and 4.3 report the variation of the $\langle l_{Path} \rangle$ for different SV diameters placed in the mono-energetic 150 MeV proton and 290 MeV/u ^{12}C ion fields. The average percentage variation, PV, is calculated using equation 4.1, where d is the number of depths in the phantom under study and $\langle l_{Path} \rangle_0$ is the $\langle l_{Path} \rangle$ of the SV at the first depth in the phantom. The PV is calculated separately for the incident primary beam (PV_P) and the secondary

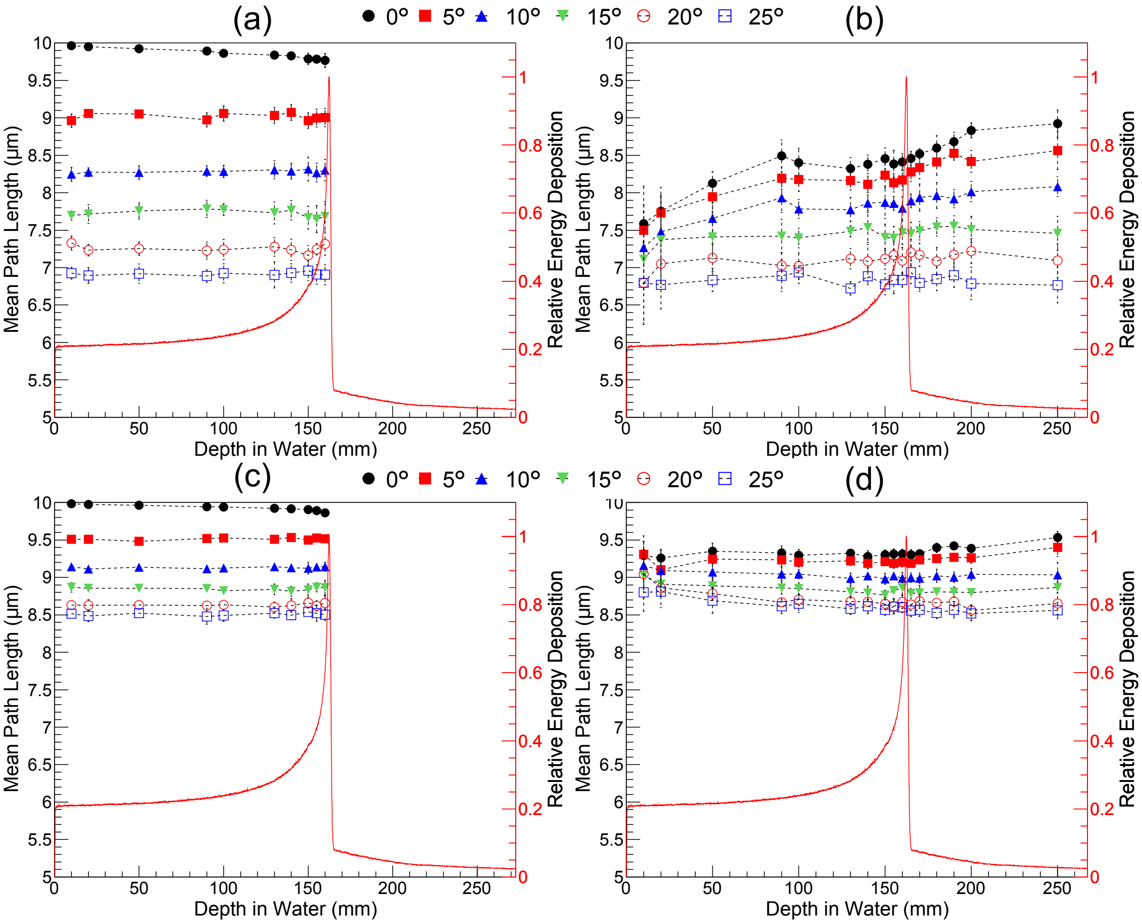

Figure 4.8: The $\langle l_{Path} \rangle$ calculated in a mono-energetic 290 MeV/u carbon beam. (a) and (b) are calculated using 10 μm diameter SV design for primary (a) and secondary ions (b), respectively. (c) and (d) also show the $\langle l_{Path} \rangle$ for primary and secondary ions, respectively, using a 20 μm diameter SV instead. The microdosimeter is placed at various tilt angles with respect to the direction of the beam (reported in the legends).

ions, (PV_S). Equation 4.2 was used to calculate the variation of the $\langle l_{Path} \rangle$ along the depth in the phantom between the primary and secondary ions ($PV_{P,S}$). The percentage variation PV_t was calculated for different tilt angles from the 0° position between the microdosimeter and the incident beam by means of equation 4.3, where $\langle l_{Path} \rangle_{i,0}$ is the $\langle l_{Path} \rangle$ at the i^{th} depth with a tilt angle of 0°. PV_t was also calculated along the depth of the Bragg curve. Also in this case, the PV_t was calculated separately for the incident primary beam ($PV_{t,P}$) and secondary ions ($PV_{t,S}$).

$$\langle PV \rangle = \frac{100\%}{d} \left(\sum_{i=0}^{d-1} \left| \frac{\langle l_{Path} \rangle_i - \langle l_{Path} \rangle_0}{\langle l_{Path} \rangle_0} \right| \right) \tag{4.1}$$

$$\langle PV_{P,S} \rangle = \frac{100\%}{d} \left(\sum_{i=0}^{d-1} \left| \frac{\langle l_{PathPrim} \rangle_i - \langle l_{PathSec} \rangle_i}{\langle l_{PathPrim} \rangle_i} \right| \right) \tag{4.2}$$

$$\langle PV_t \rangle = \frac{100\%}{d} \left(\sum_{i=0}^{d-1} \left| \frac{\langle l_{Path} \rangle_{i,t} - \langle l_{Path} \rangle_{i,0}}{\langle l_{Path} \rangle_{i,0}} \right| \right) \tag{4.3}$$

SV Diameter (μm)	Tilt angle	PV_P	PV_S	$PV_{P,S}$	$PV_{t,P}$	$PV_{t,S}$
10	0	4.66 ± 0.01	1.60 ± 0.08	25.71 ± 0.39	0 ± 0	0 ± 0
	15	$0.23 \pm 7\times10^{-4}$	4.69 ± 1.40	11.07 ± 0.18	18.18 ± 0.03	4.98 ± 1.63
	25	$0.13 \pm 4\times10^{-4}$	3.63 ± 1.05	2.28 ± 0.05	26.51 ± 0.05	5.44 ± 1.09
20	0	$2.27 \pm 8\times10^{-4}$	3.64 ± 0.04	6.33 ± 0.04	0 ± 0	0 ± 0
	15	$0.06 \pm 6\times10^{-5}$	3.43 ± 0.04	3.01 ± 0.02	8.96 ± 0.01	1.26 ± 0.03
	25	$0.12 \pm 1\times10^{-4}$	3.04 ± 0.03	7.39 ± 0.06	12.26 ± 0.01	0.77 ± 0.01
30	0	$1.25 \pm 7\times10^{-4}$	2.92 ± 0.07	3.63 ± 0.07	0 ± 0	0 ± 0
	15	$0.18 \pm 2\times10^{-4}$	5.68 ± 0.15	10.52 ± 0.15	5.43 ± 0.01	1.88 ± 0.08
	25	$0.16 \pm 3\times10^{-4}$	5.77 ± 0.16	12.54 ± 0.21	6.18 ± 0.01	2.25 ± 0.06
40	0	$0.87 \pm 4\times10^{-4}$	5.98 ± 0.15	10.07 ± 0.18	0 ± 0	0 ± 0
	15	$0.08 \pm 1\times10^{-4}$	6.03 ± 0.14	14.47 ± 0.32	$3.37 \pm 2\times10^{-3}$	1.16 ± 0.04
	25	$0.17 \pm 3\times10^{-4}$	7.67 ± 0.21	16.29 ± 0.29	$2.59 \pm 2\times10^{-3}$	3.30 ± 0.07
50	0	$0.63 \pm 3\times10^{-4}$	6.51 ± 0.15	14.13 ± 0.20	0 ± 0	0 ± 0
	15	$0.14 \pm 2\times10^{-4}$	8.45 ± 0.16	17.55 ± 0.23	$2.08 \pm 1\times10^{-3}$	1.05 ± 0.03
	25	$0.22 \pm 3\times10^{-4}$	7.48 ± 0.17	19.55 ± 0.29	$0.52 \pm 5\times10^{-4}$	3.87 ± 0.08

Table 4.2: Percentage variation of the $\langle l_{Path} \rangle$, calculated for different SV diameters, when irradiated with a 150 MeV proton beam. PV_P is calculated along the Bragg curve with respect to the first depth considered in the phantom using equation 4.1, for primary proton beam, PV_S on the other hand is calculated using only secondary ions. $PV_{P,S}$ is the variance between the primary and secondary ion's $\langle l_{Path} \rangle$, averaged over all depths, calculated using equation 4.2. PV_t is calculated along the Bragg curve, for different tilt angles with respect to 0°, for both primary ($PV_{t,P}$) and secondary ($PV_{t,S}$) ions, by means of equation 4.3.

4.3.4 $\langle l_{Path} \rangle$ in a SOBP beam

Figure 4.9 (a-b) and (c-d) show the $\langle l_{Path} \rangle$ for primary and secondary ions for the 10 μm and 20 μm SV diameter, respectively, when irradiated with a proton beam producing a clinical SOBP. The $\langle l_{Path} \rangle$ calculated when the microdosimeter is placed in a SOBP

SV Diameter (μm)	Tilt angle	PV_P	PV_S	$PV_{P,S}$	$PV_{t,P}$	$PV_{t,S}$
10	0	$1.06 \pm 3{\times}10^{-3}$	10.65 ± 0.20	16.49 ± 0.20	0 ± 0	0 ± 0
	15	$0.57 \pm 4{\times}10^{-3}$	4.57 ± 0.08	4.18 ± 0.07	21.67 ± 0.13	11.31 ± 0.10
	25	$0.25 \pm 2{\times}10^{-3}$	0.83 ± 0.02	1.30 ± 0.02	29.85 ± 0.18	18.49 ± 0.16
20	0	$0.53 \pm 4{\times}10^{-4}$	0.55 ± 0.01	6.30 ± 0.02	0 ± 0	0 ± 0
	15	$0.24 \pm 1{\times}10^{-3}$	2.09 ± 0.01	0.53 ± 0.00	10.92 ± 0.03	5.33 ± 0.02
	25	$0.20 \pm 8{\times}10^{-4}$	2.11 ± 0.02	1.71 ± 0.02	14.33 ± 0.04	7.74 ± 0.03
30	0	$0.38 \pm 4{\times}10^{-4}$	3.66 ± 0.05	2.30 ± 0.01	0 ± 0	0 ± 0
	15	$0.17 \pm 1{\times}10^{-3}$	7.38 ± 0.12	2.98 ± 0.07	6.70 ± 0.03	2.58 ± 0.02
	25	$0.45 \pm 3{\times}10^{-3}$	7.30 ± 0.07	3.98 ± 0.05	7.56 ± 0.03	2.54 ± 0.02
40	0	$0.26 \pm 2{\times}10^{-4}$	4.77 ± 0.05	1.56 ± 0.02	0 ± 0	0 ± 0
	15	$0.24 \pm 1{\times}10^{-3}$	6.25 ± 0.08	4.21 ± 0.06	4.24 ± 0.01	1.12 ± 0.01
	25	$0.41 \pm 3{\times}10^{-3}$	6.87 ± 0.07	4.44 ± 0.05	3.54 ± 0.01	0.61 ± 0.01
50	0	$0.23 \pm 1{\times}10^{-4}$	6.65 ± 0.07	2.13 ± 0.03	0 ± 0	0 ± 0
	15	$0.14 \pm 4{\times}10^{-4}$	6.42 ± 0.06	4.51 ± 0.06	2.80 ± 0.01	0.67 ± 0.01
	25	$0.16 \pm 8{\times}10^{-4}$	6.89 ± 0.07	5.16 ± 0.05	$1.13 \pm 3{\times}10^{-3}$	1.80 ± 0.01

Table 4.3: Percentage variation of the $\langle l_{Path} \rangle$, calculated for different SV diameters, when irradiated with a 290 MeV/u ^{12}C ion beam. PV_P is calculated along the Bragg curve with respect to the first depth considered in the phantom using equation 4.1, for the incident ^{12}C ion beam, PV_S on the other hand is calculated using only secondary ions. $PV_{P,S}$ is the variance between the primary and secondary ion's $\langle l_{Path} \rangle$, averaged over all depths, calculated using equation 4.2. PV_t is calculated along the Bragg curve, for different tilt angles with respect to 0°, for both primary ($PV_{t,P}$) and secondary ($PV_{t,S}$) ions, by means of equation 4.3.

produced by a clinical ^{12}C ion beam is shown in figure 4.10 (a-b) and (c-d), for 10 and 20 μm SV diameters, respectively.

For both the proton and ^{12}C ion beams, the results are similar to the mono-energetic cases (see figures 4.7 and 4.8). The 20 μm diameter is again preferable because the $\langle l_{Path} \rangle$ varies less along the Bragg curve and the variance between the primary and secondary $\langle l_{Path} \rangle$ is greatly reduced.

Estimating the $\langle l_{Path} \rangle$ using the deposited energy

Figure 4.11 shows the $\langle l_{Path} \rangle$ with respect to the energy deposited in the 10 μm diameter silicon SV and converted to be representative of muscle. The 10 μm design was used to represent an extreme case of variation between the $\langle l_{Path} \rangle$ of primary and secondary particles as well as along the depth of the Bragg curve, where using the thickness of the SV as an approximation is not appropriate, namely for proton fields. The $\langle l_{Path} \rangle$ is calculated for the primary and secondary ions, separately, with the primary ions being depicted with solid markers and secondary ions with open markers. The left plot shows the $\langle l_{Path} \rangle$ for both a mono-energetic and a SOBP proton beam and the right plot shows the same quantities for ^{12}C ion beams. For both proton and ^{12}C ion beams, it can be seen that the relationship of the $\langle l_{Path} \rangle$ with the mean peak energy deposition is valid for both a pristine beam and a SOBP which is comprised of a large range of different energy particles. This method, which allows for a quick experimental estimation of the $\langle l_{Path} \rangle$ using just the energy deposition spectra is valid not only for mono-energetic ^{12}C

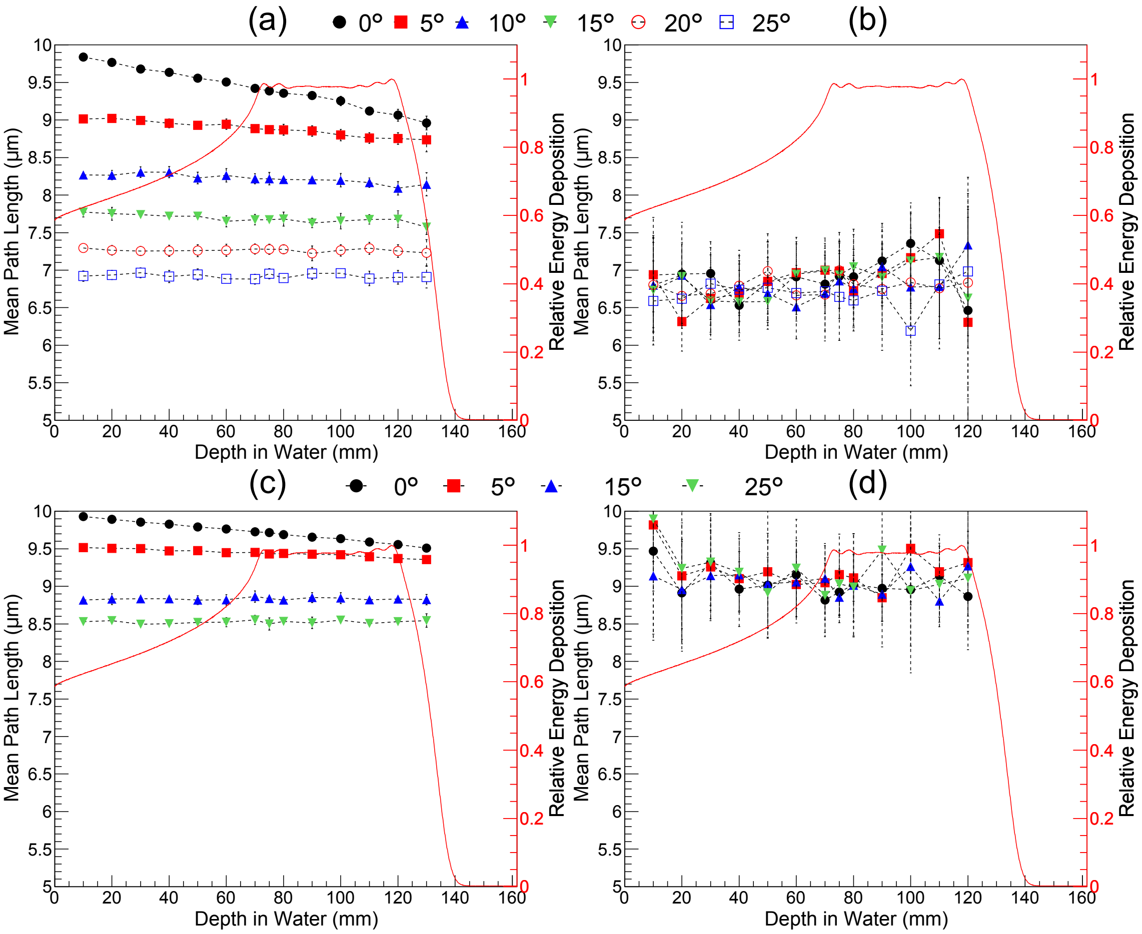

Figure 4.9: The $\langle l_{Path} \rangle$ when irradiated by a SOBP proton beam. (a) and (b) are calculated using 10 μm diameter SV design for primary (a) and secondary ions (b), respectively. (c) and (d) also show the $\langle l_{Path} \rangle$ for primary and secondary ions, respectively, using a 20 μm diameter SV instead. The microdosimeter is placed at various tilt angles with respect to the direction of the beam (reported in the legends).

ion beams, but also for mono-energetic proton and SOBP proton and ^{12}C ion beams.

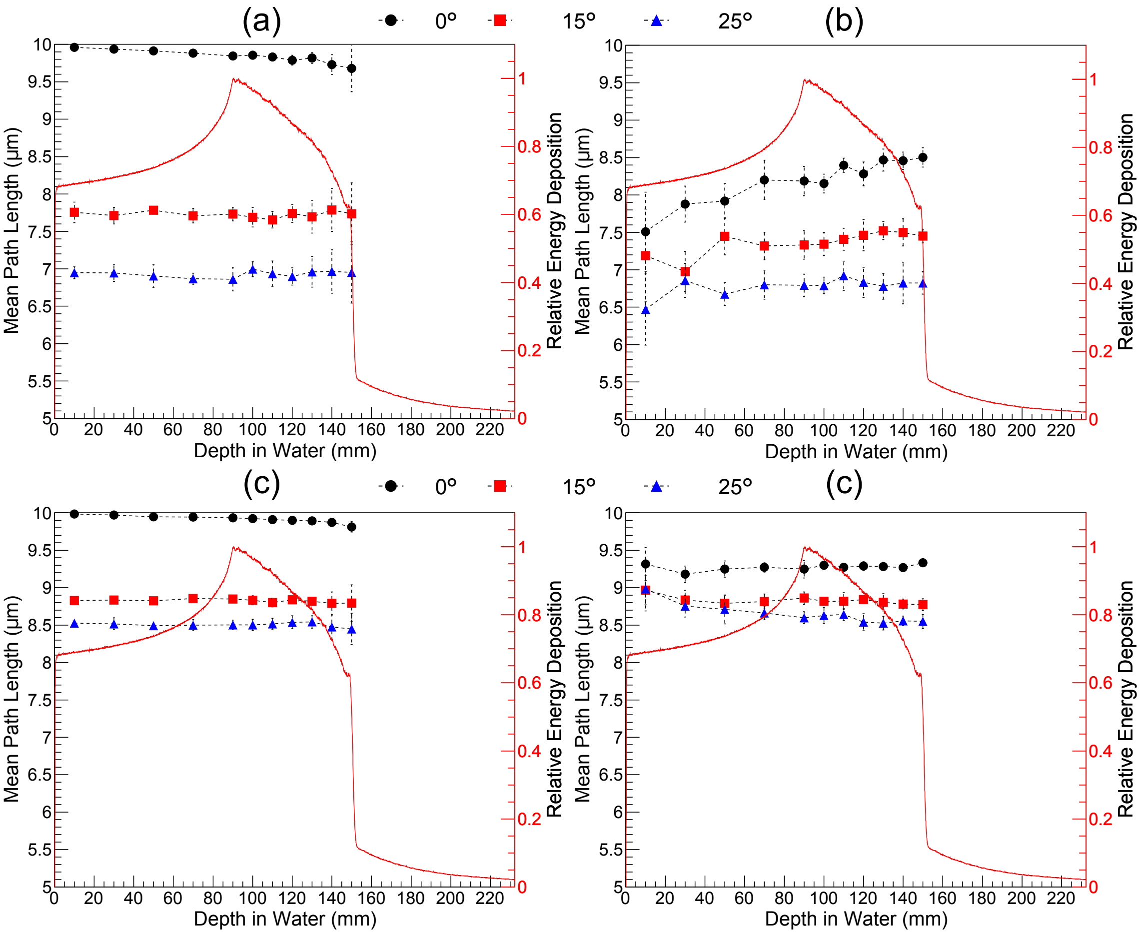

Figure 4.10: The $\langle l_{Path} \rangle$ when irradiated by a SOBP ^{12}C ion beam. (a) and (b) are calculated using 10 μm diameter SV design for primary (a) and secondary ions (b), respectively. (c) and (d) also show the $\langle l_{Path} \rangle$ for primary and secondary ions, respectively, using a 20 μm diameter SV instead. The microdosimeter is placed at various tilt angles with respect to the direction of the beam (reported in the legends).

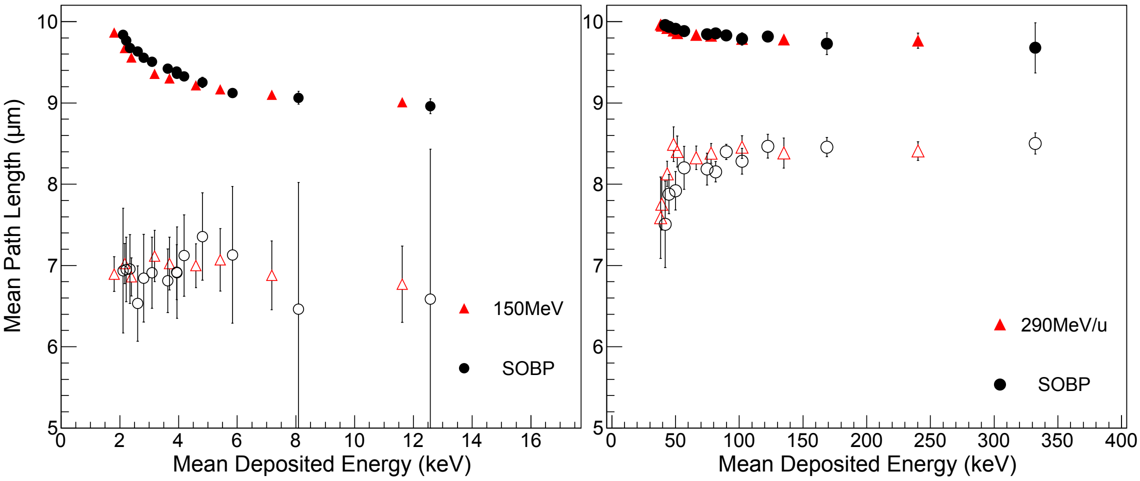

Figure 4.11: $\langle l_{Path} \rangle$ plotted against the mean energy deposition. Left depicts the $\langle l_{Path} \rangle$ for a 150MeV proton beam against a SOBP. Right depicts the $\langle l_{Path} \rangle$ for a 290 MeV/u ^{12}C ion beam against a SOBP. The filled markers represent the primary beam while the open markers represent the secondary ions. Note that the energy deposited has been converted from silicon to muscle.

4.4 Discussion

The study of the $\langle l_{Geo} \rangle$ characterised the response of the different SVs of a range of different alignments with the beam and different beam divergences. The larger diameter SVs were found to show less sensitivity to alignment than smaller diameters, while the smaller diameters saw less variation in the $\langle l_{Path} \rangle$ over the complete range of cone angles (0-90°) than the larger diameters. As can been seen in [98], which measured the angular spread of the primary and secondary ions for a ^{12}C ion beam in a water phantom, the smaller θ angles mainly correspond to the incident primary beam while fragments relate to moderate sized angles. The larger θ angles are more representative of electrons and recoiled nuclei from neutrons. The larger diameters showed smaller variation for smaller cone angles of $\sim$20° and less. For larger cone angles the $\langle l_{Geo} \rangle$ varied more for larger diameters with its value increasing with larger cone angles. This means that for primary beams with their smaller divergence the $\langle l_{Path} \rangle$ will vary less for larger diameters, however the $\langle l_{Path} \rangle$ of secondary particles will differ increasingly more compared to the $\langle l_{Path} \rangle$ of the primary beam as the divergence increases.

When considering the incident proton beam, the largest percentage variation observed in table 4.2 is with the 10 μm diameter (elongation = 1). This SV geometry corresponds to the least variation of the $\langle l \rangle$ when calculated by means of the Cauchy formula. The percentage variation of the primary beam, PV_P, along the depth of the Bragg curve decreases with increasing diameters for a tilt angle of 0° from 4.7% to 0.6%. However, as the tilt angle is increased the PV_P is reduced for all diameters and the 20 μm size has the least variance.

For secondary ions the percentage variation, PV_S, at a 0° tilt angle showed the 10 μm diameter to be the smallest with 2% and increases for larger diameter SVs. The reason for this can be seen in figure 4.4 which showed that the $\langle l_{Path} \rangle$ varied more for larger diameters when the divergences was more than $\sim$40° to 90°, which is representative of the secondary radiation field for proton beams.

The 20 μm design has the least variance between primary and secondary ions, ($PV_{P,S}$), with the exception of extreme angles where the 10 μm design varies the least, with larger diameter designs having increasingly more variance between primary and secondary ions

.

When comparing the sensitivity of alignment with the PV_t values in the last two columns it can be seen that the 10 μm design is the most sensitive to alignment, particularly for the primary beam which is the most important aspect for reducing the variation. It can be seen that as the diameter of the SV increases the PV_t for primary protons decreases slightly while for secondary ions the PV_t is similar, but as the tilt angle increases the PV_t becomes larger for larger diameters.

As discussed earlier, the primary proton beam and the secondary ions have similar lineal energies, with the consequence that different $\langle l_{Path} \rangle$ values cannot be applied to separate components of the microdosimetric spectrum. Thus the $\langle l_{Path} \rangle$ of primary and secondary ions should be similar to one another. Taking this factor into account the 20 μm diameter SV, with the $\left\langle l_{Cauchy} \right\rangle$ being equal to the SV thickness, is the most appropriate design for proton therapy microdosimetric measurements. Furthermore, with the exception of downstream BP proton measurements where the $\langle l_{Path} \rangle$ does not vary, SV designs with the $\left\langle l_{Cauchy} \right\rangle$ being less than the thickness of the detector should be avoided in proton therapy due to their large differences between their $\langle l_{Path} \rangle$ values for primary and secondary ions and larger variances with angular misalignment.

The superiority of the 20 μm design with its reduced variance of the $\langle l_{Path} \rangle$ between the primary and secondary ions can be matched by the 10 μm diameter design. Since the variance of the $\langle l_{Path} \rangle$ ($PV_{P,S}$) reduces with increasing tilt angle compared to larger designs which have increasing variance with diameter. So if the 10 μm design was intentionally placed at a tilt angle of 30° the variation would be insignificant, however this approach is not ideal since it diminishes the spatial resolution.

The summary of the variation in the $\langle l_{Path} \rangle$ for the ^{12}C ion beam shown in table 4.3 showed an increase in sensitivity to alignment by ∼2% compared to the proton beam for both the primary and secondary ions. This increase variation is due to the decreased angular divergence of both primary and secondary ions in ^{12}C ion beams.

When considering the incident ^{12}C ion beam only, the PV_P is less than 1.1% for all diameter sizes because of the small divergence of the ^{12}C ions, with PV_P decreasing slightly with increasing diameters. The PV_S for secondary ions has similar values as proton beams, a noticeable exception is for 10 μm which has a value of ∼11% compared to ∼2%, this is due to the complex radiation field in ^{12}C ion beams as the angular distribution and dominance of particles changes with depth.

When considering the variation between the primary and secondary ion's $\langle l_{Path} \rangle$ ($PV_{P,S}$), a SV diameter of 20-30 μm has the smallest variance of $\langle l_{Path} \rangle$ and in general the $PV_{P,S}$ is smaller in ^{12}C due to the dominance of forward directed fragments which have angular distributions much closer to the primary beam compared to neutron events. The diameter sizes of 20-30 μm correspond closely to the real world Mushroom and Bridge devices (another CMRP SOI microdosimeter design which is studied in chapter 7).

The sensitivity of the $\langle l_{Path} \rangle$ on the detector alignment showed that the values of $PV_{t,P}$ are similar to what was seen for the proton beam, with larger diameters having a decreased variation. The values of $PV_{t,P}$ for ^{12}C ions is slightly higher than for proton, the reason for this can be seen in figure 4.4 which showed that the largest variation in the $\langle l_{Path} \rangle$ (or $\langle l_{Geo} \rangle$, as in the figure) for smaller beam divergence. For $PV_{t,S}$ it can be seen that the variation is again similar to what was seen with proton except that for smaller diameters the $PV_{t,S}$ is greater while for larger diameters the $PV_{t,S}$ is smaller.

Thanks to the ability to distinguish between the primary and secondary ions in ^{12}C ion therapy, the choice of SV diameter is less important compared with proton beams and allows for a greater flexibility in the microdosimeter design. For instance, if the alignment of the detector with the incident beam is difficult, then a SV design with a larger diameter will offer an advantage due to the decreased variation in the $\langle l_{Path} \rangle$. Instead, for proton beams, the 20 μm diameter SV is preferable as both primary and secondary particles have closer mean path lengths.

For SOBP radiation fields the results did not differ significantly from mono-energetic beams. The $\langle l_{Path} \rangle$ has a more consistent value with a 20 μm SV diameter compared to the 10 μm SV. However, as mentioned before, the choice of diameter is not as crucial in this case due to the contribution to the microdosimetric spectra being able to be distinguished, as shown in figure 4.6. This allows different regions of the spectra to have separate $\langle l_{Path} \rangle$ values used, however for ease and simplicity this approach is not preferable.

4.5 Conclusions

This chapter studied the best diameter for a 10 μm thick silicon microdosimeter SV to reduce the variation of the $\langle l_{Path} \rangle$, when considering different positions along the Bragg curve, alignments with the direction of the incident beam and different particles of the radiation field produced by clinical proton and ^{12}C ion beams. By reducing the variation in the $\langle l_{Path} \rangle$ allows for the energy deposition to be converted to lineal energy more accurately and easily. This is important to accurately determine the microdosimetric spectra and to estimate the RBE.

It was found that for proton beams that the most appropriate microdosimeter design has SVs with 20 μm diameter. The thickness of the SV, which is 10 μm, is equal to the $\langle l_{Cauchy} \rangle$ of the SV calculated by means of the Cauchy formula. For ^{12}C ion beams the design of the SV was found to be less important than for protons. This is because the fragments produced have angular distributions closer to the primary beam than neutron events and if necessary the components of the microdosimetric spectra deriving from the incident beam and the secondary radiation field can be easily distinguished and use separate $\langle l_{Path} \rangle$ values. The 20 μm diameter is appropriate for both pristine and SOBP proton and carbon ions.

This study shows that intentionally introducing a small misalignment may reduce the variation of the $\langle l_{Path} \rangle$, the angle required being reduced with larger diameter SV designs, with an angle of $\sim 10^\circ$ required for the 20 μm design in a proton beam. This method has the largest applicability for proton beams where the lineal energies of the primary and secondary ions have similar lineal energies. Nevertheless the feasibility of this method has to be evaluated experimentally.

Proton beams were characterised with lower values of $\langle l_{Path} \rangle$ for both primary and secondary ions due to the larger associated scatter of the primary beam and dominance of neutrons in the generation of secondary ions. When placed in a mono-energetic proton beam the 20 μm diameter design, with a $\langle l_{Cauchy} \rangle$ of 10 μm the $\langle l_{Path} \rangle$ varied from 9.9 μm at the entrance of the phantom to 9.5 μm at the BP and for the ^{12}C ion beam with a change from 10 μm to 9.8 μm. While for the 10 μm diameter design with a $\langle l_{Cauchy} \rangle$ of 6.67 μm finished with $\langle l_{Path} \rangle$ values of 9.0 μm and 9.8 μm at the BP for the proton and ^{12}C ion beams, respectively.

This work demonstrated that there is a unique relationship between the $\langle l_{Path} \rangle$ in the SV and the mean energy deposited, not only for pristine proton and ^{12}C ion beams but also for clinical SOBPs. This is particularly convenient for experimental use of the microdosimeters and allows for quick and accurate determination of the $\langle l_{Path} \rangle$ using the spectra of the deposited energies.

Chapter 5

Impact of sensitive volume thickness on microdosimetric measurements in hadron therapy

Over the last two chapters the concept of the mean path length has been studied for silicon microdosimeters in hadron therapy and the design has been optimised based on the reducing the variation of the mean path length. Due to the small size of SOI's sensitive volumes (SVs), which are usually $\sim$10 μm thick, means that the fabrication of these devices can present challenges which are not as common for more conventional thickness silicon devices such as silicon spectroscopy detectors. If SOI microdosimeters could be produced with a thicker sensitive volume at a decreased price and have a minimal impact on the microdosimetric quantities, this would be advantageous for fabrication. Using the optimised design of a cylinder with a thickness equal to the mean path length the impact of the thickness on microdosimetric measurements is studied.

5.1 Introduction

Conceptually, microdosimeters are used to represent the dimensions of biological cells and estimate the biological response from radiation. Regardless of whether a cell is represented by a TEPC or a silicon SV, the choice of what size cell is the "best" to be represented is not a clear choice. Commonly, when commercial TEPCs are used for microdosimetric measurements, a simulated tissue equivalent diameter between $\sim$0.5 and 10 μm is used, while the thickness of the SVs in SOI devices are often $\sim$10 μm. However, there are over 200 different cell types in the human body which range from an average volume of $\sim$3 $\times 10^1 \mu$m^3 for a sperm cell to an average size of 4×10^6 μm^3 for oocytes [99]. The HeLa cell is commonly used in cancer research [100] and its volume ranges from $\sim$500-4000 μm^3, with an average of 3×10^3 μm^3 [101]. The shape of cells vary from type to type, with oocytes being spherical with a diameter of ~120 μm while sperm cells are more irregular with a flat disc head ~5 μm wide and ~3 μm thick and a 50 μm long tail [102]. The cell nucleus is of major importance when considering radiation damage since it contains the cell's DNA, which with sufficient damage to the DNA will cause the cell to die [103]. Due to the importance of the nucleus for cell survival and replication, the energy deposition in a cell nucleus sized volume is more relevant than a whole cell when studying the radiation damage to a cell, which is largely the assumption made when using microdosimeters. The importance of the cell nucleus for cell death is reflected in various biological model including the MKM (see section 1.6.3). In particular, for the MKM the domain size for a HSG cell, as discussed in section 1.6.3, has a radius of 0.42 μm. The domain effectively represents the SV so it is important to know how using a SV with a different size will impact the calculated properties when using the MKM. Compared to cells, the range of nuclei sizes varies considerably less, with most nuclei diameters ranging from 2 to 10 μm. With HeLa cell nuclei having volumes of ~690 μm^3 [104] [101], which if contained as a perfect sphere corresponds to a diameter of ~11 μm.

Because of the range of cell sizes and their nuclei, it is valuable to know how a microdosimetric measurement will be affected based upon the simulated size of the SV. Appendix F of the ICRU 36 report [57] compiles many studies which have investigated the effect of varying the simulated size of a SV in a TEPC on microdosimetric measurements. Such studies have mainly used the radiation field of photon and electron sources, with fewer focused on neutrons and low energy protons and α particles. Very few investigations have reported the impact of microdosimetric measurements in therapeutic hadron beams using TEPCs. There have been no extensive studies performed using silicon microdosimeters for any radiation field due to the logistics of creating a large collection of detector designs.

In addition to the consideration of cell size, the manufacturing of solid state devices with micron sized SVs, such as SOI microdosimeters, require sophisticated 3D detector technology. If thicker, off-the-shelf solutions, such as silicon diodes with a thickness of the order of 100 μm could be used as a cheaper alternative with minimal impact to microdosimetric measurements, this would be beneficial. However, the dose rates of beams which larger single SV detectors can operate in are much smaller than dedicated microdosimeter designs, which are capable of operating in therapeutic dose rates. Additionally, a single large SV, in proton therapy especially, causes a large variation in the path length of charged particles in the SV along the Bragg curve (as seen in the previous chapter). These factors would restrict the possible use of off-the-shelf solutions to low dose rate beams of heavy ions.

This chapter examines the impact on microdosimetric quantities as well as the RBE, estimated using the modified microdosimetric kinetic model (MKM) [67], for SOI designs with silicon thicknesses from 1 to 100 μm when placed in proton, ^{4}He and ^{12}C beams of therapeutic energies.

5.2 Materials and Methods

5.2.1 Simulation Setup

Geant4 (version 10.2p3) was adopted to study the impact of varying the SV size of SOI microdosimeters on microdosimetric quantities. The SV thicknesses investigated were: 1, 2.5, 5, 10, 25, 50 and 100 μm. The different microdosimeters were placed in a $30 \times 30 \times 30$ cm^3 water phantom which was irradiated in mono-energetic proton, ^{4}He and ^{12}C ion beams with initial energies of 150, 150 and 290 MeV/u, respectively. Each beam was generated with 40 cm of air between their starting position and the water phantom, as shown in figure 5.1 (a). Each beam was generated with a Gaussian distribution of 11 mm σ and an energy σ of 1, 0.35 and 0.2 % for the proton, ^{4}He and ^{12}C beams, respectively. The response of the microdosimeter was investigated along the central axis of the different beams (in-field configuration).

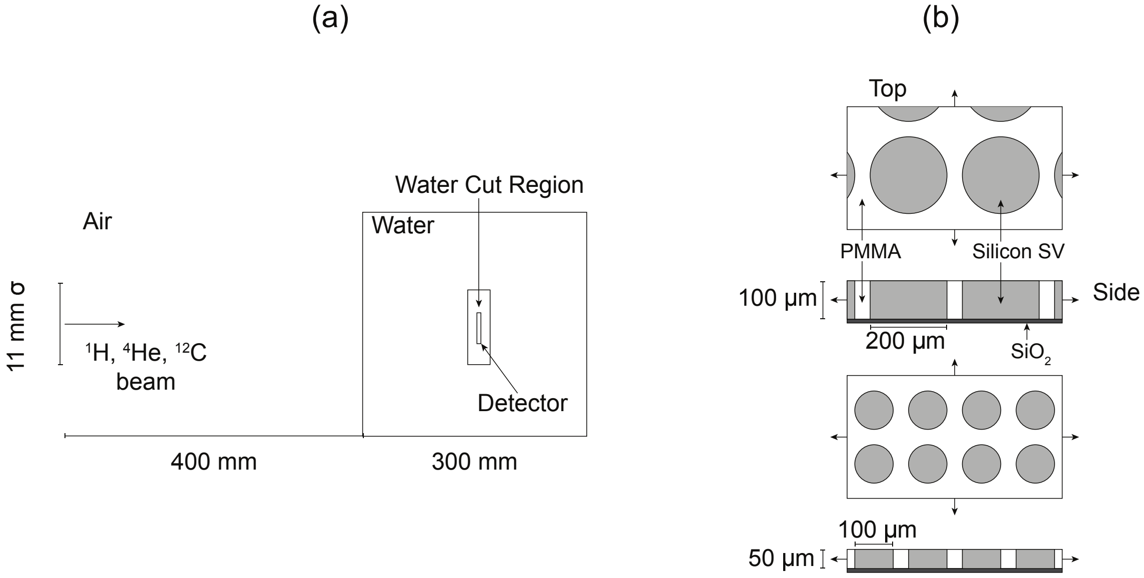

Figure 5.1: (a) Simulation setup used in this study. View of the generation of the beam incident upon the microdosimeter detector in the water phantom. (b) Shows a zoomed in region of two different sized microdosimeters with the 100 μm design on the top and a 50 μm design on the bottom, respectively. The top view of the detector is orientated as a beam's eye view, while the side view would have the beam directed downwards.

This study uses the optimised Mushroom design, investigated in the previous chapter, with the diameter of the cylinder set to be twice its height, two example thicknesses of the microdosimeter are shown in figure 5.1 (b) which shows a top and side view of the microdosimeter. The SVs cover an area of 5×5 mm^2 with a distance of 40 μm between the edges of the SVs.

The same physics used in the previous two chapters were used in this study, with the exception of electromagnetic interactions. Since the energy deposition in SVs as thin as 1 μm are studied in this chapter the low energy Livermore physics list was adopted with a production threshold of electrons, photons and positrons set to 250 eV. A secondary cut region was again adopted but the electron cut was set to 0.1 μm instead of 1 μm used in the previous studies. The cut outside of the region was set to 1 mm for both proton and ^{4}He ion beams and 2.8 mm for ^{12}C ion beams.

5.2.2 Microdosimetric quantities under investigation

In order to study the impact of the thickness of the microdosimeter, the lineal energy spectrum and the microdosimetric quantities of frequency mean lineal energy, y_F, and the dose mean lineal energy, y_D, were compared for the different thicknesses. In addition to y_F and y_D, the relative biological effectiveness at 10% cell survival, RBE$_{10}$, estimated using the modified microdosimetric kinetic model (MKM) was also used as a means of comparison.

Due to the thicker SVs investigated in this chapter compared to previous chapters, the $\langle l_{Path} \rangle$ is calculated slightly differently. Instead of replacing the silicon SV with a vacuum, the path length is calculated in the silicon volume itself, this is done since the discrepancy between these two quantities may significantly increase towards the end of the beam's range. Due to the dominance of the primary beam, the $\langle l_{Path} \rangle$ of the primary beam is used to calculate the lineal energy for a particular depth. However, if the proportion of primary ions compared to secondary ions falls below 5% then the $\langle l_{Path} \rangle$ of the secondary ions is used to calculate the lineal energy.

To compare the lineal energy distributions produced by different sized SVs the data points were fitted to a three term Gaussian distribution and the peak position and the full width at half maximum (FWHM) were compared. As with the previous chapters the energy deposition in silicon is converted to striated muscle using the conversion factors found in chapter 3. The curve fitting of the lineal energy distribution was done using the Curve Fitting tool in Matlab 2015A [105]. Various different fitting distributions were trialled and a three term Gaussian method was chosen based on its R^2 values and stability when fitting the various lineal energy distributions at different depths, beams and SV size. The fitting of the lineal energy distributions were also trialled with a Landau function by manually implementing the fitting, however this proved to be more sensitive compared to a three term Gaussian fit and having higher R^2 values. The input simulation data for the curve fits used various different binning of the lineal energy spectra. Proton data had a maximum lineal energy of 500 keV/μm and 8192 bins. ^{4}He also had a maximum of 500 keV/μm and the number of bins varied based on the depth, for depths less than 140 mm and greater than 155 mm the number of bins was 500 while for all other depths the number of bins was 2048. ^{12}C data was binned into 2048 bins with a maximum lineal energy of 1200 keV/μm. Once the fitted function was generated, the fit was evaluated for 10000 equally spaced bins which were generated with maximum energies of ~20, 200 and 200 for proton, ^{4}He and ^{12}C ions, respectively. The FWHM of the fit was then calculated "'manually"' by retrieving the energy of the peak and taking the two bins either side of the peak which corresponded to values of half the maximum of the peak.

In addition to the above quantities, the effect of the thickness on the proportion of stopper is also investigated. Here a stopper is defined as a particle which enters the SV and stops inside the SV. The proportional of particles which are stoppers are taken as the particles which stop in the SV versus the number of particles which enter the SV and exit the SV, with particles created in the SV not considered. Similarly, it is investigated whether the thickness of the SV has an impact on the approximation of the thickness of the SV used instead of the $\langle l_{Path} \rangle$.

When comparing the different above quantities between one another for the different thicknesses of the SV the percentage difference, *PD*, is used as defined in equation 5.1. SV_t is the quantity calculated for a sensitive volume with a thickness t and SV_{10} is the quantity for a SV with a thickness of 10 μm.

$$PD = \frac{SV_t - SV_{10}}{SV_{10}} 100\% \tag{5.1}$$

5.3 Results

5.3.1 Impact of SV thickness on the microdosimetric spectra

The lineal energy spectra (y) for the three different beams are shown in figure 5.2 at a depth of 10 mm (surface of the phantom) and 140 mm (~20 mm before pinnacle of BP). The plots are normalised to one for the maximum value in the distribution. An important feature is that the spectra are plotted on a linear scale instead of the more traditional semi-log scale. This is done to preserve the detail of the curves which may be diminished after rebining.

The peak position of the distributions are seen to shift to higher lineal energies when the SV size increases with the peak of the distribution becoming sharper for larger SVs. Figure 5.3 plots the peak position and the FWHM of the peak of the lineal energy spectra shown in 5.2 as well as other depths up to 160 mm. In the case of the ^{4}He and ^{12}C beams, the peak refers to the right peak in the spectra due to the primary ion beam. The peak positions and widths are the values from fitting the a three term Gaussian distribution function.

The proportion which the width of the proton peak decreases with thicker SVs does not vary significantly at different depths, with the width from a 1 μm thick SV decreasing by

∼15% when increasing the thickness to 10 μm and decreasing by ∼55% when increasing to 100 μm thick (with respect to the 1 μm thick SV).

For ^{4}He beams the width of the peak is more sensitive to SV thickness, with the peak decreasing by ∼40% when increasing the thickness to 10 μm. When the thickness of the SV increases to 100 μm from 1 μm the peak width decreases by ∼60%, which is more similar to what was seen for the proton beam. For ^{12}C the peak width decreases slightly less than the ^{4}He beam with a reduction of ∼30% and ∼40% when comparing the 1 μm thick SV to the 10 and 100 μm thick SVs, respectively.

The more traditional representation of the microdosimetric spectra, using the dose weighted distribution $d(y) = yf(y)/y_F$, is shown in figure 5.4 at a depth of 10 mm, the scale of the y-axis is in $yd(y)$ due to the linear spaced bins being re-binned into log bins [57] [106]. Instead of representing just the distribution of lineal energy events in the SV, $d(y) = (yf(y)/y_F)$ weights the distribution to higher lineal energies to represent their contribution to the dose. Once the distribution is weighted the impact of straggling is more easily seen, with the smaller SVs extending to much higher values. For the proton beam the 1 μm thick SV is seen to have a tail which extends to ∼100 keV/μm while the 10 and 100 μm thick SVs fall sharply at ∼10 and ∼1 keV/μm, respectively.

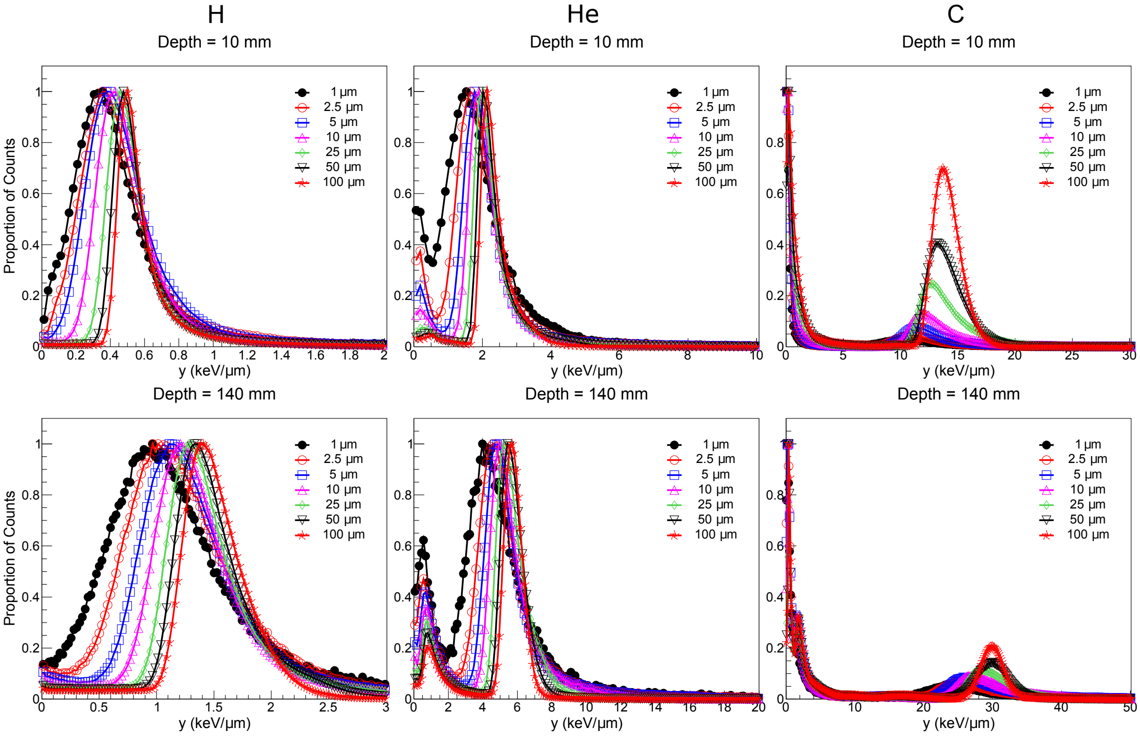

Figure 5.2: Comparison of the lineal energy spectra of different sized SVs in the different mono-energetic beams at a depth of 10 mm (top plots) and at 140 mm (bottom plots).

Table 5.1 summarises the R^2 values of the lineal energy distributions for each beam and SV size for various depths. In addition to table 5.1, figure 5.5 shows example comparisons between the lineal distributions calculated from the simulation and the three term

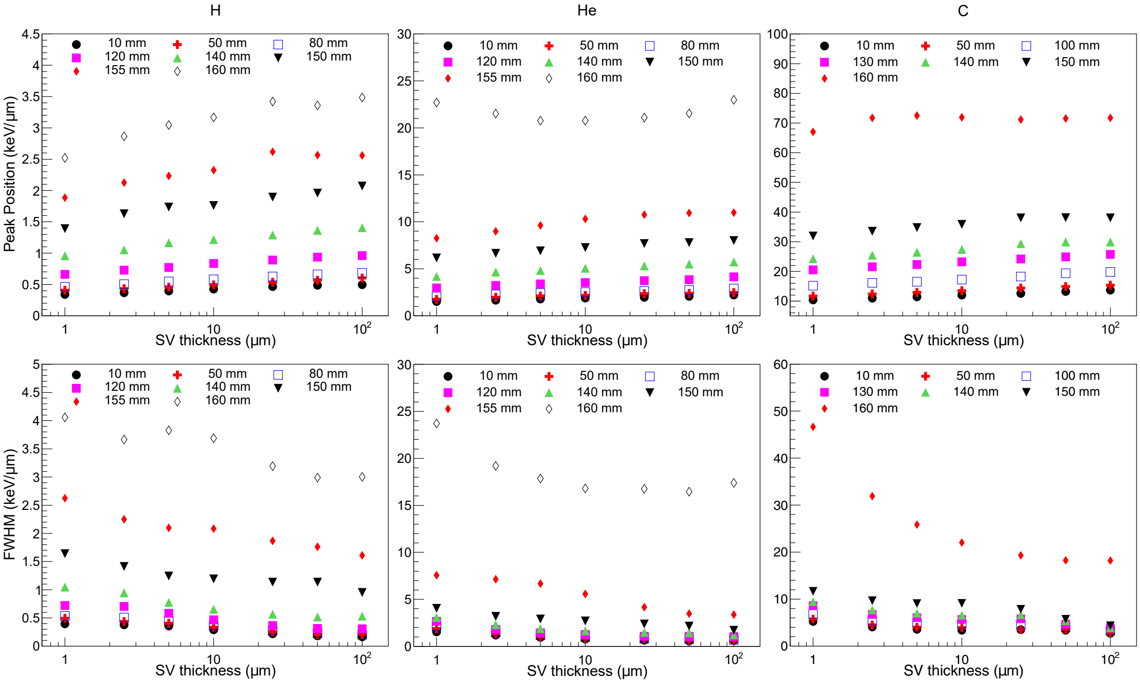

Figure 5.3: Comparison of the peak position (top) and the FWHM (bottom) of the lineal energy spectra which was fitted using a three term Gaussian function.

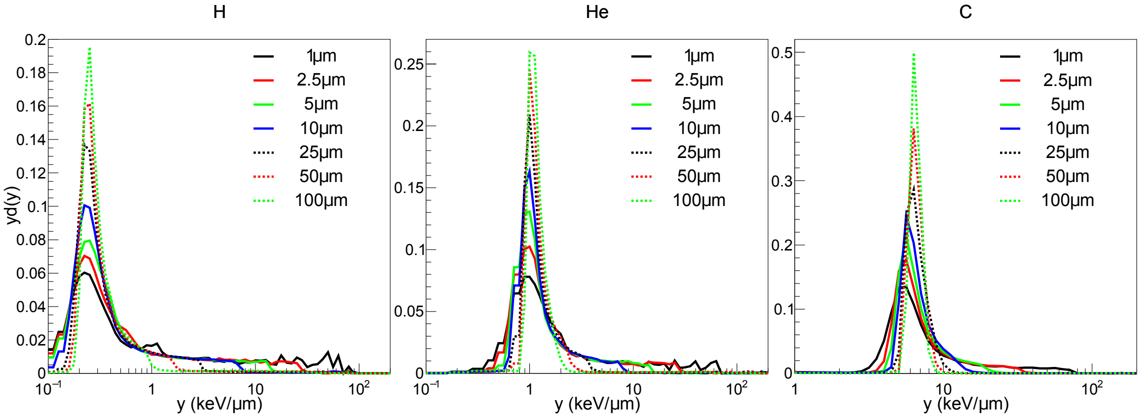

Figure 5.4: Comparison of the $yd(y)$ spectra ($d(y)$ when plotted on binned linearly) for the different sized SVs when irradiated in the three mono-energetic beams at a depth of 10 mm.

Gaussian fits for a selection of depths and SV sizes for each of the beams. In figure 5.5 the red markers are the simulation points and the black lines are the fitted functions. The peaks to the left of the main peak, which can be seen prominently on the ^{4}He and ^{12}C spectra, are due to fragments and electrons with lower LET than the primary beam. These lower lineal energy peaks are not of interest for the fitted function since only properties of the primary beam are of interest.

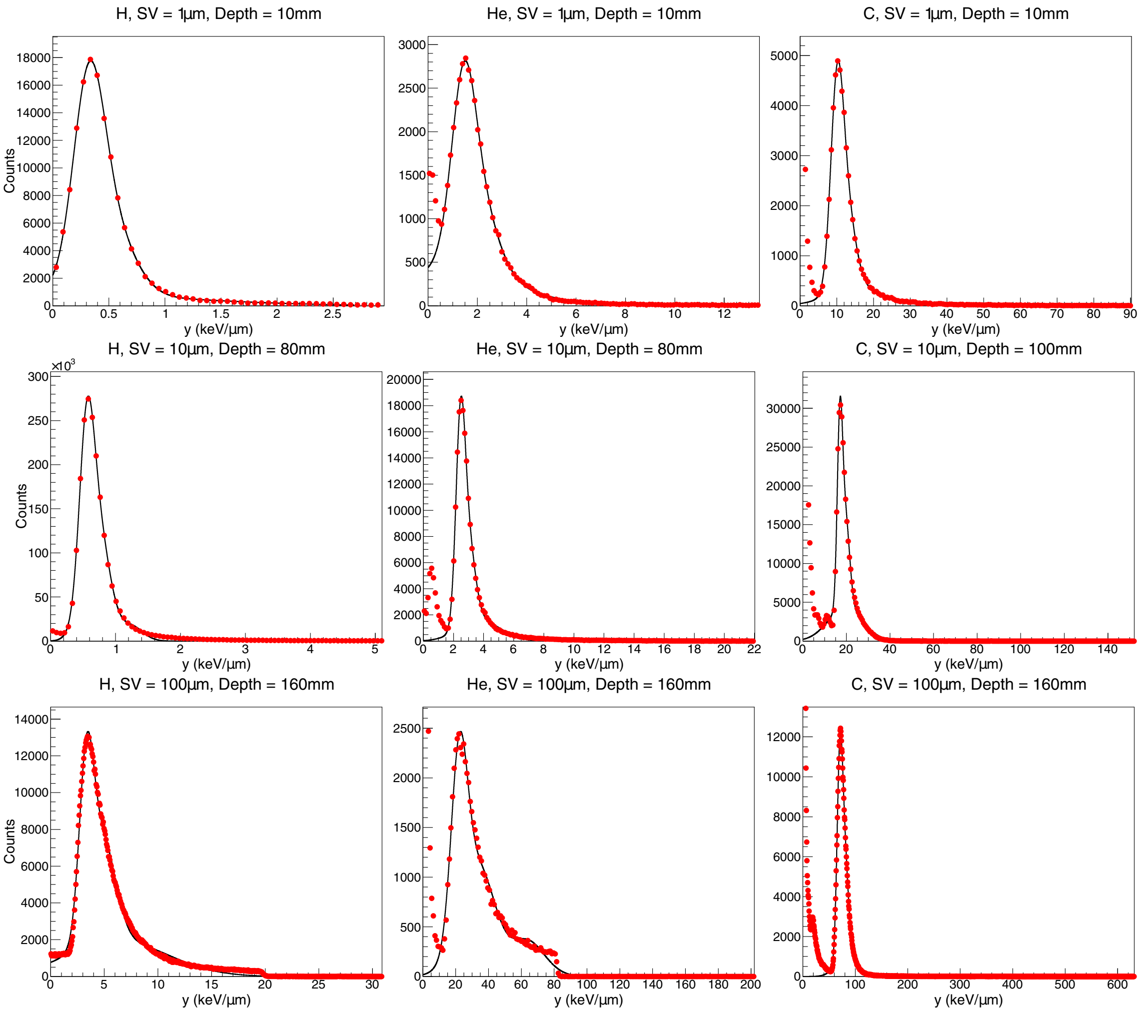

Figure 5.5: Examples of the lineal energy spectra generated by the simulation (red markers) and the three term Gaussian fit (black line).

5.3.2 Impact on y_F

The y_F depth distributions for the three mono-energetic beams are shown in figure 5.6. The percentage difference, PD, is plotted on the bottom of the curves with respect to the 10 μm thick SV. For the proton and ^{4}He beams there is very little difference between the different SVs, while the ^{12}C beam shows a considerable difference. For all beams the larger SVs are seen to have the largest y_F. The proton beams have a maximum difference of $\sim$2% at the entrance of the phantom, which gradually decreases with increasing depth.

Depth	SV thickness (μm)	Proton R^2	^{4}He R^2	^{12}C R^2
10	1	0.999752	0.9996	0.999457
	2.5	0.999708	0.998976	0.999019
	5	0.997936	0.999027	0.998615
	10	0.997015	0.998517	0.998481
	25	0.996654	0.997739	0.999298
	50	0.995613	0.99181	0.999028
	100	0.998835	0.945303	0.999489
50	1	0.997098	0.998867	0.999221
	2.5	0.999604	0.997457	0.999112
	5	0.99952	0.996759	0.998483
	10	0.999275	0.995762	0.998278
	25	0.999121	0.980097	0.997144
	50	0.995169	0.990563	0.996265
	100	0.963193	0.988699	0.997268
140	1	0.999656	0.997785	0.994625
	2.5	0.999197	0.996596	0.991232
	5	0.997171	0.998234	0.989719
	10	0.998883	0.99396	0.993035
	25	0.998383	0.996413	0.977399
	50	0.996675	0.998364	0.998807
	100	0.998888	0.993213	0.99839
150	1	0.998718	0.999191	0.991061
	2.5	0.995755	0.999272	0.990422
	5	0.995114	0.998786	0.993481
	10	0.998146	0.998139	0.996247
	25	0.997114	0.997756	0.99803
	50	0.997951	0.999678	0.998892
	100	0.997466	0.999271	0.998873
160	1	0.989475	0.996807	0.994863
	2.5	0.995733	0.998716	0.998944
	5	0.995228	0.99626	0.999598
	10	0.995611	0.997326	0.999227
	25	0.995267	0.995698	0.999367
	50	0.996231	0.996465	0.999199
	100	0.994948	0.994482	0.999134

Table 5.1: Summary of the R^2 values of the three term Gaussian fits applied to the lineal energy distributions for each of the three beams at selected depths.

The ^{12}C beam has a difference of ~40% between the case of 10 μm and the 100 μm thick SV, with the 1 μm having a value ~40% lower at the surface of the phantom and decreasing to ~±10% at 130 mm.

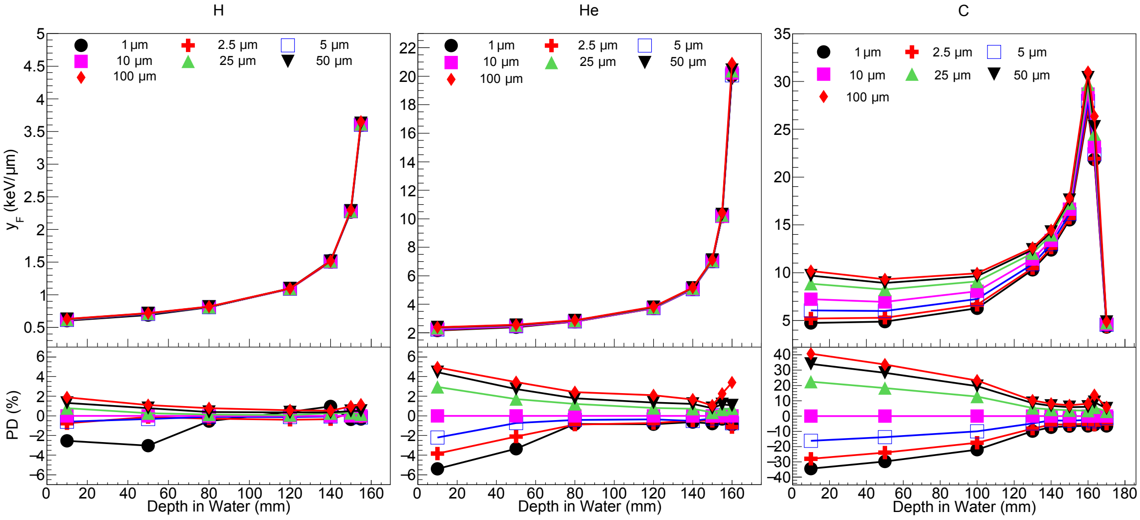

Figure 5.6: Comparison of the mean lineal energy, y_F, for a mono-energetic 150 MeV proton beam (left), a 150 MeV/u ^{4}He ion beam (middle) and a 290 MeV/u ^{12}C ion beam (right).

5.3.3 Impact on y_D

The y_D distributions along the Bragg curves of the mono-energetic beams are shown in figure 5.7 for the different thicknesses of SVs. The results differ quite drastically from the y_F distributions, with the proton beams having the largest variation while the ^{12}C beam shows the least impact from SV size. In the case of the proton beam the 1 μm thick SV has a value ~200% higher than the 10 μm thick SV with the difference decreasing after 120 mm in water. The difference of y_D quickly drops as the SV size increases. When comparing the ^{12}C beam the 1 μm thick SV has the largest difference with a value of ~30% while all other SVs have differences within ~10%.

5.3.4 Impact on RBE

The percentage difference in the RBE$_{10}$, as estimated using the MKM, along the depth of the different mono-energetic beams are shown in figure 5.8. The obtained profiles follow a similar trend as y_D, with the proton beam again having the largest impact from SV size, with the smaller sizes having larger values of RBE. For proton beams, the difference between the largest and smallest SV is ~30% while for ^{4}He and ^{12}C have a similar value of ~10%. The impact of the SV size on the RBE$_{10}$ estimation, despite following the same trend, is reduced compared to y_D. The RBE$_{10}$ is less sensitive due to the $y*$ quantity which is similar to $d(y)$ but reduces the dominance of higher y events. Additionally, RBE

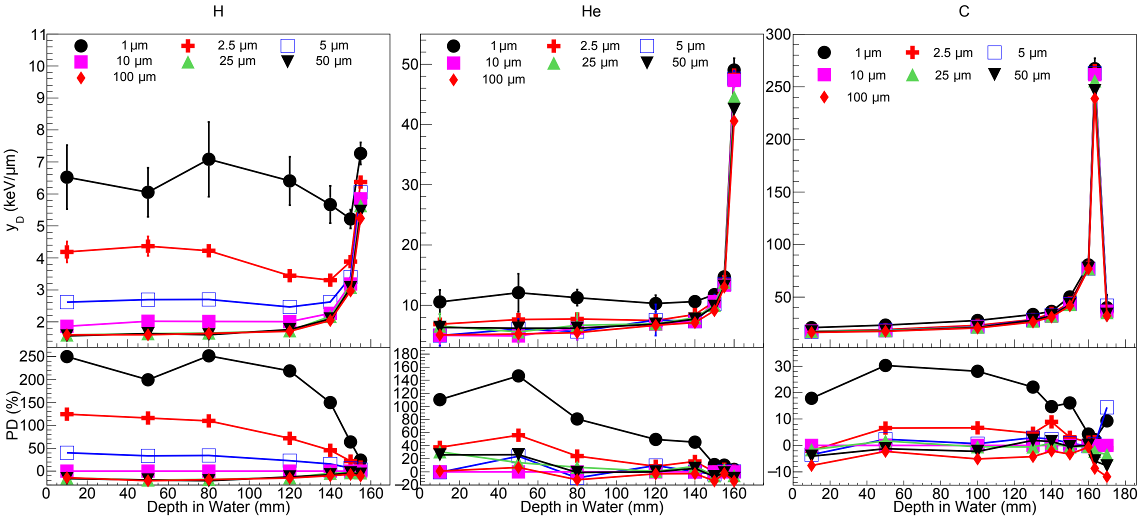

Figure 5.7: Comparison of the dose mean lineal energy, y_D, for a mono-energetic 150 MeV proton beam (left), a 150 MeV/u ^{4}He ion beam (middle) and a 290 MeV/u ^{12}C ion beam (right).

is calculated with various cell specific constants which reduces the effect of the lineal energy spectra.

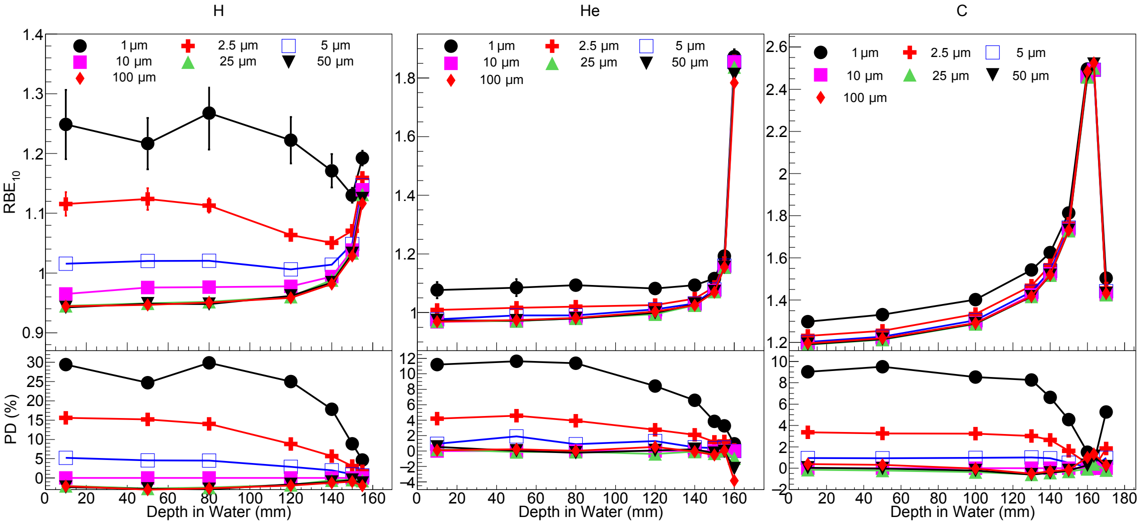

Figure 5.8: Comparison of the RBE for a mono-energetic 150 MeV proton beam (left), a 150 MeV/u ^{4}He ion beam (middle) and a 290 MeV/u ^{12}C ion beam (right).

5.3.5 Impact on the number of stoppers

The percentage of the particles which stop in the SV for different thicknesses are shown in figure 5.9 for mono-energetic proton, ^{4}He and ^{12}C ion beams. The percentage of primary ion stoppers are shown in the top three plots while the secondary ions and electrons are shown in the middle and bottom plots, respectively. For all the different particle components, the proportion of stoppers increases mostly linearly with thickness, with the 100 μm thick SV having ~100 times more stoppers for a given depth than the 1 μm thick SV.

For primary ions the three beams differ slightly from one another with the larger beams having a larger fraction of stoppers due to larger nuclear cross-sections, with ^{12}C having a total reaction cross section ∼3 times higher than protons [49] [48]. The sharp rise in stoppers at the BP is due to straggling in the range of the beam as it stops.

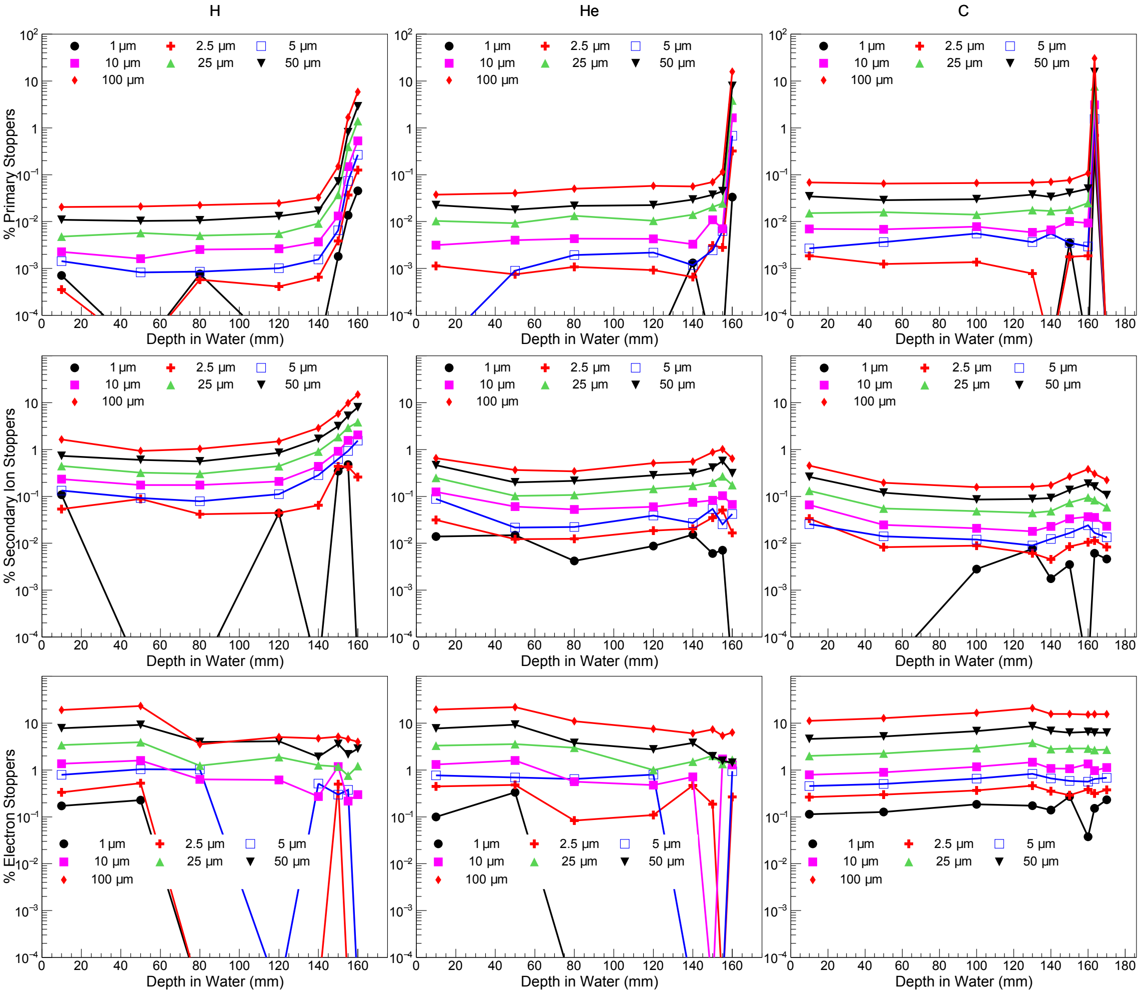

Figure 5.9: Comparison of the portion of delta electrons which stop in different SV thicknesses for a mono-energetic 150 MeV proton beam (left), a 150 MeV/u ^{4}He ion beam (middle) and a 290 MeV/u ^{12}C ion beam (right).

The secondary ions which are generated in the proton beam can be seen to have a noticeably higher percentage being stoppers, compared with the ^{4}He and ^{12}C beams. This higher proportion of stoppers is caused by secondary ion events in proton beams being dominated by recoiled protons from neutrons created by the beam. These recoiled protons have a much smaller range compared to ions created via fragmentation of the primary beam which is the dominant secondary ions in heavier ion beams. For the ^{4}He and ^{12}C beams, at the surface of the phantom there is a higher percentage of stoppers due to neutrons having their largest contribution at the surface of the phantom. At the BP the number of secondary ion stoppers have a peak, which is due to the nuclear cross-section increasing at lower energies and the fragments produced will have a smaller energy and range distribution with most stopping near the BP itself.

The percentage of delta electrons for all the beams have a similar trend of the percentage of stoppers steadily increasing with depth due to the decreasing range of the electrons generated as the primary beam slows down. One of the major reasons for the different biological impact of alternative beams is due to their different track structure [107]. Heavier beams produce a denser track structure of delta electrons which causes a greater probability for double strand breaks to occur to the DNA and is reflected in higher RBE values. Figure 5.10 shows the number of delta electrons generated directly from the primary beam ionising the water (ionisations from secondary particles are not included) when using the Livermore physics model with a production threshold of 250 eV and cut of 0.1 μm. It can be seen that the number of delta electrons produced increases for the heavier beams, with ^{4}He producing $\sim$4-5 times more electrons at all depths compared to the proton beam and ^{12}C producing $\sim$40 times the electrons than the proton beam. The different lines labelled as $> x\mu$m include only electrons which have energies greater than the CSDA range of electrons in silicon, taken from the NIST e-star database [95]. It can be seen that for all beams before $\sim$120 mm in water that approximately half of the electrons generated do not have enough energy to cross 1 μm of silicon while only $\sim$10% of electrons have an enough range to cross 100 μm of silicon.

The bottom plot of figure 5.10 shows the energy spectrum of delta electrons produced and it can be seen that the energy spectra for the proton and ^{4}He beams are very similar for each depth while the energy of the ^{12}C is approximately double for each depth.

5.3.6 The impact of using the thickness as an approximation to the $\langle l_{Path} \rangle$

Figures 5.11 and 5.12 show the impact which using the thickness of the SV as an approximation to the $\langle l_{Path} \rangle$ has on different calculated quantities for a mono-energetic proton and ^{12}C ion beam, respectively. For all quantities, with the exception of RBE$_{10}$, the proton and ^{12}C ion beams follow the same trend, with the difference between using the thickness instead of the $\langle l_{Path} \rangle$ increasing with depth as the divergence of the primary beam increases. The proton beam shows a larger difference than the ^{12}C ion due to the increased beam divergence, increasing the difference between the thickness and the $\langle l_{Path} \rangle$. The RBE$_{10}$, estimated by the MKM, in the ^{12}C ion beam shows a noticeable difference between the other quantities and the proton beam at the BP. At the BP the RBE$_{10}$ has a sharp spike in the difference between the thickness and the $\langle l_{Path} \rangle$ values, with thicker SVs having a larger increase, this spike is due to overkilling effects in the MKM where the larger thickness of the SV versus the $\langle l_{Path} \rangle$ causes a lower lineal energy. Except at the end of the beam's range, where the beam begins to stop, the thickness of the SV does not affect the discrepancy between quantities when using the thickness and the $\langle l_{Path} \rangle$.

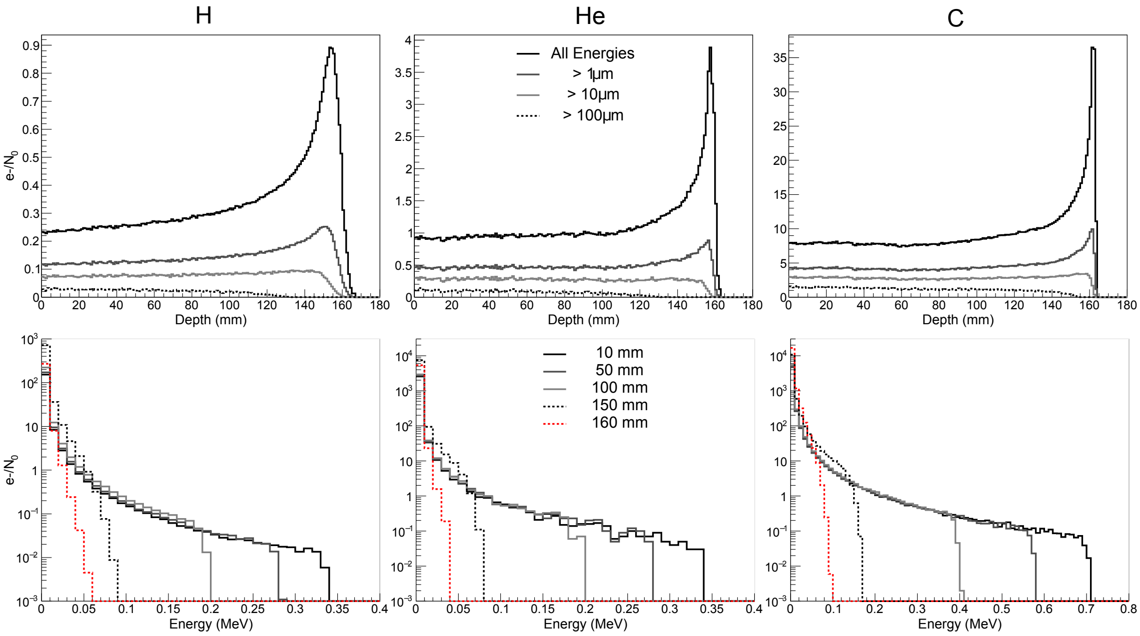

Figure 5.10: The number of delta electrons per incident particle, generated by a 150 MeV proton (left), a 150 MeV/u ^{4}He (middle) and a 290 MeV/u ^{12}C (right) beam. The top three plots shows the number of delta electrons (e^-) produced in 0.1 mm thick slices of water along the Bragg curve in water per incident primary particle. The different lines labelled as $> x\mu$m include only electrons which have energies greater than the CSDA range of electrons in silicon [95]. The bottom three plots show the energy spectrum of delta electrons at various depths along the Bragg curve.

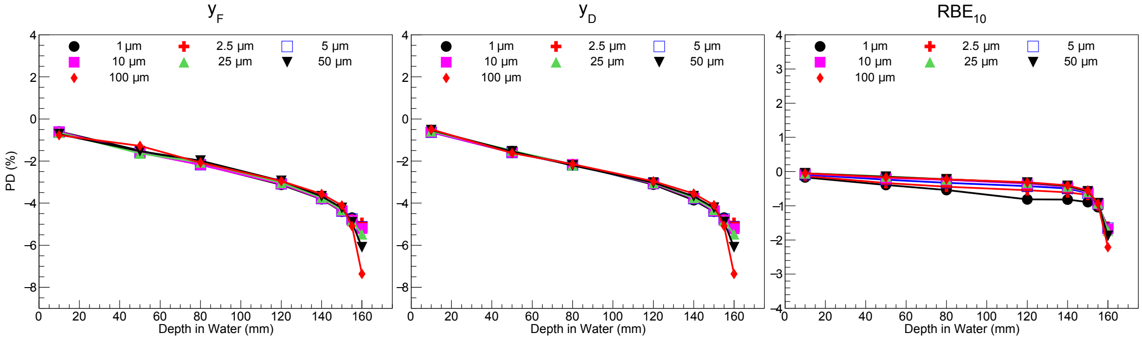

Figure 5.11: The impact which the SV thickness has on different microdosimetric quantities, in a mono-energetic proton beam, when using the thickness instead of the $\langle l_{Path} \rangle$ to calculate the lineal energy

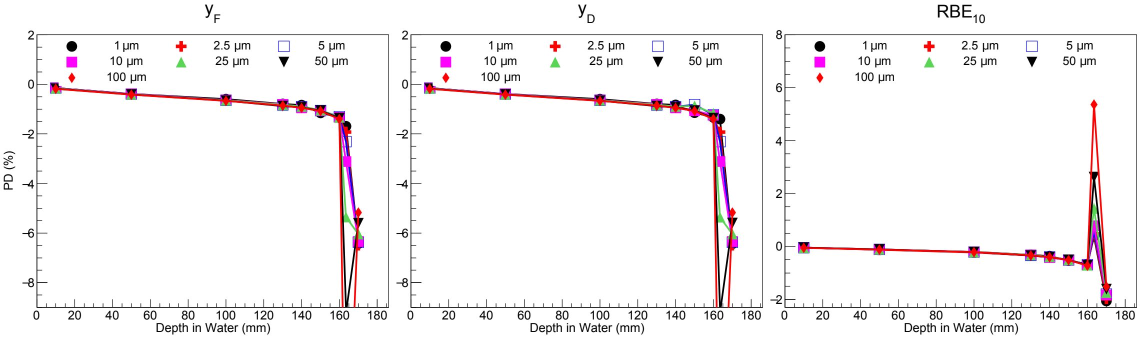

Figure 5.12: The impact which the SV thickness has on different microdosimetric quantities, in a mono-energetic ^{12}C ion beam, when using the thickness instead of the $\langle l_{Path} \rangle$ to calculate the lineal energy

5.4 Discussion

The impact of the SV size on the microdosimetric spectra and values of y_F, y_D and RBE were seen to be heavily influenced by the particular incident beam.

From the thinnest SV thickness of 1 μm to the thickest one (100 μm), all beam's lineal energy spectra were seen to have their peak shift to higher lineal energies and narrower distributions. The fluctuations of energy lost in a medium by a charged particle are dependent on the number of ionisations and excitations which occur and how much energy is transferred in each of these collisions. The number of ionisations/excitations follow a Poisson distribution while the energy transferred in these events depend on single collision spectra for the projectile and medium [7]. The number of ionisations and excitations in a medium are proportional to Z^2/v^2, where Z is the charge of the projectile and v is its velocity. The single collision spectra follows a more complex distribution, with many theoretical descriptions formulated to describe experimental distribution such as Vavilov [37]. Except for extreme relativistic energies, the maximum energy transferred to an electron is proportional to the projectile velocity squared, for the same kinetic energy a proton will have a greater velocity than heavier ions. This can be seen in figure 5.10, with protons and ^{4}He having the same maximum energy of delta electrons while the kinetic energy of the ^{4}He is four times greater than the proton, resulting in a single collision energy-loss spectra which extends to higher energies. The calculated lineal energy spectra of smaller SVs can be seen to have more prominent tails which extend to higher energies compared to larger SVs. Due to fewer ionisations occurring it is more likely to have a larger portion of these ionisations transfer energies to the electrons which is closer to the maximum possible energy.

The SV thickness affects y_F significantly for heavier ion beams and y_D for lighter beams. If the hits in the SV are processed separately to include only the incident beam and alternatively the electrons which enter the SV (not generated within the SV), their individual sensitivity to SV size can be seen. Figures 5.13 and 5.14 show y_F, y_D and RBE$_{10}$

when considering only electrons which enter the SV (top) and incident beam (bottom) for proton and ^{12}C beams, respectively.

Comparing the y_F values when processing only electron which enter the SV the difference is similar for all three beams (only proton and ^{12}C ion beams shown) . When processing only electron hits the y_F of proton and ^{4}He beams have a slight less dependence on size than the ^{12}C beam, with a difference of $\sim$20% at the surface of the phantom while the difference for an incident ^{12}C ion beam is $\sim$30%. This difference is due to the different energy spectra of delta electrons generated by the beams, with ^{12}C having a maximum energy approximately twice the proton/^{4}He beams, as shown in figure 5.10. This higher energy of delta electrons causes a greater sensitivity due to the proportion of stoppers in detector changing more along the depth of the phantom. As figure 5.10 showed, ^{12}C beams produce $\sim$40 times more electrons than protons and $\sim$10 times more than ^{4}He . This difference in the electron production causes y_F measurements in larger ion beams to be more sensitive to the SV size than for smaller ions. For ^{4}He and ^{12}C the difference in y_F for different SV sizes was seen to decrease with increased depth. As figure 5.10 shows, the proportion of stoppers increases with depth with all electrons eventually being stoppers.

Comparing the different quantities when only the incident beam is considered (bottom plots of figure 5.13 and 5.14), both beams do not have their y_F vary with SV thickness while y_D is strongly dependent. This shows that the observed variation in y_F seen in figure 5.6 is due to electrons in the radiation field. The difference in y_F when processing just primary beam events is not affected because the mean of the lineal energy is effectively representing the linear energy transfer of the incident ion, which will not vary based on the SV thickness except at very low energies where the stopping power changes rapidly. Due to the additional y dependency of y_D, the spectrum is weighted to higher energy deposition events. This weighting of the spectrum affect protons the most due to it having the largest maximum possible energy transferred to electrons when the incident beams have the same kinetic energy.

The RBE results showed a similar trend as y_D, but with a reduced difference due to the smaller impact of higher y events. The SV thicknesses between 5 and 100 μm, which are equivalent to muscle thicknesses of $\sim$8.5-175 μm, show only slight differences of $\sim$1%.

The difference between the quantities of y_F, y_D and RBE for different thicknesses are all seen to reduce with depth. For y_F this is due to the lower energy of delta electrons produced and causing the majority of electrons to stop in the SV, regardless of the thickness (see figure 5.10). The differences due to the SV thickness of y_D and RBE are instead dependent on the primary beam, as the energy of the beam decreases with depth the number of ionisations/excitations in the medium increases, creating a sharper distribution.

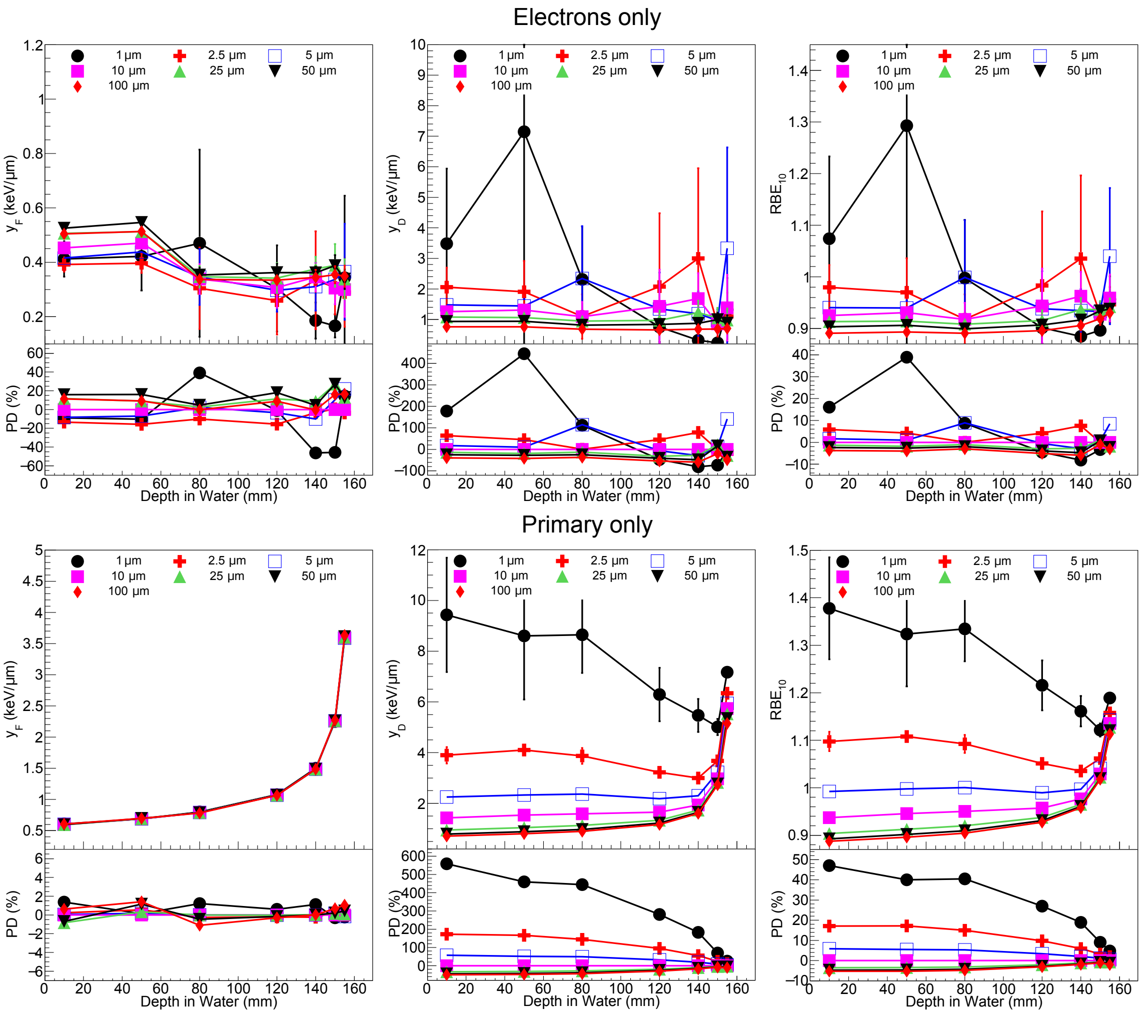

Figure 5.13: A comparison of the PD of different SV thicknesses in a mono-energetic proton beam when only electrons which are generated outside of the SV and enter are considered (top) as well as the incident primary beam (bottom).

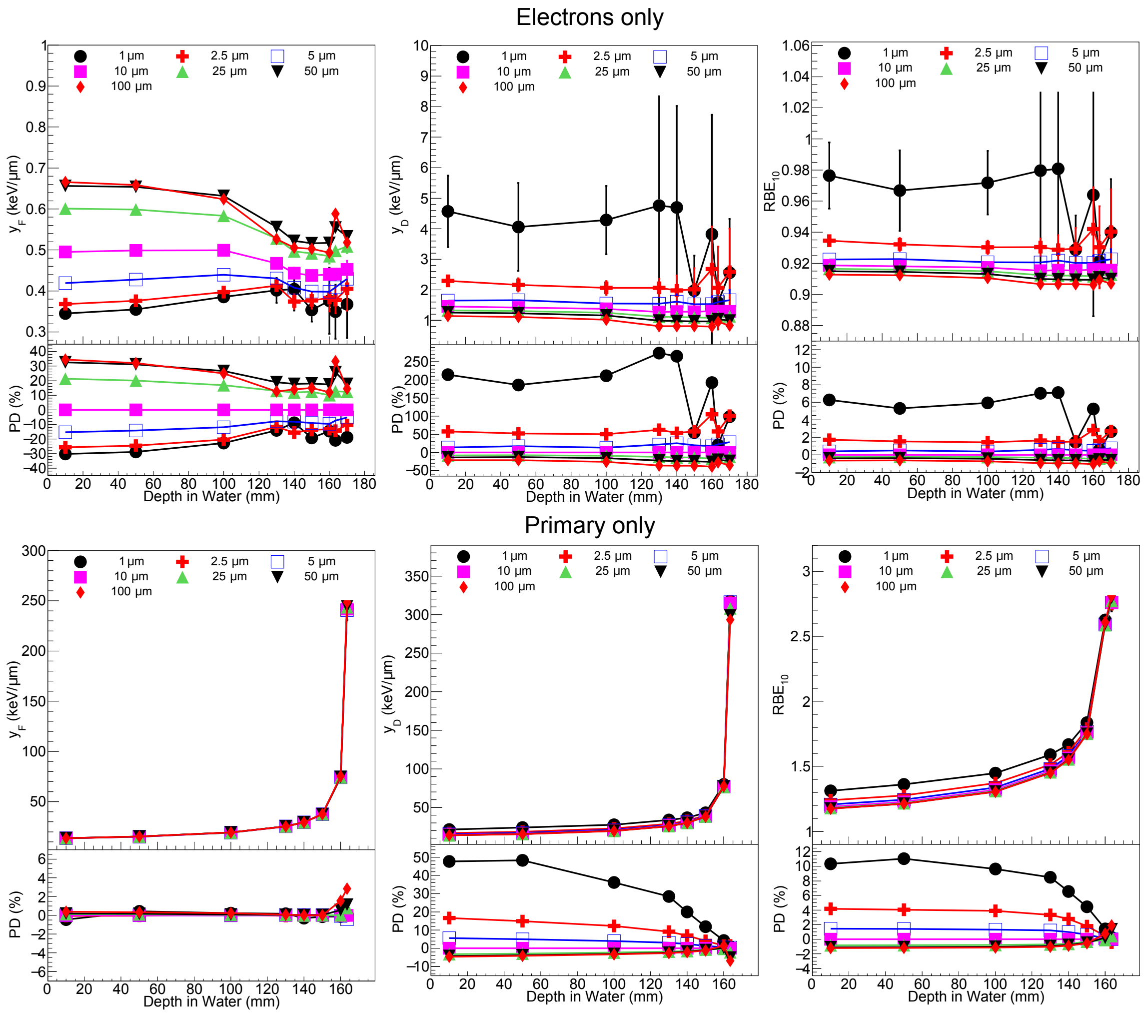

Figure 5.14: A comparison of the PD of different SV thicknesses in a mono-energetic ^{12}C ion beam when only electrons which are generated outside of the SV and enter are considered (top) as well as the incident primary beam (bottom).

5.5 Conclusions

This chapter investigated the impact of the SV thickness for SOI microdosimeters in therapeutic mono-energetic proton, ^{4}He and ^{12}C ion beams. SV thicknesses were investigated between 1 and 100 μm. This is an important consideration when comparing different studies where the SV size are not the same between the two or when using the microdosimetric spectrum as an input to a model (such as the MKM) which is based upon SVs of a particular size. Larger SV thicknesses were seen to cause the lineal energy spectra peak to be shifted to higher energies and produce a sharper peak.

The microdosimetric quantity, y_F was seen to be strongly influenced by the different electron track densities of the beams. ^{12}C had the greatest impact from the SV size due to the much higher electron production with a difference of $\sim$40% between the 1 and 10 μm thick SVs, while the proton beam only had a maximum difference of $\sim$2% and ^{4}He $\sim$6%.

In contrast to y_F, y_D was dependent on the incident primary beam, with protons being the most sensitive to different thicknesses of SV due to it having the largest possible energy transfer to electrons. The difference between 1 and 10 μm thick SVs was $\sim$250, $\sim$120 and $\sim$30% at the surface of the phantom for the proton, ^{4}He and ^{12}C beams, respectively. The calculated RBE, estimated by the MKM, had a similar dependence as y_D but with a reduced percentage difference due to higher lineal energy events having less effect. The difference at the surface between the 1 and 10 μm thick SVs was $\sim$30, 11 and 9% for the proton, ^{4}He and ^{12}C beams, respectively.

Since y_F is generally of less interest for clinical applications than y_D, the SV size when used in proton beams should be carefully considered when comparing different measurements. Since the biological estimation of the beam is more important for heavier beams and because SV sizes between 5 and 100 μm (equivalent to 8.6 and 170 μm striated muscle) showed a difference of less than 2%.

Chapter 6

Validation of the Geant4 simulation for silicon microdosimetry in heavy ion therapy

Geant4 is a very useful predictive tool to characterise the response of novel detectors when exposed to radiation fields of interest, in order to eventually identify possible issues which could emerge during the experiments, or to optimise some parameters of the experimental set-up. In order to use Geant4 as a predictive tool, it is essential to quantify its accuracy in the application scenario of interest.

This chapter describes the results of a Geant4-based simulation performed to characterise the response of the Mushroom microdosimeter when irradiated, with ion beams of interest for heavy ion therapy (HIT).

The Geant4 simulation results were compared to in-house experimental measurements in order to quantify, for the first time, the accuracy of Geant4 for experimental silicon microdosimetry in HIT. In order to perform a thorough comparison of the microdosimetry measurements, the beamline used for the experiment, the Biological Beamline, was validated against experimental measurements.

The experimental measurements shown in this chapter were performed by Dr. Linh Tran and Lachlan Chartier at the Heavy Ion Medical Accelerator in Chiba (HIMAC). They also performed scanning electron microscope (SEM) and ion beam induced charge collection (IBICC) measurements, used to characterise the Mushroom microdosimeter.

Reasonable agreement between simulation and experiment was observed, demonstrating the suitability of Geant4 as Monte Carlo simulation code to characterise the response of novel microdosimeters for HIT.

Some results from this chapter have been published in:

- “The relative biological effectiveness for carbon, nitrogen and oxygen ion beams using passive and scanning techniques evaluated with fully 3D silicon microdosimeters”, *Medical Physics*, (45), 2018

- “In-field and out-of-file application in ^{12}C ion therapy using fully 3D silicon microdosimeters”, *Radiation Measurements*, (115), 2018
- “Modelling the Biological Beamline at HIMAC using Geant4”, *Journal of Physics Conference Series*, 2019

6.1 Introduction

While proton and ^{12}C ion therapy are well established, there has been a growing trend away from finding the “best” overall ion in HIT and instead the best ion for a particular treatment [108]. Recently there has been a growing interest in treatments with alternative ion beams, such as ^{4}He and ^{16}O beams [108] as well as using multiple ions in a single treatment [109]. This new interest of alternative ions, like all radiotherapy, requires quality assurance to be performed on the beam, regardless of the type of beam, and being HIT the need to estimate its biological impact.

Up until now, ^{12}C therapy has been somewhat avoided for pediatric cases due to the prominence of the fragment tail produced [110], due to the smaller production of fragments by ^{4}He beams, ^{4}He presents an advantage over ^{12}C for pediatric cases. Additionally, compared to proton therapy, ^{4}He has less lateral scattering, producing a more conformal treatment, these two points make ^{4}He an attractive middle ground between proton and ^{12}C treatment. Furthermore, due to the lower linear energy transfer (LET)/relative biological effectiveness (RBE) of ^{4}He beams, they have a smaller error associated with the biological dose (RBE × Physical dose) delivered when compared to ^{12}C [108] due to a smaller range of RBE values at the end of the beam’s range. This growing interest in ^{4}He beams has resulted in ^{4}He HIT being implemented into treatment planning systems (TPS). For example, the TPS used at GSI for HIT, TriP98 [111], has recently added ^{4}He beams with physical and biological doses being validated against experimental data [112]. The commercial TPS RayStation has also implemented ^{4}He HIT into their TPS [113].

In contrast to lighter ions, heaver ions such as ^{16}O and ^{20}Ne offer an attractive boost in terms of LET compared to ^{12}C . The higher LET of larger ions is particularly attractive for radio-resistant tumours such as osteosarcomas [114]. Oxygen supply to tumours plays an important role in low LET radiation such as conventional x-ray therapy due to the production of free radicals which damage the cancer’s DNA (indirect damage). Hypoxic regions are often created in tumours due to blood vessels not being able to be produced fast enough to match the speed that the tumour grows, leading to regions of the tumour having different levels of blood/oxygen being supplied [30]. The oxygen enhancement ratio (OER) of hypoxic and non-hypoxic regions is approximately 3 for x-ray therapy and reduces to $\sim$1.5 for an LET in tissue of 118 keV/μm [115]. For ions larger than ^{12}C the OER is close to 1 [108] and makes the treatment of tumours more simpler due to the biological dose being almost independent of the oxygen supplied to a tumour. Another advantage of larger ions is the reduced lateral scattering, which can be beneficial when treating near critical organs. A drawback to using larger ions is the larger nuclear cross-sections compared to ^{12}C , meaning that the secondary radiation field is more complex due to the primary beam being attenuated more and generating more and heavier fragments compared to lighter ion beams [116].

Figure 6.1 illustrates the differences in the physical dose produced by different ions as well as protons. The different energy deposition profiles are from: proton, ^{4}He , ^{12}C , ^{16}O and ^{20}Ne incident on a $30 \times 30 \times 30$ cm^3 water phantom with initial energies of 150, 150, 285, 340 and 391 MeV/u, respectively. The energy deposition along the depth of the phantom is shown on the left and the lateral profile just before the BP at 150 mm is shown on the right. The effect of the different nuclear cross-sections of the different beams can be seen in the depth profiles, with the heavier beams having more pronounced fragment tails. In terms of the lateral profile a drastic difference in the width can be seen at the depth just before the BP due to multiple Coulomb scattering. The ^{4}He beam can be seen to produce a significantly smaller spread than the proton beam with a FWHM of ~4 mm versus ~8 mm. The heavier beams differ less noticeably with one another, with a FWHM close to ~1 mm.

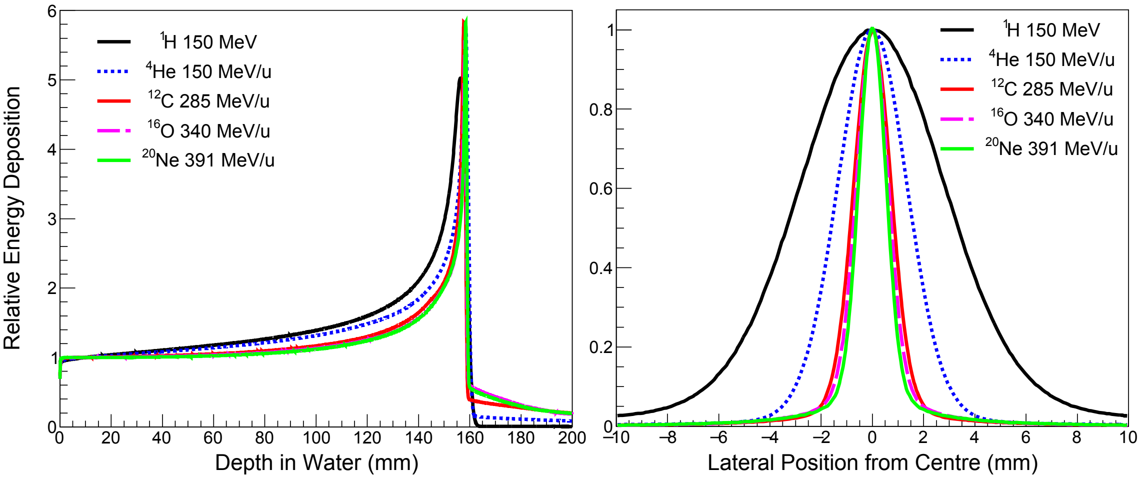

Figure 6.1: Comparison of the energy deposition along the depth (left) and the lateral profile just before the BP at a depth of 150 mm (right) in a water phantom for various different beams.

As with all radiotherapy modalities it is critical to ensure that the treatment being delivered matches the planned treatment by the TPS. Unlike conventional x-ray radiotherapy, HIT not only requires the physical dose of the beam to be considered but also the biological dose (see section 1.6. Due to the complex nature of HIT radiation fields, it is important to be able to estimate the RBE of a beam independently of the primary ion, which is particularly relevant for proposed LET scanning treatment modalities where multiple ion beams would be used [109] [117]. Due to these requirements, microdosimetry is an attractive method for characterising HIT beams, with SOI microdosimeters being particularly attractive due to their high spatial resolution and simple compact operation.

This chapter shows experimental results using the Mushroom microdosimeter irradiated in the Biological beamline at the Heavy Ion Medical Accelerator in Chiba, (HIMAC), Japan. Before comparisons are made between the experimental Mushroom results and Geant4, the Biological beamline is first modelled and validated against experimental measurements. Using the validated beamline model, the Mushroom microdosimeter was irradiated with mono-energetic ^{12}C , ^{14}N and ^{16}O beams and a spread out Bragg peak (SOBP) ^{12}C beam and compared to experimental measurements. In addition to these beams, the Mushroom was also irradiated by mono-energetic ^{4}He and ^{20}Ne beams in Geant4 to study the smallest and largest ions currently considered in HIT. As this device is the first fabricated prototype, it is important to ensure that the device is performing as expected and so the focus of this chapter is to compare the experimental measurements with the Monte Carlo toolkit Geant4. Comparisons between the experiment and simulation are performed in terms of the dose mean lineal energy (y_D) and the RBE$_{10}$, as estimated by the modified microdosimetric kinetic model (MKM) [67].

6.2 Materials and Methods

The experimental measurements presented in this chapter were all performed at the Biological Beamline at HIMAC. The Biological Beamline is modelled in Geant4 using version 10.2p2 and is validated against experimental measurements. Once the beamline was validated, the real world Mushroom microdosimeter was modelled in detailed and its response was studied in various different HIT beams.

6.2.1 The Biological beamline

A diagram of the modelled Biological beamline is shown in figure 6.2. The beamline was validated against experimental data for a mono-energetic and a SOBP ^{12}C beam. For both beams the primary ^{12}C ion is generated at the beam duct in a vacuum tube 205 cm in length. The ^{12}C beam has an initial energy of 290 MeV/u and a 0.2% energy σ. The beam is generated as a Gaussian distribution with a spot size of 3.4 mm σ.

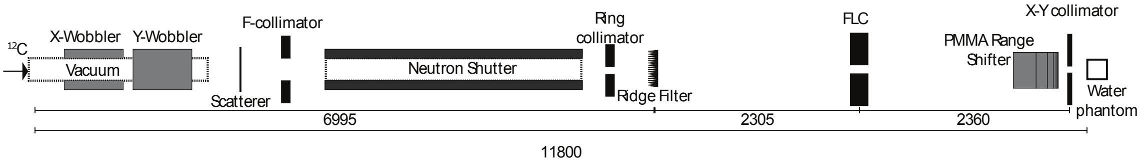

Figure 6.2: Layout of the Biological beamline modelled in Geant4, not to scale.

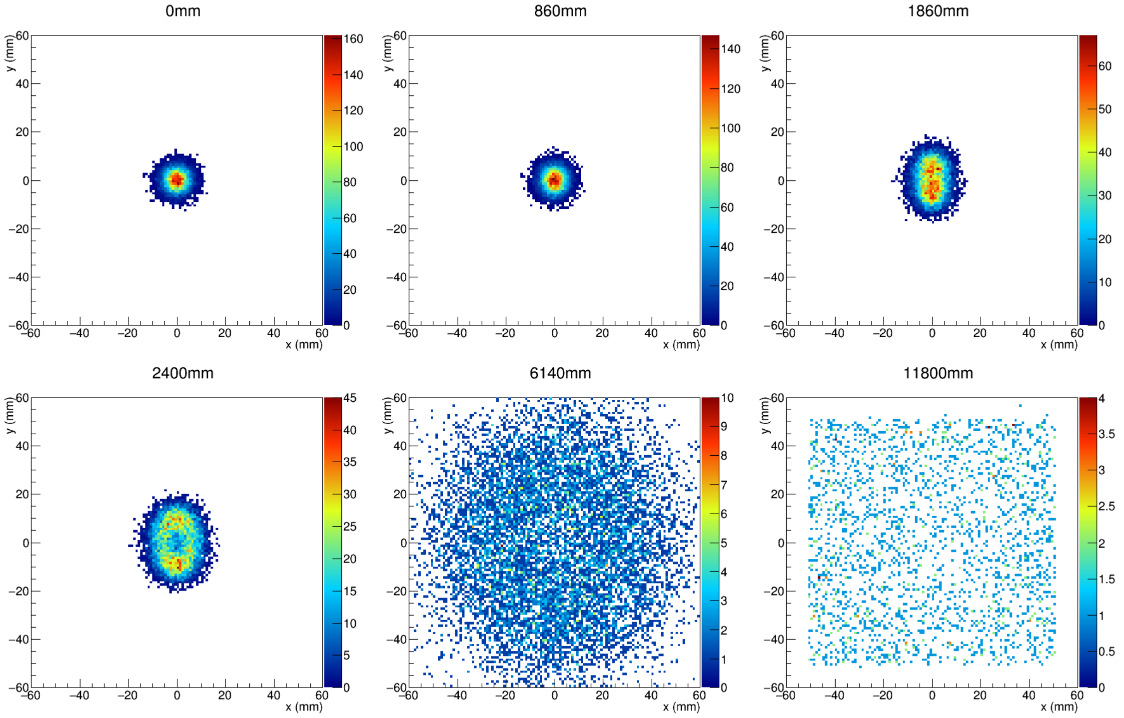

Figure 6.3: A beam's eye view of the fluence of a mono-energetic ^{12}C beam with $\sim 10^4$ primary particles at various distances from the beam duct. The 860 and 1860 mm positions correspond to the exit of the first and second wobbler magnets, respectively. The 2400 and 6140 mm distances shows the profile of the beam after traversing the scatterer and neutron shutter, respectively. The 11800 distance is the profile at isocenter after being collimated to a 100×100 mm^2 size.

The beam is then shaped to a circle by two wobbler magnets operated using the single-ring wobbling method [118]. The strength of the magnetic field at a particular time t is $B_0 \sin(\omega t)$ and $B_0 \cos(\omega t)$ for the X and Y wobbler magnets respectively, where ω is 56.41 Hz. In the simulation the period is sampled at 111 different times. Each wobbler magnet is modelled as a cylinder with a radius of 250 mm and length of 660.1 mm with a 110 mm gap between the two wobbler magnets. In the simulation a uniform magnetic field is applied to both the wobbler magnets.

Once the beam is shaped by the pair of wobbler magnets the lateral dose uniformity of the beam is improved by passing through a tantalum scatterer which is located at $\sim$2308 mm from the beam duct. The thickness of the scatterer and wobbler strength, B_0, depend on the energy and ion of the beam being delivered, as well as the field size. For the mono-energetic 290 MeV/u ^{12}C beam the B_0 is 0.045 T and the scatterer is 0.434 mm thick while the SOBP has a B_0 of 0.061 T and a scatterer thickness of 0.649 mm.

After passing through the scatterer, the beam is collimated by a 100 mm thick brass F-collimator with a diameter of 100 mm, located 2755 mm from the beam duct. After the F-collimator the contribution of neutrons in the beam is reduced by traversing a 2885 mm long vacuum neutron shutter. After exiting the neutron shutter, the beam is further collimated by a 200 mm thick brass ring collimator with a diameter of 100 mm.

In the SOBP configuration, the beam will then pass through a ridge filter (RGF), located 6995 mm from the beam duct. For a 6 cm 290 MeV/u ^{12}C SOBP the RGF is made up of 21 bars of milled aluminium 200 mm in length and $\sim$5 mm wide, each bar consists of 101 different thicknesses.

The beam then traverses a 20 cm thick aluminium, four leaf collimator (FLC) placed 9300 mm from the beam duct. The beam can then pass through various combinations of PMMA thicknesses to shift the range of the beam. The beam can then be further collimated by a 5 cm thick X-Y brass collimator, 140 mm before iso-center.

The changing shape of the beam as it traverses the beamline is shown in figure 6.3, which shows the transport of $\sim 10^4$ mono-energetic ^{12}C ions from the beam duct to the iso-center with a field size of 100×100 mm^2 set by the collimators.

For the validation of the beamline, two phantom sizes were used for scoring the lateral and depth doses with sizes of $30 \times 30 \times 30$ cm^3 and $22 \times 22 \times 26$ cm^3, respectively. The $30 \times 30 \times 30$ cm^3 phantom was used to compare measurements in the literature while the 22×22 cm^2 was compared against measurements performed by CMRP. The scoring of the lateral dose profile was done in $5 \times 5 \times 10$ mm^3 voxels at the surface of the phantom. For calculating the depth dose the phantom had 1 mm thick water cylinders with diameters of 10 mm placed along the beam axis. Experimental measurements were obtained using the PTW Pin Point Ion Chamber 31023, which has an active volume of 0.015 cm^3 with a radius of 1 mm and length of 5 mm.

Throughout the beamline there are various 10 μm thick aluminium sheets, these represent ionisation chamber (IC) monitors and the end of the first vacuum chamber and the start and end of the neutron shutter. The IC are made up of two sheets of aluminium and are positioned at 2175, 6910, 6950 and 8525 mm from the beam duct.

To describe electromagnetic interactions the *G4StandardOption3* physics list was adopted. Hadronic interactions were modelled using the Binary Intranuclear Cascade (BIC). The elastic scattering of hadrons was modelled by means of the *G4HadronElasticPhysicsHP* and the neutron High Precision (HP) model was adopted to describe neutron interactions of energies up to 20 MeV. For the beamline validation study, the water phantom a production cut size and step limit of 0.5 mm were used.

In order to validate the Geant4 simulation both lateral and depth dose profiles were compared to experimental measurements. For a 290 MeV/u mono-energetic and 6 cm SOBP ^{12}C beam experimental data from [119] and [120] were used, respectively, for the lateral dose. For both these cases the dose is measured at the surface of the phantom with an ionisation chamber with the FLC and brass collimator being fully opened. For depth dose measurements CMRP data from [121] were used for both beams. For lateral dose comparisons the maximum value in the experiment and simulation were both normalised to the same value, while for reference depth dose comparisons the first depth in the experiment was used to normalise the experiment and simulation distributions.

To investigate whether the simulation could be simplified by excluding the wobbler, the lateral and depth dose profiles were compared to the case of having the wobbler setup with the FLC and brass collimators set to a field size of 100×100 mm^2, a common field size of interest. The simplified methods consist of deactivating the wobbler magnets and generating the particles at the same beam duct position as used for the full wobbler technique. The different methods included simulating a 3.4 mm σ pencil beam (the same initial beam size used for the full wobbler method), a cone beam simulated by generating an isotropic distribution with an aperture angle of 1 degree and finally a circular beam with diameter of 100 mm and generated uniformly. A beam's eye view of the fluence using the different methods is shown in figure 6.4, the positions are at the beam duct where the beam is generated (0 mm) and just before the neutron shutter (3200 mm).

6.2.2 Microdosimeter Experiment

For the simulations of the microdosimeter in the beamline which were irradiated with a mono-energetic beam and where experimental measurements where performed, simulations were run two separate times with alternative inelastic hadronic models. The models used were the BIC and the QMD (default, not QMD-F). For the results presented below the comparisons between simulation and experiment are primarily with respect to the BIC model, with discussion of QMD results left for the Discussion section.

The experimental microdosimeter measurements were performed using a water tank

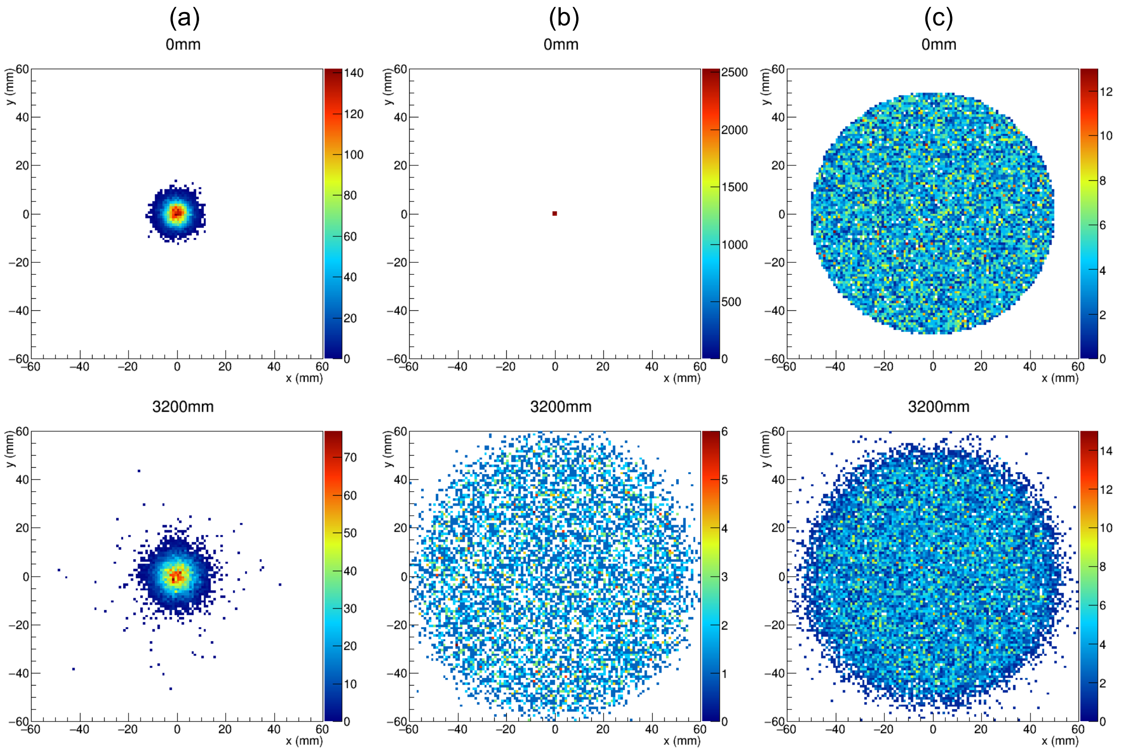

Figure 6.4: A beam's eye view of the fluence of the beam simulated with different methods at the beam duct (0 mm) and just before the neutron shutter (3200 mm). (a) 3.4 mm σ pencil beam, (b) 1° cone beam and (c) 100 mm diameter circle beam.

with 6 mm thick PMMA walls and an area of 22×22 cm^2 perpendicular with the beam and a thickness of 26 cm. The face of the phantom was positioned at the iso-centre of the beamline as shown in figure 6.2. The microdosimeter was positioned in the centre of the beam in a water proof PMMA sheath which was scanned through the radiation field by a remotely controlled X-Y motion stage.

In the experiment the Mushroom microdosimeter was irradiated with four different beams, three mono-energetic ^{12}C , ^{14}N and ^{16}O beams and a SOBP ^{12}C beam. In addition to these beams a ^{4}He and ^{20}Ne beam was simulated to compare the properties of the smallest and largest ions currently considered for HIT [122]. The different primary energies and beamline parameters of each beam simulated are summarised in table 6.1, all beams were collimated to 100×100 mm^2 by the X-Y brass collimators just before the phantom.

Some important properties of the different beams are listed below:

- The ^{12}C beams' energies were tuned to 288.6 MeV/u from the provided experimental value of 290 MeV/u to match the observed depth for the mono-energetic beam in the experiment.
- The SOBP ^{12}C beam used the 5 mm thick aluminium ridge filters.
- Both the ^{12}C beams used the full wobbler magnet setup while the ^{14}N and ^{16}O

Ion	Primary Energy (MeV/u)	Energy Sigma (%)	Ta Thickness (mm)	B_0 (T)	PMMA range shifter (mm)
^{4}He	150	0.35	0.215	Cone	0
^{12}C (SOBP)	288.6	0.2	0.649	0.061	0
^{12}C	288.6	0.2	0.434	0.045	0
^{14}N	180	0.36	0.434	Cone	0
^{16}O	400	0.15	0.649	Cone	86
^{20}Ne	400	0.15	0.756	Cone	0

Table 6.1: Summary of the different configurations used for each beam. Note: in the Wobbler strength column (B_0) a value of "Cone" means that a 1° cone beam was used instead of using the wobbler magnets to shape the beam.

beams used the simplified approach tested below in section 6.3.1 of generating a cone beam with a divergence of 1°.

- The ^{16}O beam is the only beam to use PMMA range shifters with a total thickness of 86 mm or a water equivalent thickness (WET) of ∼100 mm and are positioned approximately 300 mm upstream from the water phantom. The range shifter was used because the beam's range was too large (∼190 mm) to study the BP region in the 160 mm thick water phantom. Despite the range shifter, the depths for the ^{16}O beam are quoted with reference to the depth in the water phantom itself and does not add the additional 100 mm WET of the range shifter.

The following section describes the modelling of the Mushroom microdosimeter used in the water phantom and how it is positioned in a water proof PMMA sheath.

Air trenched Mushroom microdosimeter

The Mushroom microdosimeter was modelled in Geant4 based on the images created using a scanning electron microscope (SEM). Diagrams and images of the Mushroom are shown in figure 6.5, with the top right being an SEM image and the remaining diagrams being screenshots from the Geant4 simulation. This device is the first generation of its design used by CMRP and exploits 3D technology [123], which has the advantages of: radiation hardness, fast collection times, well defined SVs and low depletion voltages [84].

The Mushroom is fabricated from a high-resistivity p-type silicon of 10 kΩcm and the structural design is refereed to as a trenched 3D. The SV has a trenched hollow core and hollowed semi-circles which extend ∼2.7 μm from the SV to reduce charge generated outside of the SV from being collected. The SVs cover an area of $\sim 2.5 \times 2.5$ mm^2 and are connected into arrays of 50×50 rows and columns by aluminium contacts. The SVs have a thickness of 9.1 μm and a diameter of 28.5 μm. On the top surface of the SV there is a 0.85 μm thick overlayer of SiO_2 directly on top of the silicon. On the bottom of the silicon SV there is also a 0.85 μm thick SiO_2 insulator layer which is above a 300 μm thick silicon base. The aluminium contacts which connect the SVs together into arrays were modelled as having a width of 3.75 μm and thickness of 1 μm.

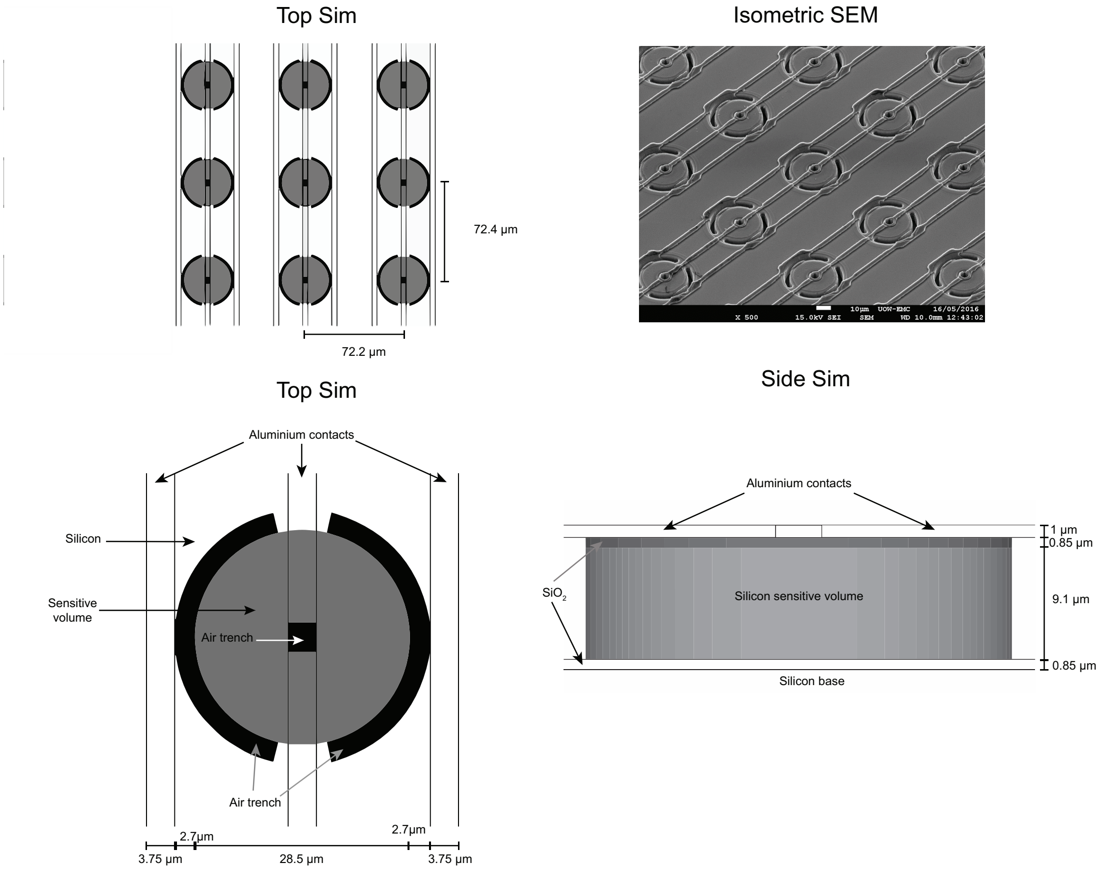

Figure 6.5: The Mushroom microdosimeter modelled in Geant4 and an SEM image (top right) of the real world device.

Due to this being the first version of the Mushroom microdosimeter fabricated, there are inevitably some minor shortcomings to be improved with revised versions. The main short coming of this first generation device is the charge collection uniformity, which has already been greatly improved in the second fabricated Mushroom. A two dimensional map of the charge collected from the air trenched Mushroom microdosimeter can be seen in the right plot of figure 6.6. The collected charge was produced by the ion beam induced charge collection (IBICC) technique at ANSTO using the Heavy Ion Microprobe [77] by raster scanning a 5.5 MeV α beam with a diameter of $\sim$1 μm. The high energy peak seen on the right, above 1000 keV, is due to alpha particles depositing energy in the SV. The blue regions in the 2D map cause the low energy peak below 200 keV in the MCA spectrum and are due to charge being collected from under the aluminium contacts which connect the SVs together. Much of these low energy events are removed when setting the energy threshold in the experiment, however, particles with high LET can cause events to be counted from this region. Further discussion on the charge collection properties of the Mushroom can be found in [124].

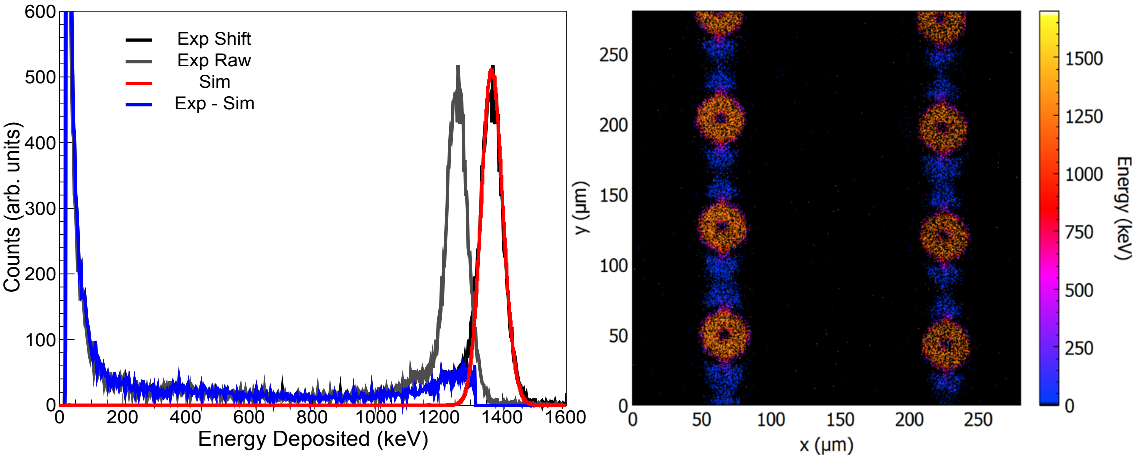

Figure 6.6: Left: Comparison of the energy deposition spectra of experiment and simulation when irradiated with a 5.5 MeV alpha beam. The different spectra includes the simulation, featuring a single Gaussian peak from the alpha beam, the raw output from the experiment and its corrected spectra which shifts the raw spectrum based on its charge collection efficiency. Finally, the difference between the shifted experiment spectrum and the simulation spectrum is also shown. Right: The corresponding 2D charge collection profile map when irradiating the device with the 5.5 MeV alpha beam.

μ^+ probe

The micro-plus (μ^+) probe is an in-house, CMRP designed and built probe which provides a compact and low noise readout system. For the HIMAC experiments simulated in Geant4 of this chapter, the μ^+ probe was placed inside a water proof PMMA sheath and mounted into a moveable X-Y stage, which allows the probe to be set to different positions in the water phantom with a precision of less than a mm.

A screenshot of the μ^+ probe placed in a water proof PMMA sheath, modelled in Geant4, is shown in figure 6.7. The PMMA sheath is modelled as a $30 \times 30 \times 30$ mm^3 block covered with a 75 μm thick aluminium layer. At the top of the PMMA sheath, where the beam is incident, there is a 16×16 mm^2 cutout which is 4.7 mm thick. This cutout is done to minimise non-water material inline of the beam, with the water proof sheath only adding a 0.5 mm thickness of PMMA to the beam before the detector. Below the 0.5 mm thick PMMA window there is 0.5 mm of air before a 0.1 mm thick high density polyethylene (HDPE) which shields the detector from visible light. Below the HDPE film there is another 0.53 mm of air before the top surface of the Mushroom microdosimeter. The detector is mounted onto an aluminium oxide dual in-line (DIL) package which is on a PCB modelled as pyrex glass. The real μ^+ probe slides into the PMMA sheath which is why it appears to "float" in the simulation screenshot.

When measurements are made using the water proof sheath the reported "depth" is given in terms of the water equivalent thickness (WET) from the face of the water phantom (6 mm of PMMA) to the surface of the detector. This involves using conversion factors calculated using Geant4, by simulating the BP positions for different beam energies and materials. The conversion factor is calculated by taking the ratio of the BP position in water to the other material, which is similar to taking the average ratio of the stopping powers of the two materials. The materials before the detector and their thicknesses, as well as their converted WETs are shown in table 6.2.

Item	Material	Thickness (mm)	Conversion factor	WET (mm)
Water phantom wall	PMMA	6	1.16	6.96
Probe window	PMMA	0.5	1.16	0.58
Top air gap	Air	0.53	0.001	0.00053
Black film	HDPE	0.1	1	0.1
Bottom air gap	Air	0.53	0.001	0.00053

Table 6.2: Summary of the different materials, their thicknesses and WETs from the start of the water phantom case to the face of the detector.

The maximum energy deposition set in the experiment was ~22 MeV which was divided into 4096 energy bins, the same energy binning used in the experiment was also adopted for analysing the simulation data.

6.2.3 Comparisons between experiment and simulation

The quantities used to compare simulation and experiment in this chapter are the dose mean lineal energy, y_D, and the relative biological effectiveness at 10% survival, RBE$_{10}$ as described in sections 1.5.1 and 1.6.3, respectively. The quantities are compared between simulation and experiment by using the percentage difference, *PD*, as defined in equation 6.1, where *Exp* is the value of the quantity from the experiment for the particular depth

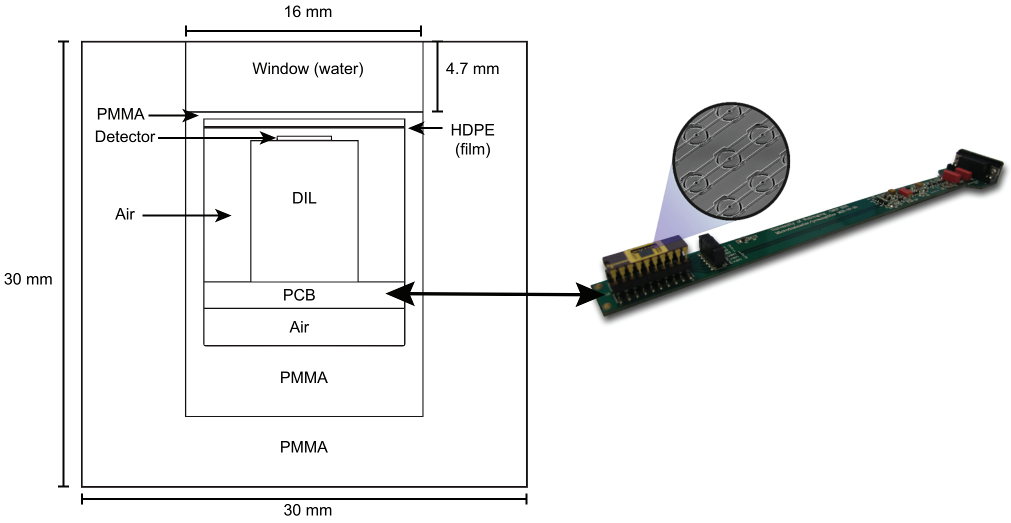

Figure 6.7: Left: Screenshot of the μ^+-probe inside of the waterproof PMMA sheath modelled in Geant4. The probe is positioned in the water phantom such that the beam would be directed perpendicularly downwards in the diagram. Right: image of the real μ^+-probe with the Mushroom microdosimeter mounted into the DIL package.

and *Sim* is the value from the simulation.

$$PD = \left(\frac{\text{Exp-Sim}}{\text{Exp}}\right) \times 100\% \tag{6.1}$$

Since the SV of the Mushroom is silicon it is converted to represent a tissue equivalent material (striated muscle) by multiplying by the conversion factor κ of 0.57, calculated in chapter 3. The lineal energy, y, is calculated from the energy deposition, E, by dividing by the mean path length of the silicon SV ($\langle l_{Path,Si} \rangle$) instead of the mean chord length (Cauchy) as shown in equation 6.2. In this chapter, the approximation of using the thickness of the SV (9.1 μm) instead of the calculated mean path length is used, based on the results found in chapters 3 and 5.

$$y = \frac{\kappa E}{\langle l_{Path,Si} \rangle} \tag{6.2}$$

6.3 Results

6.3.1 Validation of the Biological beamline modelled in Geant4

Comparison against experimental measurements

Figure 6.8 shows the comparison of simulation and experimental data in terms of the lateral and depth dose profiles with the percentage difference (PD) plotted at the bottom. The PD was calculated using equation 6.1. Overall, the agreement between simulation and experiment is satisfactory for both the lateral and depth dose profiles.

The lateral dose profiles at the surface of the phantom are shown for a mono-energetic beam (a) and a SOBP (b). It can be seen that for the pristine beam there is excellent agreement between the experiment and simulation with a difference of less than 0.5% in the treatment field between ±50 mm. At the sharp penumbra the difference increases to a maximum of ∼2.5%, however due to the rapidly changing dose in this region experimental positioning becomes more sensitive. For the SOBP there is visibly less agreement, with the treatment field varying between ∼2%, however the penumbra gives agreements within ∼1%.

The depth dose distributions for a mono-energetic and SOBP 290 MeV/u ^{12}C beam are shown in (c) and (d), respectively. Both setups have a collimation size of 100 × 100 mm^2 for both the FLC and brass collimator. For the mono-energetic beam the overall shape agrees very well, however the difference between the simulation and the experiment gradually increases with depth and has a maximum of ∼8% at the pinnacle of the BP. The SOBP depth dose (d) shows a more stable difference between the simulation and the experiment with a difference between ∼2%. Like with the mono-energetic beam the SOBP beam also has a maximum difference at the end of the SOBP range, these regions have sharp dose gradients and are sensitive to slight misplacements or energy differences of the delivered beam.

Simplified simulations techniques to model the effect of the wobbler

A comparison of the different simplified simulation techniques is shown in figure 6.9, with the plotted percentage differences being calculated with respect to the full wobbler method.

The lateral dose is compared using a mono-energetic beam collimated to a 100 × 100 mm^2 field and is shown in (a). It can be seen that the cone beam reproduces the lateral beam profile of the wobbler setup very well, with a difference within $\sim$2% for the treatment field with the difference increasing at the penumbra, while both the point and circle beams agree very poorly.

The depth dose, using the different simulation techniques is shown in (b) for the mono-energetic beam and (c) for the SOBP. For the mono-energetic beam the different methods of modelling the beam do not vary strongly with one another, with the cone beam not differing significantly. The pencil and circle beams are very similar to one another, with them both increasing in difference with depth compared to the wobbler method, with a difference of $\sim$1% higher at the pinnacle of the BP, after the BP they both under respond compared to the wobbler with a difference which increases with depth. For the case of the SOBP (c), shows a much more prominent difference between the cone beam compared to the point and circle beams. Without the angular spread, the point and circular beams create a flatter dose over the range of the SOBP between 85 and 145 mm, with a maximum difference of $\sim$15% at the end of the SOBP. Using a cone beam configuration provides a simplified simulation model which results in very small differences compared to the full wobbler configuration. The simulation is simplified by not having to add magnetic field properties to volumes and merge multiple magnetic field times. This simplification in the simulation does not translate to an increase in runtime provided.

6.3.2 Mono-energetic 290 MeV/u ^{12}C beam

The dose weighted microdosimetric spectra displayed on a semi-log scale, $yd(y)$, at various depths in the water phantom along the mono-energetic ^{12}C beam can be seen in figure 6.10. The top left plot shows the microdosimetric spectra at the entrance of the phantom (18.91 mm) while 149 mm corresponds to the pinnacle of the BP. The contribution to the total dose deposited in the detector, produced by different particle types, is reported in the simulation results as well. The ^{12}C peak (dashed green line) on the right of the spectra is observed to dominate the spectra, with secondary fragments only making noticeable contributions at the distal part of the BP and beyond. From the entrance of the phantom to the pinnacle of the BP, the lineal energy of the ^{12}C peak increases from $\sim$10 to $\sim$100

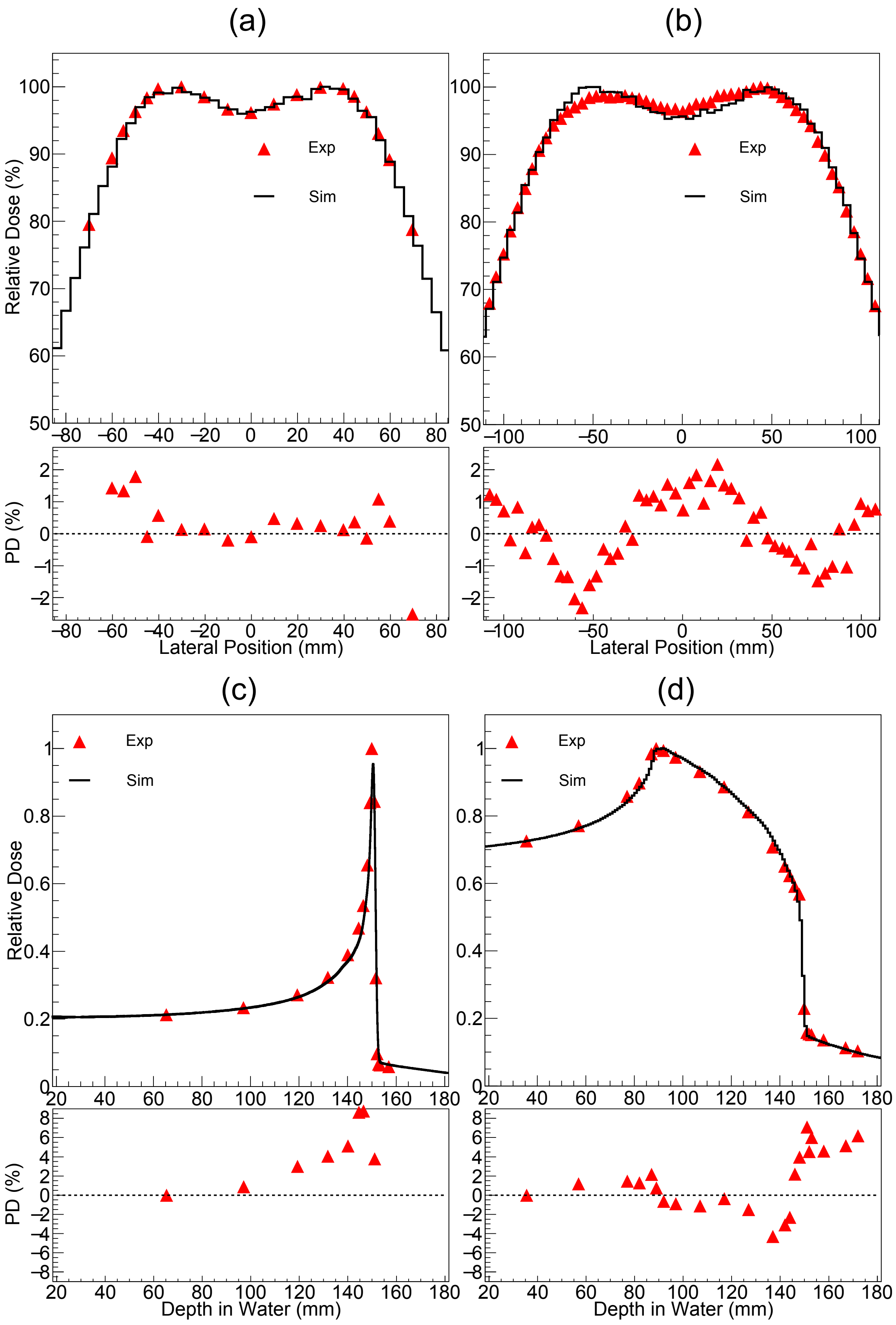

Figure 6.8: Comparison between the relative dose calculated by means of the simulation and experiment with the percentage difference (PD) plotted on the bottom. Plots (a) and (b) show the lateral dose at the surface of the phantom for a mono-energetic (a) and 6 cm SOBP (b) 290 MeV/u ^{12}C beam. Plots (c) and (d) compare the depth dose distribution for the mono-energetic (c) and SOBP (d) beams.

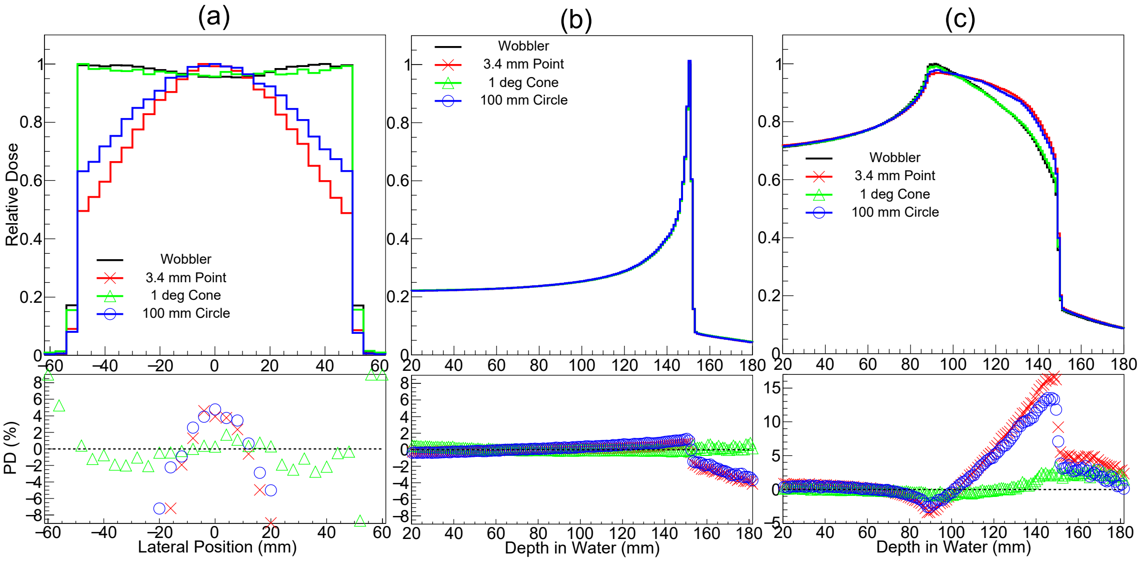

Figure 6.9: Comparison of the lateral dose for a mono-energetic beam (a) and the depth dose of a mono-energetic (b) and a SOBP (c) when using different methods to model the effect of the wobbler on the beam shape. The percentage difference (PD) is calculated with respect to the dose distributions using the wobbler simulation.

keV/μm with a stopper peak (see section 1.5.2) being seen at the far right of the spectrum with a lineal energy of ~700 keV/μm. At the end of an ion's range, its LET increases rapidly, meaning that a small change in depth of a few 100 microns can drastically change the value of y_D. This rapid change in LET, together with the sharp dose gradients at the end of an ion's range, mean that with the current estimated positional uncertainty in the water phantom of ~1 mm, that at the distal edge the agreement between experiment and simulation can be seen to increase.

After the the incident beam has stopped, the microdosimetric spectrum is significantly different as it is produced by the secondary mixed radiation field only. The lineal energy peak of the microdosimetric spectrum 6 mm from the pinnacle of the BP (155 mm) can be seen to align reasonably well when comparing simulation results and experimental measurements, with the peak being mostly from boron fragments. However, at the lower lineal energies the simulation is seen to have an excessive proportion of lighter fragments compared to larger fragments, with ^{4}He being very dominant in the simulation.

The calculated values of y_D and RBE$_{10}$, using the MKM, are shown in figure 6.11, with y_D values on the top and RBE$_{10}$ values on the bottom. The left plots show the entire range of measured values while the right plots show an enlarged view of the BP region. For reference the energy deposition along the phantom is plotted in red.

Comparing the y_D values of experiment and simulation, excellent agreement is observed for both the values and the shape, particularly at the BP. Upstream of the BP region, the y_D is seen to be fairly constant with a value of ~20 keV/μm reaching a maximum of 250 keV/μm (simulation) to 300 keV/μm (experiment). It can be seen that for a few depths upstream of the BP, particularly at 18.91 mm, that the error bars of the simu-

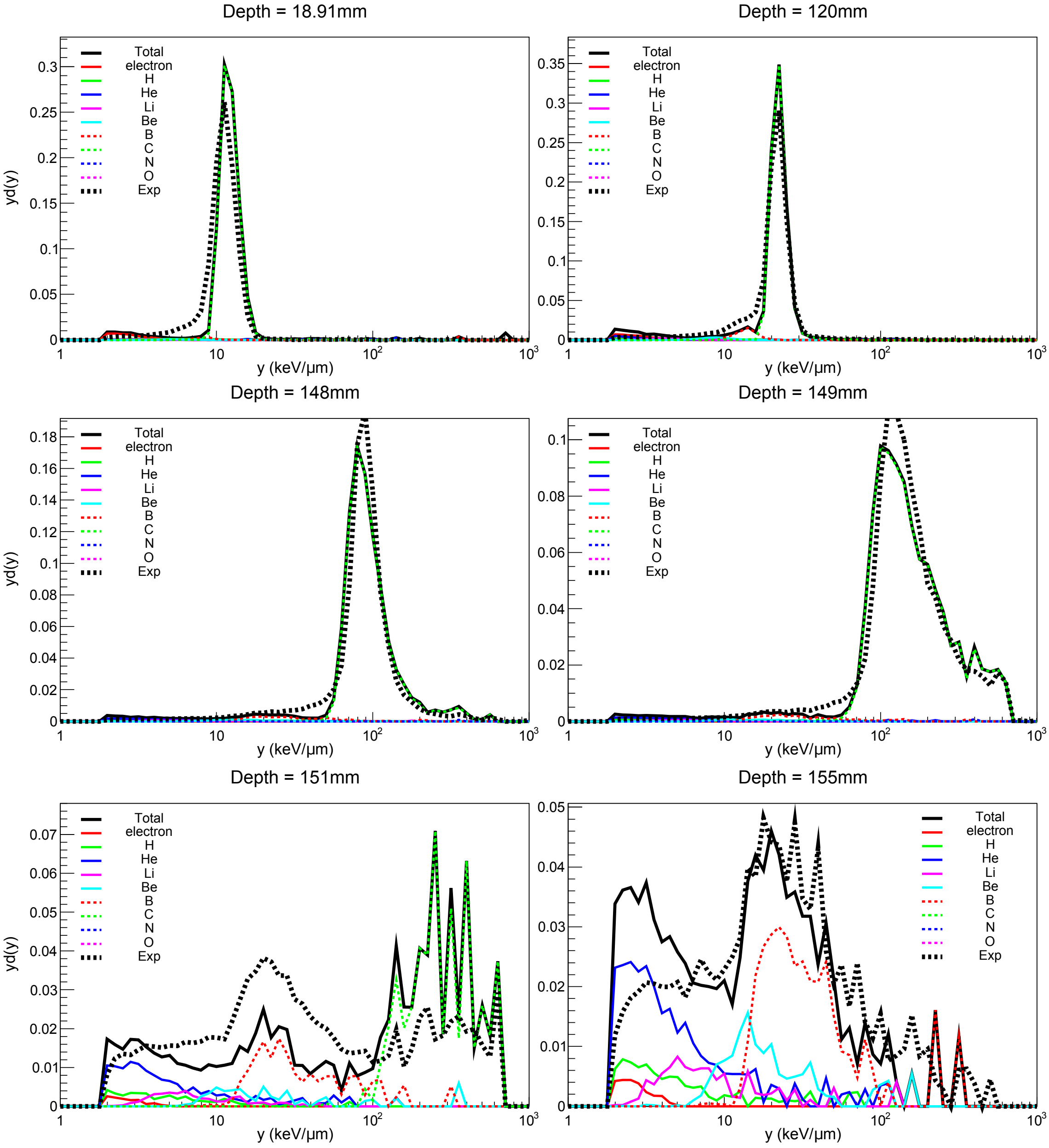

Figure 6.10: Comparison of the results of the Geant4 simulation (continuous line) and the experimental measurements (dashed line). The microdosimetric spectra are obtained for a mono-energetic 290 MeV/u ^{12}C ion beam at various depths, with the pinnacle of the BP occurring at approximately 149 mm.

lation are quite large compared to other depths. This large error bar occurs due to a few high LET particles depositing energy in the SV such as the 700 keV/μm event, which can be seen in the earlier microdosimetric spectrum (figure 6.10). Excluding depths before the BP with large error bars, the difference between simulation and experiment is $\sim$10%. At the BP region and its pinnacle, the agreement for y_D is within $\sim$5%, however at the distal edge of the BP and beyond the agreement decreases. Downstream of the BP the simulation is consistently lower than the experiment. Which as discussed with the microdosimetric spectra in figure 6.10, the simulation saw an overproduction of lighter fragments (mostly likely He fragments) with respect to heavier fragments.

For RBE$_{10}$ values the agreement is slightly better than the y_D results, with the difference being $\sim$2% before the distal part of the BP. The RBE$_{10}$ has noticeably less fluctuations than y_D due to y_D's y^2 proportionality causing rare high y events to cause a larger skew which the MKM reduces the effect of high lineal energy events over 150 keV/μm. At the entrance of the phantom the RBE$_{10}$ is $\sim$1.17 and reaches a maximum at the pinnacle of the BP with a value of $\sim$2.9.

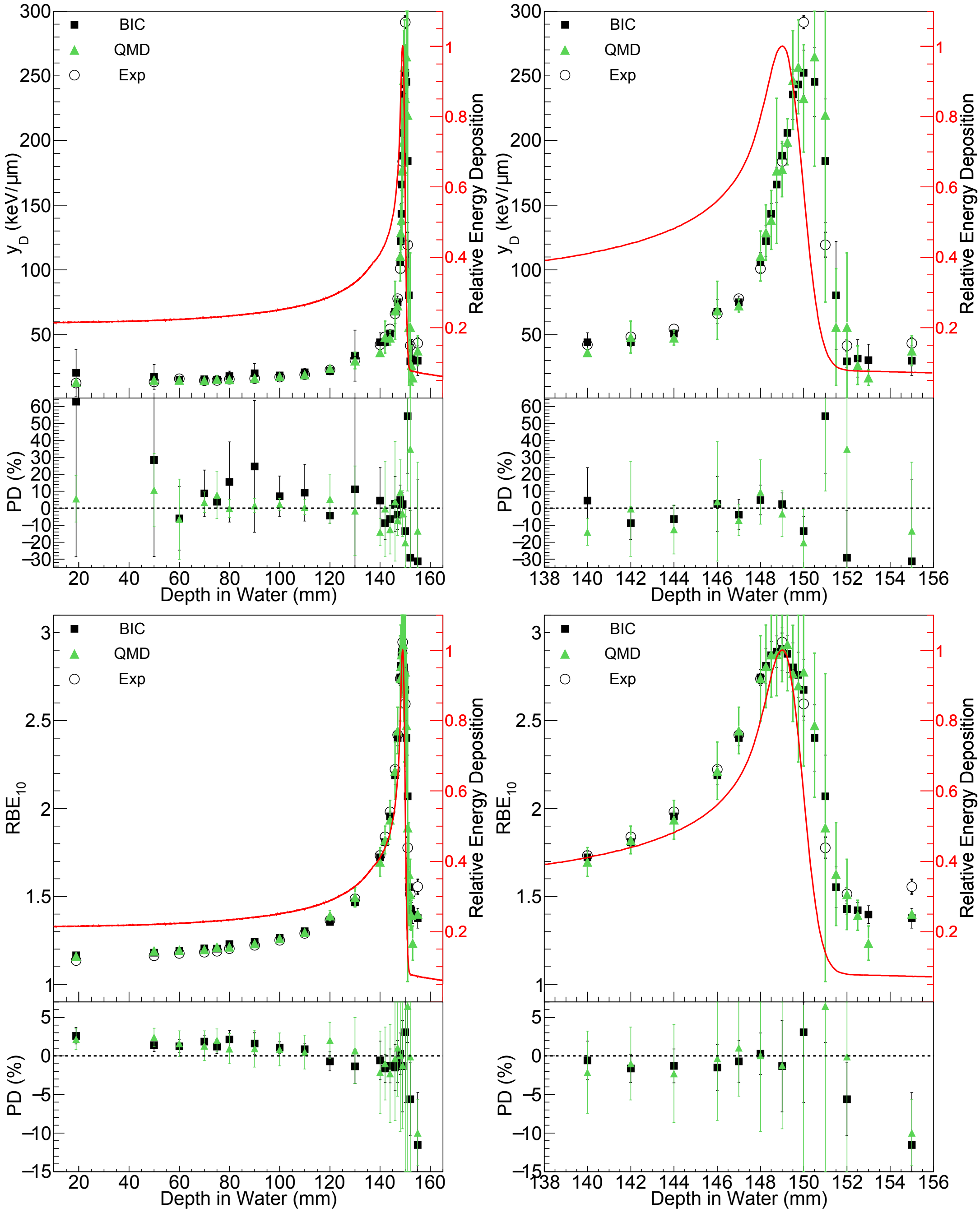

Figure 6.11: Calculated y_D (top) and RBE$_{10}$ (bottom) values in the 290 MeV/u ^{12}C ion beam using the spectra from the Mushroom microdosimeter of both the experiment and simulation. The right plot shows a zoomed in view of the BP region of the left plot.

6.3.3 Mono-energetic 180 MeV/u ^{14}N beam

A selection of microdosimetric spectra at different depths in the water phantom (upstream and downstream of the BP), when irradiated with a mono-energetic 180 MeV/u ^{14}N beam is shown in figures 6.12 and 6.13, respectively. The stopper peak can be seen to occur at a higher lineal energy of $\sim$900 keV/μm compared to $\sim$700 keV/μm seen for the ^{12}C ion beam. For the downstream depths , better agreement is observed between simulation and experiment compared to what was seen with ^{12}C . This can be attributed to the smaller range of the ^{14}N beam, which is 100 mm less than the ^{12}C beam, leading to a reduced fragment build up and causing heavier fragments, such as boron, to have a much shorter range after the BP. The fragment energy peaks of the simulation and experiment again align well with one another and beyond 55 mm ^{4}He is the dominant fragment for both simulation and experiment.

A comparison between the experiment and simulated y_D and RBE$_{10}$ are shown in figure 6.14, respectively. Good agreement is again seen between experiment and simulation, with downstream of the BP having much better agreement compared to ^{12}C due to the reduced contribution from larger fragments. The agreement between experiment and simulation is similar to ^{12}C , with agreement being $\sim$10% for y_D before the distal BP and $\sim$2% for RBE$_{10}$. The y_D is seen to have a value of $\sim$28 keV/μm at the entrance of the phantom and reaches a value of $\sim$400 keV/μm at the distal edge of the BP at $\sim$50.5 mm. The RBE$_{10}$, the entrance has a value of $\sim$1.5 at the entrance of the phantom and reaches a maximum of $\sim$3.1 just before the pinnacle of the BP. The RBE$_{10}$ is seen to peak before the BP compared to the ^{12}C ion beam which peaks at the BP itself due to the higher LET of the ^{14}N beam causing over-killing effects (see section 1.6) to occur earlier along the Bragg curve.

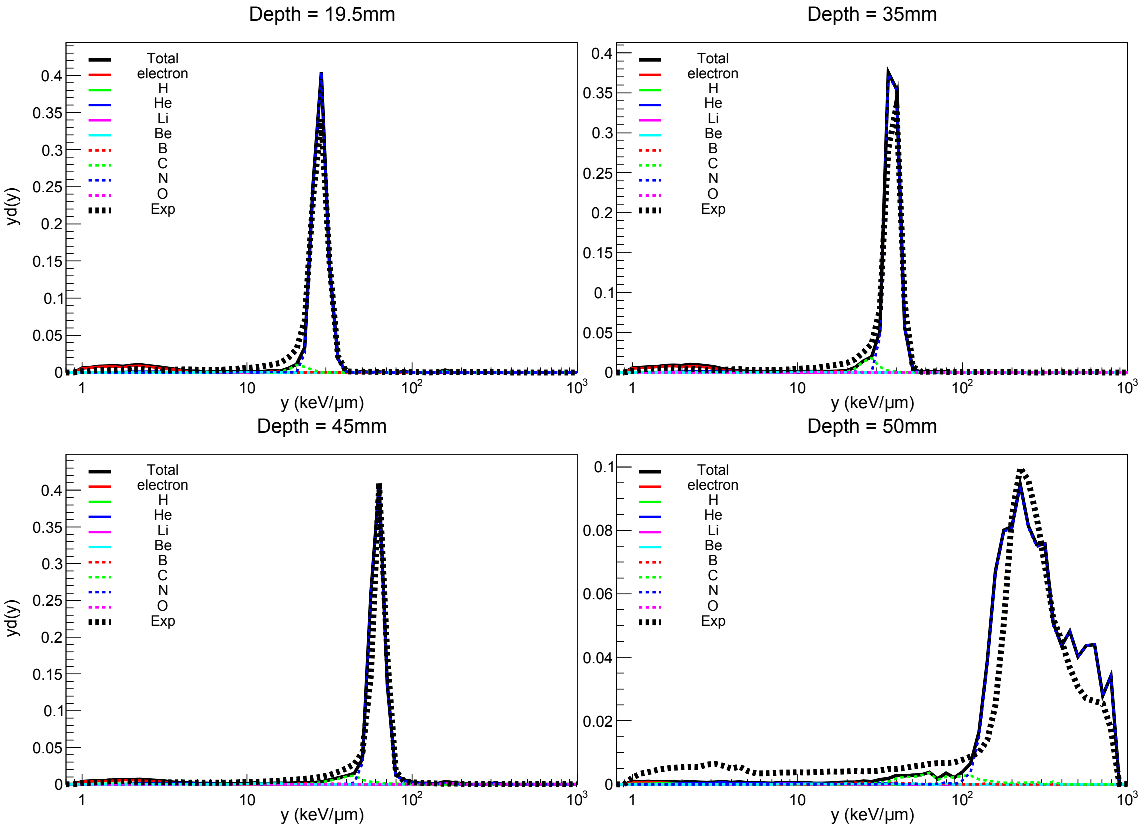

Figure 6.12: Comparison between the microdosimetric spectra of the simulated Mushroom detector and the experimental device when irradiated with a mono-energetic 180 MeV/u ^{14}N beam at various depths in the phantom, in positions before the BP.

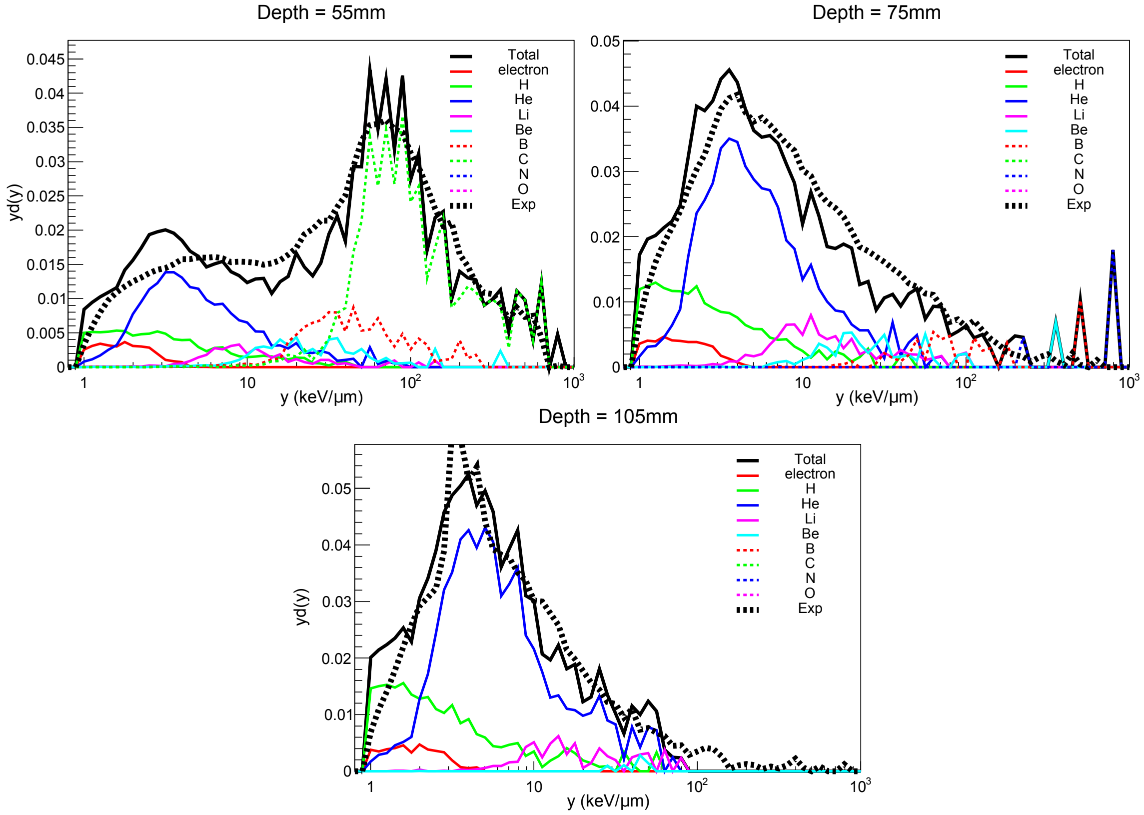

Figure 6.13: Comparison between the microdosimetric spectra of the simulated Mushroom detector and the experimental device when irradiated with a mono-energetic 180 MeV/u ^{14}N beam at various depths (indicated on top of the figures) downstream of the BP (which occurs at 49.5 mm).

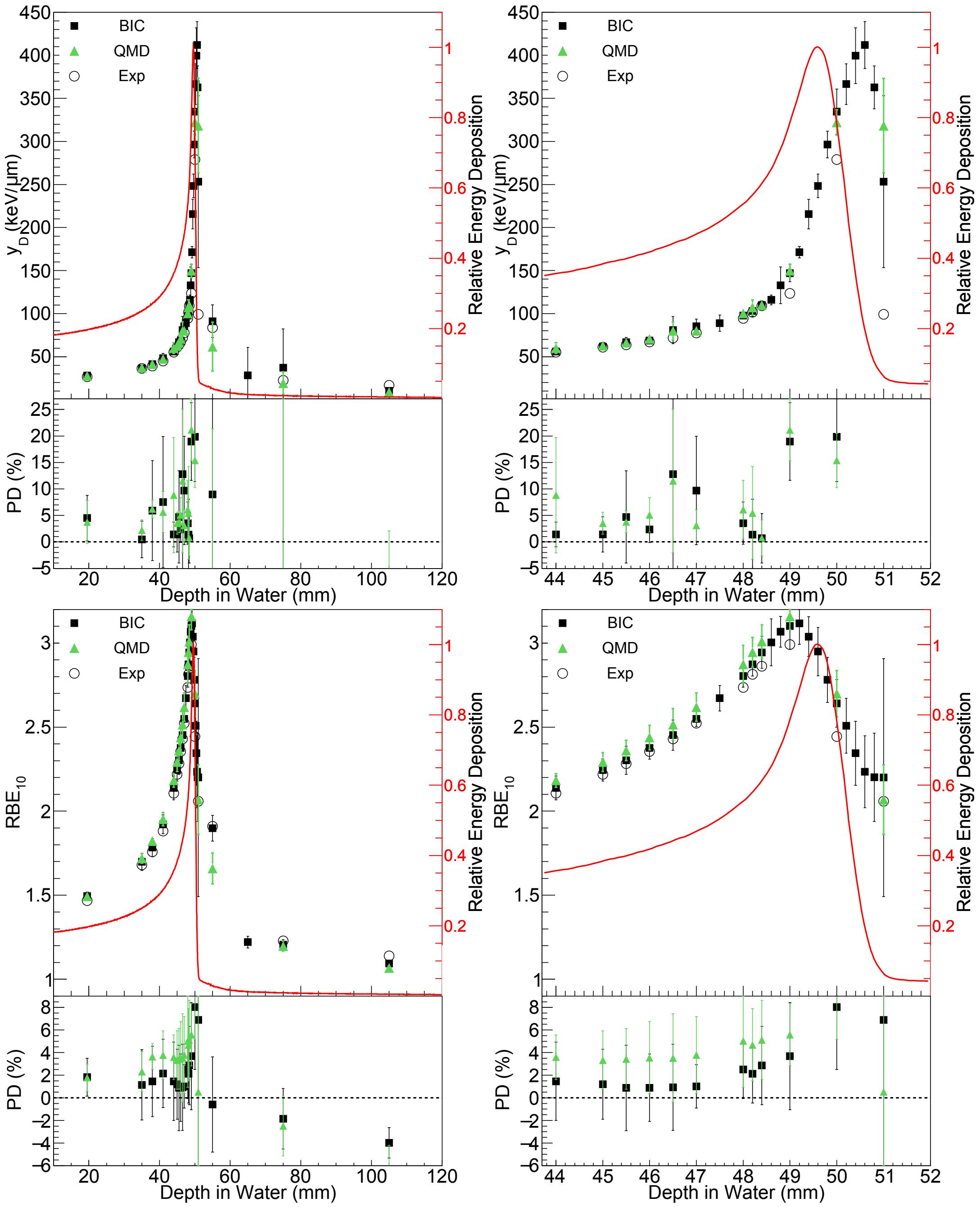

Figure 6.14: y_D (top) and RBE$_{10}$ (bottom) values values in the 180 MeV/u ^{14}N beam using the spectra from the Mushroom microdosimeter of both the experiment and simulation. The right plot shows a zoomed in view of the BP region of the left plot.

6.3.4 Mono-energetic 400 MeV/u ^{16}O beam

The microdosimetric spectra in the case of a mono-energetic ^{16}O ion beam for various depths in the phantom, up and downstream of the BP are shown in figures 6.15 and 6.16, respectively. It should be re-iterated here that the ^{16}O beam had a 100 mm WET (corresponding to 86 mm of PMMA) placed approximately 30 cm before the phantom to shift the location of the BP in the water phantom. Despite the use of the range shifter the depths quoted here are with respect to the detector's position inside the water phantom. Comparing the microdosimetric spectra upstream of the BP, experiment and simulation agree well in terms of position and shape of the incident ^{16}O ion beam, with the stopper peak increasing to a higher lineal energy of $\sim$1000 keV/μm. Due to the larger range of the ^{16}O beam, the downstream spectra present a more similar trend to the ^{12}C beam than the ^{14}N beam, with a more noticeable over contribution of lighter fragments (with He fragments again being the most represented in the simulation). This observed trend of more lighter fragments present in the simulation than experiment agrees with the fragment study shown in chapter 2. In the earlier chapter, it was seen that larger fragments gave less agreement than lighter ones, in terms of the angular distribution. Larger fragments showed a broader distribution than experimental measurements, which would cause an over presence from lighter fragments in the center of the beam as seen in the downstream microdosimetric spectra.

The y_D and RBE$_{10}$ values along the depth of the phantom are shown in figure 6.17. As with the previous beams y_D gives an agreement of $\sim$10% and RBE$_{10}$ $\sim$2%, both before the distal edge of the BP, after the BP the discrepancy becomes larger due to the fragmentation model accuracy. The y_D has a value of $\sim$22 keV/μm at the entrance of the phantom and increases to a value of $\sim$320 keV/μm just at the start of the distal edge of the BP at $\sim$93 mm. The RBE$_{10}$, has a value of 1.35 at the entrance of the water phantom and reaches a maximum of 2.9 just before the pinnacle of the BP due to over-killing. The values of y_D and surface RBE$_{10}$ values of ^{16}O ions are slightly lower than ^{14}N ions. This is due to the much smaller range of ^{14}N causing less straggling to occur as well as a smaller contribution from fragments due to a reduced fragment build up curve.

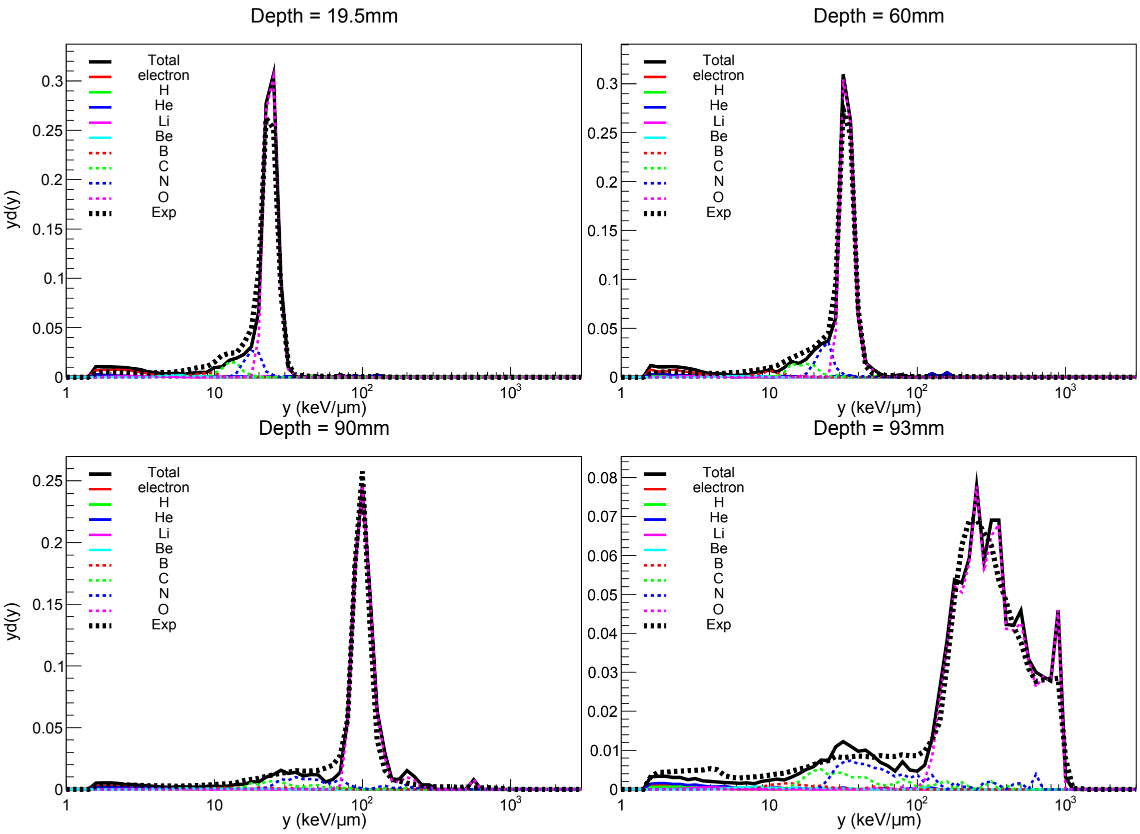

Figure 6.15: Comparison between the microdosimetric spectra of the simulated Mushroom detector and the experimental device when irradiated in a mono-energetic 180 MeV/u ^{14}N beam at various depths within the primary beam range.

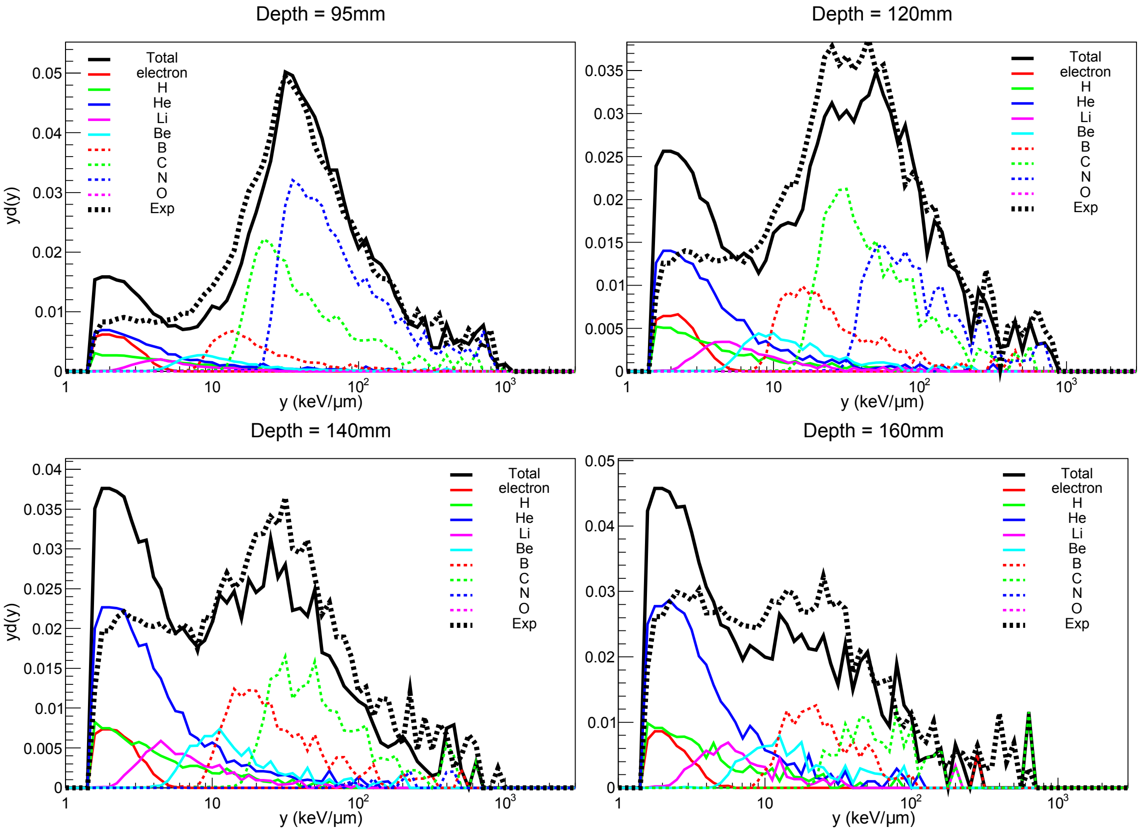

Figure 6.16: Comparison between the microdosimetric spectra of the simulated Mushroom detector and the experimental device when irradiated in a mono-energetic 180 MeV/u ^{14}N beam at various depths downstream of the BP.

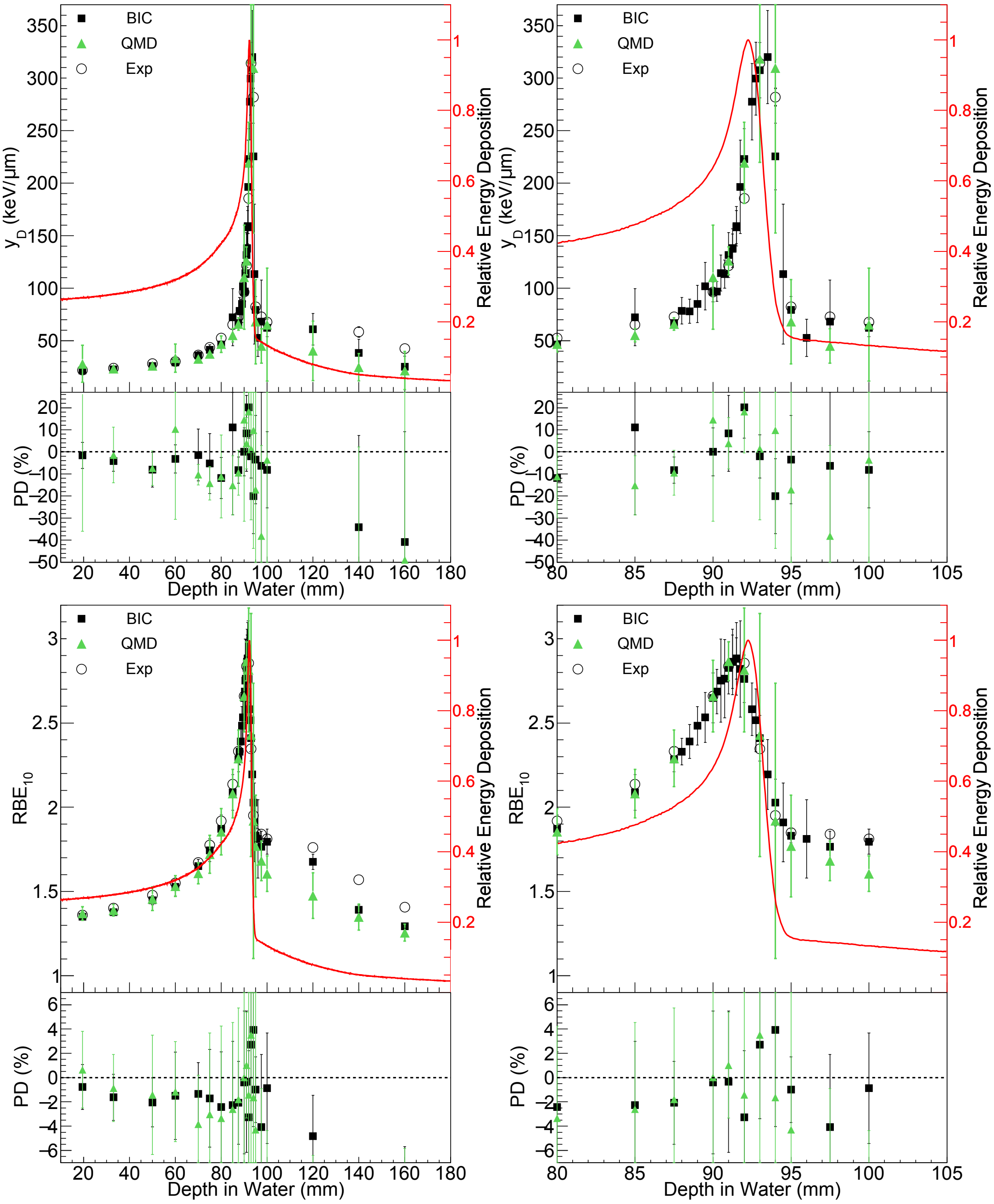

Figure 6.17: Calculated y_D (top) and RBE_{10} (bottom) values in the 400 MeV/u ^{16}O beam using the spectra from the Mushroom microdosimeter of both the experiment and simulation. The right plot shows a zoomed in view of the BP region of the left plot.

6.3.5 Mono-energetic 150 MeV/u ^{4}He and 400 MeV/u ^{20}Ne beam

The y_D profiles at the BP region are shown in figure 6.18 for both incident ^{4}He (left) and ^{20}Ne (right) beams. The RBE$_{10}$ profiles for the two beams are shown in figure 6.19.

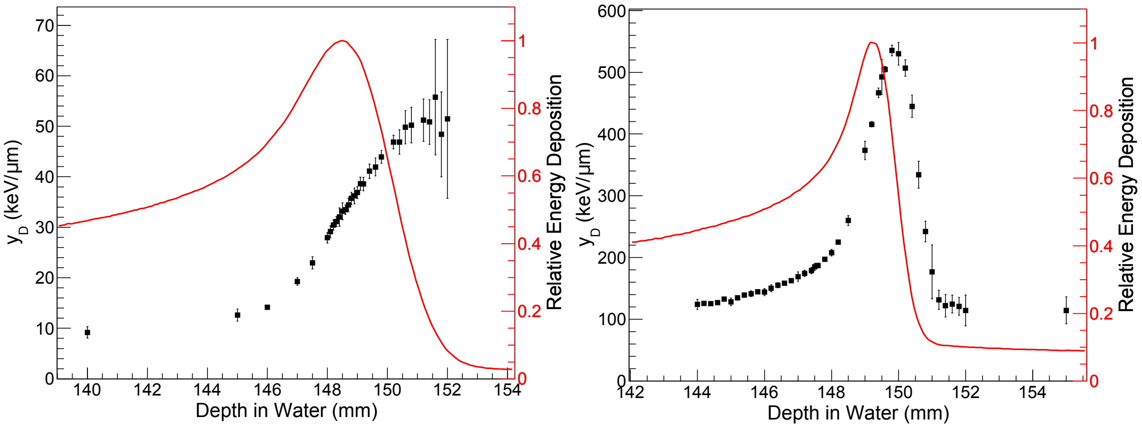

Figure 6.18: Calculated y_D values for a 150 MeV/u ^{4}He beam (left) and a 400 MeV/u ^{20}Ne beam (right) at the BP.

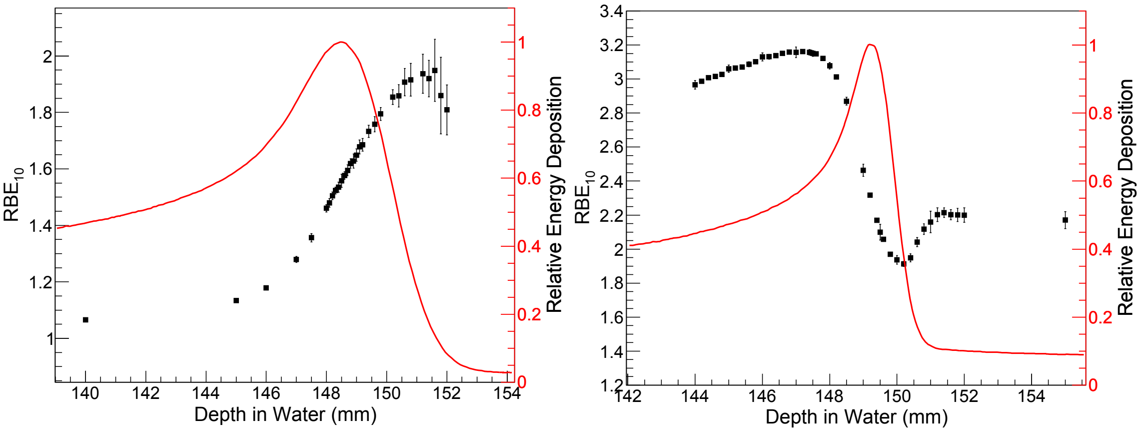

Figure 6.19: Calculated RBE$_{10}$ values for a 150 MeV/u ^{4}He beam (left) and a 400 MeV/u ^{20}Ne beam (right) at the BP.

The RBE$_{10}$ profile of the ^{20}Ne beam shows the most drastic difference in terms of the shape compared to the other beams, with a pronounced minimum of 1.9 at a depth of $\sim$150 mm, which coincides with the maximum of the y_D value of 500 keV/μm. Once y_D begins to reduce due to the greater impact from secondary fragments the RBE reaches a secondary peak at $\sim$151.5 mm with a value of 2.2 before reducing again due to the larger fragments stopping.

In contrast to the other beams, especially ^{20}Ne , the lower LET of the ^{4}He beam causes very little impact in terms of over-killing. The RBE$_{10}$ peaks at the very distal edge of the BP at $\sim$152 mm with a value of $\sim$1.9 which also coincides with the maximum y_D of $\sim$56 keV/μm, compared to the over-killing value used in the MKM of 150 keVμm. The difference in the RBE_{10} of the beams is largely due to the different track structures of the different particles which was illustrated and discussed previously in figure 1.12.

6.3.6 SOBP ^{12}C beam

Figure 6.20 shows microdosimetric spectra at various depths along the ^{12}C SOBP from both the experiment and the simulation. The ridge filter used is designed to produce a SOBP which delivers a uniform biological dose 60 mm in size in water, which starts and ends at approximately 90 and 150 mm, respectively. The simulation and experiment again match one another fairly well in terms of the response due to the incident ^{12}C ion beam. The spectra before the start of the SOBP treatment field at $\sim$90 mm are fairly similar to the mono-energetic ^{12}C beam, with the width of the ^{12}C peak being slightly broader due to the mix of many energies. Close to 90 mm the spectrum differs noticeably compared to the mono-energetic ^{12}C beam, with a prominent high energy tail becoming present. This tail, which includes stoppers, occurs due to the lower energy components of the beam having a rapidly increasing LET at the end of their range.

Comparison between the experimental and simulation values of y_D and RBE_{10} are shown in figures 6.21 and 6.22, respectively. It can be seen, like the mono-energetic beams, that the y_D and RBE_{10} have a similar shape as one another except at the end of the primary beam's range where over-killing effects occur. The RBE_{10} at the entrance can be seen to be slightly higher than the mono-energetic ^{12}C beam, due to the presence of lower energy ^{12}C ions. Conversely, at the end of the primary beam's range the maximum RBE_{10} is around 10% lower due to the greater contribution of fragments. The agreement between simulation and experiment is similar to what was found for the mono-energetic beams, with the agreement being within $\sim$2% up until the distal edge, where the positioning accuracy becomes very important and downstream where the fragments generated by the simulation have a discrepancy with experiment.

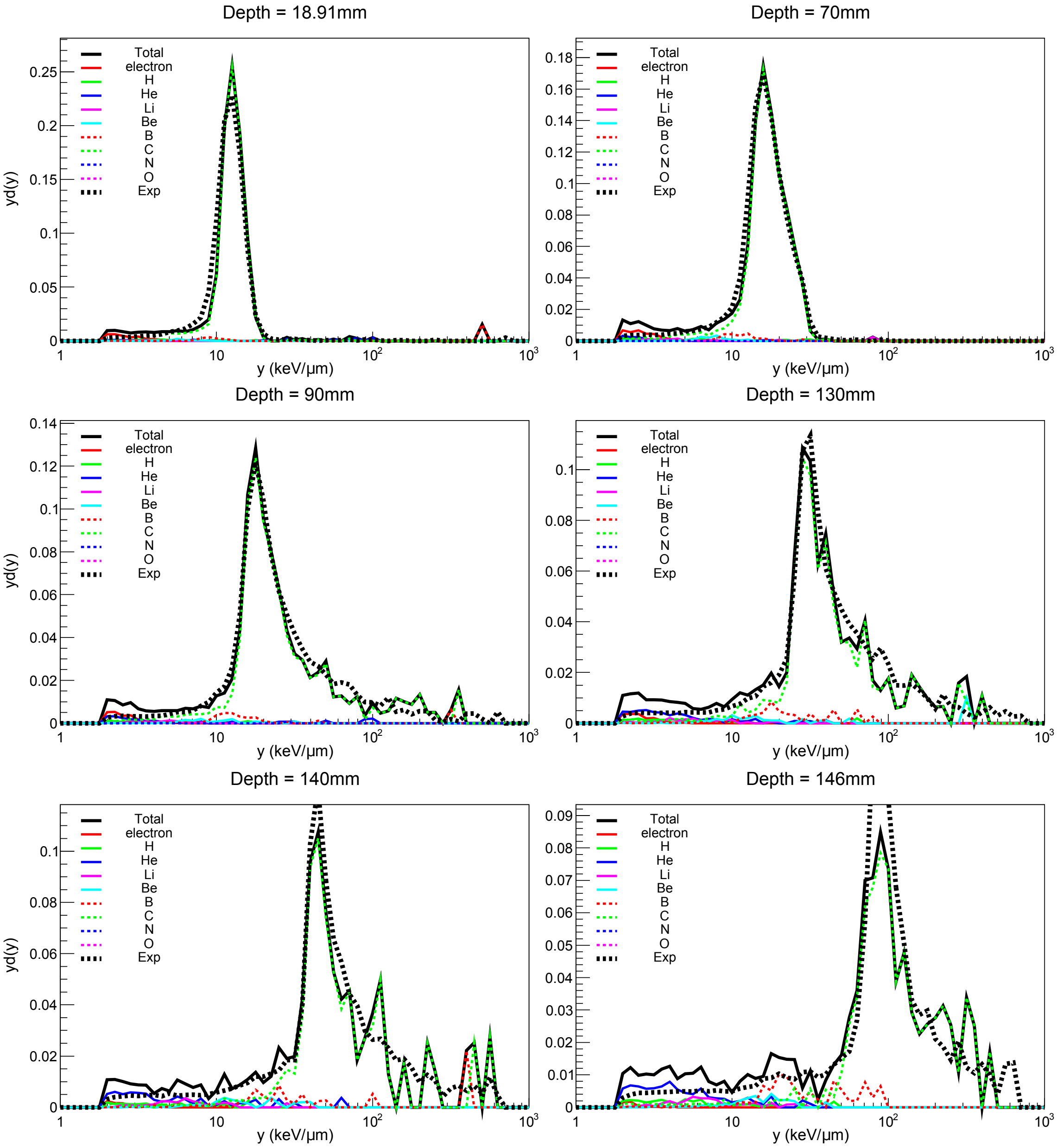

Figure 6.20: Comparison between the microdosimetric spectra of the simulated Mushroom detector and the experimental device when irradiated in a 290 MeV/u ^{12}C SOBP beam at various depths, with the start of the treatment field being $\sim$90 mm and the end being $\sim$150 mm.

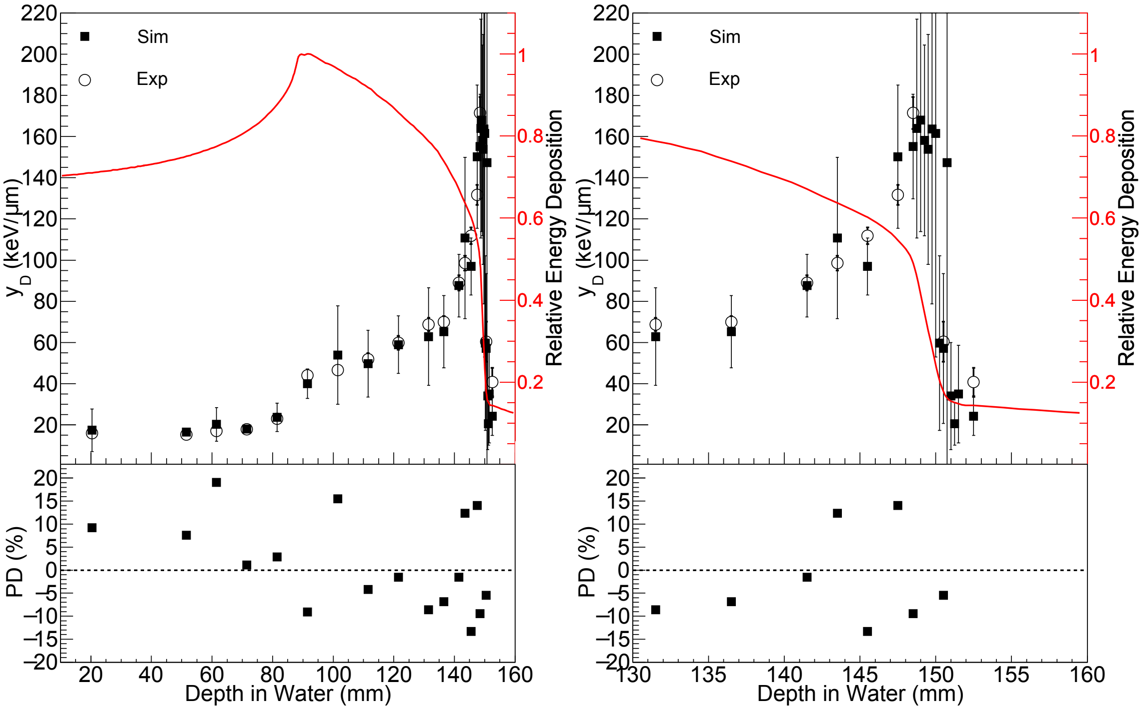

Figure 6.21: Calculated y_D values of experiment and simulation when irradiating the Mushroom microdosimeter in a 290 MeV/u ^{12}C SOBP beam.

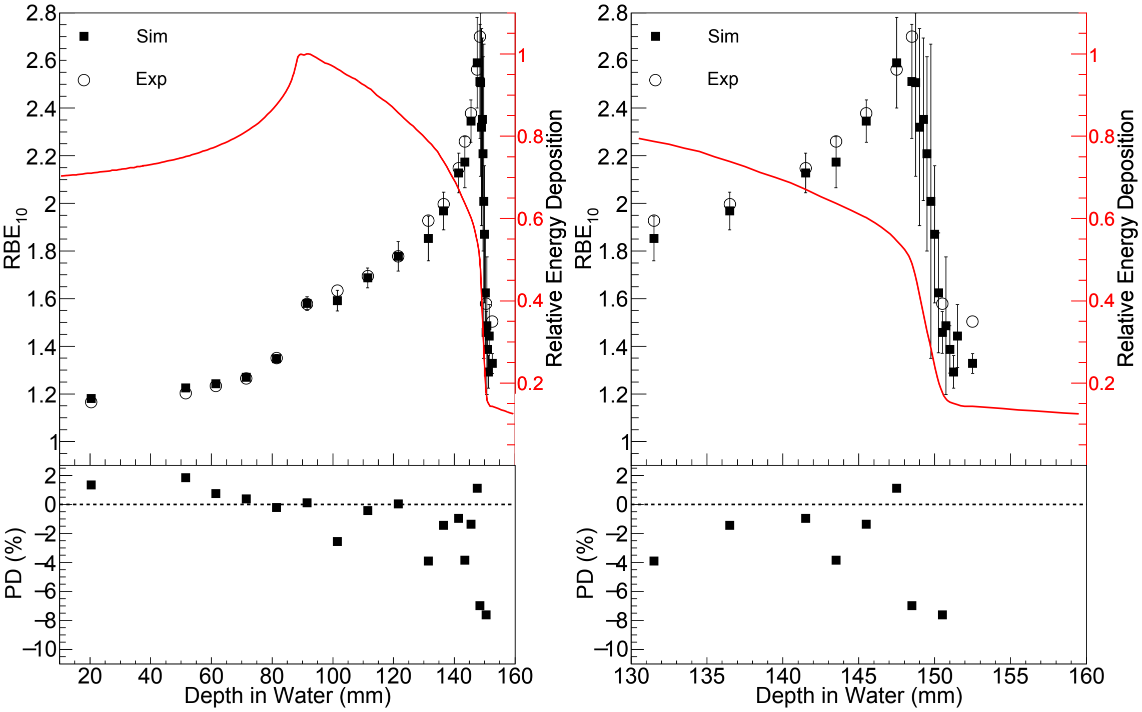

Figure 6.22: Calculated RBE_{10} values of experiment and simulation when irradiating the Mushroom microdosimeter in a 290 MeV/u ^{12}C SOBP beam.

6.4 Discussion

6.4.1 Effect of charge collection on measurements

When comparing the microdosimetric spectra of the simulation and the experiment there is reasonable agreement for both the primary ^{12}C peak and the fragment distribution. However, the experiment shape of the $yd(y)$ spectra have a more pronounced low energy tail left of the primary ^{12}C peak compared to the simulation. This tail is likely not due to the underproduction of boron fragments, which can be seen to coincide with the most prevalent part of the tail, but instead be due to the charge collection uniformity of the device.

In order to take this charge collection effect into account and to see its impact, the charge collection distribution was applied when processing the simulation data. To apply this distribution the experiment energy deposition spectrum was first scaled by 1.087 to shift the peak to align it with the simulation, which corresponds to a charge collection efficiency of $\sim$92%. Once the experiment spectrum is shifted the simulation peak is subtracted from the shifted spectrum and results in the blue spectrum shown in the left plot of figure 6.6. The ratio of the subtracted counts to the total experiment counts was found to be 0.67, or 33% of events (before setting a threshold) are due to events in the actual "SV". In the simulation, each track which deposits energy in the SV is stored as a single hit (list mode) which can be post-processed after the simulation has run. The charge collection distribution was taken into account by the simulation when processing each recorded hit to have a 33% chance that 100% of its energy deposited is added as a hit to the spectrum. The remaining 67% of events have their energy deposition randomly scaled using the subtracted spectrum as a probability distribution.

The impact of applying this charge collection distribution to the simulation is compared in figure 6.23, using the first four depths shown in figure 6.10. The plots show the experiment and total simulation with no charge collection applied (Sim No CCE), in addition, the total $yd(y)$ of the simulation when applying the distribution (Sim CCE Total) as well as just the ^{12}C component (Sim CCE C). It can be seen that the energy deposition of the primary beam changes slightly, with it having a more prominent low energy ^{12}C tail formed. Downstream depths are not shown but the impact of applying the charge collection distribution to these depths have an even less significant impact, due to the fragments having a broad energy distribution. The overall impact of applying the charge collection distribution to the simulation has very little effect on the calculated y_D and RBE$_{10}$. The small impact on the microdosimetric spectrum and values demonstrates the favourable characteristics of the detector and for this reason no distribution has been applied to the simulation data.

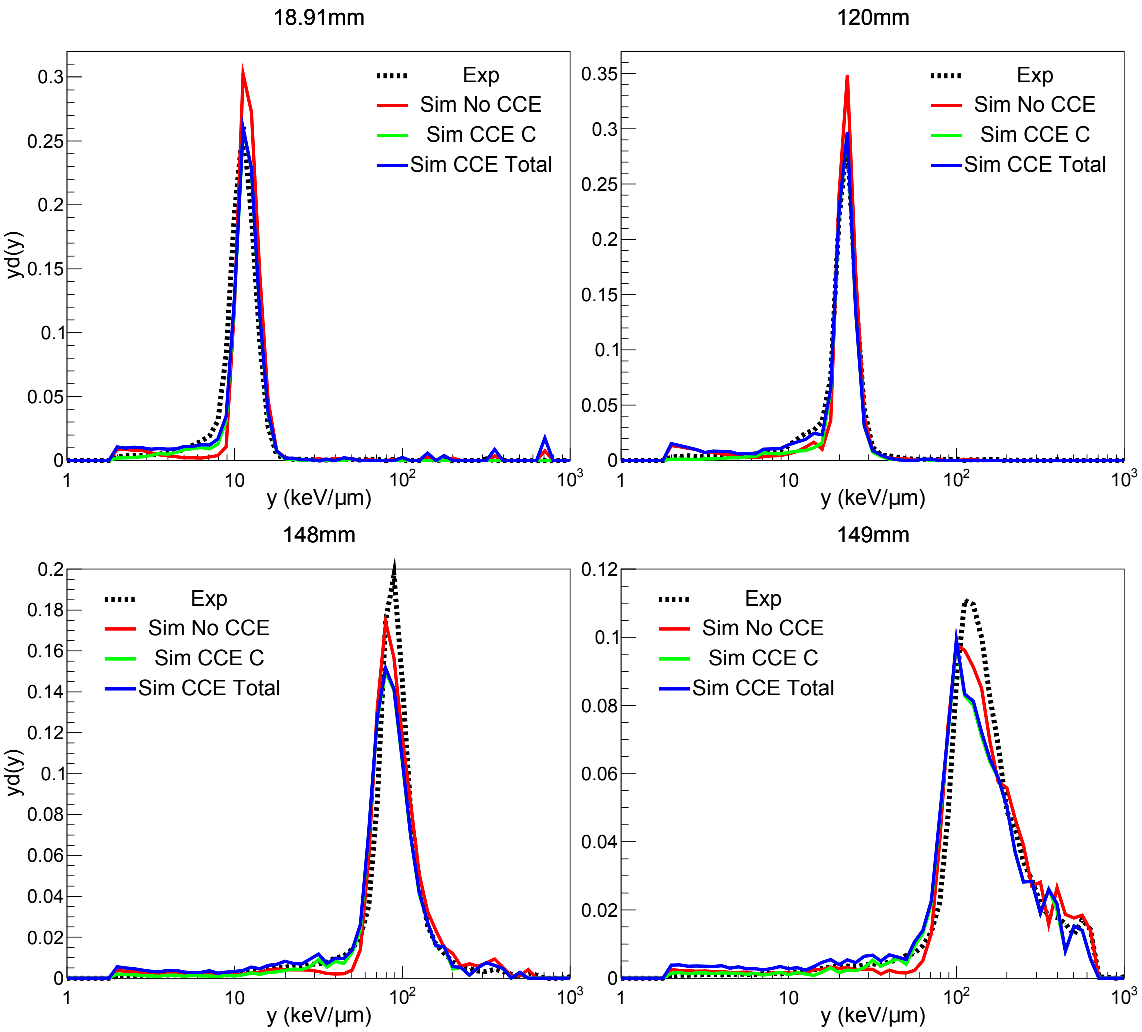

Figure 6.23: Comparison of the microdosimetric spectra between the experiment and the simulation, with the simulation being shown with (Sim CCE) and without applying the charge collection efficiency distribution (Sim No CCE). The "Sim CCE C" plot shows the carbon component of the spectra after applying the charge collection distribution.

6.4.2 Summary of beam characteristics

A summary of the quantities of interest for the five simulated beams are shown in table 6.3.

Beam	BP position (mm)	Entrance y_D	Maximum y_D (keV/μm)	Entrance RBE$_{10}$	Maximum RBE$_{10}$	RBE$_{10}$ position before BP (mm)
150 MeV/u ^{4}He	152.2	6	56	0.97	1.95	-2.6 $\pm$ 0.1
288.6 MeV/u ^{12}C	149	22	300	1.17	2.91	0.0 $\pm$ 0.1
180 MeV/u ^{14}N	49	28	411	1.50	3.12	0.6 $\pm$ 0.1
400 MeV/u ^{16}O	91.5 (191.5)	22	320	1.35	2.88	0.8 $\pm$ 0.1
400 MeV/u ^{20}Ne	147.2	34	545	1.63	3.16	2.0 $\pm$ 0.1

Table 6.3: Summary of the difference between the pinnacle BP position and the maximum RBE$_{10}$ position for different beams. Note that in the second column (BP position) the value of 91.5 mm for 400 MeV/u ^{16}O refers to the depth in the phantom while the 191.5 mm adds 100 mm WET of PMMA used to shift the position.

The third column from the left summarises the value of y_D at the entrance ($\sim$20 mm) and the maximum observed value, which corresponds to the distal edge of the BP for all cases. The values of y_D for ^{14}N are seen to be higher compared to and ^{16}O . This can be attributed to the range of ^{14}N being much shorter than the other beams, which results in a smaller contribution from fragments at the end of the range of the primary beam and more of the primary beam with a higher lineal energy. Additionally, due to the smaller range of the ^{14}N beam results in less straggling of the primary beam results in a sharper distribution of primary ions at the end of the range. The ^{4}He beam has an entrance y_D $\sim$4-6 times smaller than the other beams while its maximum is $\sim$6-10 times smaller. This shows the importance of accurate planning for heavier ion beams due to a slight shift in the range having significant effect.

The fourth column presents the entrance RBE$_{10}$ value as calculated by the modified MKM and the maximum whose position varies for all the beams, with its position relative to the pinnacle BP given in the final column on the right. A pronounced offset between the RBE$_{10}$ and physical dose, such as with ^{20}Ne , has the effect of creating a broader biological dose at the BP compared to ^{12}C . ^{12}C has the pinnacle of dose and RBE$_{10}$ aligned resulting in a sharper biological dose profile for a mono-energetic beam.

6.4.3 Comparison of the BIC and QMD models

As the incident primary ion traverses the target it will be attenuated based on its total reaction cross-section. As the primary ion beam attenuates it will produce different fragments based on the charge and mass changing cross-sections of the ion. The total reaction cross section of different projectiles and targets are generally well described in Geant4 and agree well with experimental measurements. The production cross sections of fragments are much more complex to describe due to not only needing to describe their production but also their angular and energy distributions. The ability of Geant4 to describe experimental measurements of the attenuation of a beam versus the production of fragments can be seen online (`https://geant-val.cern.ch/`), in particular the Charge Changing Cross-Section test (CCCStest), which compares the total and charge changing cross-sections in Geant4 for a ^{12}C ion beam. Additionally, the Hadron Data test (TestHD) compares the total reaction cross-section for various projectiles/targets and energies.

Due to the higher lineal energy of the incident primary beam compared to secondary fragments and its attenuation being fairly well described, the agreement between experiment and simulation is fairly consistent for all beams before the BP, with an agreement between $\sim$10% for y_D and $\sim$2% for RBE$_{10}$. For RBE$_{10}$ values the agreement is slightly better than the y_D results, with the difference being $\sim$2% before the distal part of the BP. As mentioned earlier, the RBE$_{10}$ has noticeably less fluctuations than y_D due to y_D's y^2 proportionality causing infrequent high y events to cause a larger skew which the MKM reduces the effect of high lineal energy events over 150 keV/μm.

The observed agreement upstream reflects the dominance of the primary incident beam on the microdosimeter response, while the agreement downstream of the BP is due to the fragments generated by the model used. The alignment of the peaks of the microdosimetric spectra suggest that the model is adequate at generating the energy distribution of fragments. Downstream of the BP for the ^{12}C and ^{16}O ion beams, which have a significantly larger range than ^{14}N which causes a greater fragment build-up as mentioned earlier, it was observed that there were more lighter fragments present in the simulation than experiment. This trend mimics the fragment study of chapter 2. The fragment study showed that, in general, larger fragments gave less agreement than lighter ones, in terms of the angular distribution. Larger fragments showed a broader distribution than experimental measurements, which would cause an over presence from lighter fragments in the center of the beam as seen in the downstream microdosimetric spectra. This effect is seen the most in this current work for the ^{16}O ion beam, where the agreement reduces the further downstream of the BP from 140 mm to 160 mm, where the effect of the angular distributions of fragments is amplified.

Due to the dominance of the primary beam, the results do not differ significantly between BIC and QMD upstream of the BP, both in terms of the microdosimetric spectra and the y_D and RBE$_{10}$ quantities. Figure 6.24 show the microdosimetric spectra of the BIC and QMD models for each beam 5 mm downstream of the BP, with each particle's components being shown for QMD. Downstream of the BP, QMD shows a greater contribution from lighter ions and BIC having a greater contribution of fragments with a charge of 1 less than the primary ion (Boron for ^{12}C , Carbon for ^{14}N and Nitrogen for ^{16}O). This observation is consistent with the observed results shown in chapter 3 and results in QMD having slightly smaller values than BIC for y_D and RBE$_{10}$, this is most readily seen for ^{16}O which has the largest primary ion range. The lower values obtained with the QMD models result in larger differences between experiment compared to the BIC model. An important consideration when choosing a model for Monte Carlo simulations is the computational resources required. As reported previously in chapter 3, the runtime of QMD for thick targets was ∼2-8 times longer than the BIC model, for this study the observed increase in runtime for most depths was mostly between 2-3 times longer. Due to this significant increase in runtime for very little difference in results, particularly for positions where the primary ions reach the detector, it can be difficult to justify the use of the QMD model over the BIC model for the configuration studied here.

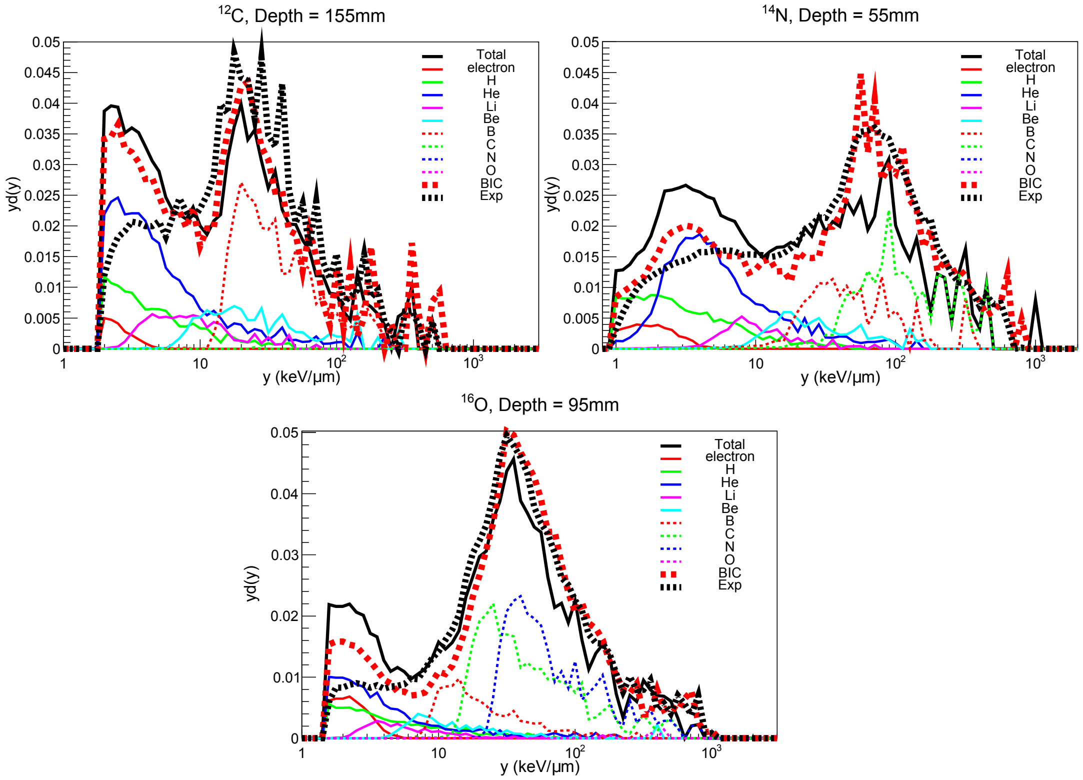

Figure 6.24: Comparison of the microdosimetric spectra between the BIC and QMD models as well as the experiment. For these plots the different particle components are shown for the QMD model.

6.5 Conclusion

Monte Carlo codes are widely used to study the complex mixed HIT radiation field as well as to model the response of novel microdosimeter detectors when irradiated with HIT beams. Therefore it is essential to validate MC codes against experimental measurements. This chapter presented the modelling of the Biological Beamline at HIMAC, NIRS, using Geant4. The beamline was validated against experimental measurements for a mono-energetic and SOBP 290 MeV/u ^{12}C beam. Comparisons with experiment for the lateral beam profile showed good agreement for both mono-energetic and SOBP beams, with differences of ∼0.5% and 2% in the treatment field, respectively. For the depth dose profiles, both beams gave good agreement in the overall shape, however both have a maximum difference with the experiment at the end of the BP where measurements are especially sensitive. In order to simplify the simulation by excluding the wobbler system a number of alternative methods were modelled. It was found that for both lateral and depth dose profiles simulating a cone beam provided very good agreement compared to modelling the full wobbler system.

Using the validated Geant4 model of the Biological beamline, the response of the first generation silicon Mushroom microdosimeter was investigated in five mono-energetic beams, including ^{4}He , ^{12}C , ^{14}N , ^{16}O and ^{20}Ne beams, with all but the ^{4}He and ^{20}Ne beams being compared to experiment. In addition to the mono-energetic beams, a SOBP ^{12}C beam was also investigated and compared to experimental measurements.

The mono-energetic ion beams were compared and the difference of the RBE$_{10}$ (calculated by the modified MKM) peak location due to over-killing was quantified. In the case of the ^{4}He beam irradiation, the RBE$_{10}$ reached a maximum at the very distal part of the BP, 2.6 mm from the pinnacle, due to no real over-killing occuring which is reflected by the maximum y_D of 56 keV/μm versus the over-killing parameter value of 150 keV/μm. ^{12}C was seen to have the physical dose coincide with the RBE$_{10}$ peak. ^{14}N and ^{16}O had a similar shift to one another with the RBE$_{10}$ peaks 0.6 and 0.8 mm before the pinnacle of the BP, respectively, while ^{20}Ne RBE$_{10}$ peaked 2 mm before the BP.

Experimental measurements and simulation results agree reasonably well along the primary ion beam. This demonstrates the suitability of Geant4 for experimental microdosimetry and the favourable characteristics of the device in terms of charge collection efficiency and uniformity of the device. Before the distal edge of the BP the simulation and experiment agreed within $\sim$10% for y_D and $\sim$2% for RBE$_{10}$. Downstream of the BP there was less agreement observed between simulation and experiment, with the simulation having lower values of y_D and RBE$_{10}$ due to the higher representation of lighter fragments compared to heavier fragments. At 70 mm downstream of the BP, the difference for ^{16}O increased to $\sim$40% and $\sim$10% for y_D and RBE$_{10}$, respectively, compared to $\sim$10% and $\sim$2% before the BP, respectively. However, the ^{14}N beam gave fairly good agreement downstream of the BP due to the smaller range of the beam causing lighter fragments to dominate, with the difference at 55 mm downstream of the BP being $\sim$5% for both y_D and RBE$_{10}$. Despite the contribution of fragments not giving the best agreement between experiment and simulation, the lineal energy peaks of the fragment distributions did give good agreement. The trends of fragments seen between simulation and experiment from the Mushroom microdosimeter agree with the results from the earlier chapter, where angular distributions of fragments were compared to experiment and showed larger fragments having broader angular distributions.

Chapter 7

Theoretical evaluation of the “Bridge” SOI microdosimeter for pencil beam scanning in proton therapy

This chapter describes the theoretical characterisation of the “Bridge” SOI microdosimeter, a novel design by the Centre For Medical Radiation Physics, for its use for quality assurance of a scanning pencil proton therapy beam. The design of the microdosimeter is characterised in terms of its path length in the radiation field. Additionally, the sheath which houses the microdosimeter in experiments is examined if it perturbs the radiation field in any significant manner. Simulation results are compared against experimental measurements to use as an insight into the experimental measurements. Experiments were performed by Dr. Linh Tran and Lachlan Chartier at the Massachusetts General Hospital (MGH), to evaluate the performance of the device. Using Geant4, certain experimental methodologies used, namely the choice of the maximum detectable energy deposition, are investigated to understand their impact upon the microdosimetric measurements and quantities.

Work from this chapter has been published in:

“Characterisation of proton pencil beam scanning and passive beam using a high spatial resolution solid state microdosimeter”, *Medical Physics*, (44), 2017

7.1 Introduction

As with all charged particles, as a proton beam traverses a target and loses energy, its linear energy transfer (LET) will increase, changing the amount of energy transferred in a given thickness of material as well as creating denser track structures of electrons towards the end of the path. As with other hadron beams, this increase in LET and track density changes the relative biological effectiveness (RBE) of the beam, as explained in section 1.6. This is evident from experimental measurements which have shown that the RBE can reach a values of ∼1.7 in proton beams at the distal edge of the Bragg peak (BP) [65]. Despite it being known that the RBE can vary significantly at the end of the beam's range, proton therapy treatment plans adopt a constant RBE value of 1.1 [125]. The currently used value of 1.1, is based on the averaging of many in-vitro and in-vivo studies performed in the middle of spread out Bragg peaks (SOBPs) with doses of mostly 6-8 Gy per fraction [126]. Compared to heavy ion therapy, which does not have a significant dose dependence on RBE, proton beams have been shown to have a dependency with dose which is observed for fractions less than ∼4 Gy [72], with the RBE increasing with smaller dose fractions. This dose dependency is relevant since proton therapy treatment plans generally deliver single fractions using the Atomic Energy Agency standard of 2 Gy [73]. The variability in the RBE at the end of the beam's range is particularly important since treatment margins will encompass healthy tissue [127]. When the surrounding organs are sensitive, such as the spinal chord treatment of pediatric cases, the chance of normal tissue complication increases [128].

In recent years there has been growing interest in the variability of the RBE in proton therapy and how to account for it in treatment planning. One popular proposed method to take into account the variability of RBE consists of the adoption of the dose-averaged LET, $\mathrm{LET_D}$ in treatment planning systems [129] [130]. The $\mathrm{LET_D}$ can be calculated in a few slightly different ways [131], though the method which shows good stability in terms of scoring volume size and has been shown to give the best agreement with microdosimetric quantities [132] is shown in equation 7.1.

$$\mathrm{LET_D} = \frac{\sum_{i=1}^{n} \varepsilon_i \times \mathrm{LET}_i}{\sum_{i}^{n} \varepsilon_i} \tag{7.1}$$

Where i is the step number of a particle track traversing a scoring volume and ε_i is the energy deposited in the step, LET_i is the LET of the particle at the start of the step. $\mathrm{LET_D}$ is a theoretical quantity and is calculated using Monte Carlo techniques and cannot be measured experimentally. $\mathrm{LET_D}$ is similar to the microdosimetric quantity the dose mean lineal energy, y_D, however discrepancies exist between the two quantities due to the LET not accounting for delta electron production (see section 1.3.2), but as the range of delta electrons becomes smaller the difference between the two decreases [58].

Optimising treatment plans using the $\mathrm{LET_D}$ instead of physical dose does present advantages in terms of reducing the variability between the delivered plan being closer to an actual biological dose [133]. However $\mathrm{LET_D}$ is a theoretical value and the treatment delivered by the treatment planning system (TPS) still should be verified that it matches with the planned treatment in terms of the LET distribution of the particles and not just the physical dose. To achieve this the LET/lineal energy must be able to be measured experimentally, such measurements can be performed using a microdosimeter. This chapter presents microdosimetric measurements performed in a therapeutic proton beam using the CMRP designed Bridge silicon microdosimeter, SOI devices being particularly well suited to routine quality assurance measurements in proton therapy thanks to their high spatial resolution and ease of use. Experimental measurements taken with the Bridge microdosimeter are compared to simulation results to evaluate the response of the detector. The design of the detector, such as the bridging volumes connecting the sensitive volumes (described below in Materials and Methods), is also studied using the simulation to see if they impact the response significantly compared to an isolated SV design, like the Mushroom in the previous chapter.

7.2 Materials and Methods

This chapter describes the use of the Bridge microdosimeter to characterise a proton pencil beam scanning (PBS) system for infield measurements in a single mono-energetic "spot" beam. Comparisons between a Geant4 simulation and the experiment are performed to evaluate the performance and the response of the device.

The experimental measurements were performed in an IBA proton PBS system, also known as a modulated scanning system, at the Massachusetts General Hospital (MGH) using a universal nozzle. The general schematic of a PBS beam is shown in figure 7.1, more detailed information can be found in [134]. A PBS system involves treating a target volume by splitting up the volume into multiple layers which are irradiated with different energy beams. Since the proton beam is accelerated in a cyclotron the energy being delivered is varied by using an energy degrader. Once the beam energy is lowered to treat a certain target layer the layer is irradiated using multiple spots which are individually focused with a certain magnetic field strength set by the X and the Y scanning magnets. The PBS system differs from the passive HIMAC setup from the previous chapter which passes a beam with a fixed energy through a magnetic field and delivers dose to different depths in the patient by passing through a ridge filter. For a treatment plan generated by the TPS it is possible to retrieve a collection of weights which include the energy, size and position of the beam when it reaches the plane of the iso-centre.

The Bridge microdosimeter was simulated when exposed to a mono-energetic spot beam using Geant4 version 10.1. For the mono-energetic beam (single delivered spot beam) the initial beam position was simulated with 40 cm of air before the water phantom as shown in figure 7.2. The configuration of the detector in the water phantom uses the same setup as the previous chapter, with the Bridge microdosimeter placed in a water proof PMMA sheath and scanned through the centre of the beam. The initial energy in the simulation was tuned to match the range of experimental depth dose measurements, which were acquired with an ionisation chamber. The primary energy was tuned to a value of 131.5 MeV with an energy sigma of 1% and Gaussian shaped lateral dose profile

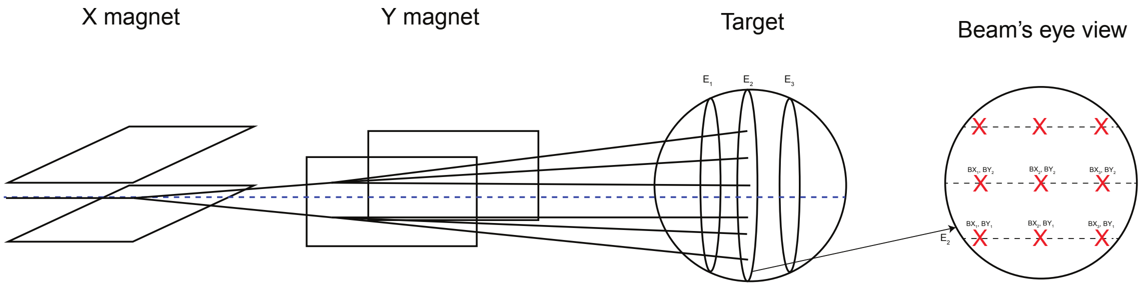

Figure 7.1: Simple representation of a PBS beam. The target volume is divided into multiple energy layers, with each layer made up of many individual "beam spots", with each spot having its own value of X and Y magnetic field strengths to steer the beam to the correct position. The far right part of the figure shows the beam's eye view of a particular target layer with multiple beam spots with unique values of magnetic field strengths.

with a $\sigma =$ of 11 mm (FWHM = 25.91 mm), based on values from the TPS.

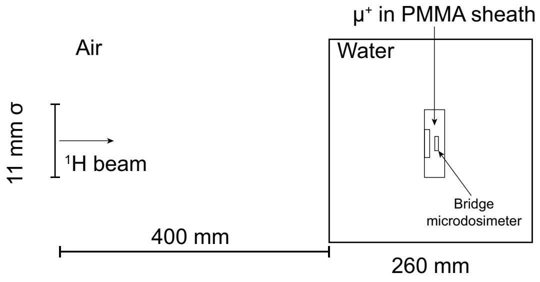

Figure 7.2: Simulation setup used for the MGH PBS proton therapy beam line.

7.2.1 Bridge microdosimeter

A zoomed in section of the modelled Bridge microdosimeter used in this study can be seen in figure 7.3. The device is made up of arrays of 10 μm thick high resistivity n-type silicon sensitive volumes (SVs) with an area of 30 $\times$ 30 μm, the SVs are connected into arrays by smaller "bridging" volumes which the device's name is derived from. These smaller bridging volumes are also 10 μm thick but have an area of 15 $\times$ 20 μm and have the same silicon characteristics as the SVs. In total there are 4248 SVs on the Bridge microdosimeter, made up of 59 rows and 72 columns. On top of the SVs and bridging volumes there is a 1.7 μm thick overlayer of SiO_2 and at the centre of the SV overlayer there is an aluminium rectangular prism with an area of 8×8 μm^2, also with a thickness of 1.7 μm. Centered on top of the aluminium prism there is a further SiO_2 layer with a thickness of 1.43 μm and area of 10.5×10.5 μm

The SVs and bridging volumes are supported on a 1 μm thick SiO_2 layer on top of a 300 μm thick low resistivity silicon wafer for support. The three dimensional SVs and bridging volumes are formed via plasma etching. As can be seen in the SEM image in figure 7.4 the plasma etching is done very accurately and produces a well defined volume which is important when using a $\langle l \rangle$ or $\langle l_{Path} \rangle$ value for the conversion of energy deposition to lineal energy. The design also provides excellent charge collection efficiency and uniformity throughout the device which can be seen on the right image of figure 7.4. More details of the fabrication and characteristics of the device can be found in [135] and [136], the first publication provides characterisation using the first version of the Bridge design which did not feature a fully etched design while the later publication features the second version which had etching fully done and is the version which all results in this chapter are in reference to.

As with the Mushroom microdosimeter, investigated in the previous chapter, the Bridge microdosimeter is mounted onto the MicroPlus (μ^+) probe which provides a low noise readout. The μ^+ probe and Bridge are then housed inside the same PMMA sheath discussed in the previous chapter with the same overlayer materials summarised in table 6.2 and figure 6.7.

The Bridge was simulated in the μ^+ probe and PMMA sheath, placed in the centre of the water phantom like in the experiment. The experimental data acquired with the Bridge (MCA spectrum) had a maximum energy of 2455 keV with 4096 bins, the maximum energy deposition aquired in the experiment is a somewhat low value ($\sim$142 keV/μm in terms of lineal energy). This maximum detectable energy deposition was adopted in order to take advantage of the high energy resolution at low energies due to the low noise readout provided by the μ^+ probe. This energy range should be ample for the primary proton beam due to the maximum stopping power in water being $\sim$85 keV/μm [96]. However for heavier hadrons, particularly ^{4}He particles which have a maximum LET of $\sim$230 keVμm [137], this range may significantly effect measured quantities by not detecting these higher energy events. To investigate the impact of not having these high LET events recorded in the microdosimetric spectra and their effect on quantities, the maximum energy deposition in the simulation was varied from the experimental maximum of 2.5 MeV to five times this value to 12.2 MeV. For simplicity the experimental value is quoted as 2.5 MeV, however the true value is 2454.81 keV and is what is used in the simulation as well.

The mean path length, $\langle l_{Path} \rangle$, of the Bridge microdosimeter was investigated in the radiation field by using the same method as described in chapter 3, where the silicon SV and bridging volume is replaced with vacuum and the path length of charged particles traversing the device is recorded. Due to the bridging volumes between the SVs, compared to the isolated SVs of the Mushroom design described in previous chapters, particles should be more susceptible to passing through multiple volumes such as a SV and a neighbouring bridging volume. Due to the secondary radiation field having a larger angular distribution the secondary radiation field may have a skew to more energy being deposited for lateral events. The effect which the bridging volume plays on the $\langle l_{Path} \rangle$ compared to an iso-

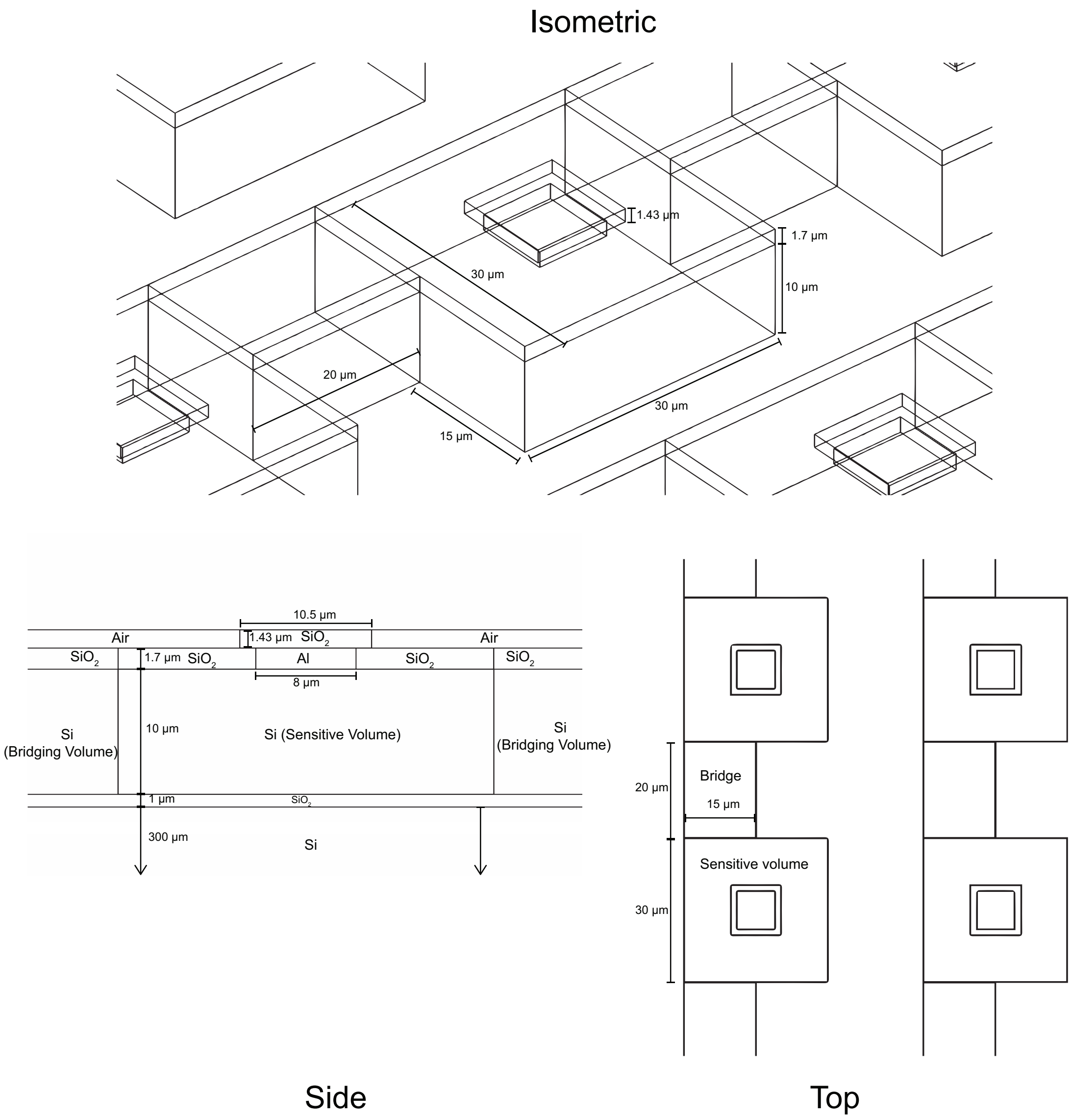

Figure 7.3: A screenshot of the Bridge microdosimeter modelled in Geant4 showing three different views. The screenshots show a zoomed in region of the device which has in total 59 rows of SVs each with 72 columns (4248 SVs in total).

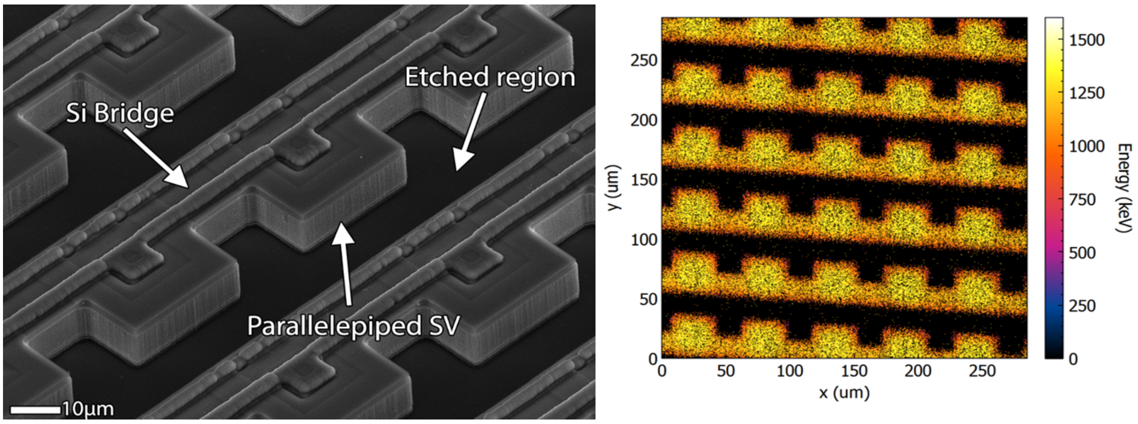

Figure 7.4: Left: An SEM image of the Bridge microdosimeter showing an isometric view of the silicon which has been etched away to form SVs connected together with smaller bridging volumes. Right: A charge collection map of the Bridge microdosimeter obtained using the IBIC technique. Images recreated from [136] courtesy of L. Tran.

lated SV design (such as the Mushroom) was investigated by processing events with and without summing up the path which particles traversed the bridging volume.

To see if the probe and sheath which the Bridge is housed in perturbs of the radiation field significantly, the PMMA sheath and probe were removed, leaving just the detector directly in water. Additionally, the SV and the bridging volumes were replaced with the muscle and the aluminium and SiO_2 overlayers were removed, this was to ensure that any high energy events that were seen were “real” and not due to particles generated in the housing or the detector itself.

7.2.2 Physical quantities under investigation

As with the previous chapter, the quantities compared between experiment and simulation were the frequency mean lineal energy, y_F, and the dose mean lineal energy, y_D, as well as the biological effectiveness at 10% cell survival, RBE_{10}, estimated using the modified microdosimetric kinetic model (MKM). As mentioned above, the RBE in proton therapy is inversely proportional to the dose when less than 4 Gy is delivered in a fraction [72]. Because of this the MKM approach, which was used for ^{4}He , ^{12}C , ^{14}N , ^{16}O and ^{20}Ne beams in the previous chapter, is changed to take into account the RBE dependence on the dose [74]. So instead of the RBE taking the form shown in equation 7.2 for ions heavier than protons, the RBE takes the form as shown in equation 7.3, which is denoted as RBE_d to emphasise the dose dependence.

$$RBE_{10} = \frac{2\beta D_{10,x-ray}}{\sqrt{\alpha^2 - 4\beta\ln(0.1)} - \alpha} \tag{7.2}$$

$$RBE_D = \frac{2\beta D_p}{\sqrt{\alpha_X^2 + 4\beta\left(\alpha D_p + \beta D_p^2\right)} - \alpha_X} \tag{7.3}$$

Where $D_{10,x-ray}$ is the required dose by x-rays to reach 10% cell survival and has a value of 5 Gy for HSG cells and α_X is cell specific and has a value of 0.164 Gy^{-1}. D_p is the physical dose delivered to the cell from the proton beam. In this study D_p is the value along the Bragg curve when 1.82 Gy is delivered at the pinnacle of the BP (standard 2 Gy fraction divided by the RBE value usually adopted clinically of 1.1). One additional difference between this chapter's RBE values compared to the previous chapter is that the error bars in this chapter includes uncertainties related to the cell properties, this results in error bars noticeably larger than the previous chapter. The previous chapter had error bars derived only from the statistical uncertainty due to the extra number of points and an additional model being compared (QMD) making comparison difficult in some cases to see all points clearly.

7.3 Results and Discussion

7.3.1 Radiation Field

The energy deposition in the water phantom due to the mono-energetic beam is shown in figure 7.5. The left plot in the figure shows the Bragg curves of the simulation and the experiment while the right plot shows the two dimensional energy deposition distribution in the phantom. In terms of energy deposition the simulation agrees well with the experimental measurements, with a maximum difference of 2% between the two Bragg curves. The pinnacle of the BP occurs at 123 mm for both simulation and experiment, with the experimental data having an associated uncertainty of 1 mm in the range.

The secondary radiation field is shown in figure 7.6. In particular, the left plot shows the fluence of various ion species throughout the phantom while the right figure shows the yield (N) of particles along the depth of the phantom with respect to the number of incident particles (N_0). The secondary radiation field is dominated by neutron production. Helium ions are the most dominant fragments with ∼2 helium ions produced for every 10^5 primary protons.

7.3.2 Determination of the $\langle l_{Path} \rangle$ of the Bridge microdosimeter

The $\langle l_{Path} \rangle$ values along the Bragg curve for the mono-energetic spot beam are shown in figure 7.7 on the left, the secondary markers refer to secondary ions only and no other charged particles, such as electrons. The open markers represent the $\langle l_{Path} \rangle$ for just the SV in the absence of the bridging volumes. The right plot in figure 7.7 shows the percentage difference between the $\langle l_{Path} \rangle$ when the distance a charged particle traverses the bridging volumes are not considered.

The $\langle l_{Path} \rangle$ of the primary beam can be seen to remain fairly constant, with it decreasing

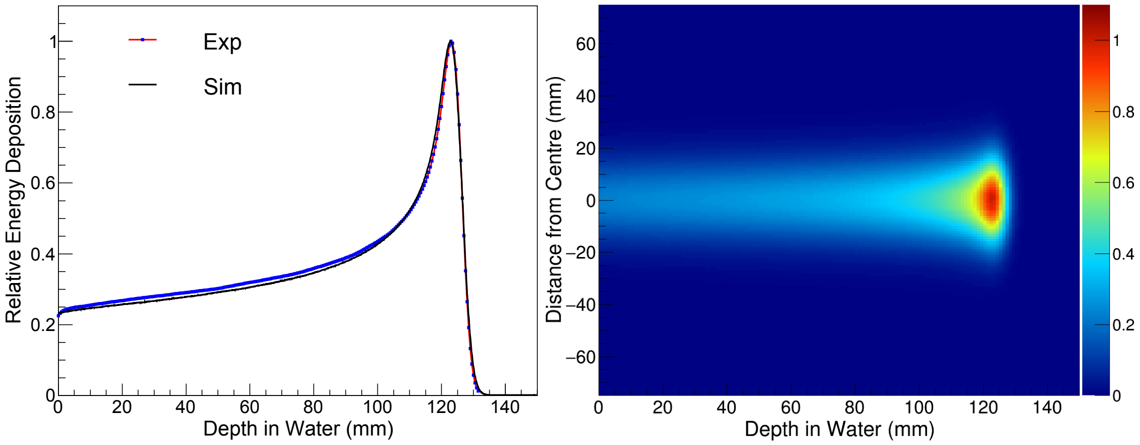

Figure 7.5: The energy deposited within the water phantom. The left plot shows the energy deposited along the Bragg Curve for the simulation against experimental measurements, the maximum of the plots are normalised to 1. The right plot shows the 2D energy deposition within the phantom.

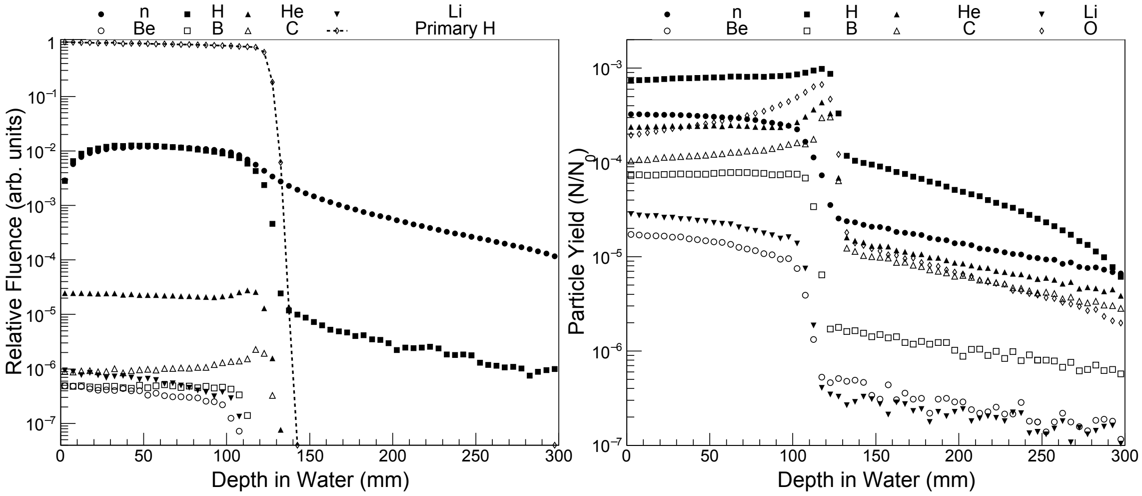

Figure 7.6: Left: The fluence of various particles along the depth of the beam. Right: The production of secondary particles along the depth of the phantom per incident primary proton (N_0)

only by ∼2% due to divergence of the beam from 9.94 μm at 22 mm depth to 9.75 μm at 130 mm. The results are very similar to the values presented in chapter 4 for the 30 μm diameter cylinder SOI design, which, similarly to the Bridge design, has a $\langle l_{Cauchy} \rangle$ of 12 μm for the SVs. One notable difference between the Mushroom and the Bridge design is that for the secondary ions (which is dominated by recoiled nuclei in proton therapy) the $\langle l_{Path} \rangle$ of the Bridge is ∼4.5% higher than the Mushroom design. This higher value is due to the SVs being connected together with the $15 \times 20 \times 10$ μm^3 bridging volumes. This allows the recoiled ions with larger angular distributions to pass through SV and bridging volumes and thus causing an increase in the path length. It can be observed that the bridging design of connecting the SVs together has very little impact on the primary beam with the $\langle l_{Path} \rangle$ being ∼0.2% higher at 22 mm depth and as the beam diverges deeper in the phantom from multiple Coulomb scattering the difference between the $\langle l_{Path} \rangle$ length increases to ∼0.75% at the BP.

Due to the results above, the $\langle l_{Path} \rangle$ values used for the conversion from the energy deposited spectrum (MCA) to the microdosimetric spectrum ($f(y)$) was done by taking the mean of all proton paths, including both primary and secondary protons.

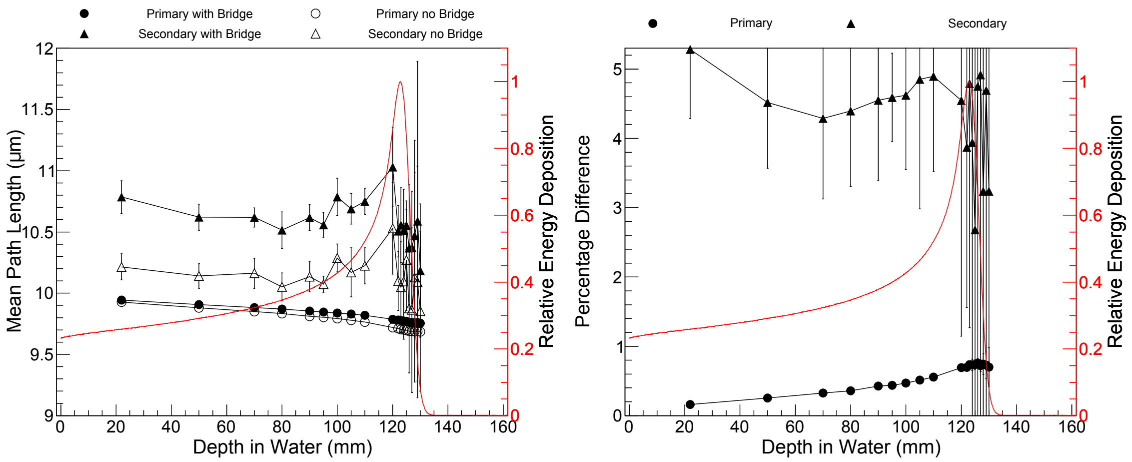

Figure 7.7: Left: The calculated $\langle l_{Path} \rangle$ values of the primary beam and secondary ions when the bridging volumes are present (real device) and when the bridge volumes are removed. Right: The percentage difference between the $\langle l_{Path} \rangle$ values along the Bragg curve when calculated with bridging volumes present and absent.

7.3.3 Microdosimetric spectra in the PBS beam

Sample microdosimetric spectra from the Bridge microdosimeter at various depths along the Bragg curve from both the simulation (solid black line) and the experiment (dashed line) are shown in figure 7.8. Different coloured lines show the contribution of different particles to the total microdosimetric spectra of the simulation. A general good agreement is observed between the spectra of the simulation and the experiment except at depths near the BP where the positioning accuracy becomes the most sensitive. A possible misalignment can be seen at 122 mm depth where the experimental peak shifts to lower energies compared to the simulation but at 126 mm the two energy peaks re-align. Looking at the contributions to the spectra using the simulation, before the BP it can be seen that the delta electrons generated outside of the Bridge contribute a significant amount to the energy deposited. Up until ∼115 mm in depth the delta electrons have a higher lineal energy peak compared to the primary beam, with a value slightly higher than 2 keV/μm, with its distribution not changing significantly. The primary and secondary protons have very similar lineal energy distribution due a large number of the secondary protons being produced via elastic collisions.

At depths of 126 and 129 mm, a noticeable low energy peak at ∼0.6 keV/μm can be observed in figure 7.9. This bump is present in the experiment but not in the simulation. It begins to form at a depth of ∼120 mm and grows larger for deeper positions within the phantom. This peak can be attributed to the charge collection in the device. Towards the edges of the device, where contacts are located, some charge is collected which is not generated within the SV or bridge volumes. The charge collected in this region is very low compared to the charged collected actual SV and bridging volumes, events from this region are mostly removed with thresholding in the experiment. However, as the beam reaches the end of its range its higher LET shifts the energy deposited in this region to be large enough to be recorded in the experiment.

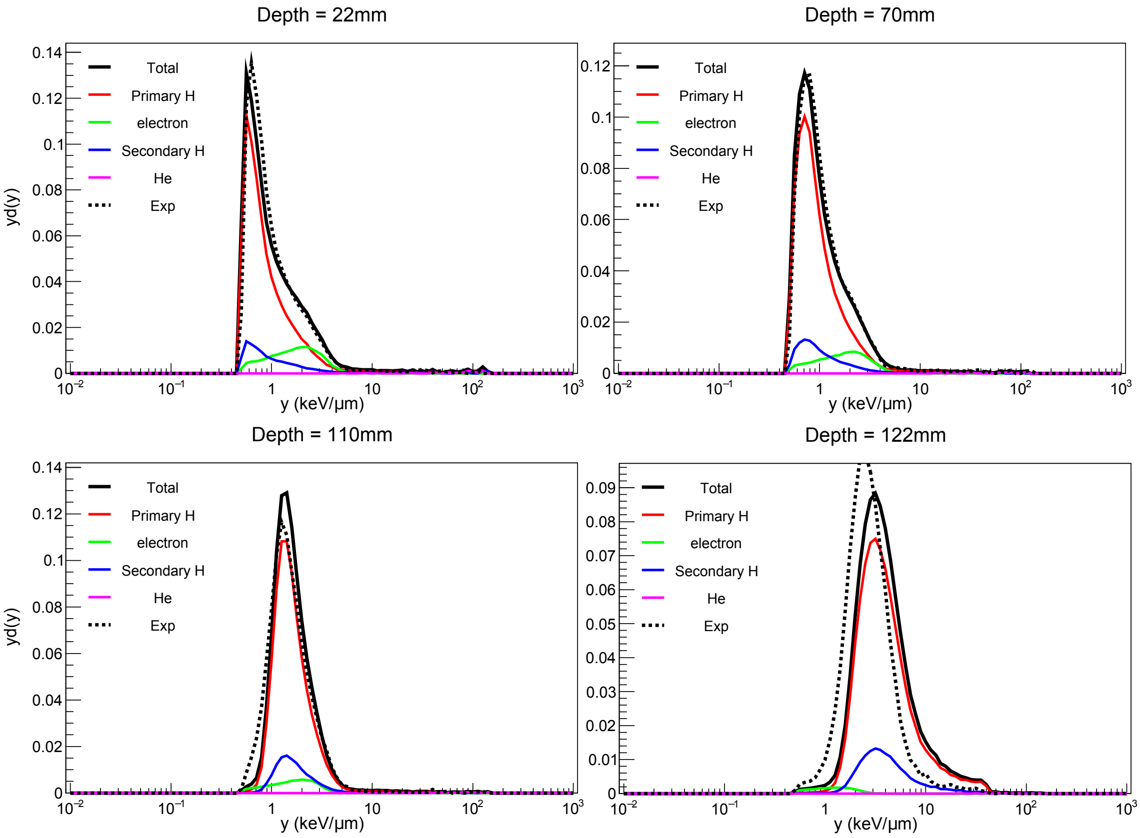

Figure 7.8: Comparison between the microdosimetric spectra of experiment and simulation at selected depths in the water phantom up to the pinnacle of the BP (123 mm).

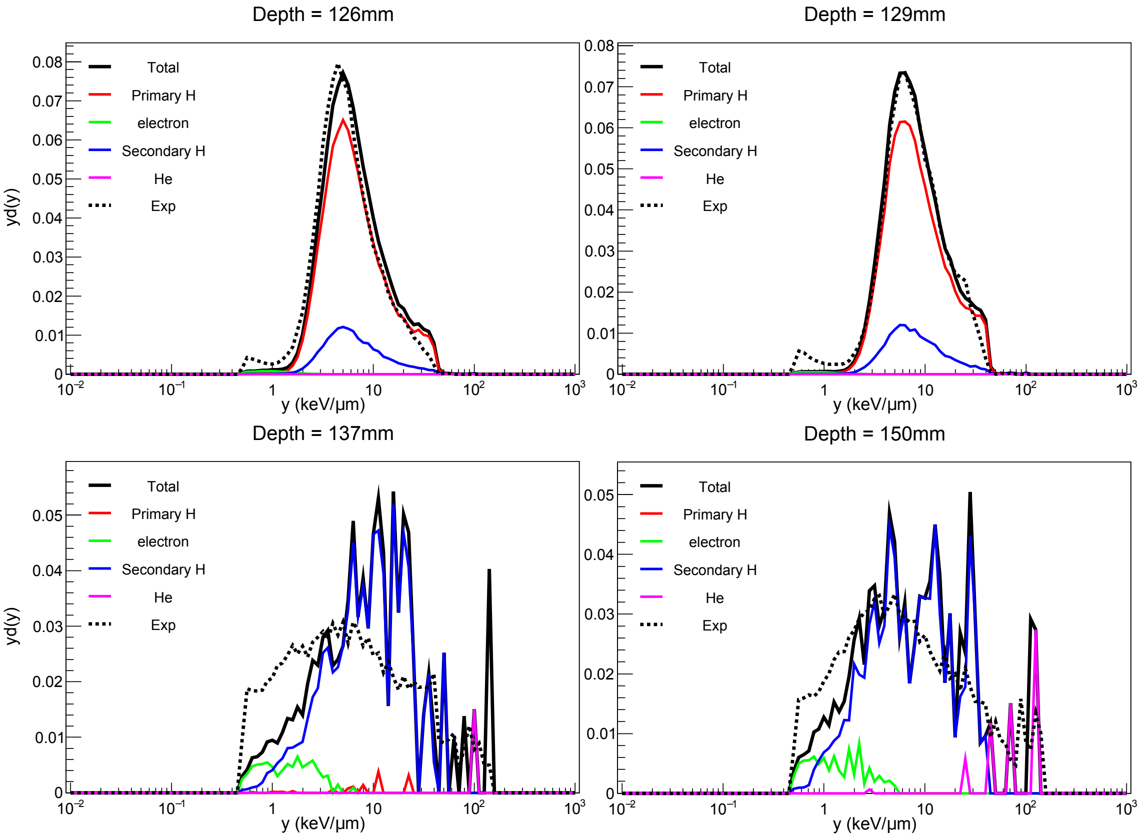

Figure 7.9: Comparison between the microdosimetric spectra determined with the experiment and the simulation at the distal edge of the BP as well as downstream of the BP where the primary beam has fully stopped within the water.

7.3.4 Microdosimetric quantities of the PBS beam

A comparison of experimental and simulation values of y_D are shown in figure 7.10, with the right plot showing an enlarged region of the BP. The value of y_D stays fairly constant up until the BP with a value of $\sim$2 keV/μm. Once near the BP, at $\sim$115 mm depth, y_D begins to continually grow, reaching $\sim$5 keV/μm at the pinnacle of the BP. Then it constantly increases to 11 keV/μm at 130 mm depth. Very good agreement is observed between the experiment and the simulation, indicating the Bridge microdosimeter has favourable charge collection characteristics. One notable discrepancy can be seen at the distal edge of the BP where the experiment and simulation show a possible misalignment of $\sim$1 mm. The low energy peak caused by the low energy charge collection was found not to be the cause of this shift by removing events with a lineal energy below 1 keVμm, this resulted in a slight increase of 2% of y_D events at the distal edge. A reason for the shift between experiment and simulation values may be that the beam energy used was tuned to match the range of experimental ionisation chamber measurements. These measurements may be based on the centre position of the ionisation chamber instead of the amount of water in front of it, which is the case for the microdosimeter. This could result in a shifted range in the experiment.

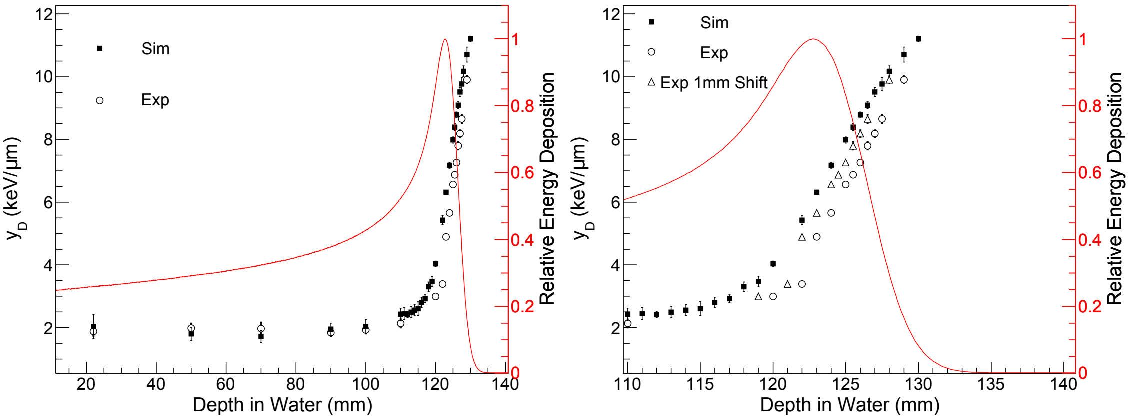

Figure 7.10: The calculated y_D of both experiment and simulation. The right side shows an enlarged view of the BP region with an additional data set showing the experimental values when shifted by 1 mm (triangle marker).

The RBE values calculated using the MKM from equation 7.3 are shown in figure 7.11, with the right plot showing the BP being enlarged. The large increase in RBE at the end of the primary protons' trajectory is due to a combination of the increasing LET of the proton beam as well as the decreasing amount of deposited dose, which as mentioned earlier, for doses below 4 Gy the RBE of a proton beam increases. The effect which dose has on the calculated RBE with the parameters used for the MKM is shown in figure 7.12. The RBE values calculated are shown for doses between 0.1 and 100 Gy delivered to the pinnacle of the BP, 1.82 Gy has a line drawn between its points and is the standard fraction size for a proton delivery.

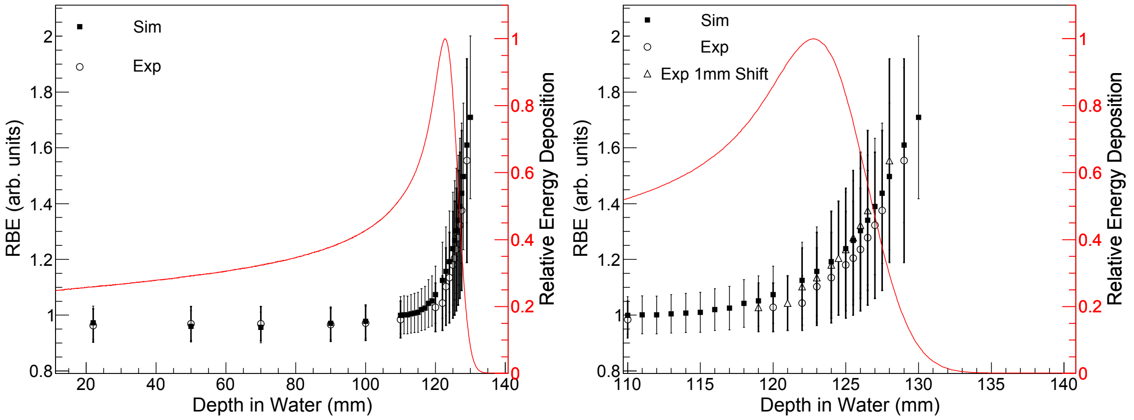

Figure 7.11: The calculated RBE using equation 7.3 of both experiment and simulation. The right side shows an enlarged view of the BP region with an additional data set showing the experimental values when shifted by 1 mm (triangle marker). The right plot shows the BP zoomed in.

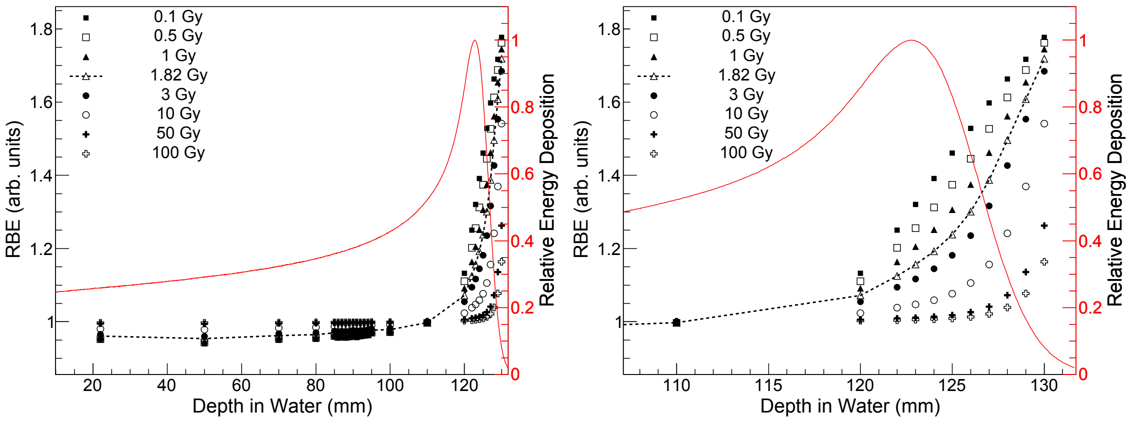

Figure 7.12: The calculated RBE using equation 7.3 and different values of dose being delivered to the pinnacle of the BP. The dose with the dashed line with a value of 1.82 Gy represents the standard fraction size for dose delivery and is the dose used for this section.

7.3.5 Effect of the maximum recorded energy on the microdosimetric spectra and values

Figure 7.13 shows the microdosimetric spectra obtained for the Bridge device, at various depths in the water phantom, in the spot beam with a maximum acceptance energy of 12.2 MeV. The dashed vertical line represents the cutoff energy of 2.4 MeV used in the experiment with the maximum value on the y-axis being set to show the contribution of high lineal energy events easier. The legend of the plot also includes the contribution to the response due to Na, Mg, Al and Si recoiled nuclei which are not “real” events but are generated within the detector unit. It can be seen that some events generated in the detector occur both above and below the threshold energy. Additionally, the most prevalent contributor is He for the depths shown. For comparison, the microdosimetric spectra from replacing the silicon SVs and bridging volumes with striated muscle are shown in figure 7.14.

Comparing the microdosimetric spectra of silicon and striated muscle, the prevalence of He events above the 2.4 MeV energy threshold are similar to one another, indicating that “real” events are excluded with an energy deposition threshold of 2.4 MeV.

Events above the 2.4 MeV threshold contribute the most at the surface of the phantom. Since the total inelastic cross-section remains fairly constant above low energies [49] this means that the production of high LET particles does not vary significantly. Because of this, as the primary protons decreases in energy (increasing LET) the contribution from secondary ions to the total dose diminishes and reduces its contribution to the total dose and the value of y_D. This is reflected in comparing the y_F values, shown in figure 7.15. Here it can be seen that the values of y_F agree much more than the y_D values of the maximum energy thresholds of 2.4 and 12.2 MeV each other. The better agreement of y_F

is due to y_F weighting the most frequent events, consisting of the primary proton beam and its delta electrons (see Discussion section of chapter 5 for more explanation).

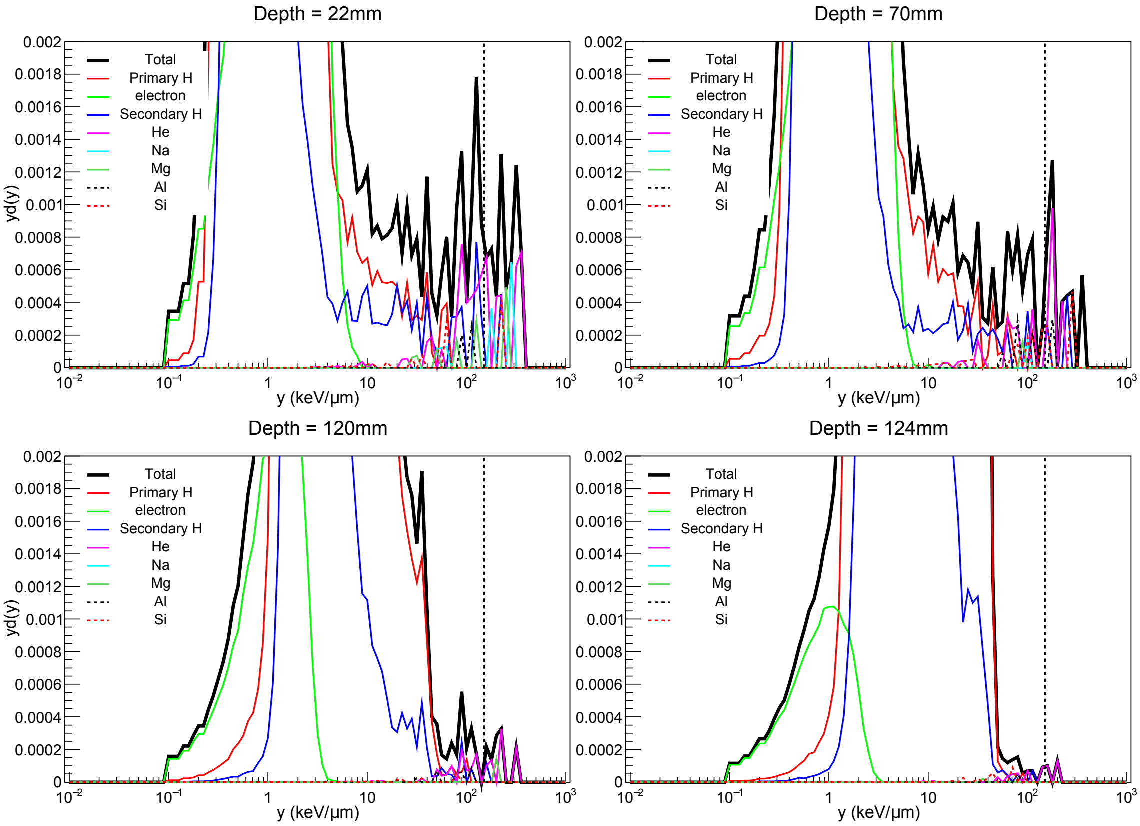

Figure 7.13: The microdosimetric spectra of the Bridge microdosimeter in the MGH PBS beam with the maximum energy being increased from 2.4 MeV to 12.2 MeV. The dashed vertical line represents the threshold energy used in the experiment. The maximum value of the y-axis has been set to show the contribution of high lineal energy events. The maximum value of the y-axis has been set to show the contribution of high lineal energy events.

7.3.6 Effect of the detector and probe construction on the response of the Bridge design

A comparison between the y_F, y_D and RBE values for the real bridge device in a probe and sheath compared to an "ideal" microdosimeter made out of muscle using different maximum energies is shown in figure 7.15. It can be seen that y_F does not significantly vary for either material or maximum energy. For the RBE there is a slight difference at the surface of the phantom while for y_D the muscle is seen to be systematically higher between $\sim$60 and 120 mm. The reason is that the muscle volume has the same thickness as the silicon (10 μm) but not the same equivalent thickness (17.25 μm). As seen in chapter 5, thinner SVs had more straggling in the energy deposited in the SV which caused y_D values to be higher for smaller SVs. At the surface of the phantom (22 and 50 mm) there is not an obvious difference between muscle and silicon, this could be attributed to that

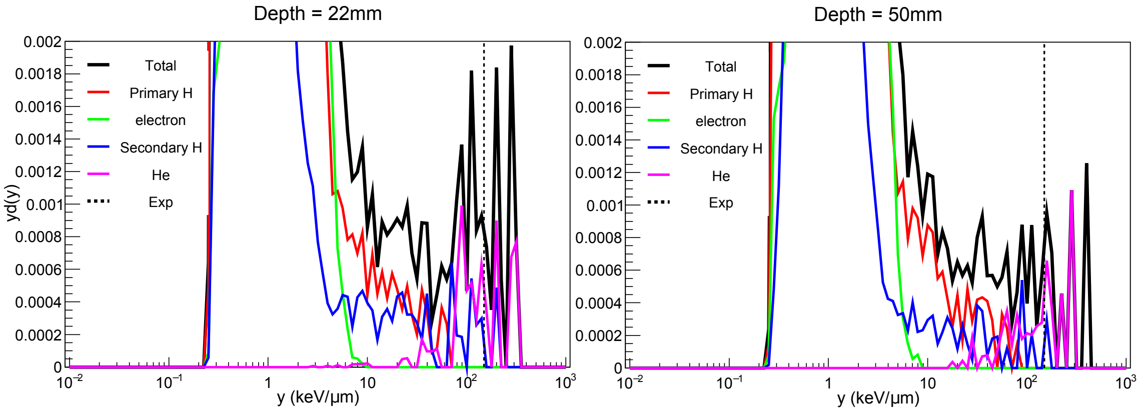

Figure 7.14: The microdosimetric spectra of the Bridge microdosimeter constructed with striated muscle instead of silicon with a maximum energy of 12.2 MeV. The dashed vertical line represents the threshold energy used in the experiment.

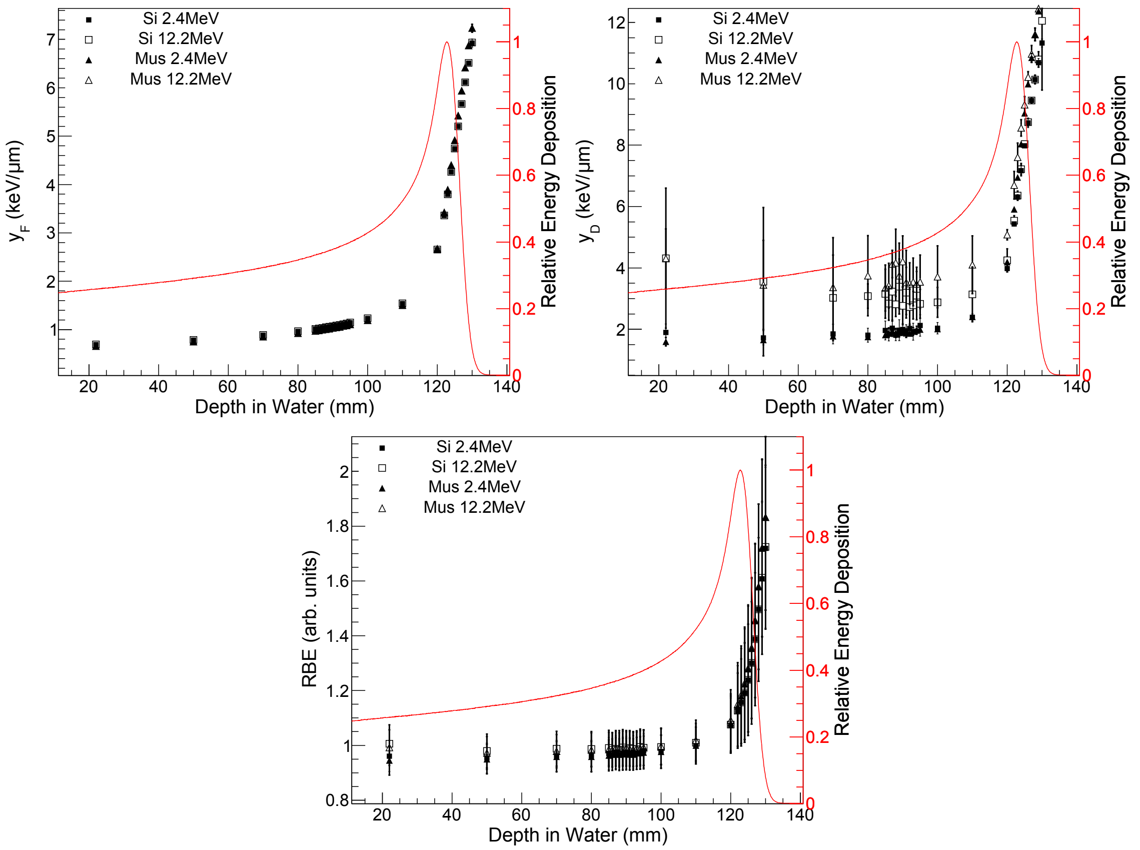

Figure 7.15: Comparison of the response of a probeless Bridge detector made of Si and muscle for maximum energies of 2.4 MeV (same as experiment) and 12.2 MeV.

these high surface values of y_D are due to a few helium ions while the difference in y_D arises from the straggling of the primary beam itself.

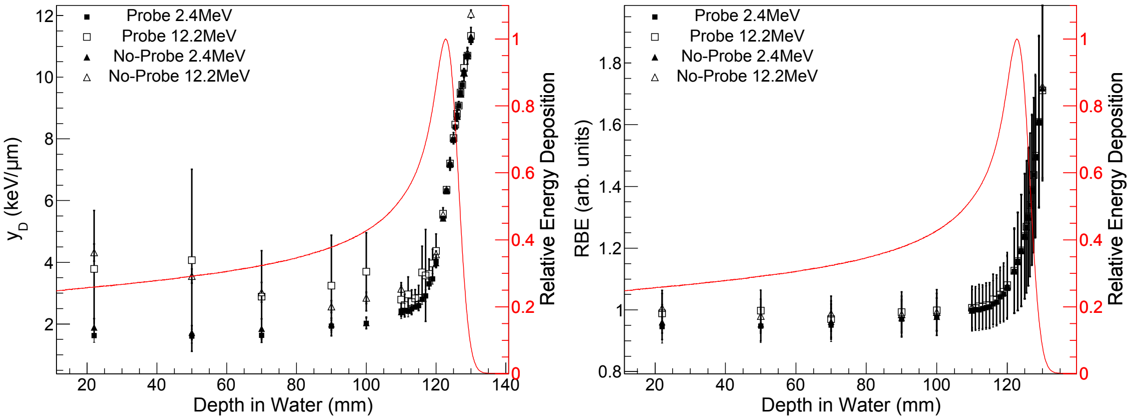

Figure 7.16: Comparison of the response of detector placed in the PMMA probe and the detector placed directly in the water phantom.

7.4 Conclusion

In this chapter the Bridge microdosimeter was studied in a therapeutic proton PBS beam using a single beam spot. Experimental measurements were compared to Geant4 simulations and generally showed good agreement in terms of the microdosimetric spectra, y_F, y_D and RBE, indicating the strong performance of the device.

Comparisons between the microdosimetric spectra showed good agreement between experiment and simulation, indicating favourable charge collection properties of the device. At the distal edge of the BP there was some discrepancy between the experiment and simulated microdosimetric spectra, with the experiment showing a small bump at $\sim$0.6 keV/μm. This bump is likely due to low charge collection from charge generated outside of the SVs and bridging volumes. This only occurs when the beam's LET increases and the events are higher than the energy threshold set in the experiment. The effect of this low charge collection region does not have a significant effect on calculated quantities, with removing these events resulting in a change of less than 2% to y_D.

Comparison of y_D and RBE values, estimated using the MKM, both showed good agreement between experiment and simulation. Both y_D and RBE followed a similar shape with a fairly constant value up until the BP with values of $\sim$2 keV/μm and 1, respectively. While at the distal part of the BP the values reached values of 11.4 keV/μm and 1.7 at 130 mm for y_D and RBE, respectively. Some discrepancy was found in the distal edge of the BP where the positioning accuracy is the most critical, with a shift of $\sim$1-2 mm observed between experiment and simulation. This shift may have been contributed by the primary energy used in the simulation tuned to match the range of ionisation chamber measurements.

The mean path length of the Bridge micodosimeter was studied in the radiation field and the effect of the bridging volumes connecting the sensitive volumes was seen to have very little impact on the response. Compared to having no bridging volumes the $\langle l_{Path} \rangle$ of the the incident beam increased a maximum of 0.75% at the BP while the $\langle l_{Path} \rangle$ of secondary ions increased ∼4.5% due to the greater angular distribution.

The energy deposition range recorded by the detector was varied in the simulation from the value of 2.5 MeV used in the experiment and was increased to 12 MeV. It was found that increasing the maximum energy threshold has a significant impact on the y_D value for positions at the start of the Bragg curve due to high energy helium ion events generated from nuclear interactions. At deeper depths the impact of the helium ions becomes less pronounced as the primary proton beam's LET increases, with the distal edge of the BP having very little difference.

Chapter 8

Conclusion and Recommendations

This thesis presented a simulation study, using the Geant4 toolkit, on the use of silicon microdosimetry in hadron therapy and evaluation of available fragmentation models in Geant4.

Fragmentation is an important process to be considered in heavy ion therapy, the alternative fragmentation models, BIC, QMD and INCL++, available in Geant4 were benchmarked against experimental data for a ^{12}C beam incident upon water. In general, simulation fragment yields were seen to agree between 5-40% with experimental measurements. For angular distributions the INCL++ model was seen to agree the best amongst the models, with all models having better agreement for lighter fragments. For energy distributions the BIC and QMD models were seen to perform similar to one another, with both performing better than the INCL++ model. Performing regression testing of the models for various versions of Geant4 showed how the fragment yields of each model could vary significantly from version to version, with the model giving the best agreement with experiment changing from version to version. Due to these fluctuations from release to release, this test is now part of the system testing of Geant4 with users being able to view any changes between versions. However, further experimental data using different energies and targets, relevant to medical physics, should be added to the test to minimise systematic errors. In addition to more energies and targets, alternative ion beams should also be included as part of testing and monitoring.

Validation of Geant4 was also performed for its use as an investigation tool in solid state microdosimetry. The first generation CMRP designed Mushroom microdosimeter was modelled in ^{12}C , ^{14}N and ^{16}O ion beams and compared to experimental measurements. Comparing the energy deposition of the experiment and simulation showed good agreement, indicating the favourable charge collection properties of the device. Using the experimental measurements it was also possible to perform validation of Geant4 for the use of silicon microdosimetry in heavy ion therapy. Similarly, comparisons between experiment and simulation for the use of the Bridge silicon microdosimeter in proton therapy were made and yielded in good agreement as well.

The conversion of the energy deposition in silicon to tissue equivalent lineal energy for a Mushroom microdosimeter design was studied in a ^{12}C ion beam. It was found that a single conversion factor was satisfactory, with values of 0.57 and 0.54 for striated muscle and water, respectively. Performing the same study for a proton beam gave conversion factors of 0.58 and 0.56, with the later value agreeing with literature. However, when converting the energy deposition to lineal energy it was found that the conventional method of using the mean chord length was not appropriate in hadron therapy due to the strong directionality of the radiation field. Instead, it was found that the mean path length, where the path of charged particles traversing the SV in the actual radiation field, was more appropriate.

Using the method of the mean path length the design of the SV was optimised by reducing the variance of the mean path length in various different proton and ^{12}C ion beam radiation fields. It was found that the design of the SV was more sensitive in proton beams then ^{12}C ion beams due to the greater divergence of the primary beam and a secondary radiation field which is dominated by neutrons compared to fragments in the ^{12}C beam case. Overall, it was found that the design of a non-spherical sensitive volume should have a thickness equal to the mean chord length of the same volume.

Adopting the optimised SV design with the thickness equal to the mean chord length, the impact of the thickness on the microdosimetric measurements was studied. It was determined that y_F was impacted the most by thickness in heavier ion beams due to the greater density of delta electrons. Conversely, y_D was seen to be effected the greatest by SV thickness for lighter ions due to fewer collisions occurring in the SV than heavier ions, creating more broader distributions. For RBE calculations, as estimated by the microdosimetric kinetic model, gave a difference of $\sim$1% between a 5 μm thick and 100 μm thick silicon SV in a ^{12}C ion beam.

Bibliography

[1] J. T. Bushberg, *The Essential Physics of Medical Imaging*. Lippincott Williams and Wilkins, second ed., 2002.

[2] R. R. Wilson, "Radiological use of fast protons," *Radiology*, vol. 47, no. 5, pp. 487–491, 1946. PMID: 20274616.

[3] W. Saunders, J. R. Castro, G. T. Y. Chen, J. M. Collier, S. R. Zink, S. Pitluck, T. L. Phillips, D. Char, P. Gutin, G. Gauger, C. A. Tobias, and E. L. Alpen, "Helium-ion radiation therapy at the lawrence berkeley laboratory: Recent results of a northern california oncology group clinical trial," *Radiation Research*, vol. 104, no. 2, pp. S227–S234, 1985.

[4] `https://www.ptcog.ch/`.

[5] W. T. Chu, B. A. Ludewigt, and T. R. Renner, "Instrumentation for treatment of cancer using proton and lightion beams," *Review of Scientific Instruments*, vol. 64, no. 8, pp. 2055–2122, 1993.

[6] `https://acrf.com.au/on-cancer/`.

[7] H. H. Rossi and M. Zaider, *Microdosimetry and its applications*. Springer, 1996.

[8] O. Actis, D. Meer, S. Knig, D. C. Weber, and A. Mayor, "A comprehensive and efficient daily quality assurance for PBS proton therapy," *Physics in Medicine and Biology*, vol. 62, pp. 1661–1675, feb 2017.

[9] L. T. Tran, L. Chartier, D. Bolst, A. Pogossov, S. Guatelli, M. Petasecca, M. L. F. Lerch, D. A. Prokopovich, M. I. Reinhard, B. Clasie, N. Depauw, H. Kooy, J. B. Flanz, A. McNamara, H. Paganetti, C. Beltran, K. Furutani, V. L. Perevertaylo, M. Jackson, and A. B. Rosenfeld, "Characterization of proton pencil beam scanning and passive beam using a high spatial resolution solidstate microdosimeter," *Medical Physics*, vol. 44, no. 11, pp. 6085–6095.

[10] L. T. Tran, D. Bolst, S. Guatelli, A. Pogossov, M. Petasecca, M. L. F. Lerch, L. Chartier, D. A. Prokopovich, M. I. Reinhard, M. Povoli, A. Kok, V. L. Perevertaylo, N. Matsufuji, T. Kanai, M. Jackson, and A. B. Rosenfeld, "The relative

biological effectiveness for carbon, nitrogen, and oxygen ion beams using passive and scanning techniques evaluated with fully 3d silicon microdosimeters," *Medical Physics*, vol. 45, no. 5, pp. 2299–2308.

[11] I. J. Chetty, B. Curran, J. E. Cygler, J. J. DeMarco, G. Ezzell, B. A. Faddegon, I. Kawrakow, P. J. Keall, H. Liu, C.-M. C. Ma, *et al.*, "Report of the aapm task group no. 105: Issues associated with clinical implementation of monte carlo-based photon and electron external beam treatment planning," *Medical physics*, vol. 34, no. 12, pp. 4818–4853, 2007.

[12] F. Schultz, J. Geleijns, F. Spoelstra, and J. Zoetelief, "Monte carlo calculations for assessment of radiation dose to patients with congenital heart defects and to staff during cardiac catheterizations," *The British journal of radiology*, vol. 76, no. 909, pp. 638–647, 2003.

[13] S. Dowdell, C. Grassberger, and H. Paganetti, "Four-dimensional monte carlo simulations demonstrating how the extent of intensity-modulation impacts motion effects in proton therapy lung treatments," *Medical physics*, vol. 40, no. 12, 2013.

[14] F. Cadini, D. Bolst, S. Guatelli, C. Beltran, M. Jackson, and A. B. Rosenfeld, "Neutron shielding for a new projected proton therapy facility: A geant4 simulation study," *Physica Medica*, vol. 32, no. 12, pp. 1862 – 1871, 2016.

[15] M. Sakama, T. Kanai, Y. Kase, K. Yusa, M. Tashiro, K. Torikai, H. Shimada, S. Yamada, T. Ohno, and T. Nakano, "Design of ridge filters for spread-out bragg peaks with monte carlo simulation in carbon ion therapy," *Physics in Medicine and Biology*, vol. 57, pp. 6615–6633, oct 2012.

[16] D. Bolst, S. Guatelli, L. Tran, and A. Rosenfeld, "Optimisation of the design of soi microdosimeters for hadron therapy quality assurance," *Physics in Medicine and Biology*, 2018.

[17] J. Allison *et al.*, "Geant4 developments and applications," *IEEE Transactions on Nuclear Science*, vol. 53, pp. 270–278, Feb 2006.

[18] S. Agostinelli *et al.*, "Geant4 —a simulation toolkit," *Nuclear Instruments and Methods in Physics Research Section A: Accelerators, Spectrometers, Detectors and Associated Equipment*, vol. 506, no. 3, pp. 250 – 303, 2003.

[19] J. Allison *et al.*, "Recent developments in geant4," *Nuclear Instruments and Methods in Physics Research Section A: Accelerators, Spectrometers, Detectors and Associated Equipment*, vol. 835, pp. 186 – 225, 2016.

[20] R. Brun, R. Hagelberg, M. Hansroul, and J. C. Lassalle, *Simulation program for particle physics experiments, GEANT: user guide and reference manual*. Geneva: CERN, 1978.

[21] G. Battistoni, J. Bauer, T. T. Boehlen, F. Cerutti, M. P. W. Chin, R. Dos Santos Augusto, A. Ferrari, P. G. Ortega, W. Kozowska, G. Magro, A. Mairani, K. Parodi, P. R. Sala, P. Schoofs, T. Tessonnier, and V. Vlachoudis, "The fluka code: An accurate simulation tool for particle therapy," *Frontiers in Oncology*, vol. 6, p. 116, 2016.

[22] T. Goorley, M. James, T. Booth, F. Brown, J. Bull, L. J. Cox, J. Durkee, J. Elson, M. Fensin, R. A. Forster, J. Hendricks, H. G. Hughes, R. Johns, B. Kiedrowski, R. Martz, S. Mashnik, G. McKinney, D. Pelowitz, R. Prael, J. Sweezy, L. Waters, T. Wilcox, and T. Zukaitis, "Initial mcnp6 release overview," *Nuclear Technology*, vol. 180, no. 3, pp. 298–315, 2012.

[23] T. Sato, Y. Iwamoto, S. Hashimoto, T. Ogawa, T. Furuta, S. ichiro Abe, T. Kai, P.-E. Tsai, N. Matsuda, H. Iwase, N. Shigyo, L. Sihver, and K. Niita, "Features of particle and heavy ion transport code system (phits) version 3.02," *Journal of Nuclear Science and Technology*, vol. 55, no. 6, pp. 684–690, 2018.

[24] B. A. Faddegon, M. Asai, J. Perl, C. Ross, J. Sempau, J. Tinslay, and F. Salvat, "Benchmarking of monte carlo simulation of bremsstrahlung from thick targets at radiotherapy energies," *Medical physics*, vol. 35, no. 10, pp. 4308–4317, 2008.

[25] M. Testa, J. Schümann, H.-M. Lu, J. Shin, B. Faddegon, J. Perl, and H. Paganetti, "Experimental validation of the topas monte carlo system for passive scattering proton therapy," *Medical physics*, vol. 40, no. 12, 2013.

[26] A. Lechner, V. Ivanchenko, and J. Knobloch, "Validation of recent geant4 physics models for application in carbon ion therapy," *Nuclear Instruments and Methods in Physics Research Section B: Beam Interactions with Materials and Atoms*, vol. 268, no. 14, pp. 2343 – 2354, 2010.

[27] T. T. Böhlen, F. Cerutti, M. Dosanjh, A. Ferrari, I. Gudowska, A. Mairani, and J. M. Quesada, "Benchmarking nuclear models of fluka and geant4 for carbon ion therapy," *Physics in Medicine and Biology*, vol. 55, no. 19, p. 5833, 2010.

[28] M. D. Napoli, C. Agodi, G. Battistoni, A. A. Blancato, G. A. P. Cirrone, G. Cuttone, F. Giacoppo, M. C. Morone, D. Nicolosi, L. Pandola, and et al., "Carbon fragmentation measurements and validation of the geant4 nuclear reaction models for hadrontherapy," *Physics in Medicine and Biology*, vol. 57, p. 76517671, Feb 2012.

[29] "ICRU Report 85-fundamental quantities and units for ionizing radiation (revised)," *International Commission on Radiation Units and Measurements*, 2011.

[30] D. Schardt, T. Elsässer, and D. Schulz-Ertner, "Heavy-ion tumor therapy: Physical and radiobiological benefits," *Rev. Mod. Phys.*, vol. 82, pp. 383–425, Feb 2010.

[31] W. H. B. M.A. and R. K. B.Sc., "Xxxix. on the particles of radium, and their loss of range in passing through various atoms and molecules," *The London, Edinburgh, and Dublin Philosophical Magazine and Journal of Science*, vol. 10, no. 57, pp. 318–340, 1905.

[32] N. Bohr, "Lx. on the decrease of velocity of swiftly moving electrified particles in passing through matter," *The London, Edinburgh, and Dublin Philosophical Magazine and Journal of Science*, vol. 30, no. 178, pp. 581–612, 1915.

[33] B. Bethe, "Zur theorie des durchgangs schneller korpuskularstrahlen durch materie," *Annalen der Physik*, no. 5, pp. 324–400, 1930.

[34] F. Bloch, "Zur bremsung rasch bewegter teilchen beim durchgang durch materie," *Annalen der Physik*, vol. 408, no. 3, pp. 285–320, 1933.

[35] M. J. Berger, M. Inokuti, H. H. Andersen, H. Bichsel, D. Powers, S. . M. Seltzer, D. . Thwaites, and D. E. Watt, "Report 49," *Journal of the International Commission on Radiation Units and Measurements*, vol. os25, no. 2, p. NP, 1993.

[36] "ICRU Report 36-Stoppping of ions heavier than helium," *International Commission on Radiation Units and Measurements*, 2005.

[37] P. V. Vavilov, "Ionization losses of high-energy heavy particles," *Sov. Phys. JETP*, vol. 5, pp. 749–751, 1957. [Zh. Eksp. Teor. Fiz.32,920(1957)].

[38] H. Pagnetti, *Proton Therapy Physics*. CRC Press, first ed., 2012.

[39] G. Moliere, "Theorie der streuung schneller geladener teilchen ii mehrfach-und vielfachstreuung," *Zeitschrift fr Naturforschung A*, 1948.

[40] V. L. Highland, "Some practical remarks on multiple scattering," *Nuclear Instruments and Methods*, vol. 129, no. 2, pp. 497 – 499, 1975.

[41] S. Tavernier, *Experimental Techniques in Nuclear and Particle Physics*. Springer, first ed., 2010.

[42] Y.-S. Tsai, "Pair production and bremsstrahlung of charged leptons," *Reviews of Modern Physics*, vol. 46, no. 4, p. 815, 1974.

[43] D. Schardt, T. Elsässer, and D. Schulz-Ertner, “Heavy-ion tumor therapy: Physical and radiobiological benefits,” *Rev. Mod. Phys.*, vol. 82, pp. 383–425, Feb 2010.

[44] INTERNATIONAL ATOMIC ENERGY AGENCY, *Cyclotron Produced Radionuclides: Physical Characteristics and Production Methods*. No. 468 in Technical Reports Series, Vienna: INTERNATIONAL ATOMIC ENERGY AGENCY, 2009.

[45] W. D. Newhauser and R. Zhang, “The physics of proton therapy,” *Physics in Medicine Biology*, vol. 60, no. 8, p. R155, 2015.

[46] M. Chadwick and P. Young, “Endf/b-vi mod 3 evaluation,” June 1996.

[47] M. Chadwick and P. Young, “Endf/b-vi mod 2 revisions,” July 1998.

[48] S. Kox, A. Gamp, C. Perrin, J. Arvieux, R. Bertholet, J. F. Bruandet, M. Buenerd, R. Cherkaoui, A. J. Cole, Y. El-Masri, N. Longequeue, J. Menet, F. Merchez, and J. B. Viano, “Trends of total reaction cross sections for heavy ion collisions in the intermediate energy range,” *Phys. Rev. C*, vol. 35, pp. 1678–1691, May 1987.

[49] J. J. H. Menet, E. E. Gross, J. J. Malanify, and A. Zucker, “Total-reaction-cross-section measurements for 30-60-mev protons and the imaginary optical potential,” *Phys. Rev. C*, vol. 4, pp. 1114–1129, Oct 1971.

[50] W. Newhauser and M. Durante, “Assessing the risk of second malignancies after modern radiotherapy,” *Nat. Rev. Cancer*, vol. 11, pp. 438–448, 2011.

[51] E. Haettner, H. Iwase, M. Krmer, G. Kraft, and D. Schardt, “Experimental study of nuclear fragmentation of 200 and 400 mev/ u 12 c ions in water for applications in particle therapy,” *Physics in Medicine and Biology*, vol. 58, no. 23, p. 8265, 2013.

[52] J.-J. Gaimard and K.-H. Schmidt, “A reexamination of the abrasion-ablation model for the description of the nuclear fragmentation reaction,” *Nuclear Physics A*, vol. 531, no. 3, pp. 709 – 745, 1991.

[53] A. V. Ivantchenko, V. N. Ivanchenko, J.-M. Q. Molina, and S. L. Incerti, “Geant4 hadronic physics for space radiation environment,” *International Journal of Radiation Biology*, vol. 88, no. 1-2, pp. 171–175, 2012.

[54] J. M. Quesada, V. Ivanchenko, A. Ivanchenko, M. A. Cortés-Giraldo, G. Folger, A. Howard, and D. Wright, “Recent developments in pre-equilibrium and de-excitation models in geant4,”

[55] `http://geant4.web.cern.ch/geant4/UserDocumentation/UsersGuides/PhysicsReferenc`

[56] H. Rossi and M. Zaider, *Microdosimetry and Its Applications*. Springer Berlin Heidelberg, 1996.

[57] "ICRU Report 36-Microdosimetry," *International Commission on Radiation Units and Measurements*, 1970.

[58] A. M. Kellerer, "2 - fundamentals of microdosimetry," in *The Dosimetry of Ionizing Radiation* (K. R. KASE, B. E. BJRNGARD, and F. H. ATTIX, eds.), pp. 77 – 162, Academic Press, 1985.

[59] L. Chartier, L. T. Tran, D. Bolst, S. Guatelli, A. Pogossov, D. A. Prokopovich, M. I. Reinhard, V. Perevertaylo, S. Anderson, C. Beltran, N. Matsufuji, M. Jackson, and A. B. Rosenfeld, "Microdosimetric applications in proton and heavy ion therapy using silicon microdosimeters," *Radiation Protection Dosimetry*, pp. 1–7, 2017.

[60] A. M. Kellerer, "Chord length distributions and related quantities for spheroids," *Radiation Research*, vol. 98, pp. 425–437, 1984.

[61] J. Kingman, "Mean free paths in a convex reflecting region," *Journal of Applied Probability*, vol. 2, no. 1, pp. 162–168, 1965.

[62] A. M. Kellerer, "Considerations on the random traversal of convex bodies and solutions for general cylinders," *Radiation Research*, vol. 47, no. 2, pp. 359–376, 1971.

[63] P. Bradley, *The Development of a Novel Silicon Microdosimeter for High LET Radiation Therapy*. PhD thesis, University of Wollongong, 2000.

[64] T. K. P. Metcalfe and P. Hoban, *The Physics of Radiotherapy x-rays and electrons*. Medical Physics Publishing, second ed., 2007.

[65] H. Paganetti, A. Niemierko, M. Ancukiewicz, L. E. Gerweck, M. Goitein, J. S. Loeffler, and H. D. Suit, "Relative biological effectiveness (rbe) values for proton beam therapy," *International Journal of Radiation Oncology Biology Physics*, vol. 53, no. 2, pp. 407 – 421, 2002.

[66] G. Barendsen, "Impairment of the proliferative capacity of human cells in culture by -particles with differing linear-energy transfer," *International Journal of Radiation Biology and Related Studies in Physics, Chemistry and Medicine*, vol. 8, no. 5, pp. 453–466, 1964.

[67] Y. Kase, T. Kannai, Y. Matsumotot, Y. Furusawa, H. Okamato, T. Asaba, M. Sakama, and H. Shinoda, "Mirodosimetric measurements and estimation of human cell survival for heavy-ion beams," *Radiation Research Society*, vol. 166, pp. 629–638, 2006.

[68] L. Jones, P. Hoban, and P. Metcalfe, "The use of the linear quadratic model in radiotherapy: a review," *Australasian Physics & Engineering Sciences in Medicine*, vol. 24, no. 3, pp. 132–146, 2001.

[69] M. Scholz and G. Kraft, "Track structure and the calculation of biological effects of heavy charged particles," *Advances in Space Research*, vol. 18, pp. 5–14, 1996.

[70] R. B. Hawkins, "A statistical theory of cell killing by radiation of varying linear energy transfer," *Radiation Research*, vol. 140, pp. 366–374, 1994.

[71] H. H. Rossi, "The effects of small doses of ionizing radiation," *Physics in Medicine and Biology*, vol. 15, no. 2, p. 255, 1970.

[72] B. Jones and R. G. Dale, "Estimation of optimum dose per fraction for high let radiations: Implications for proton radiotherapy," *International Journal of Radiation Oncology*Biology*Physics*, vol. 48, no. 5, pp. 1549 – 1557, 2000.

[73] T. I. Marshall, P. Chaudhary, A. Michaelidesov, J. Vachelov, M. Davdkov, V. Vondrek, G. Schettino, and K. M. Prise, "Investigating the implications of a variable rbe on proton dose fractionation across a clinical pencil beam scanned spread-out bragg peak," *International Journal of Radiation Oncology*Biology*Physics*, vol. 95, no. 1, pp. 70 – 77, 2016. Particle Therapy Special Edition.

[74] Y. Kase, W. Yamashita, N. Matsufuji, K. Takada, T. Sakae, Y. Furusawa, H. Yamashita, and S. Murayama, "Microdosimetric calculation of relative biological effectiveness for design of therapeutic proton beams," *Journal of Radiation Research*, vol. 54, no. 3, p. 485, 2013.

[75] `http://www.fwt.com/detector/support/LET12_manual.PDF`.

[76] J. F. Dicello, H. I. Amols, M. Zaider, and G. Tripard, "A comparison of microdosimetric measurements with spherical proportional counters and solid-state detectors," *Radiation Research*, vol. 82, no. 3, pp. 441–453, 1980.

[77] R. Siegele, D. D. Cohen, and N. Dytlewski, "The ansto high energy heavy ion microprobe," *Nuclear Instruments and Methods in Physics Research Section B: Beam Interactions with Materials and Atoms*, vol. 158, no. 1, pp. 31 – 38, 1999.

[78] A. B. Rosenfeld, "Novel detectors for silicon based microdosimetry, their concepts and applications," *Nuclear Instruments and Methods in Physics Research Section A: Accelerators, Spectrometers, Detectors and Associated Equipment*, vol. 809, pp. 156 – 170, 2016. Advances in detectors and applications for medicine.

[79] L. Chartier, *A new generation of thin silicon microdosimeters for heavy ion therapy*. PhD thesis, University of Wollongong, 2014.

[80] L. Chartier, L. T. Tran, D. Bolst, D. A. Prokopovich, M. I. Reinhard, M. Petasecca, M. Lerch, M. Povoli, A. Kok, N. Matsufuji, M. Nancarrow, and A. B. Rosenfeld, "Characterization of a large area thinned silicon microdosimeter for space and particle therapy," *IEEE Transactions on Nuclear Science*, vol. 62, pp. 3003–3011, Dec 2015.

[81] A. L. Ziebell, W. H. Lim, M. I. Reinhard, I. Cornelius, D. A. Prokopovich, R. Siegele, A. S. Dzurak, and A. B. Rosenfeld, "A cylindrical silicon-on-insulator microdosimeter: Charge collection characteristics," *IEEE Transactions on Nuclear Science*, vol. 55, pp. 3414–3420, Dec 2008.

[82] N. S. Lai, W. H. Lim, A. L. Ziebell, M. I. Reinhard, A. B. Rosenfeld, and A. S. Dzurak, "Development and fabrication of cylindrical silicon-on-insulator microdosimeter arrays," *IEEE Transactions on Nuclear Science*, vol. 56, pp. 1637–1641, June 2009.

[83] J. Livingstone, D. A. Prokopovich, M. L. F. Lerch, M. Petasecca, M. I. Reinhard, H. Yasuda, M. Zaider, J. F. Ziegler, V. L. Pisacane, J. F. Dicello, V. L. Perevertaylo, and A. B. Rosenfeld, "Large area silicon microdosimeter for dosimetry in high let space radiation fields:charge collection study," *IEEE Transactions on Nuclear Science*, vol. 59, pp. 3126–3132, Dec 2012.

[84] A. Kok, G. Anelli, C. DaVia, J. Hasi, P. Jarron, C. Kenney, J. M. adn S. Parker, J. Segal, S. Watts, and E. Westbrook, "Inactivation of human kidney cells by highenergy monoenergetic heavy-ion beams," *Nuclear Instruments and Methods in Physics Research A*, vol. 560, pp. 127–130, 2006.

[85] P. D. Bradley and A. B. Rosenfeld, "Tissue equivalence correction for silicon microdosimetry detectors in boron neutron capture therapy," *Medical Physics*, vol. 25, no. 11, pp. 2220–2225, 1998.

[86] S. Guatelli, M. I. Reinhard, B. Mascialino, D. A. Prokopovich, A. S. Dzurak, M. Zaider, and A. B. Rosenfeld, "Tissue equivalence correction in silicon microdosimetry for protons characteristic of the leo space environment," *IEEE Transaction on Nuclear Science*, vol. 55, pp. 3407–3413, 2008.

[87] L. T. Tran, S. Guatelli, D. A. Prokopovich, M. Petasecca, M. L. F. Lerch, M. I. Reinhard, J. F. Ziegler, M. Zaider, and A. B. Rosenfeld, "A novel silicon microdosimeter using 3d sensitive volumes: Modeling the response in neutron fields typical of aviation," *IEEE Transaction on Nuclear Science*, vol. 61, no. 4, pp. 1552–1557, 2014.

[88] D. Johnson, Y. Chen, and S. Ahmad, “Dose and linear energy transfer distributions of primary and secondary particles in carbon ion radiation therapy: A monte carlo simulation study in water,” *Journal of Medical Physics*, vol. 40, no. 4, pp. 214–219, 2015.

[89] Nose, Hiroyuki, Aso, Tsukasa, Kase, Yuki, Matsufuji, Naruhiro, and T. Kanai, “Verification of biological dose calculation for carbon ion therapy with a monte carlo method,” *Journal of Medical Physics*, vol. 28, no. 4, pp. 131–141, 2009.

[90] `http://www.jcprg.org/master/exfor/D/d0589.txt`.

[91] J. Dudouet, D. Cussol, D. Durand, and M. Labalme, “Benchmarking geant4 nuclear models for hadron therapy with 95 mev/nucleon carbon ions,” *Phys. Rev. C*, vol. 89, p. 054616, May 2014.

[92] V. N. Ivanchenko, O. Kadri, M. Maire, and L. Urban, “Geant4 models for simulation of multiple scattering,” *Journal of Physics: Conference Series*, vol. 219, no. 3, p. 032045, 2010.

[93] E. Haettner, “Experimental study on carbon ion fragmentation in water using gsi therapy beams,” Master’s thesis, KTH Engineering Sciences, 2006.

[94] H. Geissel, H. Weick, C. Scheidenberger, R. Bimbot, and D. Gards, “Experimental studies of heavy-ion slowing down in matter,” *Nuclear Instruments and Methods in Physics Research Section B: Beam Interactions with Materials and Atoms*, vol. 195, no. 12, pp. 3 – 54, 2002.

[95] `http://physics.nist.gov/PhysRefData/Star/Text/ESTAR.html`.

[96] `https://physics.nist.gov/PhysRefData/Star/Text/PSTAR.html`.

[97] `http://http://www.nist.gov/pml/data/xraycoef/`.

[98] N. Matsufuji, M. Komori, H. Sasaki, K. Akiu, M. Ogawa, A. Fukumura, E. Urakabe, T. Inaniwa, T. Nishio, T. Kohno, and T. Kanai, “Spatial fragment distribution from a therapeutic pencil-like carbon beam in water,” *Physics in Medicine and Biology*, vol. 50, no. 14, p. 3393, 2005.

[99] `http://book.bionumbers.org/how-big-is-a-human-cell/`.

[100] J. R. Masters, “Hela cells 50 years on: the good, the bad and the ugly,” *Nature Reviews Cancer*, vol. 2, p. 289320, 2002.

[101] `http://bionumbers.hms.harvard.edu//bionumber.aspx?id=101402&ver=14`.

[102] D. J. SMITH, E. A. GAFFNEY, J. R. BLAKE, and J. C. KIRKMAN-BROWN, "Human sperm accumulation near surfaces: a simulation study," *Journal of Fluid Mechanics*, vol. 621, p. 289320, 2009.

[103] H. Nikjoo, D. Emfietzoglou, T. Liamsuwan, R. Taleei, D. Liljequist, and S. Uehara, "Radiation track, dna damage and responsea review," *Reports on Progress in Physics*, vol. 79, no. 11, p. 116601, 2016.

[104] G. Maul and L. Deaven, "Quantitative determination of nuclear pore complexes in cycling cells with differing dna content," *The Journal of Cell Biology*, vol. 73, no. 3, pp. 748–760, 1977.

[105] MATLAB, *version 8.5.0 (R2015a)*. Natick, Massachusetts: The MathWorks Inc., 2015.

[106] P. D. Bradley, A. B. Rosenfeld, and M. Zaider, "Solid state microdosimetry," *Nuclear Instruments and Methods in Physics Research B*, vol. 184, pp. 135–157, 2001.

[107] J. Kiefer and H. Straaten, "A model of ion track structure based on classical collision dynamics (radiobiology application)," *Physics in Medicine Biology*, vol. 31, no. 11, p. 1201, 1986.

[108] F. Tommasino, E. Scifoni, and M. Durante, "New ions for therapy," *International Journal of Particle Therapy*, vol. 2, no. 3, pp. 428–438, 2015.

[109] T. Inaniwa, N. Kanematsu, K. Noda, and T. Kamada, "Treatment planning of intensity modulated composite particle therapy with dose and linear energy transfer optimization," *Physics in Medicine Biology*, vol. 62, no. 12, p. 5180, 2017.

[110] M. Rovituso and C. L. Tessa, "Nuclear interactions of new ions in cancer therapy: impact on dosimetry," *Translational Cancer Research*, vol. 6, 2017.

[111] M. Krämer and M. Durante, "Ion beam transport calculations and treatment plans in particle therapy," *The European Physical Journal D*, vol. 60, pp. 195–202, Oct 2010.

[112] K. Michael, S. Emanuele, S. Christoph, R. Marta, T. Walter, M. Andreas, K. Robert, K. Wilma, B. Stephan, T. Thomas, P. Katia, and D. Marco, "Helium ions for radiotherapy? physical and biological verifications of a novel treatment modality," *Medical Physics*, vol. 43, no. 4, pp. 1995–2004.

[113] `https://www.raysearchlabs.com/`.

[114] C. Kurz, A. Mairani, and K. Parodi, “First experimental-based characterization of oxygen ion beam depth dose distributions at the heidelberg ion-beam therapy center,” *Physics in Medicine Biology*, vol. 57, no. 15, p. 5017, 2012.

[115] E. A. Blakely, C. A. Tobias, T. C. Yang, K. C. Smith, and J. T. Lyman, “Inactivation of human kidney cells by highenergy monoenergetic heavy-ion beams,” *Rev. Mod. Phys.*, vol. 80, pp. 122–160, Feb 1979.

[116] I. Schall, D. Schardt, H. Geissel, H. Irnich, E. Kankeleit, G. Kraft, A. Magel, M. Mohar, G. Mnzenberg, F. Nickel, C. Scheidenberger, and W. Schwab, “Charge-changing nuclear reactions of relativistic light-ion beams (5 z 10) passing through thick absorbers,” *Nuclear Instruments and Methods in Physics Research Section B: Beam Interactions with Materials and Atoms*, vol. 117, no. 3, pp. 221 – 234, 1996.

[117] M. Krämer, E. Scifoni, F. Schmitz, O. Sokol, and M. Durante, “Overview of recent advances in treatment planning for ion beam radiotherapy,” *The European Physical Journal D*, vol. 68, p. 306, Oct 2014.

[118] S. Yonai, N. Kanematsu, M. Komori, T. Kanai, Y. Takei, O. Takahashi, Y. Isobe, M. Tashiro, H. Koikegami, and H. Tomita, “Evaluation of beam wobbling methods for heavy-ion radiotherapy,” *Medical Physics*, vol. 35, no. 3, pp. 927–938, 2008.

[119] `http://wrmiss.org/workshops/sixteenth/Ploc.pdf.`

[120] S. Yonai *et al.*, “Monte carlo study on secondary neutrons in passive carbon-ion radiotherapy: Identification of the main source and reduction in the secondary neutron dose,” *Medical Physics*, 2009.

[121] L. T. Tran, L. Chartier, D. Bolst, J. Davis, D. A. Prokopovich, A. Pogossov, S. Guatelli, M. I. Reinhard, M. Petasecca, M. L. Lerch, N. Matsufuji, M. Povoli, A. Summanwar, A. Kok, M. Jackson, and A. B. Rosenfeld, “In-field and out-of-file application in 12c ion therapy using fully 3d silicon microdosimeters,” *Radiation Measurements*, vol. 115, pp. 55 – 59, 2018.

[122] T. Inaniwa and N. Kanematsu, “Adaptation of stochastic microdosimetric kinetic model for charged-particle therapy treatment planning,” *Physics in Medicine & Biology*, vol. 63, p. 095011, may 2018.

[123] S. I. Parker, C. J. Kenney, and J. Segal, “3da proposed new architecture for solid-state radiation detectors,” *Nuclear Instruments and Methods in Physics Research Section A: Accelerators, Spectrometers, Detectors and Associated Equipment*, vol. 395, no. 3, pp. 328–343, 1997.

[124] L. T. Tran, L. Chartier, D. A. Prokopovich, D. Bolst, M. Povoli, A. Summanwar, A. Kok, A. Pogossov, M. Petasecca, S. Guatelli, M. I. Reinhard, M. Lerch, M. Nancarrow, N. Matsufuji, M. Jackson, and A. B. Rosenfeld, "Thin silicon microdosimeter utilizing 3-d mems fabrication technology: Charge collection study and its application in mixed radiation fields," *IEEE Transactions on Nuclear Science*, vol. 65, pp. 467–472, Jan 2018.

[125] H. Paganetti, "Relative biological effectiveness (rbe) values for proton beam therapy. variations as a function of biological endpoint, dose, and linear energy transfer," *Physics in Medicine Biology*, vol. 59, no. 22, p. R419, 2014.

[126] "ICRU Report 78-Prescribing, recording, and reporting proton-beam therapy," *International Commission on Radiation Units and Measurements*, 2007.

[127] H. Paganetti, "Relating the proton relative biological effectiveness to tumor control and normal tissue complication probabilities assuming interpatient variability in /," *Acta Oncologica*, vol. 56, no. 11, pp. 1379–1386, 2017. PMID: 28918679.

[128] C. R. Peeler, D. Mirkovic, U. Titt, P. Blanchard, J. R. Gunther, A. Mahajan, R. Mohan, and D. R. Grosshans, "Clinical evidence of variable proton biological effectiveness in pediatric patients treated for ependymoma," *Radiotherapy and Oncology*, vol. 121, no. 3, pp. 395 – 401, 2016.

[129] N. Bassler, O. Jkel, C. S. Sndergaard, and J. B. Petersen, "Dose- and let-painting with particle therapy," *Acta Oncologica*, vol. 49, no. 7, pp. 1170–1176, 2010.

[130]

[131] D. A. Granville and G. O. Sawakuchi, "Comparison of linear energy transfer scoring techniques in monte carlo simulations of proton beams," *Physics in Medicine Biology*, vol. 60, no. 14, p. N283, 2015.

[132] M. A. Corts-Giraldo and A. Carabe, "A critical study of different monte carlo scoring methods of dose average linear-energy-transfer maps calculated in voxelized geometries irradiated with clinical proton beams," *Physics in Medicine Biology*, vol. 60, no. 7, p. 2645, 2015.

[133] S. J. McMahon, H. Paganetti, and K. M. Prise, "Let-weighted doses effectively reduce biological variability in proton radiotherapy planning," *Physics in Medicine Biology*, vol. 63, no. 22, p. 225009, 2018.

[134] J. B. Farr, F. Dessy, O. De Wilde, O. Bietzer, and D. Schnenberg, "Fundamental radiological and geometric performance of two types of proton beam modulated discrete scanning systems," *Medical Physics*, vol. 40, no. 7, p. 072101.

[135] L. T. Tran, L. Chartier, D. A. Prokopovich, M. I. Reinhard, M. Petasecca, S. Guatelli, M. L. F. Lerch, V. L. Perevertaylo, M. Zaider, N. Matsufuji, M. Jackson, M. Nancarrow, and A. B. Rosenfeld, "3d-mesa bridge silicon microdosimeter: Charge collection study and application to rbe studies in^{12}cradiation therapy," *IEEE Transactions on Nuclear Science*, vol. 62, pp. 504–511, April 2015.

[136] L. T. Tran, L. Chartier, D. Bolst, D. A. Prokopovich, S. Guatelli, M. Nancarrow, M. I. Reinhard, M. Petasecca, M. L. F. Lerch, V. L. Pereverlaylo, N. Matsufuji, D. Hinde, M. Dasgupta, A. Stuchbery, M. Jackson, and A. B. Rosenfeld, "3D silicon microdosimetry and RBE study using ^{12}C ion of different energies," *IEEE Transactions on Nuclear Science*, vol. 62, pp. 3027–3033, Dec 2015.

[137] `https://physics.nist.gov/PhysRefData/Star/Text/ASTAR.html`.